Escherichia coli Chromosomes in the Crowded Cellular Environment

A Dissertation Presented for the

Doctor of Philosophy

Degree

The University of Tennessee, Knoxville

Da Yang

May 2020

to light, and

the virtue of ignorance...

The Blind Men and the Elephant.

A Hindoo Fabel

— a poem by John Godfrey Saxe

I.
It was six men of Indostan
To learning much inclined,
Who went to see the Elephant
(Though all of them were blind),
That each by observation
Might satisfy his mind.

II.
The *First* approached the Elephant,
And happening to fall
Against his broad and sturdy side,
At once began to bawl:
"God bless me!—but the Elephant
Is very like a wall!"

III.
The *Second*, feeling of the tusk,
Cried: "Ho!—what have we here
So very round and smooth and sharp?
To me 't is mighty clear
This wonder of an Elephant
Is very like a spear!"

IV.
The *Third* approached the animal,
And happening to take
The squirming trunk within his hands,
Thus boldly up and spake:
"I see," quoth he, "the Elephant
Is very like a snake!"

V.
The *Fourth* reached out his eager hand,
And felt about the knee.
"What most this wondrous beast is like
Is mighty plain," quoth he;
"'T is clear enough the Elephant
Is very like a tree!"

VI.
The *Fifth*, who chanced to touch the ear,
Said: "E'en the blindest man
Can tell what this resembles most;
Deny the fact who can,
This marvel of an Elephant
Is very like a fan!"

VII.
The *Sixth* no sooner had begun
About the beast to grope,
Than, seizing on the swinging tail
That fell within his scope,
"I see," quoth he, "the Elephant
Is very like a rope!"

VIII.
And so these men of Indostan
Disputed loud and long,
Each in his own opinion
Exceeding stiff and strong,
Though each was partly in the right,
And all were in the wrong!

MORAL.
So, oft in theologic wars
The disputants, I ween,
Rail on in utter ignorance
Of what each other mean,
And prate about an Elephant
Not one of them has seen!

Acknowledgments

First and foremost, the unwavering support from my parents has made this work a possibility. More importantly, they have given me an intellectual intuition of the physical world.

Secondly, I would like to express my profound gratitude to my advisor Prof. Jaan Männik. He has allocated funding to support this work. He has given me directions for research. He has worked tirelessly to get our work published. He has taught me how to observe.

Additionally, I sincerely thank my advisor, Männik, Dr. Soctt T. Retterer, and the other members (former or current) of the Männik. Laboratory of Cellular Biophysics for all the stimulus discussions, all the late nights, and all the unforgiving moments. With them, I have grown both professionally and personally. These members are Ryan Hefti, Matthew W. Bailey, Jaana Männik, Anna D. Jennings, Clayton M. Greer, Branndon P. Jones, Bryant E. Walker, and Sriram Tiruvadi Krishnan.

Moreover, I thank Dayrl P. Briggs, Dale K. Hensley, Bernadeta R. Srijanto, Kevin C. Lester, Leslie L. Wilson, Ivan I. Kravchenko, Nick V. Lavrik, and Jason D. Fowlkes for assisting my work in the cleanroom at Oak Ridge National Laboratory. I thank Michael Duff, Deepika Nambiar, and Elizabeth Howell for facilitating the osmolality measurements. I thank Dmitry Voylov, Hongbo Feng, Gao Chen, Jun Yan, Yongfeng Wang, Jiang Liu, Guoliang Li, and Alexander Kisliuk for the precious information and emotional support. I thank Fabai Wu, Cees Dekker, Joe Lutkenhaus, and Rodrigo Reyes-Lamothe for pervading bacterial strains. I thank Tony Shen, Daniel E. Castillo, and George Siopsis for helping me getting started with the dynamics simulations. I thank Conrad L. Woldringh, Arieh Zaritsky, James C. Weisshaar, Alexei P. Sokolov, Maxim Lavrentovich, and Lloyd M. Davis for their insightful and inspiring suggestions, and constant encouragement.

Last but not least, I thank the Department of Physics and Astronomy for taking a chance with me.

Abstract

DNA is a heteropolymer molecule, which carries the genetic information in all cellular organisms. DNA must be compacted by more than a thousandfold to fit into the cells. In bacterial cells, the compaction results in the formation of a distinct organelle-like entity termed the nucleoid, which fills a portion of the cellular volume and harbors chromosomal DNA. The broader question addressed in this dissertation is how the genetic information, embodied in the chromosome, is physically organized.

For bacterial cells, DNA binding proteins, supercoiling, macromolecular crowders, and transient DNA attachments to the cell membrane have all been implicated in affecting the size of the nucleoid. However, it has been unclear how significant the role each of these factors play. In particular, there have been no quantitative measurements on how the concentration of macromolecular crowders in the cell modulates the size of the nucleoid.

To answer this question, we developed three microfluidic lab-on-a-chip platforms enabling us to apply mechanical or osmotic perturbations to cells in various growth conditions and thereby to change the crowder concentration of those cells. We found that a 30% increase in the crowder concentration from their physiological levels led to a 3-fold decrease in the nucleoid's volume. The compaction was anisotropic–higher along the long axes of the cell–at low crowding levels. At higher crowding levels, the nucleoid became spherical, and its compressibility nearly vanished. Results from our Langevin dynamics simulations were in semi-quantitative agreement with these experimental findings.

Moreover, we found that the compressibility of the nucleoid was not affected by cell growth rates nor by a prior halting of transcription. These results implied that in addition to poly-ribosomes, cytoplasmic proteins had a significant contribution in determining the size of the nucleoid. This finding contradicts what has been postulated in this field. In compacting nucleoids, the contribution

from poly-ribosomes dominated at faster growth rates and cytoplasmic proteins at slower rates. Altogether, our results provided further support to the idea that molecular crowding is the major factor in compacting the bacterial DNA to a nucleoid, which forms a phase-separated entity distinct from the rest of the cell.

Table of Contents

1 Introduction and General Information **1**

1.1 Why Study Bacteria? . . . 1

1.2 Genetic Information and Its Flow in Bacteria . . . 3

1.3 Spatial Organization of Genetic Information in *E. coli* . . . 4

1.3.1 Cellular Environment . . . 7

1.3.1.1 Cell Envelope . . . 8

1.3.1.2 Cytoplasm . . . 8

1.3.1.3 Z-Ring and Its Positioning . . . 9

1.4 Polymer Physics Based Estimation of Nucleoid Sizes . . . 11

1.4.1 Chain Models . . . 11

1.4.1.1 The Ideal Chains . . . 11

1.4.1.2 Worm-like Chains and the Kuhn Length . . . 11

1.4.1.3 Excluded Volume Interactions and Self-Avoiding Walks . . . 12

1.4.2 Super Coiled DNA and Randomly Branched Polymer . . . 15

1.4.2.1 DNA Supercoiling and Topology of cccDNA . . . 15

1.4.2.2 Size Estimation of Super Coiled DNA . . . 19

1.5 Further Compaction of the *E. coli* Chromosomal DNA . . . 19

1.5.1 Nucleoid Associated Proteins . . . 20

1.5.2 Structure Units and Macrodomains . . . 22

1.5.3 Effects of Transcription, Translation, and Transertion . . . 23

1.6 Macromolecular Crowding, Phase Separation, and Free Energy . . . 24

1.6.1 Crowding and the Nucleoid as a Phase . . . 24

1.6.2 Size Estimation of Super Coiled DNA by Minimizing Free Energy 27
1.6.2.1 Randomly Branched Polymer 27
1.6.2.2 Coarse-Grained DNA String-Beads 27
1.7 Recent Advances in Understanding Nucleoid Compaction 30
1.8 Outline of This Dissertation 32

2 Materials and Methods **33**
2.1 Bacterial Strains and Growth 33
2.1.1 *E. coli* Strain Construction 33
2.1.2 Culturing *E. coli* Cells 34
2.1.2.1 Preparation for Dead-End Mother-Machine Experiments 34
2.1.2.2 Preparation for Microvalve Experiments 35
2.1.2.3 Preparation for Microanvil Experiments 35
2.1.3 Chemical Treatments of the Bacterial Cells in the Dead-End Mother-Machine Platform 36
2.1.3.1 Hyper-/Hypo-osmotic Treatments of the Bacterial Cells 36
2.1.3.2 Rifampicin Treatment 36
2.1.4 Spectrophotometry 37
2.2 Microscopy and Image Analysis 37
2.2.1 The Imaging System 37
2.2.1.1 Numerical Aperture 37
2.2.1.2 The Camera and Optical Filters 39
2.2.2 Measuring the Point Spread Function 39
2.2.3 Image Analysis 41
2.2.3.1 Cell Axis 41
2.2.3.2 Length Measurements 41
2.2.3.3 Width Measurements 42
2.2.3.4 Determination of Crowder Concentration Based on the Intensity of Fluorescent Reporters 43
2.2.3.5 Estimations of Volume and Aspect Ratio from Lengths and Widths 44
2.3 Statistical Analysis Methods 44

2.4 Material and Fabrication of Microfluidic Chips . . . 45
2.4.1 Material . . . 45
2.4.2 Microchip Fabrication . . . 46
2.5 Fabrication of Silicon Wafers . . . 49
2.5.1 Electron Beam Lithography Layers . . . 49
2.5.2 Photolithography Layers . . . 50
2.6 Stress Analyses of the PDMS Pressure Actuators . . . 51
2.7 Langevin Dynamics Simulations . . . 51
2.7.1 The Procedure . . . 51
2.7.2 Velocity Verlet Algorithm . . . 52
2.7.3 Interactions . . . 53
2.7.4 Fluctuation-Dissipation Theorem and the Langevin Equation . . . 54
2.7.5 The Model . . . 55
2.7.6 Dynamical Properties of the Model . . . 57

3 Development and Characterization of Microfluidic Platforms 65

3.1 Mother Machine Platform . . . 66
3.1.1 Motivation . . . 66
3.1.2 Design and Fabrication of Mother-Machine Devices . . . 67
3.1.3 Dependence of Mother Cell Growth on the Channel Width . . . 68
3.1.4 Dependence of Mother Cell Growth on Channel Lengths . . . 73
3.1.5 Mechanical Impediments to Cell Growth in 1D Cultures . . . 75
3.1.6 Cell Shape Shows Adaptations to Channel Geometry . . . 80
3.1.7 Is Mass Transport Limiting Cell Growth in Channels? . . . 81
3.1.8 Mechanical Constraints to Cell Growth . . . 85
3.1.9 Implications to Bacterial Growth in Microfluidic Devices and in Natural Microenvironments . . . 86
3.2 Development and Testing of Microvalves . . . 87
3.2.1 Motivation . . . 87
3.2.2 Design of the Microvalve Devices . . . 88
3.2.3 Modeling . . . 89

3.2.4 Comparison of modeling with experimentally measured flow channel profiles . 91
3.2.5 Cell deformations using pressure actuated valves 93
3.2.6 Remarks 95
3.3 Development and Testing of Microanvils 97
3.3.1 Design of the Microanvil Devices 97
3.3.2 Stress Analyses of the Microanvils 97
3.3.3 Cellular Response to the Microanvils 99
3.3.4 Compression of Nucleoids by Microvalves 101

4 Macromolecular Crowding Compacts *Escherichia coli* Chromosomes into Nucleoids 103

4.1 Motivations 103
4.2 Compaction of the Nucleoid under Osmotic Shock Is Anisotropic and Larger than Compaction of the Cytoplasm 104
4.3 Nucleoid Compaction Is a Second Order Phase Transition and Independent of Growth Conditions 112
4.4 Mechanical Squeezing Measurements Confirm Osmotic Shock Data 121
4.5 Transertion Linkages and Crowding by Polysomes Have a Limited Effect on Nucleoid Size in Slow Growth Conditions 124
4.6 Effect of Osmotic Shock on Nucleoids after Rifampicin Treatment 127
4.7 Crowding Model Qualitatively Agrees with Experimental Findings 132
4.8 Smooth Coil-Globule Transition of Nucleoids in the Cellular Environment 135
4.9 Anisotropic Compressibility of the Nucleoid and Bottlebrush-Like Organization of the Chromosome 137
4.10 Interplay of Different Crowders in Compacting the Nucleoid 138
4.11 Role of Transcription in Determining the Global Size of the Nucleoid 140
4.12 Physiological Consequences of Nucleoid Size 140

5 Concluding Remarks 143

6 Outlook on Future Work 146

6.1 Design of Valve Chips with Tapered Anvils 147

6.1.1 Design of Valve Post Chips with Tapered Posts . . . 147
6.1.2 Searching for Corresponding Reactive Ion Etching Parameters . . . 151
6.2 Septum Constriction Induces Partitioning of Nucleoids During Cell Division . . . 151
6.2.1 Motivation . . . 151
6.2.2 Mechanical Squeezing Induces Movement of Nucleoids During Cell Division . 151
6.2.3 Equilibrium Thermodynamics Allows Triple Deletion Cells to Survive . . . 153
6.2.4 Mode of Septum Constriction Has No Effect on Cell Division Success Rate . 156
6.2.5 Longer Cells Are More Likely to Survive Division Plane Offset . . . 156
6.2.6 Further Experiments . . . 158

Bibliography **161**

Appendices **184**

A Control-Layer PDMS Holder . . . 185
B Protocol of Fabricating the First Electron Beam Lithography Layer on a Silicon Wafer 186
B.1 Exposing a Wafer Spin Coated With ZEP520A to Electron Beam . . . 186
B.2 Developing ZEP520A at Room Temperature . . . 186
B.3 Chromium Physical Vapor Deposition . . . 187
B.4 Lift-Off e-Beam Resist at Room Temperature . . . 187
B.5 Reactive Ion Etching . . . 187
C A Sample ESPResSo Script in the Scripting Language Tcl . . . 189
D Estimation of Crowder Dimensions . . . 204
E License . . . 207

Vita **208**

List of Tables

2-1 List of *E. coli* strains used in this dissertation 40

4-1 The average cytoplasm and nucleoid dimensions and doubling times. 106
4-2 List of mother-machine measurements 108
4-3 Slopes of linear fittings shown in Figure 4-3 and 4-5. 109
4-4 Estimation of ribosome and protein numbers is slow and moderately fast growth conditions. 119

List of Figures

1-1 Leeuwenhoek's single lens microscopes and first description of bacteria. 2
1-2 Primary and secondary structure of dsDNA. 5
1-3 The processes of the central dogma. 6
1-4 Map of a typical *E. coli* gnome and schematic of an *E. coli* cell. 7
1-5 Four molecular mechanisms that have been identified in spatial coordination between the chromosome and divisome in *E. coli*. 10
1-6 Chain configurations and water channel for a confined chain. 14
1-7 TEM image of a liberated *E. coli* chromosome. 16
1-8 *E. coli* topoisomerase. 18
1-9 A schematic representation of the *E. coli* chromosome and of liberated nucleoids. . 20
1-10 DNA binding properties of NAPs. 21
1-11 The coarse-grained model of bacterial chromosomal DNA. 22
1-12 Various effects on nucleoid conformation. 25
1-13 Collapse of a flexible chain by crowding agents. 29
1-14 *In vitro* and numerical results of dsDNA compaction. 31

2-1 The imaging system. 38
2-2 Measuring the point spread function. 40
2-3 The chemistry of oligomeric PDMS curing into elastomer. 46
2-4 Process flow for multilayer soft-lithography. 48
2-5 The WCA and the FENE Potentials 54
2-6 A typical conformation of one ring polymer in a cylindrical confinement visualized by VMD. 56

2-7 Dynamical properties of single polymers . . . 57
2-8 Anomalous diffusion exponents of open and closed chains in various cylindrical confinements. . . . 59
2-9 Anomalous diffusion closed-chained polymers in various volume fractions of crowders (Part I). . . . 61
2-10 Projected sizes of the ring model at various crowder levels. . . . 62
2-11 Anomalous diffusion closed-chained polymers in various volume fractions of crowders (Part II). . . . 63

3-1 Design of the mother machine platform. . . . 69
3-2 Bacterial growth in channels. . . . 69
3-3 Images of cells in a 0.7 μm wide and 15 μm long channel. . . . 70
3-4 Dimensions of the mother cell and its doubling times in dead-end channels of different widths. . . . 71
3-5 Coefficient of variations for cell length, width and volume distributions. . . . 72
3-6 Dimensions and doubling times of mother cells in channels of different lengths. . . . 74
3-7 Mother cell length, width, volume and doubling time as a function of channel length for channels with and without BSA passivation. . . . 76
3-8 Cell growth in 100 μm long channels. . . . 78
3-9 Cell growth in 200 μm long channels with 0.1% BSA. . . . 79
3-10 Comparing modeling and experimental data on doubling times. . . . 83
3-11 Design of microvalve device experiment. . . . 88
3-12 Modeling the closure of small pressure actuated valves. . . . 90
3-13 Comparison of modeling and actual valve closure. . . . 92
3-14 Application of pressure actuated valves to study effects of uniaxial compression to *E. coli* cells. . . . 94
3-15 Design of the microanvil device. . . . 98
3-16 Stress analyses of the microanvils. . . . 99
3-17 Cellular response to the microanvil at various control pressure. . . . 100
3-18 Artificial cell division. . . . 101
3-19 Nucleoids response to the microanvil. . . . 102

4-1 Compaction of the cytoplasm and nucleoid by hyperosmotic shocks. 105
4-2 Kinetics of the cytoplasm and nucleoid compaction during hyperosmotic shocks. . . 107
4-3 Change in nucleoid dimensions as a function of the change in external osmolality. . 110
4-4 Comparison of nucleoid widths during 1 M NaCl shock to the widths of 100 nm fluorescent beads. 111
4-5 Measured widths and aspect ratios of nucleoids. 113
4-6 Comparison of cellular crowder concentrations determined using two different methods (Part I). 114
4-7 Extracting principle curves of the change in nucleoid dimensions as a function of the change in crowder concentrations. 115
4-8 Change in nucleoid dimensions as a function of the change in crowder concentration. 116
4-9 Comparison of cellular crowder concentrations determined using two different methods (Part II). 117
4-10 Changes of cell and nucleoid dimensions under osmotic shock in medium where K^+ are substituted by an equal amount of Na^+. 120
4-11 Measurements of nucleoid compaction during cell squeezing. 122
4-12 Comparison of data from squeezing measurements to osmotic shock measurements. 123
4-13 Change in nucleoid dimensions under rifampicin treatment in moderately fast and slow growth conditions. 125
4-14 Growth curves prior to and during rifampicin treatment. 126
4-15 Effect of osmotic shock after rifampicin treatment in slow growth. 128
4-16 Effect of osmotic shock after rifampicin treatment in moderately fast growth. 129
4-17 Nucleoid length as a function of normalized cell cycle time. 130
4-18 Nucleoid widths before and during different treatments. 131
4-19 Nucleoid images before and after rifampicin treatment. 133
4-20 Comparing modeled and observed nucleoids. 136
4-21 Nucleoid homeostasis in the presence of crowders. 142

6-1 Finite element analysis (Part II). 148
6-2 Finite element analysis (Part III). 149
6-3 Finite element analysis (Part I). 150

6-4 RIE for tapered anvils (Part I). 152
6-5 RIE for tapered anvils (Part II). 153
6-6 Nucleoid deformation and displacement due to squeezing 154
6-7 Effect of septum closing with various speed. 155
6-8 Parameters describing the dependencies of cell division success rate on the offset of division plane placement. 157
6-9 Success rate for asymmetric cell divisions of different mode of septum closing. . . . 159
6-10 Success rate for asymmetric cell divisions of various cell lengths. 160

List of Attachments

• Supplementary Movies

M3-1.avi Cells growing in a $0.8 \times 15\ \mu m^2$ channel.

M3-2.avi Cells growing in a $0.9 \times 20\ \mu m^2$ channel.

M3-3.avi Cells moving out from a $0.7\ \mu m$ channel.

M3-4.avi Cells in a $100\ \mu m$ long channel w/o BSA.

M3-5.avi Cells in another $100\ \mu m$ long channel w/o BSA.

M3-6.avi A long channel with cells grown tilted relative to the channel axis in the initial stages of pressure buildup, the broadening is not uniform.

M3-7.avi Another long channel with cells grown tilted relative to the channel axis in the initial stages of pressure buildup, the broadening is not uniform.

M3-8.avi Cells in a $100\ \mu m$ long channel with BSA.

M4-1.avi Slow growing cells treated with 1.0 M NaCl.

M4-2.avi Moderately fast growing cells treated with 1.0 M NaCl.

M4-3.avi Slow growing cells squeezed using the microanvil device.

M4-4.avi Slow growing cells treated with Rifampicin then 0.6 M NaCl.

M4-5.avi Moderately fast growing cells treated with Rifampicin then 1.0 M NaCl.

Chapter 1

Introduction and General Information

The biophysics of *Escherichia coli* (*E. coli*) chromosomes is the subject of study for this dissertation. At first glance, the bacterium merely grows and divides. Over a cell cycle (from one cell division to the next) of an *E. coli* cell, the chromosome elongates as the cell envelope elongates, and separate into two sister chromosomes just before the cell divides. Carefully observations have revealed that the intracellular molecular machines, smaller than the wavelength of viable light, operate at astonishing speed and precision. Nevertheless, though the body of knowledge of the molecular machinery is extensive, the level of compaction (over 1000 fold) of the *E. coli* chromosomes could not be fully explained. The broader question addressed in this dissertation is how the genetic information, embodied in the chromosome, is physically organized.

1.1 Why Study Bacteria?

In 1676, Antonie Philips van Leeuwenhoek, a cloth merchant from Delft, the Netherlands, first observed bacteria through the single-lens microscope of his own making (Figure 1-1 A) [Por76; oEB01]. In 1683, his drawing of bacteria was given in a letter to the Royal Society (No. 39, Figure 1-1 B). Ever since the letter, advances in microscopy have been driving discoveries related to bacteria. Nevertheless, the next advance in bacteriology had to wait for some two hundred years–in part, because Leeuwenhoek never revealed some critical techniques of his lens making and no one was able to see bacteria again until over a century later. In the 1800s, the germ theory of disease was formally established, and so was bacteriology [Wor05]. From then on, the study of

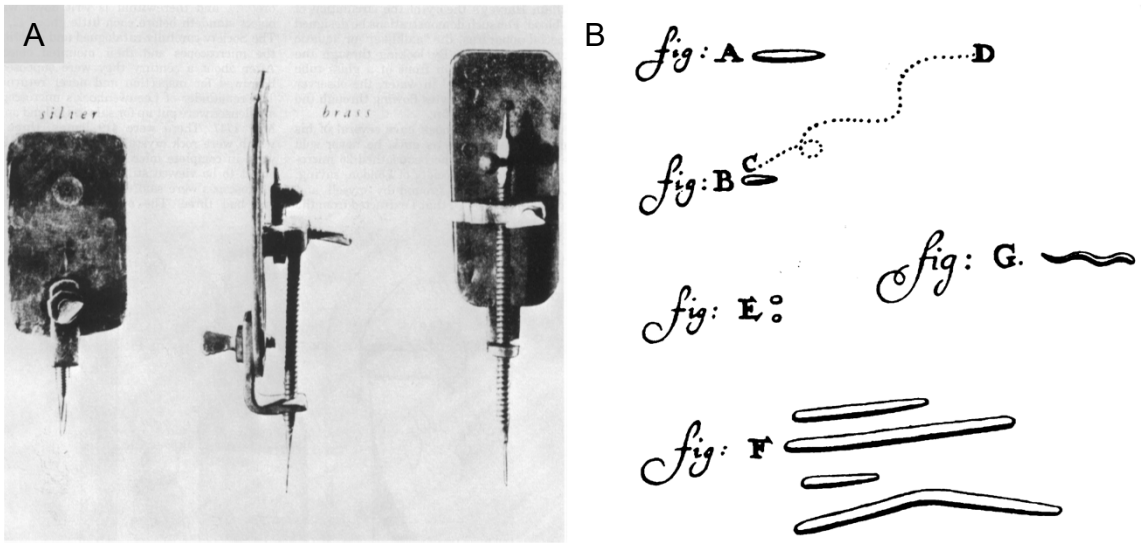


Figure 1-1 : Leeuwenhoek's single lens microscope and first description of bacteria. (A) Three microscopes made and used by Leeuwenhoek between 1673 and 1723. Left, Front or viewing side showing small lens in the metal plate; center longtitudinal view; right back view of instrument. (B) Leeuwenhoek's drawings of bacteria (*bacilli*, *cocci*, *spirillum*) from the human mouth as described in letter no. 39 to the Royal Society, 17 September 1683. Both panels of this figure are reproduced from Porter (1976) [Por76].

bacteria has been chiefly motivated by questions related to health. The revelation of the mutualistic relationship (mutual dependence) between us and our gastrointestinal microbiota did not happen until modern times [SS16]. It is now realized that an individual is not just the mammalian cells but also includes one's microbiome, the bacterial communities covering one's skin, in one's digestive tract, and other openings.

Not only in and around us do bacteria live. By taxonomic groups, the bacteria kingdom makes up the second-largest portion of the biomass on earth. A study surveyed the total mass of carbon contended in different taxa. The study finds that bacteria make up about 15% of the total biomass on earth, while the entire humankind together makes up about 0.01% [BOPM18]. More importantly, the ecological functions of bacteria are vital to other taxa, such as nitrogen fixation, vitamin B-12 syntheses, and biodegradation [FCS+13; WB18]. Foremostly, nitrogen as a chemical element exists in all nucleic acids, which carry the blueprints of life, and amino acids, which are the building blocks of proteins. Nevertheless, many organisms cannot utilize atmospheric nitrogen. In nitrogen fixation, atmospheric nitrogen molecules (N_2) are converted to ammonia (NH_3), which can be used

by plants as a supply of nitrogen. The biofixation of nitrogen is only achieved by bacteria. While lightning also produces a small amount of nitrates (NO_x), 98% (by weight of nitrogen atoms) of the global natural source of reactive nitrogen (N_r) are fixated by bacteria [FCS+13] . Meanwhile, vitamin B-12 is synthesized only by certain bacteria and archaeons, but not by plants [WB18]. Last but not least, as the chief decomposer of metabolically inactive animal tissues and wastes of carnivores, bacteria recycle a significant portion of the chemical elements for the ecosystem at large. Furthermore, because of their robustness in growth and relative simplicity in structure, bacteria have been engineered to produce biomolecules by large volumes, such as insulin [BBS+14] and soon–vitamin B-12 [FKZ17].

Much of what we know of bacterial behaviors and physical and chemical principles governing their function have been derived from studies of few organisms. These so-called model organisms include *Escherichia coli* (*E. coli*), *Bacillus subtilis*, *Caulobacter crescentus*, and *Vibrio fluvialis*. Of these four, *E. coli* is the most studied. There are extensive studies into its genetic, physiology, biochemistry, and molecular biology mechanisms. Because of that, *E. coli* will continue to be a preferred model system for prokaryotic research [JCZ13; SG01]. Taking the wealth of information available for this organism and the ease to cultivate and manipulate its genetic information, *E. coli* is subject of study for this dissertation. The broader question addressed in this dissertation is how the genetic information is physically organized in the bacterial cell.

1.2 Genetic Information and Its Flow in Bacteria

It is a truth universally acknowledged that deoxyribonucleic acid (DNA) carries genetic information from generation to generations in all cellular organisms. Before putting the organization of DNA into a cellular context, we briefly discuss its fundamental biochemistry. The polymeric chains of DNA are composed of four different deoxyribonucleic nucleobases (adenine [A], thymine [T], cytosine [C], and guanine [G]). In general, two DNA chains are intertwined (dsDNA) and form a right-handed double-helical structure. The two helices have complementary chemical composition. For each A (resp. G) base in one strand, a corresponding T (resp. C) base is in the other strand, and *vice versa*. These complementary bases are hold together via hydrogen bonds. There are two hydrogen bonds in an $A=T$ pair and three hydrogen bonds in a $G\equiv C$ pair. The double-helical structure gives dsDNA high rigidity compared to most chemically synthesized polymers

(See Figure 1-2). For lengths $\leq 50\ nm$, dsDNA can be considered as a stiff rod while for most synthetic organic polymers the corresponding length regime is typically $1 \sim 2\ nm$.

"Biological information is stored in DNA as the sequence of bases [Bot15]." And base pairing makes the dsDNA a redundant information storage. This information is used by a cell to synthesize different ribonucleic acids (RNAs) and proteins. The latter carry out essentially all cellular chemical processes including duplicating dsDNA itself. However, the synthesis of proteins does not use information in dsDNA directly. Instead, based on a DNA template, a complimentary template is synthesized using bases of RNA. In RNA, an U (uracil) base is used in the place of each T base. The synthesis of RNA based on DNA template is referred to as transcription. Transcription is carried out by a multi-protein complex termed the RNA polymerase (RNAP). Nevertheless, only a small proportion of the RNA transcripts are used as templates for Protein synthesis proper. Cells use RNA in myriad of ways. Majority of the RNA transcripts (85%) are used as parts of machinery that synthesizes proteins. The core of this machinery is the ribosome complex. A bacterial ribosome is about 20 nm diameter and consist half RNA and half proteins by mass. They are by far the largest enzyme complexes in most bacterial cells and one of the main sources of macromolecular crowding. To synthesize a protein ribosome assembles over a different RNA molecule termed the messenger RNA (mRNA). By feeding mRNA through its central channel ribosome converts the mRNA sequence to protein sequence. The latter is made up of 20 different α-amino carboxylic acid (amino acids). In this conversion, every three bases of RNA code one amino acid. There are 64 possible permutations of three bases of RNA but only twenty possible amino acids. So, multiple mRNA base triplets (termed codons) encode for the same amino acids. The whole process of converting mRNA sequence to DNA sequence is called translation. Altogether, the genetic information flows from DNA to mRNA via transcription and from mRNA to protein sequence via translation. This fundamental principle, referred to as the central dogma of molecular biology for legacy reasons, is universal to all cellular life. Therefore, studying these processes in bacteria also shines light on what occurs in human cells (See Figure 1-3).

1.3 Spatial Organization of Genetic Information in *E. coli*

The chromosomal DNA is the physical embodiment of the genetic information in *E. coli*. How this pair of very long polymeric molecules is packed within the cells affects how the genetic information

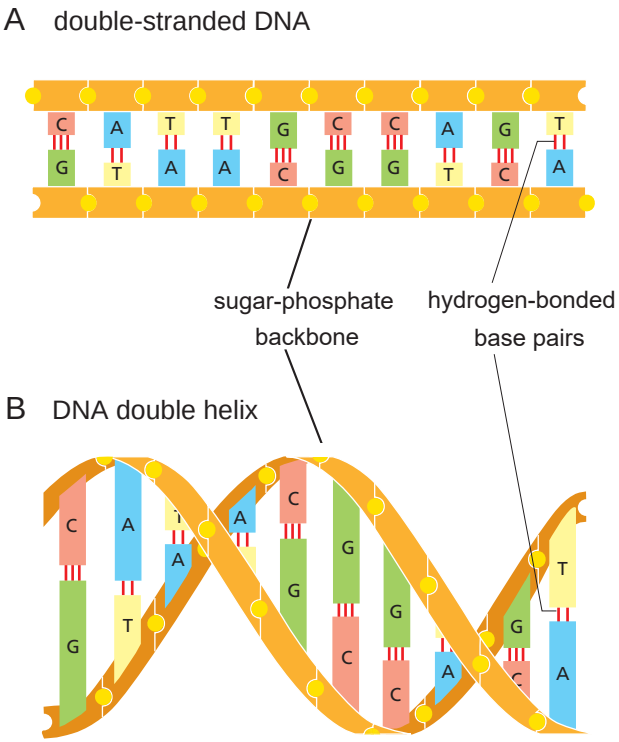


Figure 1-2 : Primary and secondary structure of dsDNA. (A) A normal DNA molecule consists of two such complementary strands. The nucleotides within each strand are linked by strong (covalent) chemical bonds; the complementary nucleotides on opposite strands are held together more weakly, by hydrogen bonds. (B) The two strands twist around each other to form a double helix—a robust structure that can accommodate any sequence of nucleotides without altering its basic structure. This figure are reproduced from Alberts et al. (2014) [AJL+14].

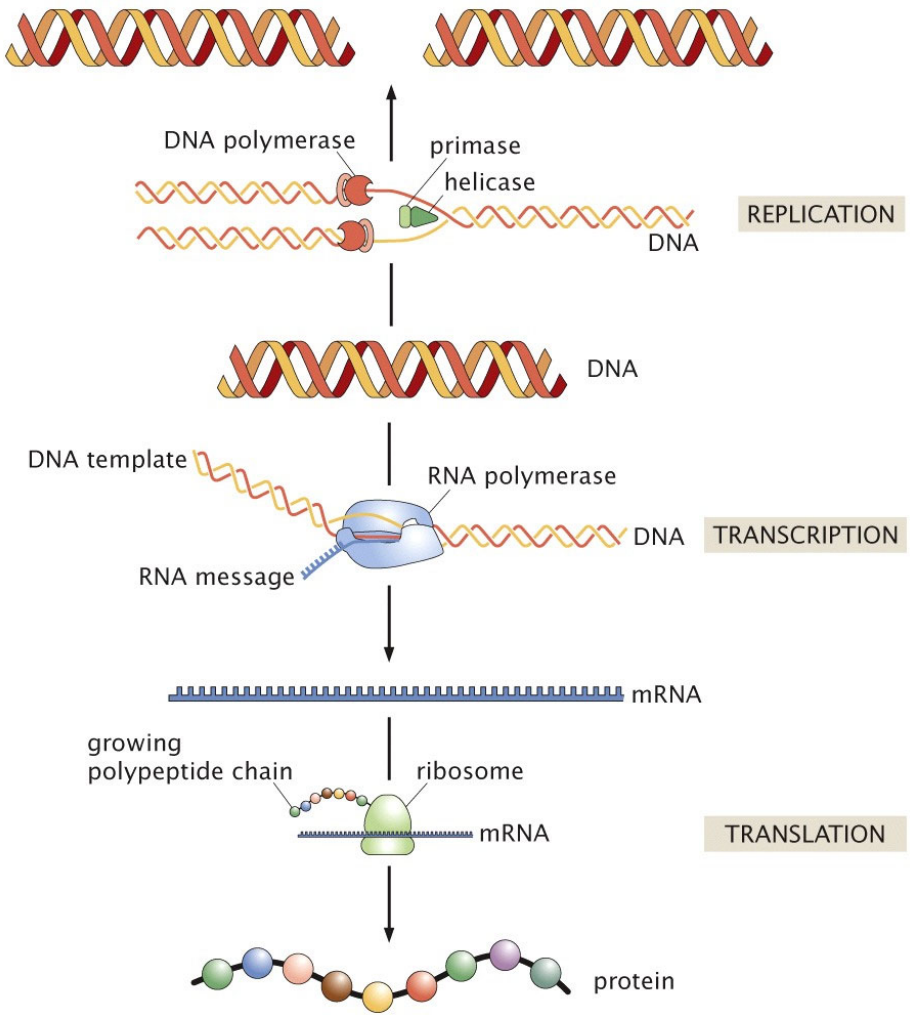


Figure 3.12 Physical Biology of the Cell, 2ed. (© Garland Science 2013)

Figure 1-3 : The processes of the central dogma. DNA is replicated to make a second copy of the genome. Transcription refers to the process in which RNA polymerase makes an mRNA molecule. Translation refers to the synthesis of a polypeptide chain whose sequence is dictated by the arrangement of nucleotides of mRNA. This figure is reproduced from Phillips et al. (2012) [PKT+12].

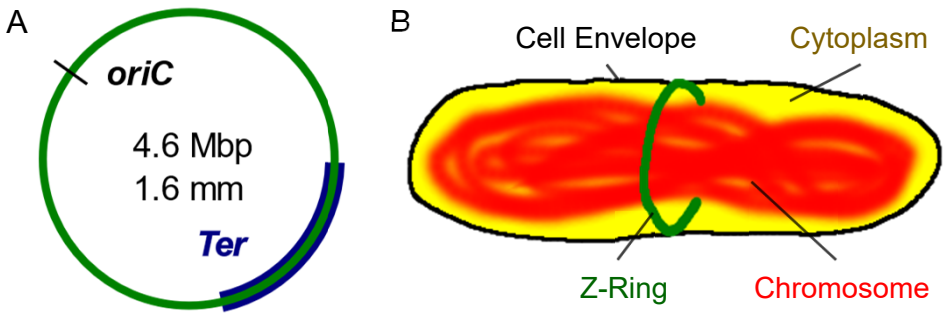


Figure 1-4 : (A) Map of a Typical *E. coli* Gnome. Blue is the terminus region where *m*atS sites span and *o*riC is the origin of replication. **(B) Schematic of an *E. coli* Cell.** The cell envelope is shown in black, the chromosome is shown in red, the division apparatus is shown in green and the cytoplasm is shown in yellow.

can be accessed and turned into enzymes and structural proteins in the cell. In addition to transcription, the physical organization of the chromosomal DNA can also be expected to affect other essential DNA related transactions. These include DNA replication and DNA repair processes, which are critical for cell survival and propagation. The organization of DNA can be expected to affect key cellular processes.

The chromosome of *E. coli* is organized around a pair of covalently closed circular DNA (cccDNA) molecules, which contains 4.6 million base pairs (*Mbp*) of dsDNA and is about 1.6 *mm* long (prior to the initiation of DNA replication, Figure 1-4 A). This circular polymer is decorated by different proteins that bind to it throughout its length. Those proteins either bind to specific DNA sequences or bind to DNA nonspecifically. DNA, together with the associated proteins, is referred to as the chromosome. The 1.6 *mm* long chromosomal cccDNA fits into the micrometer-sized cell and forms a distinct compacted structure termed the nucleoid (Figure 1-4 B). Unlike eukaryotic cells, bacteria (with few exceptions) have no membranes surrounding their chromosomes. Why and what determines the size of the nucleoid is the main question addressed in this dissertation.

1.3.1 Cellular Environment

The formation of nucleoids cannot be understood without a cellular context. Therefore, I describe how the *E. coli* cell is organized beyond its chromosome. In this subsection, I give a brief overview on the cell biology of the cell envelope, cytoplasm and the cell division machinery. These structures

directly interact with the chromosome and are important in understanding the compaction DNA into nucleoid.

1.3.1.1 Cell Envelope

The cell envelope of *E. coli* is composed of a thin peptidoglycan cell wall sandwiched between an inner and outer membranes. The space between the inner and outer cell membrane, the periplasmic space, contains, in addition to the cell wall, a concentrated gel-like matrix of proteins [SKW10]. Both inner and outer membranes of *E. coli* are composed of semipermeable lipid bilayers, which allows water and small non-polar molecules to diffuse through. Nevertheless, simple diffusion through the lipid bilayers cannot fully account for the entire water movement across cell envelopes. Aquaporins [BKC+99; ZVL+13] and mechanosensitive channels [ZWF+12; PR03] provide the substantial portion of the water permeability through the cell envelope.

The cell wall consist of chemically cross-liked peptidoglycan, which is single-layered for most of the cell surface area [YJPB99]. The peptidoglycan cell wall is the stress-bearing structure that sets a limit to cell shape [HMW+08]. The stress arise from osmotic pressure difference between the inside and the outside of the cell. That pressure difference is called the turgor pressure. For *E. coli* cells, the turgor pressure has been estimated to lie between 0.3 and 3 atmospheric pressure (atm) [BLY+16]. Deng et al. have measured the tensile modulus of the peptidoglycan cell wall and the turgor pressure of live *E. coli* cells, using atomic force microscopy (AFM) [DSS11]. They found the turgor pressure in live *E. coli* cells to be $29 \pm 3\ kPa$. They also found the tensile modulus in axial direction is about half of that in the circumferential direction.

1.3.1.2 Cytoplasm

Delimited by the cell envelope, the *E. coli* cytoplasm is about 80% water by weight and by volume. The rest of the cytoplasm is made up of deoxyribose nucleotides (DNA), about 10^6 cytoplasmic proteins, ribonucleic acids (RNAs), and other small molecules [PKT+12]. Many larger molecular complexes (e.g., ribosomes) are constituted by those molecules [PSC+14]. The volume fraction of cytoplasmic proteins is at least 20% in *E. coli* cells [ZT91]. Depending on the growth conditions, each *E. coli* cell can have $8,000 \sim 73,000$ ribosomes [BD08]. Approximately, an assembled 70S

ribosome can be considered as a sphere with a diameter of about $20nm$ [SBH+05]. The ribosomes make up at least 3% of the cell volume.

When multiple ribosomes associate with a single mRNA, they form a poly-ribosome (polysome). In *E. coli*, almost all translationally active ribosomes are part of polysomes [DZW+17]. The typical number of ribosomes in a polysome is about ten [MBL+11]. Therefore, in the cytoplasm, particles that are larger than a few nanometers in size are the larger cytoplasmic proteins, 30S and 50S ribosomal subunits, tRNA, and poly-ribosomes (polysomes). We will further discuss this portion of the cellular content in Chapter 4.

1.3.1.3 Z-Ring and Its Positioning

The Z-ring is named after the principle component of the *E. coli* division apparatus, tubulin homolog protein FtsZ, which forms a protofilament ring [EAO10]. It assembles at the cell middle when a bacterium is about to divide [EAO10; RKV13]. After its assembly, a gap between two segregated chromosomes forms and aligns to this machinery. Then the assembled Z-ring contracts and the cell divides into two [BBW+14]. The alignment and the action timing of the ring-like machinery to this inter-nucleoid gap are crucial to preserving the hereditary integrity of this species.

Three known mechanisms are ensuring the precision alignment in *E. coli* [See Figure 1-5, MB15]. The nucleoid occlusion system relies on SlmA bind to specific DNA sequences that are distributed throughout the chromosomes but absent from the Ter regions (Figure 1-5 A). SlmA is thought to prevent Z-ring formation nearby; consequently, when the DNA replication is nearly complete, only the Ter region is present at cell middle, and Z-ring formations are allowed [DKG11]. The MinCDE system oscillates between cell poles (Figure 1-5 B). They spend more time at cell poles than at the cell middle and prevent Z-ring formation near cell pole [Lut07]. Last but not least, a positive regulation system has recently been discovered [BBW+14]. Similar and contrary to SlmA, the macrodomain Ter protein, MatP, bind to specific DNA sequences that are only present in the Ter regions (Figure 1-5 C). It crosslinks the Ter macrodomain and links the Ter macrodomain to the Z-ring through Z-ring associated proteins [EBD+12].

When one or more of those Z-ring positioning systems are defective, Z-rings often form over one of the sister nucleoids and contracts. This often causes the nucleoid to translocate (Figure 1-5

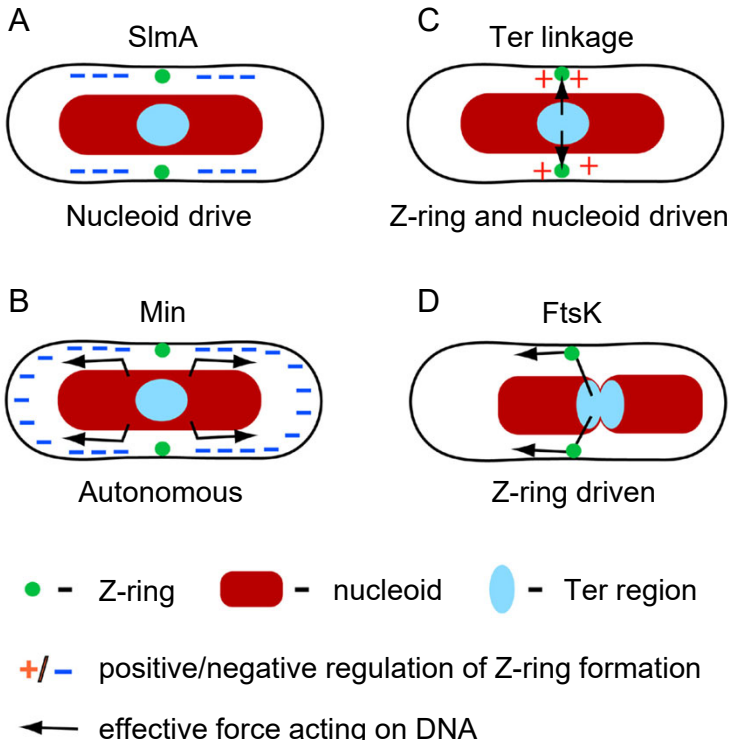


Figure 1-5 : Four molecular mechanisms that have been identified in spatial coordination between the chromosome and divisome in *E. coli*. (A) SlmA-mediated nucleoid occlusion is a nucleoid driven mechanism which negatively regulates Z-ring formation in the vicinity of the chromosome except at the replication terminus region. (B) The Min system is independent of the nucleoid but it has been implicated in segregating and separating nucleoids. The Min system negatively regulates Z-ring formation at cell poles. (C) The Ter linkage is involved in determining the location of the Z-ring by a positive regulatory mechanism. The linkage is also involved in holding the Ter region fixed relative to the divisome. (D) FtsK translocase pumps DNA across the divisome in a directed manner leading to repositioning of chromosomes. This figure is reproduced from [MB15].

D) and avoid of being guillotined [MBOM17]. What drives the nucleoid away from the divisome is not well-understood. We will further discuss this portion of the cellular content in Chapter 6.2.

1.4 Polymer Physics Based Estimation of Nucleoid Sizes

Recall from previous sections, the chromosomal DNA in *E. coli* consists of a pair of long polymeric molecules. Polymer physics theories provide a governing framework to understand how the 1.6 mm long pair of molecules is compacted to fit inside micron-sized *E. coli* cells. The central goal for this section is to explain the observed size of the bacterial chromosome within the cell. Taking the complexity of bacterial cell many factors are expected to contribute.

1.4.1 Chain Models

I start with the simplest polymer physics models then add more and more details to the models.

1.4.1.1 The Ideal Chains

Polymers with no interactions between monomers except the separation and connection by the many bonds along the chain are freely jointed chains (or ideal chains). This is the simplest polymer chain model. The conformation of freely jointed chains follows the path of a random walk. Hence, the fractal dimension is 2. As a convention, we typically discuss the scaling exponent ν, which is the multiplicative inverse of the fractal dimension. When the number of subunits, N, is large, the chain becomes self-averaging. Therefore, for a freely jointed chain, its radius of gyration,

$$R_g \propto N^{1/2}. \tag{1.1}$$

Here R_g is defined by

$$R_g^2 \equiv \frac{1}{2N^2} \sum_{i,j} (\boldsymbol{r}_i - \boldsymbol{r}_j)^2 . \tag{1.2}$$

1.4.1.2 Worm-like Chains and the Kuhn Length

Worm-like chains are polymers that are semi-flexible: successive segments are close to being colinear, i.e., very small bond angle. Kratky and Porod first introduced this model in 1949 [KP49]. This is a good model for very stiff polymers, such as dsDNA [RC03]. We characterize the stiffness

of a worm-like chain using the persistence length l_p. If two segments (bonds) of a polymer are at contour distance s from each other, the persistence length of this polymer fulfills the following equation,

$$\langle \boldsymbol{u}_0 \cdot \boldsymbol{u}_1 \rangle = \exp(-s/l_p), \tag{1.3}$$

where $\boldsymbol{u}_0$ and $\boldsymbol{u}_1$ are unit vectors tangent to those two segments, respectively.

When the contour length of a worm-like chain, L, is orders of magnitude longer than its persistence length, we can treat the chain as a collection of freely jointed Kuhn segments. The length of each Kuhn segment is called the Kuhn length, b, where $b = 2l_p$. For dsDNA, $l_p \approx 50\ nm$ [TH90] and $b \approx 100\ nm$. Hence, a 1.6 mm long covalently closed circular (ccc) dsDNA has about $16,000$ Kuhn segments, and Rubinstein & Colby (2003) has given a formula for calculating the radius of gyration of a closed-chained polymer [RC03],

$$R_g = \sqrt{\frac{Nb^2}{12}} \tag{1.4}$$

$$= 3.61\ \mu m. \tag{1.5}$$

This is about seven to eight times the length of what we observe in living cells.

1.4.1.3 Excluded Volume Interactions and Self-Avoiding Walks

Real DNA chains are not ideal. Each base pair of dsDNA carries 2 e^- charge. In the short range (few nm), they strongly repel each other. In the simplest approximation, the electrostatic interactions are screened by ions and water at a longer distance and the interactions are modeled as excluded volume interaction. The Flory-Huggins solution theory is a very successful attempt to describe the size of polymers in blends or solutions. For the precision required by this subsection, we are not discussing beyond what this theory predicts about linear polymers. For polymer chains with strongly asymmetric cylindrical Kuhn segments of length, b, and diameter, d ($d = 2\ nm$ for dsDNA, or a few nm longer when consider the screening of electrostatic interactions), the excluded volume, v, in a good solvent is in the range, $0 < v < b^2 d$. The total free energy in the Flory approximation

is the sum of the energetic interaction and the entropic contributions:

$$\begin{aligned} F &= F_{int} + F_{ent} && (1.6)\\ &\approx k_B T \left(v\frac{N^2}{R^3} + \frac{R^2}{Nb^2} \right). && (1.7) \end{aligned}$$

See [RC03] for detailed derivations. Hence, R is the end-to-end distance and the balanced size can be found by solving

$$\begin{aligned} 0 &= \frac{\partial F}{\partial R} && (1.8)\\ &= -3vN^2R^{-4} + 2N^{-1}b^{-2}R, && (1.9) \end{aligned}$$

and we have

$$\begin{aligned} R &= v^{1/5}b^{2/5}N^{3/5} && (1.10)\\ &= b\bar{v}^{1/5}N^{3/5}. && (1.11) \end{aligned}$$

where the reduced excluded volume, $\bar{v} \equiv v/b^3$, and the scalar coefficient, $1.5^{1/5}$, is treated as 1.

At $v = b^2d$, $\bar{v} = d/b$, we have $R = 15\ \mu m$. This is about twelve times what we observe in living cells. The excluded volume of a Kuhn segment could be smaller; nevertheless it could not be smaller than the volume of the Kuhn segment. At $v = bd^2$, $\bar{v} = (d/b)^2$, which is close to 0, we have $R = 6.9\ \mu m$. This is about five times the length of what we observe in living cells.

Now, if we confine the polymer in a cylinder with a diameter, D, it experiences biaxial compression, i.e., the compression forces act in two directions. "On length scales smaller than D, sections of the chain do not 'know' that it is compressed, and their statistics are still the same as the statistics of an undeformed chain [RC03]." (See Figure 1-6.) Thus, the polymer can be viewed as a collection of blobs of size, D, each has g Kuhn monomers, and we have $D = v^{1/5}b^{2/5}g^{3/5}$ and

$$\begin{aligned} g &= \left(Dv^{-1/5}b^{-2/5} \right)^{5/3} \\ &= \left(D\bar{v}^{-1/5}b^{-1} \right)^{5/3} \\ &= \bar{v}^{-1/3} \left(\frac{D}{b} \right)^{5/3}. && (1.12) \end{aligned}$$

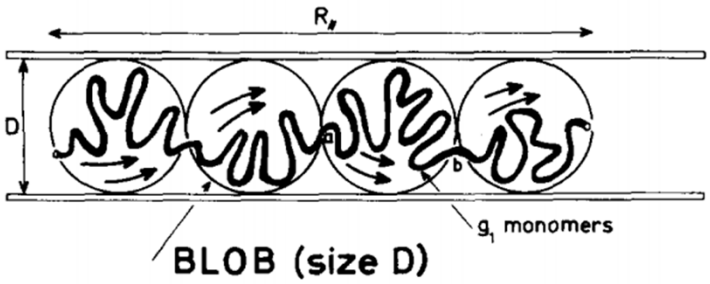


Figure 1-6 : Chain configurations and water channel for a confined chain. The statistical fluctuations of the local concentration allow for a relative easy flow of the solvent through the chain (or vice versa). This figure is reproduced from [BdG77].

Strictly following the blobs forming assumption, the compression blobs repel each other and fill the pore in a sequential array. The end-to-end distance of the polymer along the axis of the cylinder of confinement:

$$R_{/\!/} = D\left(\frac{N}{g}\right) \tag{1.13}$$

$$= DN\bar{v}^{1/3}\left(\frac{b}{D}\right)^{5/3}$$

$$= \bar{v}^{1/3}\left(\frac{b}{D}\right)^{2/3} Nb. \tag{1.14}$$

However, the volume in the tube not filled by those blobs should not be a complete void. If a part of the polymer is used to fill that volume, the length of the sequential array of blobs will be reduced. Thus, the length given by Equation 1.14 is the upper limit. For the lower limit, we assume the average density calculated from Equation 1.12 is the average density of the whole, i.e., $g/v_{blob} = N/v_{whole}$, which yields $R_{/\!/} = 2/3\, D(N/g)$ or 2/3 of the upper limit. This should be the lower limit because the density filling the volume not filled by those blobs originally should be lower. With $D = 0.6\ \mu m$, at $\bar{v} = d/b$. The resulted chain (of blobs) length $R_{/\!/}$ is $86 \sim 130\ \mu m$. At $\bar{v} = (d/b)^2$. The resulted chain length of $R_{/\!/}$ is $23 \sim 35\ \mu m$.

The calculations in this subsection assume the chromosomal DNA being an open chain in good solvent. The corresponding values for a closed chain of the same contour length should be less than but at least half of the values for open chains, while the scaling exponent is preserved [ANH+06]. All models examined thus far cannot fit into an *E. coli* cell.

1.4.2 Super Coiled DNA and Randomly Branched Polymer

In *E. coli* cells, the supercoiled chromosomal DNA has many plectonemes of various lengths. We can model it as a randomly branched polymer, a branched polymer of plectonemes. For an introduction of DNA topology, see Mirkin (2005) [Mir05].

1.4.2.1 DNA Supercoiling and Topology of cccDNA

It is well known from TEM images that bacterial chromosomal DNA is forming coils where one dsDNA strand wraps around the other (Figure 1-7). These coils are referred to as the supercoils. They arise from helical structure of dsDNA. In the relaxed double helix each strand of DNA wraps around the other at a rate of $10.4 \sim 10.6$ bp/turn. Each wrap around is considered a link and it adds a unit to the total linking number of two single DNA strands.

While the dsDNA forms a double helical structure, the helix itself twists and turns into different conformations. The topology of these twists-and-turns often formulated with the classical Gauss linking number, usually denoted by a two-letter notion Lk. For a closed chain DNA, Lk is an integer invariant. It refers to the number of times the two helical strands are interwound [FCR+09]. For two directed, non-intersecting, and closed paths in space, C_1 and C_2, we can calculate their linking number by

$$Lk = \frac{1}{4\pi} \oint_{C_1} \oint_{C_2} \frac{d\boldsymbol{r}_1 \times d\boldsymbol{r}_2 \cdot (\boldsymbol{r}_1 - \boldsymbol{r}_2)}{|\boldsymbol{r}_1 - \boldsymbol{r}_2|^3}. \tag{1.15}$$

where, $\boldsymbol{r}_1$ and $\boldsymbol{r}_2$ are tangent vectors in C_1 and C_1, respectively. A fundamental mathematical result for a closed is the Călugăreanu-White-Fuller theorem [Cĕ61; Whi69; Ful71; Ful78],

$$Lk = Tw + Wr. \tag{1.16}$$

where, Tw is called the twist and Wr is called the writhe. Tw describes the rate of two strains of a dsDNA wrap around the contour of the helix; and Wr describes the rate of the double helix crosses itself.

For dsDNA, it is natural to use base pair length as a metric. Hence, linking number density of native and relaxed dsDNA is about 0.1 turn/bp. Here, we define the specific linking difference of a given segment of dsDNA,

$$\sigma = \frac{Lk}{Lk_0} - 1. \tag{1.17}$$

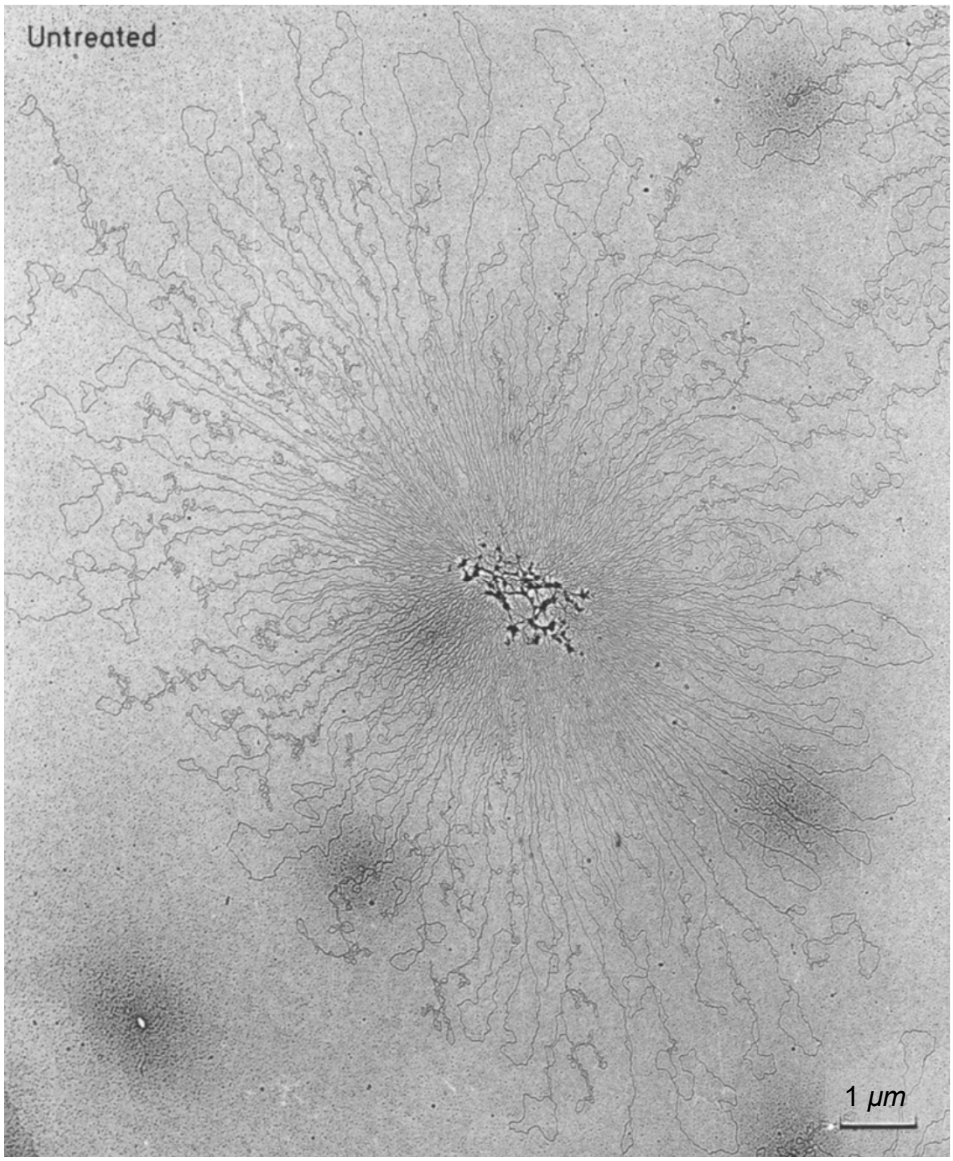


Figure 1-7 : Transmission electron microscope image of a liberated *E. coli* chromosome. Typical results with hypophases containing 0.4 *M* salt. Untreated Chromosome 3 min. after spreading, with electron-dense core and loops of DNA. Example has loops radiating from a single center and was, therefore, termed "well-organized." This chromosome had 141 ± 3 loops loops (134, 141, 142, 144, 144) and, possibly, a fork in the loop at about one o'clock. This figure is reproduced from [KB76].

where Lk is the linking number of the same segment, and Lk_0 is the linking number of the native form dsDNA of the same length. For one genome equivalent of DNA, $Lk_0 \approxeq 4.5 \times 10^5$. When the specific linking difference of a given dsDNA is less (resp. greater) than zero, we call the dsDNA negatively (resp. positively) supercoiled. Supercoiled dsDNA would have a higher free energy density [BM05].

However, replication and transcription create torsional stress in dsDNA. In front of moving DNA and RNA polymerases, the local specific linking difference needs to be close to -1. The excess torsion ahead of those polymerases could easily stall them [MBW13]. To prevent this happening, torsional stress ahead of replication forks is released by DNA gyrase tetramer, a type II topoisomerase [Figure 1-8 A, Hig07]. This action thus introduces negative supercoiling and relieves extra twist ahead of replication forks. The torsional stress created for those polymerases are released by an other type I topoisomerase, Topo I. Topo I cuts one of the dsDNA strand and let the other pass through this cut then recombine the cut strand in an ATP independent manner. This action relaxes the negative supercoiling [Figure 1-8 B, Cha01]. In addition, another type II topoisomerase, Topo IV, allows the stochastic driven double stranded passage of dsDNA. Topo IV rapidly simplifies DNA networks that become tangled into knots and catenated links between sister strands during DNA replication, transcription, and recombination [Figure 1-8 C, Hig07].

Topo I not exactly balance torsional stress created by gyrase and DNA and RNA polymerases. In *E. coli*, measurements have shown that the global specific linking difference, σ, is about -0.05 [MBvdHvN14]. Torsional stress related to non-zero σ is partially relieved by converting some of the twists to bends of the molecule. These bends lead to coiled structures–the supercoils. The number of times one dsDNA strand wraps around another in the supercoil are characterized by writhe, Wr. For a given Lk, decreasing Tw leads to equally increasing Wr. Theoretically, Tw and Wr can be found for given Lk by minimizing free energy of DNA considering it as an elastic rod with bending and torsional rigidity.

In the recent decades, with advances in imaging and sequencing techniques and genetic engineering, it has been revealed that supercoils play a fundamental role in organizing bacterial chromosome on length scales of 10 kb ($\sim$300 nm contour length) [WMLR13]. First, by negative supercoiling, plectonemic supercoils are generated, forming topologically isolated domains, sizes of which are on average 10 kb. For *E. coli*, in particular, the domain barriers are not placed stably at

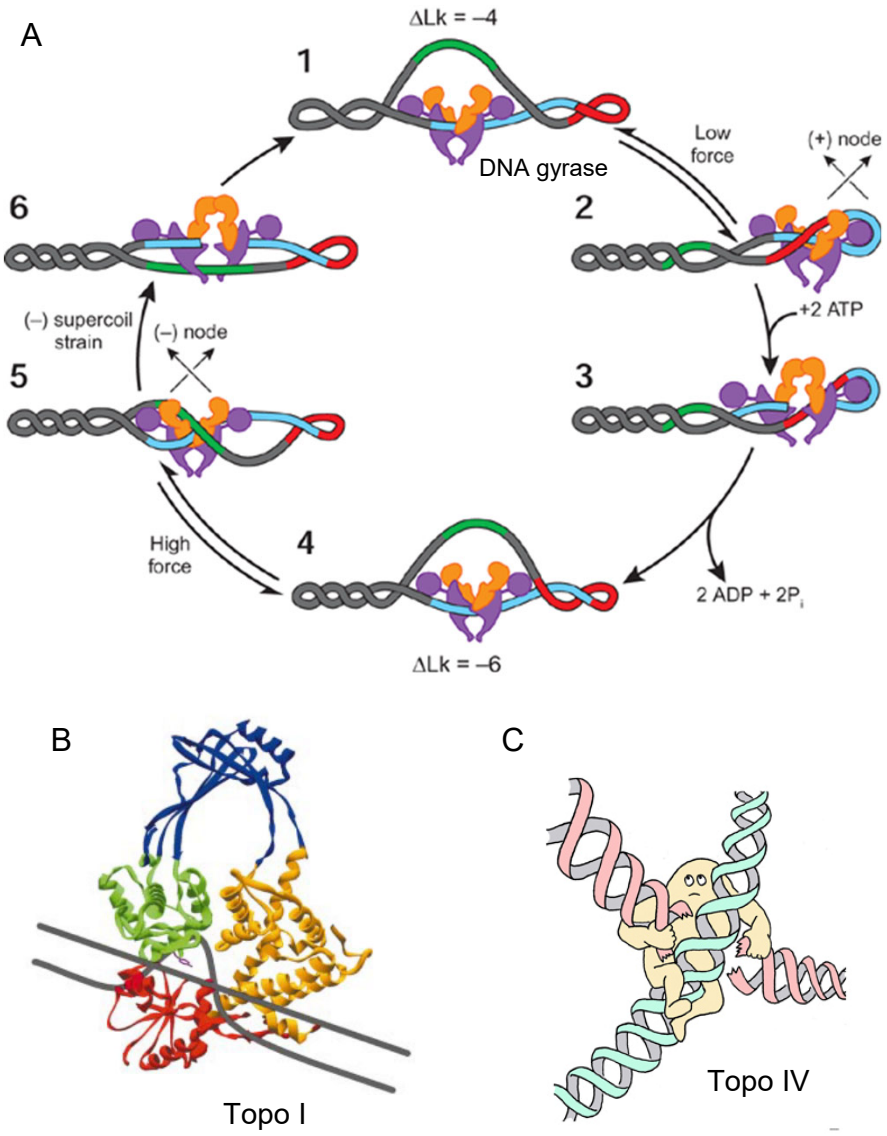


Figure 1-8 : *E. coli* topoisomerase. (A) DNA gyrase reaction mechanism for producing and removing (−) supercoils. Subunits of DNA gyrase form a heterotetramer with two GyrA protomers (purple) and two GyrB protomers (orange). In the supercoiling model, the sign of the cross or node is (+) for introducing negative supercoils and (−) for removing negative supercoils. (B) Structural representation of *E. coli* Topo I, an ATP independent type I topoisomerase. It relaxes the excessive torsional stress in dsDNA. (C) A carton of *E. coli* Topo IV. It allows the double stranded passage of dsDNA. Panel A is reproduced from [Hig07]. Panel B is reproduced from [Cha01].

fixed sites. The stochastic nature of the generation and displacement of domain barriers has been proposed [PHAC04].

DNA supercoiling can be expected to compact chromosomal DNA [WJW95]. It has been proposed that individual supercoils can nematically align at densities, 13 g/l, which could lead to a compacted polymer [Odi98]. Although such DNA densities are present in the *E. coli* nucleoid, correlations between DNA supercoiling levels and nucleoid size were not observed *in vivo* under inhibition of gyrase activity [SWvdW+02; CGJ+13]. However, supercoiling dependent shrinkage of nucleoid has been reported *in vitro* [RFK07].

1.4.2.2 Size Estimation of Super Coiled DNA

The supercoiled chromosomal DNA forms a randomly branched polymer. It has been estimated that a plectonemic coil has a diameter $d_s \approx 26\ nm$, and persistence length $Ps \approx 80\ nm$ [WAOW12]. The specific linking difference in *E. coli* is about $\sigma = -0.05$. Considering the plectonemic formation relieves the stress in the dsDNA supercoil, the energy-wise effective value of σ is estimated to be $\sigma_{\text{eff.}} = -0.025$ [BC87]. Hence, we view the DNA supercoil as N_s segments of length $As = 2 \cdot Ps = 158\ nm$, where the contour length of the supercoil, $L_s = 630\ \mu m$. Meanwhile, the supercoil is branched with a branching density $\Lambda_s = 0.71$, where $\Lambda_s \equiv n_3/N_s$ and n_3 is the number of trifunctional branches. Hence, Cunha et al. (2001) [CWO01] wrote down the end-to-end distance of this branched super coil before considering excluded volume interactions,

$$R_u = 0.399 N_s^{1/2} \Lambda_s^{-1/10} d_s^{1/5} A_s^{4/5} \tag{1.18}$$

$$\equiv b_s N_s^{1/2}. \tag{1.19}$$

This leads to the estimate $R_u = 3.3\ \mu m$. (See Figure 1-9.) All models examined so far yielded estimates much larger than an *E. coli* cell.

1.5 Further Compaction of the *E. coli* Chromosomal DNA

Entropy and supercoiling alone could not produce a chromosome small enough to fit into an *E. coli* cell. We review the factors to which the further compaction of DNA have been attributed, i.e., nucleoid associated proteins (NAPs) [She03; Dam05; DD10; WLC+11], and osmotic

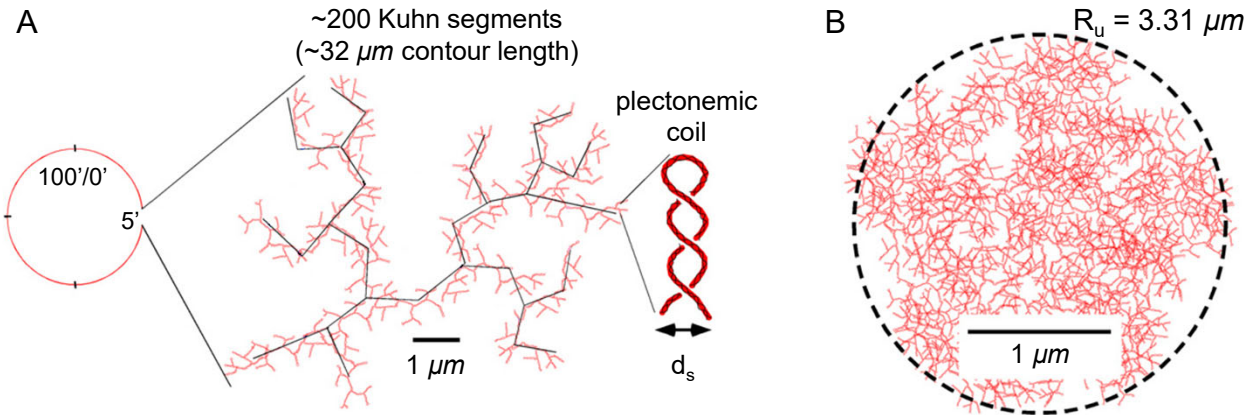


Figure 1-9 : A schematic representation of the *E. coli* chromosome and of liberated nucleoids. (A) A 5 min.-segment of the chromosome (total 100 min.) is drawn as a randomly branched chain of 200 Kuhn segments, which is a fractal. The plectonemic coil has a diameter d_s. (B) Representation of the branched supercoil with a theoretical end-to-end distance (R_u) of 3.31 μm. This figure is reproduced from [WAOW12].

compaction induced by cellular crowders [Odi98; dV10; MFC06]. Transcription and translation, and attachments to cell membrane also play roles in compacting and organizing the chromosomal DNA [Wol02; BCMW14; CCQ+09; HYGJM12].

1.5.1 Nucleoid Associated Proteins

In addition to supercoiling, nucleoid associated proteins are expected to contribute to DNA compaction. Having no specific compartment, the chromosomal DNA is free to interact with a plethora of enzymes, proteins, metabolites, and other molecules throughout the cell cycle [Figure 1-10, KMJK18].

Several NAPs bends dsDNA. The heat unstable nucleoid proteins, HupA and HupB forms and functions as a heterodimer. The dimer sharply bends the dsDNA [KMJK18]. The factor for inversion stimulation, Fis forms and functions as a homodimer. The dimer bends the dsDNA to $50 \sim 90°$ [KMJK18]. The integration host factor, IhfA and IhfB forms and functions as a heterodimer. The dimer bends the dsDNA to $160 \sim 180°$ [KMJK18]. In addition, the histone-like nucleoid structuring protein, H-NS has been characterized as both a DNA-structuring protein and transcriptional regulator with predominant repressing functions [PW10]. It forms dimers that bridges relative distant DNA loci. The leucine responsive regulatory protein, LRP is another NAP

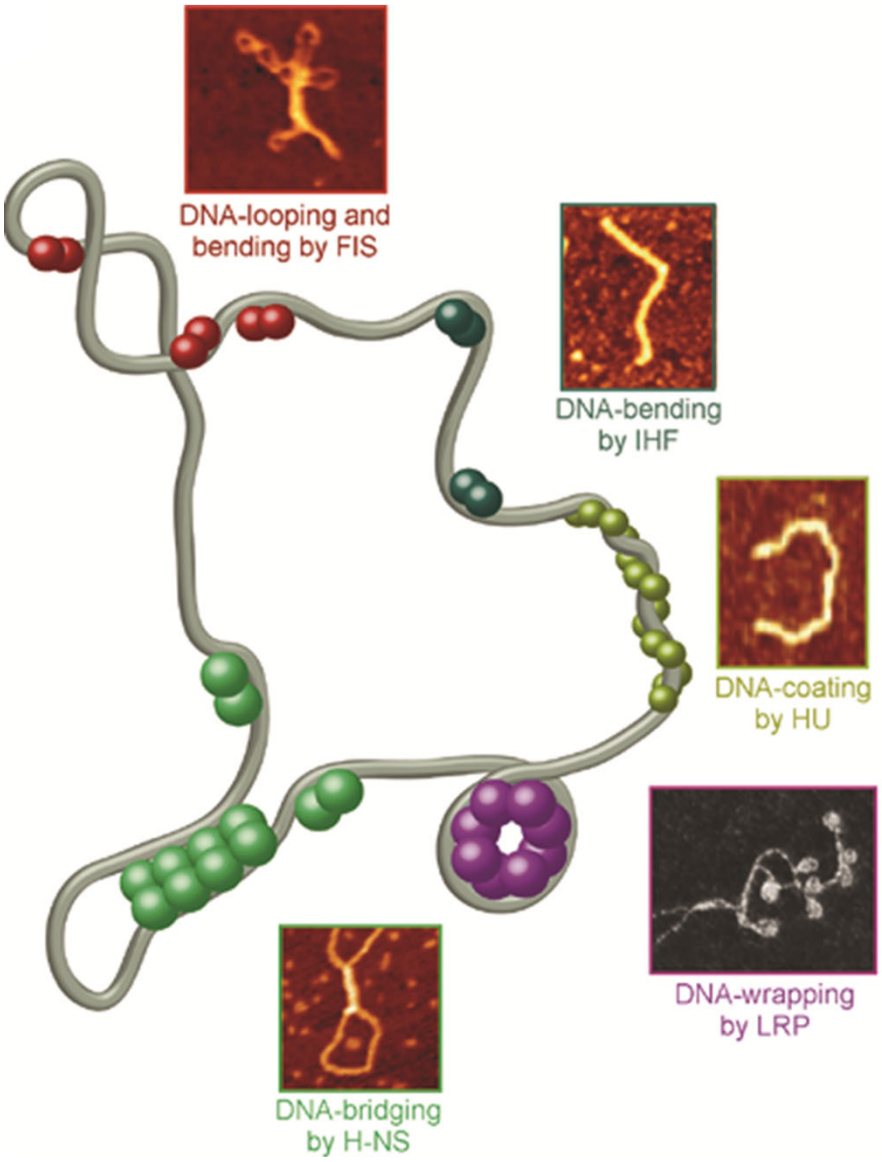


Figure 1-10 : DNA binding properties of NAPs. Different modes of DNA structuring by NAPs are schematically illustrated. For each NAP a schematic drawing and a corresponding AFM image is shown. Different effects of NAP binding on the target DNA are displayed: plectonemic loop (FIS), sharp DNA bends (IHF), DNA-coating (HU), DNA-wrapping (LRP) and DNA-bending and bridging (H-NS). This figure is reproduced from [PW10].

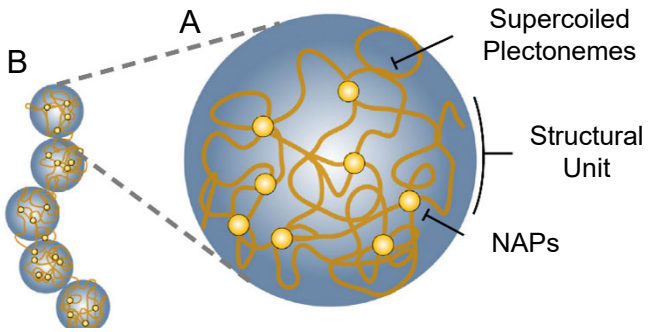


Figure 1-11 : The coarse-grained model of bacterial chromosomal DNA. (A) Structural unit. Structural units of supercoiled plectonemes of DNA are locally stabilized to form a crosslinked gel by various NAPs and aggregation. (B) DNA string-beads model. A chromosome is considered to be a chain of spherical structural units. This figure is reproduced from [SBdH+15].

that regulates transcription. It forms octamers and have the dsDNA wrap around it. All those proteins do not have a strong preference to particular DNA sequences, but SlmA and MatP do. (See Section 1.3.1.3.)

Although those NAPs, which can bridge (H-NS) and bend (HU, Fis, IHF) chromosomal DNA, are abundantly present in *E. coli* during its lag-phase growth [DKG11; DD10; KMJK18]. They appear to affect chromosome conformations only at the local and intermediary scales–in regions spanning less than 300 *kbp* [LCM+18]. Moreover, the removal of most of these binding proteins from the cell one at a time does not change the nucleoid size [WSK+19; WMLR13]. The exception is the low-abundance MatP, which anchors the replication terminus region to the divisome [EBD+12; MCY+16] and conveys different organization to this 800 *kbp* long domain [MPS+08; LCM+18]. Also, the condensin-like structural maintenance of chromosome homolog MukBEF has been reported to lead to global-scale decondensed chromosomes [NS14] possibly via DNA looping mechanisms [TBE+17].

1.5.2 Structure Units and Macrodomains

With further aid from NAPs, supercoiled plectonemes of DNA are locally stabilized to form a cross-linked gel and aggregate (Figure 1-11 A) [JW10]. From lysed cells, structure units of chromosomal DNA have been observed. Kim et al. have performed structural analyses of lysogeny broth (LB) grown *E. coli* chromosomes under atomic force microscopy and found a fundamental

fibrous structure with a diameter of 80 nm in both stationary phase and log phase chromosomes, and of a 40 nm structure only in log phase chromosomes [KYH+04]. By fluorescence correlation spectroscopy, structure units have been found to be corresponding to $10 \sim 100$ kb of DNA [RFK07]. Although, it is not clear how the sizes and shapes of these structure units would change upon lysis of cell, structural units are significantly larger than most cellular crowders. Hence, a chromosome can be considered as a linear chain of spherical structural units (Figure 1-11 B).

Furthermore, the chromosome DNA in *E. coli* is thought to be organized into four macrodomains, i.e., origin (Ori), terminus (Ter), left, and right. These large regions are $0.8 \sim 1$ Mbp in size. Segregation of most bacterial chromosomes can be broken down into three discrete steps: separation of the newly replicated origins; bulk chromosome segregation; and resolution and transport of the replication termini at the division septum [WMLR13].

1.5.3 Effects of Transcription, Translation, and Transertion

The *E. coli* cell is far from thermal equilibrium. The size of nucleoid can be expected to be affected by non-equilibrium processes taking place with DNA. The two dominant non-equilibrium processes occurring with DNA are replication and transcription. Inhibition of transcription by a drug (rifampicin) has been shown to lead short term compaction of the nucleoid at time scale of about 5 min. [BCMW14; BCW15]. At longer time scales nucleoid expands gradually until it fills almost all the cytoplasmic volume and distinct nucleoid phase disappears. The short-time scale effects have been explained by so-called transertion effect. Transertion refers to a molecular link between chromosomal DNA and cell membrane. They are thought to consist of RNA polymerase, transcribed mRNA, translating ribosomes, and the membrane protein that has inserted its N-terminal domain into the cell membrane. It has been well-established that transcription and translation occur simultaneously in *E. coli* [Wol02]. Moreover, the transertion hypothesis posits that nascent membrane proteins can insert their N-terminal membrane helixes to plasma membrane while the rest of the protein is still synthesized. These linkages could expand the nucleoid. The hypothesis leads to prediction that if transcription or translation are inhibited then the nucleoid compacts. Indeed, this is observed in experiments [LRG12; BCMW14; BSGW12] and further tested in Chapter 4.

1.6 Macromolecular Crowding, Phase Separation, and Free Energy

While all the processes described in the previous section (Section 1.5) have been extensively studied, none of them appear to be capable of explaining the extent of the compaction needed to confine DNA into the experimentally observed nucleoid sizes. A number of theoretical [Odi98] and modeling studies [MBL+11; SBdH+15; SCM14; KJJ+15; Joy18] have pointed out that macromolecular crowders can be the main mechanism for the compaction of chromosomal DNA. In the seminal work, Odijk (1998) proposed that crowders and DNA separate into two distinct phases in an *E. coli* cell, a nucleoid and cytosolic phase [Odi98]. The nucleoid phase contains the chromosome and is depleted of cytoplasmic proteins, whereas the cytosolic phase has an excess number of soluble proteins. Several modeling studies have confirmed these predictions [MBL+11; SBdH+15; SCM14; KJJ+15]. However, all these results are based on equilibrium thermodynamics and coarse-grained models of the DNA and the cytoplasm. It is unclear to what degree these approaches are valid for living cells, which are far out of equilibrium and whose DNA has a complex folding structure.

It has been reported that the macromolecular composition of the bacterial cell is related to its metabolic activity [BD08; SMK58], so is the nucleoid phenotype. We have clearly observed the difference in cell and nucleoid sizes, and nucleoid phenotypes, in different types of growth medium. In a minimal medium ($\sim$100 min. cell cycle), nucleoids appear to be somewhat homogeneous (Figure 1-12 A). However, cells grown in a rich medium ($\sim$20 min. cell cycle), have more structured nucleoid. In particular, the chromosome mass forms dense foci near the peripheries of a nucleoid and neck-like structure can be found connecting these dense foci [Figure 1-12 B, MCY+16]. I think this is a result of higher transcription activities in fast growth conditions causing the formation of more transcription foci (Figure 1-6 B); however, I do not expect a significant change in the volume fraction of crowders.

1.6.1 Crowding and the Nucleoid as a Phase

Chromosomes of live *E. coli* cells interact with macromolecular crowders at significant volume fractions. In aqueous solution a chromosomal DNA can be thought of as a string of blobs with each blob having some diameter, say a [HBD07]. These blobs have excluded volume interactions between

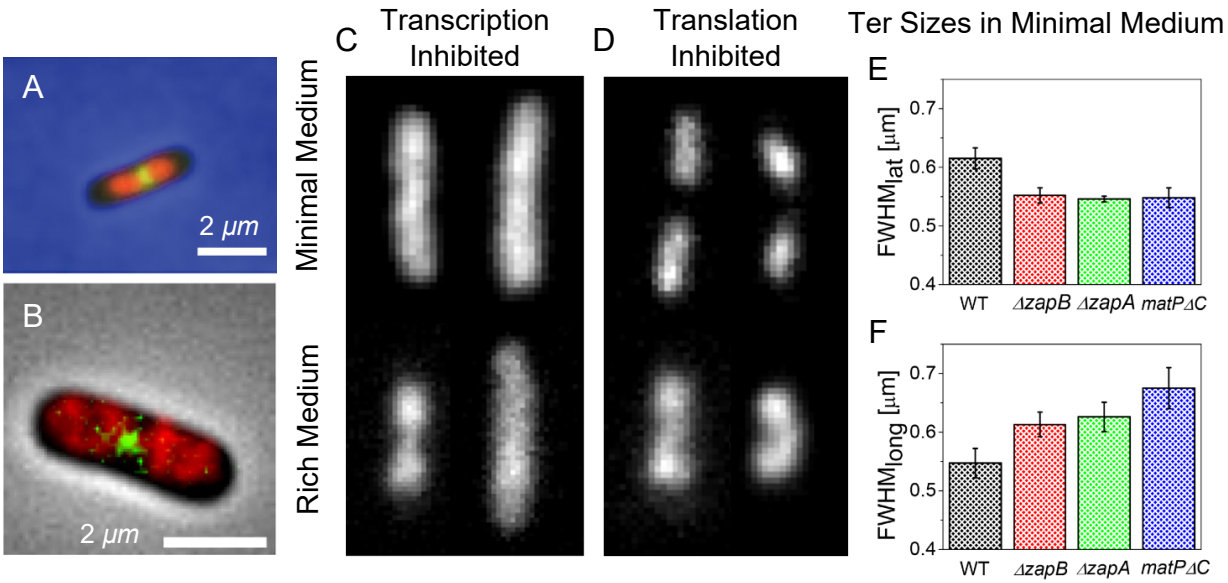


Figure 1-12 : Various effects on nucleoid conformation. (A) Composed image of a wild-type cell in minimal medium. Red is the nucleoid fluorescent image; green is the Ter region fluorescent image, and blue is the phase contrast image. (B) Composed image of a wild-type cell in rich medium. The cell shown is the same strain as in (A). Here the phase contrast image is shown in gray. (C) Effect of transcription inhibition. Two images on the left are captured just after treatment with rifampicin, and the right two images are captured while after the treatment. (D) Effect of transcription inhibition. Similar arrangement of images than (C) [HYGJM12]. (E) Widths of the Ter foci in the longitudinal direction. Average lateral widths for WT, ΔzapB, ΔzapA and matPΔC strains. The error bars are standard error of the mean (S.E.M.) based on the replicate measurements. (F) The same measurements as shown in (E) in the longitudinal direction. Panel A, B, E, and F are reproduced from [MCY+16]. Panel C and D are reproduced from [HYGJM12].

them, which prevent them from overlapping. Each blob executes a random thermal motion. So, this string of blobs is thought to follow the self-avoiding chain model. What the blob sizes are and how uniform they are in *E. coli* is not universally agreed. Pelletier et al. have estimated the total number of structural units per single stationary phase chromosome to be between $Na = 16$ ($a = 440$ nm) and $Na = 71$ ($a = 130$ nm) [PHH+12]. In the case of exponential phase chromosomes, we expect the overall nucleoid sizes to be larger, and the diameter of the structural units to be smaller. In our previous work on coarse grained molecular dynamics (MD) modeling, we choose $Na = 150$ ($a = 80$ nm) for one genome equivalent of chromosome [MCY+16]. This is based on observations reviewed in Section 1.5.2 on page 22 In the literature, simulations with total numbers of structural units in range $Na = 60 \sim 440$ has been carried out for MD modeling [SCM14; CYWL15; KJJ+15; JKJ+15]. From the results of simulating DNA confined with difference sizes of crowding agents at the same time, Kim et al. find the compactness of DNA is a function of $a_c^2 \rho_c$, where, for a given c, a_c is the diameter of crowding agent c and ρ_c is its numerical density [KJJ+15]. From results of simulating DNA segregation, Chen et al. suggest attractive interactions between the polymer and a small number of crowders can significantly facilitate the chain segregation [CYWL15]. Both aforementioned simulations and our previous work model the DNA as string-beads and are carried out using Langevin dynamics simulations. Osmotic compaction is a counter intuitive result of the second law of thermal dynamics. For the entropy to increase, a poly-disperse set of particles would mix well. However, when a polymer consist of large structure units (larger than other particles in the system), it is entropically favorable for the polymer to collapse such that the smaller particles have more free volume. Once that collapse happens, there is a globe polymer phase and a polymer-free phase in that system. The concentration of the small particles in the globe polymer phase is less than that in the polymer free phase. Therefore, the polymer experiences a pressure difference from inside and outside of its boundary compaction it. In this context, we call this pressure osmotic pressure. The small particles is some times called the crowders, and the effect of compaction is referred to as crowding. Living cells contain a rich variety of biomacromolecules. By measuring the dry mass of *E. coli* cells, it has been estimated that the volume fraction of all macromolecules is on the order of $20 \sim 30\%$ [EM06].

1.6.2 Size Estimation of Super Coiled DNA by Minimizing Free Energy

1.6.2.1 Randomly Branched Polymer

In the seminal work, Odijk proposed that crowders and DNA separate into two distinct phases in an *E. coli* cell, a nucleoid and a cytosolic phase [Odi98]. The work considered a system constituted of monodisperse globular proteins (diameter, $a_c = 4.6\ nm$) and supercoiled randomly branched DNA (contour length, L = 1600 μm; effective exclusion radius, $E \approx 4.7\ nm$; superhelix persistence length, $L_s = 630\ \mu m$; superhelix diameter, $d_s = 22\ nm$). The system is similar to what is illustrated in Figure 1-9.

He wrote,

$$\beta F_{\text{total}} = m \ln \frac{m}{V} - m + mg(\bar{v}) + \frac{mB_c}{V} + \frac{B_s}{V}. \tag{1.20}$$

where m is the number of crowders within the volume V. The first three terms are the contribution from the interaction among protein crowders (the third term was neglected in calculations); the fourth term is the contribution from protein-DNA interactions (with $B_c \equiv \pi L E^3 \approx 0.111\ \mu m^3$); and the last term is the contribution from DNA self-interactions (with $B_s = \frac{\pi}{4} L_s^2 d_s \approx 710\ \mu m^3$) [Some of the numerical values are listed in WO99].

Following his theory, the nucleoid volume of *E. coli* is numerically calculated to be 0.068 fL which is within an order of magnitude correct to our current understanding [YMRM20]. This is about a third of what we have observed in living cells. Nevertheless, if we calculate nucleoid volume from the observed radii of gyration, we have $V_{n,\,\text{obs.}} = 4/3\pi R g_{\text{Ma}} R g_{\text{mi}}^2 = 0.087\ fL$, which is off by 30%.

1.6.2.2 Coarse-Grained DNA String-Beads

Another attempt was made by Kim et al. [KJJ+15]. The analytical part of the work considered a system constituted of monodisperse globular crowders (diameter a_c) and a open chain of DNA structure units (diameter a). The system is similar to what is illustrated in Figure 1-11. In similar notions, they wrote,

$$\beta F_{\text{total}} = m \ln \frac{m}{V} - m + B_2 \frac{m^2}{V} + \frac{5}{8} B_2^2 \frac{m^3}{2V^2} + \frac{A}{D}\left(\frac{R_0^2}{R} + \frac{R^2}{2R_0}\right) + \frac{N^3 a^6}{R^2 D^4} + \beta F_{\text{dep}}. \tag{1.21}$$

where, D is the diameter of the cylindrical constrain, R_0 is the end-to-end distance of the DNA chain in absence of crowders. The first four terms are the contribution from the interaction among the crowders and the second virial coefficient,

$$B_2 = 4 \cdot \frac{4\pi}{3} \left(\frac{a_c}{2}\right)^3 . \tag{1.22}$$

The fifth term is the (renormalized) Flory free energy of a confined chain in the absence of crowders. In that expression, A is a numerical prefactor, which can be adjusted for the best fit to numerical data. The second last term is a standard three body interaction energy. This term captures DNA monomer-monomer interactions.

The last term is the free energy reduction due to the depletiong of crowder from the chain and is related to F_{crowd}

$$\begin{aligned} F_{\text{dep}} &= V_{\text{dep}} \left(-\frac{\partial F_{\text{crowd}}}{\partial V}\right) \\ &= V_{\text{dep}} \Pi_{\text{crowd}}. \end{aligned}$$

Here V_{dep} is the volume of the depletion zone and Π_c is the osmotic pressure from the crowders. It can be expressed as

$$\begin{aligned} V_{\text{dep}} &= \frac{4\pi}{3} \left(\frac{a + a_c}{2}\right)^3 - \Delta V_{\max} \\ &= \frac{\pi}{12} a \left(2a^2 + 6aa_c + 3a_c^2\right). \end{aligned} \tag{1.23}$$

Meanwhile, an under estimation of the depletion zone volume is given by $V_{\text{dep}} - \frac{4\pi}{3}\left(\frac{a}{2}\right)^2$. This estimation yielded better quantitative agreement with their simulations (Figure 1-13). As Kim et al. pointed out, the measure of crowding should be $\Psi \equiv a_c^2 \rho_c$, which was estimated to be about 22 μm^{-1}. This value corresponds to volume fraction $\Phi = 43\%$, and $R/R_0 \approx 0.5$ based on Figure 1-13. We have done similar simulations with closed chains of DNA structure units. Further discussions are given in Section 2.7 on page 51.

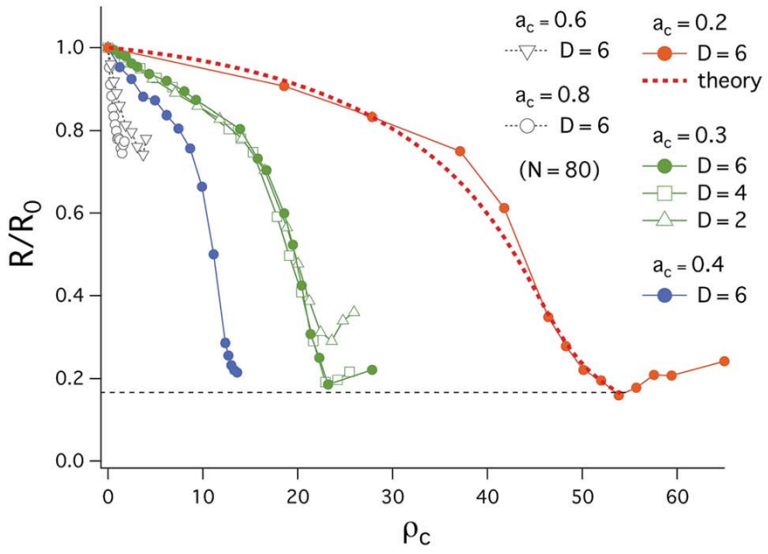


Figure 1-13 : Collapse of a flexible chain ($N = 80$) by crowding agents in a cylindrical space as a function of the density ρ_c of crowding particles for the mono-disperse. As ρ_c increases, the confined chain shrinks in size. Here, R/R_0 is the reduced chain size with R_0 being the equilibrium size in the absence of crowding particles. The chain size reaches a minimum at a certain value of ρ_c. A few curves for $a_c = 0.3$ corresponding to different D values (green) tend to collapse onto each other. This implies that cylindrical confinement enters into the picture through R_0. The dotted line was obtained by minimizing free energy.

1.7 Recent Advances in Understanding Nucleoid Compaction

To date, quantitative experimental tests to verify these models have been carried out *in vitro*, using purified DNA [ZSvKvdM09] or DNA liberated from cells [CWO01; PHH+12]. In these studies, charge-neutral polymers, dextran or polyethylene glycol (PEG), have been used as crowding agents to mimic the cytoplasmic environment even though most cytosolic crowders do not have a neutral charge. All these experiments agree that crowding can lead to significant compaction of the DNA. However, the data are in disagreement if the compaction occurs abruptly via a first order coil-globule phase transition with an observed metastable state [PHH+12] or gradually via a second order transition as the concentration of crowding agents increases [CWO01].

It has been shown, *in vitro*, that uncharged polymer crowding agent can generate an entropic (depletion) force; consequently, compact dsDNA in various confinement to sizes (assuming the scaling law $Rg \propto N^{3/5}$ [Kam93; DRLP+07]) small enough to fit in a cell. Extensive *in vitro* studies of dsDNA compaction in different confinement and by dextran or PEG as crowding agents [JvdMD11; PHH+12; HBD07; ZSvKvdM09] have been carried out (Figure 1-14 A). The common characterization of crowding agent concentration is volume fraction. In experiments with bulk phase (unconfined) single molecule λ-DNA, the dsDNA coil size monotonically decreases with increasing volume fraction of crowding agents. This reduction of coil size can be explained by an increasing inward osmotic pressure (Figure 1-14 B). Nevertheless, when confined by a nanoslit or nanotube, non-monotonic changes in coil size with increasing volume fraction of crowding agents are observed. The DNA coils initially swell, reaches an apex, and eventually compresses. This can be explained by the projected area of the DNA coils to the imaging plane being significantly higher than the projected area of the same to a vertical plane (Figure 1-13 C). In this case, the reduction in coil volume is not presented in the projection to the imaging plane. Furthermore, in nanoslit measurements, as volume fraction of dextran is increased the aspect ratio of DNA conformation, ($R_{\mathrm{M}}/R_{\mathrm{m}}$) decreases (Figure 1-14 D).

However, the data are in disagreement if the compaction occurs abruptly via a first order coil-globule phase transition with an observed metastable state [PHH+12] or gradually via a second order transition as the concentration of crowding agents increases [CWO01].

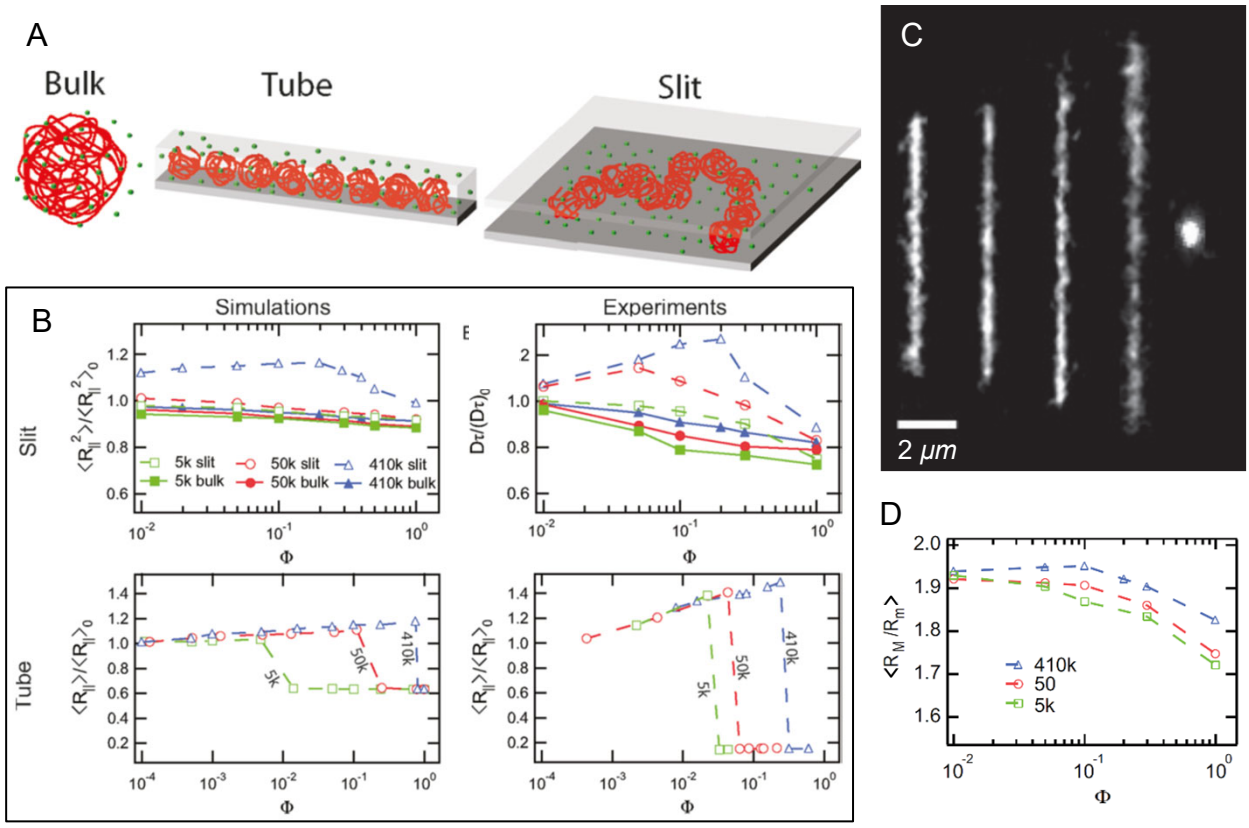


Figure 1-14 : *In vitro* and numerical results of dsDNA compaction. (A-B) Experimental designs, and experimental and simulation results from [ZSvKvdM09]. (C) Montage of fluorescence images of T4-DNA in 300 $nm \times 300\ nm$ channels and 1×T buffer (2.9 mM TrisCl, 7.1 mM Tris, pH 8.5) crowded by dextran with volume fractions of 0, 4.2×10^{-4}, 4.2×10^{-3}, 4.2×10^{-2}, 6.3×10^{-2} from left to right (reproduced from [ZSvKvdM09]). Notice the differentiation in volume fractions of the last two frames, and how abrupt the coil-globe phase transition is. (D) Experimental measurements of $\langle R_M/R_m \rangle$ for λ-DNA in nanoslits from the supporting information of [JvdMD11].

1.8 Outline of This Dissertation

In this dissertation we chemically and mechanically perturbed cellular organization in a controlled fashion, while following the cellular response at single cell level in real time using a high resolution wide field epifluorescence microscope. In addition, we looked for insights from simulations using a string-bead representation of the *E. coli* chromosome.

In Chapter 2, I summarize the general material and methods used in the latter chapters of this dissertation. In Chapter 3, I describe three different microfluidic platforms used in this dissertation. In Chapter 4, I discuss the compaction of *E. coli* nucleoid by macromolecular crowding. In Chapter 5, I summarize the work presented in this dissertation. In Chapter 6, I discuss the outlook on further work and summarize some preliminary results we already have.

Most of the writing in Chapter 3 has been published as articles:

- Yang, Da, Clayton M. Greer, Branndon P. Jones, Anna D. Jennings, Scott T. Retterer, and Jaan Männik. "Characterization of Small Microfluidic Valves for Studies of Mechanical Properties of Bacteria." *Journal of Vacuum Science & Technology B, Nanotechnology and Microelectronics: Materials, Processing, Measurement, and Phenomena* 33, no. 6 (2015): 06F202.

- Yang, D., A. D. Jennings, and J. Männik. "Microfluidic Platform for Studies of Self-Organizing Processes in a Bacterial Cell." Chap. Micro, Nano & Bio Fluidics In *Techconnect Briefs 2016. Vol. 3 Biotech, Biomaterials and Biomedical*, edited by Matthew Laudon, Bart Romanowicz and TechConnect World Innovation Conference and Expo. 188-91. Danville, CA: TechConnect 2016, 2016.

- Yang, D., A. D. Jennings, E. Borrego, S. T. Retterer, and J. Männik. "Analysis of Factors Limiting Bacterial Growth in PDMS Mother Machine Devices." *Front Microbiol* 9 (May 2018): 871.

Chapter 4, parts of Chapter 2 supporting the former, and Appendix D has been published as an article:

- Yang, Da, Jaana Männik., Scott T. Retterer, and Jaan Männik. "The Effects of Polydisperse Crowders on the Compaction of the *Escherichia coli* Nucleoid." *Molecular microbiology* (2020 Jan 21)

Chapter 2

Materials and Methods

2.1 Bacterial Strains and Growth

All *E. coli* strains studied in this dissertation were derivatives of wild-type *E. coli* K-12 having either MG1655 [GRSL81] or BW25113 [DW00] background. They were nonpathogenic strains of *E. coli* and had been cultivated and prepared in a biosafety level one laboratory. A list of all strains used in this dissertation and their genotypes is given in Table 2-1. A description of their cultivation and preparation is given in Section 2.1.2.

2.1.1 *E. coli* Strain Construction

All *E. coli* strains used are listed in Table 2-1. In strains BW25113+GFP and DY1, a cytoplasmic GFPmut 2 fluorescent label was expressed from a plasmid [CVF96]. In strains AJ5 and JM57, a cytoplasmic label was created by replacing the *leuB* gene with a fluorescent protein sequence using lambda red recombination [MLC10]. In strains DY3, a cytoplasmic label was created by inserting a fluorescent protein sequence behind the 3' end of the *leuB* gene using lambda red recombination. Meanwhile, each of strains JMAH9, JM57, and DY3 has a nucleoid fluorescent label. Those nucleoid fluorescent labels were created by replacing gene *hupA* with a sequence coding a HupA fluorescent fusion protein, where the linker-fluorophore sequence succeeds the 3' end of the *hupA* sequence, using P1 transduction [TCC07]. Strain JMAH9 has its *matP* gene replaced with a sequence coding a MatP fluorescent fusion protein, where the linker-fluorophore sequence succeeds the 3' end of the *matP* sequence, using P1 transduction. Furthermore, cell division in each of strains DY1

and DY3 can be inhibited by exposure to Isopropyl β-D-1-thiogalactopyranoside (IPTG). Those strains was transformed with plasmid pA3 containing a *sulA* sequence controlled by an IPTG inducible promoter [DML08]. The transformations were carried out with a Bio-Rad MicroPulser electroporator (Bio-Rad, CA).

2.1.2 Culturing *E. coli* Cells

In general, bacterial cells were grown then imaged in M9 minimal medium (Teknova), supplemented with 2 mM magnesium sulfate ($MgSO_4$), at at 28℃. Depending on the growth condition, selection markers and defects in strains, and specific treatments required by experiments, various chemicals were supplemented to the growth media. These chemicals include carbon sources (glucose or glycerol), amino acids supplements, selection antibiotics, and other chemical for specific treatments to the cells and the apparatus.

Three different growth conditions were used in this dissertation. In the slow growth condition, 0.3% glycerol (volume/volume, final concentration) was added to the growth media. For strains AJ5 and JM57, where *leuB* was deleted but not replaced, 100 $\mu g/mL$ leucine was added to the growth media. In the moderately fast growth condition, 0.5% glucose (weight/volume) and 0.2% casamino acids (Fisher Scientific) was added to the growth media. In the fast growth condition, either EZ Rich Defined Medium (Teknova, Inc., CA) supplemented with 0.2% glucose or Lysogeny broth (LB) without supplements was used instead of the M9 medium. The strains were first cultivated on a 2% agar plate with appropriated growth media and selection antibiotic(s). Then, single colonies were introduced to liquid growth media with selection antibiotic(s).

For strains DY1 and DY3, 0.2% glucose was added to LB agar plates.

2.1.2.1 Preparation for Dead-End Mother-Machine Experiments

For each dead-end mother-machine experiment, $2 \sim 4$ ml of stationary phase (after overnight growth) cell culture was concentrated by centrifugation, in the presence of 0.5 $\mu g/mL$ of bovine serum albumin (BSA, Sigma-Aldrich) to a volume that is $3 \sim 10$ times the volume of the pellet. The pellet was an aggregation of cell resulted from the centrifugation. Then $2 \sim 3$ μL of re-suspended culture is pipetted into the main flow channel of a dead-end microfluidic mother machine (see Section 2.4 on Page 45). The cells were then allowed to populate the dead-end channels for $1 \sim 2$ hrs.

Once these channels were sufficiently populated, tubing was connected to the device, and a flow of fresh growth medium supplemented with BSA (0.5 $\mu g/ml$, unless otherwise specified) was started. This medium contained no antibiotics. A flow was maintained at 5 $\mu L/min.$ throughout each experiment using an NE 1000 Syringe Pump (New Era Pump Systems, NY). To ensure a steady-state growth, the cells were left to grow in channels for at least 14 hrs (16 hrs for slow growth) before starting imaging.

2.1.2.2 Preparation for Microvalve Experiments

For each microvalve experiment, single colonies of BW25113+GFP from LB agar plates were introduced to LB liquid media. After over night growth, a series (typically two sequences) of dilutions and incubations was made. The final dilutions had an $OD_{600} \approx 0.01$ and was directly injected into the microvalve chips for experiments.

2.1.2.3 Preparation for Microanvil Experiments

For each microanvil experiment, single colonies of DY1 or DY3 were introduced to M9 supplemented with 2 mM $MgSO_4$, 0.5% glucose, and 20 $\mu g/mL$ of chloramphenicol, then grown overnight. The overnight culture was diluted to an $OD_{600} \approx 0.002$ in fresh M9 medium supplemented with 2 mM $MgSO_4$, 0.3% glycerol, and 50 nM IPTG to induce expression of the extrachromosomal *sulA* gene. After 2 hrs. (6 hrs. for DY3), the cells were filamentous and contained multiple nucleoids. The cell culture was very diluted and was directly injected into the microanvil chips for experiments. For each dead-end mother-machine experiment, $2 \sim 4$ mL of stationary phase (after overnight growth) cell culture was concentrated by centrifugation, in the presence of 0.5 $\mu g/mL$ of bovine serum albumin (BSA, Sigma-Aldrich) to a volume that is $3 \sim 10$ times the volume of the pellet. The pellet was an aggregation of cell resulted from the centrifugation. Then $2 \sim 3$ μL of re-suspended culture is pipetted into the main flow channel of a dead-end microfluidic mother machine (see Section 2.4 on Page 45).

2.1.3 Chemical Treatments of the Bacterial Cells in the Dead-End Mother-Machine Platform

To rapidly swap the growth medium in a dead-end mother-machine chip (see Section 2.4 on Page 45), an additional liquid inlet to the chip was utilized. This technique enabled us to treat the cells with various chemicals without interrupting the time-lapse imaging and to observe the immediate responses of single cells.

In general, treatment chemicals were supplemented to the growth media. The resultant treatment medium was loaded in a syringe and connected to the microfluidic chip via a separate tubing. The treatment media delivery was also controlled by a syringe pump. To prevent the treatment medium reaching the cells prematurely, the tubing was backfilled with the regular medium before it was connected to the chip. Cells were typically imaged in regular medium for 4 hrs. before the treatment. Then the growth medium flow was stopped for 60 s and the treatment medium started subsequently. All media flow were maintained at 5 μL/min.

2.1.3.1 Hyper-/Hypo-osmotic Treatments of the Bacterial Cells

For hyperosmotic treatments of *E. coli*, the growth media were supplemented with different concentrations ($0.1 \sim 1.0$ M) of NaCl. For hypoosmotic treatments, autoclaved deionized (DI) water supplemented with BSA was used instead of regular growth media. The final osmolality of growth media were measured using a Vapro© 5520 vapor pressure osmometer (Wescor Inc., UT) after each experiment. The osmolality values returned by the instrument were in units of $mOsm/kg$.

2.1.3.2 Rifampicin Treatment

For rifampicin treatment, a separate tubing was connected to the microfluidic chip that contained regular growth media supplemented with 300 $\mu g/mL$ rifampicin. If a subsequent hyperosmotic shock was specified for the experiment, cells were imaged in the presence of rifampicin for 25 min. (30 min. for slow growth) before the hyperosmotic shock ($0.1 \sim 1.0$ M) of NaCl) was delivered to cells. In those experiments, the 300 $\mu g/mL$ concentration of rifampicin were maintained in the hyperosmotic media.

2.1.4 Spectrophotometry

The attenuation coefficients of visible light at certain wavelengths are measured using a Thermo Scientific GENESYS 20 Visible Spectrophotometer (Thermo Fisher Scientific, MA) for the liquid analytes. The common logarithm (with base 10) of the attenuation coefficient is called the optical density (OD). For bacterial cell cultures, ODs are measured at wavelengths of 600 nm—hence, the notion OD_{600}.

2.2 Microscopy and Image Analysis

Microscopic imaging of live bacterial cells is the integral part of the experimental methods used in this dissertation. A digital camera optically coupled to a microscope was used to capture images. The images were processed and analyzed in the MATLAB© (MathWorks, MA) environment.

2.2.1 The Imaging System

A Nikon© Ti-E inverted epifluorescence microscope (Nikon Instruments, Japan) with a 100X (numerical aperture, N.A. = 1.45) oil immersion phase contrast objective was used for imaging all bacterial cells. Here, epifluorescence means the excitation radiation was delivered through the viewing objective to the sample. The model of the objective used was CFI Plan Apochromat λ100x oil [Ph3 DM] (Nikon Instruments, Japan). It was designed to work with #1.5 coverslips (0.17 mm thick glass). It had a working distance of 0.13 mm. (See Figure 2-1.)

2.2.1.1 Numerical Aperture

The object side numerical aperture (NA) is a measure of how much light from a point source at the object side focal point can be collected by the objective in question. It is formally defined by the following equation,

$$\mathrm{NA} = n \sin(\theta). \tag{2.1}$$

Here, n is the index of refraction of the media behind which the objective is working and θ is the angular aperture, which is half of the apex angle of the cone of light that can enter the objective from its object side focal point. For the aforementioned 100X objective, an optical oil was applied between the front lens of the objective and the glass coverslip, which carried the bacterial cells of

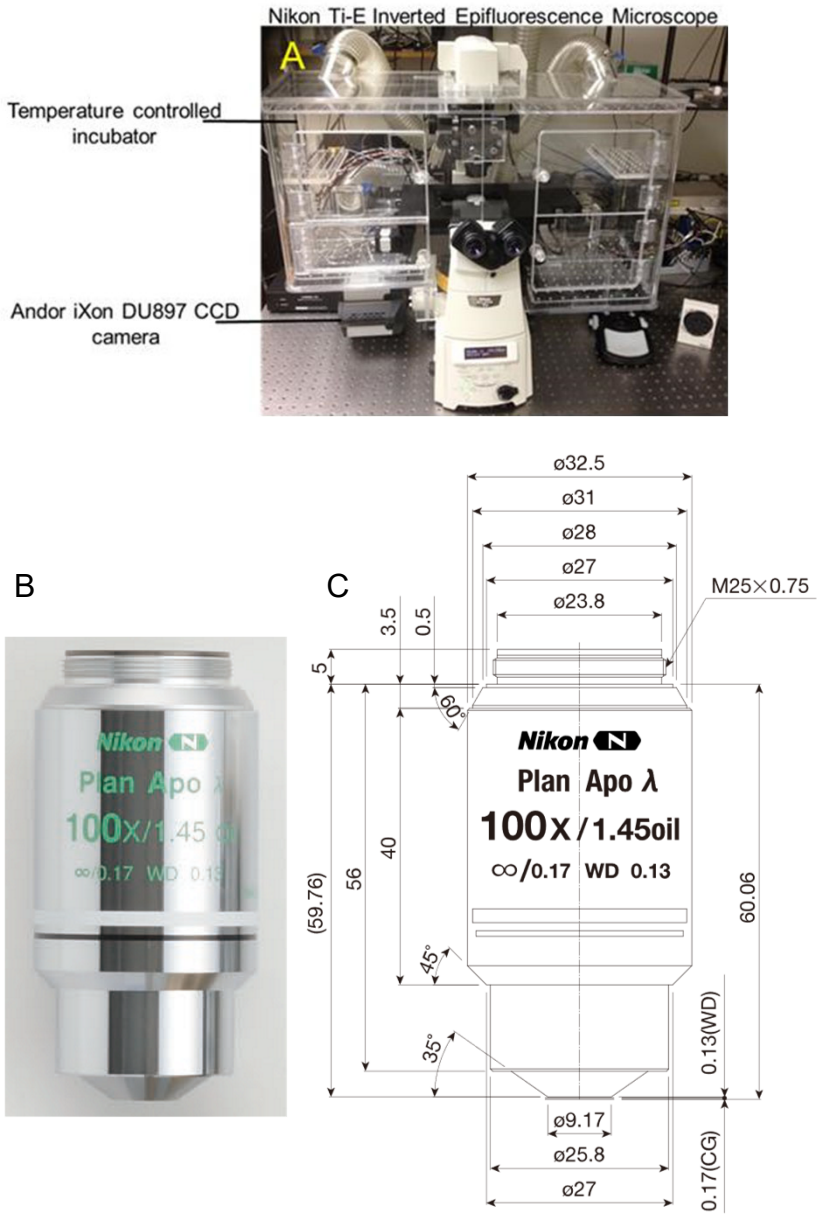


Figure 2-1 : The imaging system. (A) A photograph of the Nikon Ti-E inverted epifluorescence microscope. (B) A photograph of a objective of the same model used in this dissertation. The front lens faces toward the bottom of the page. (C) A technical drawing with mechanical dimensions of the same objective. Panel A is reproduced from [Bai16], Panel B and C are reproduced from the Nikon Website (https://www.nikon.com/).

interest on the other side. Across the visible range of light and at temperatures of our experiments, the microscope immersion oil had an index of refraction, $n \approx 1.52$.

2.2.1.2 The Camera and Optical Filters

All images were captured on an iXon DU897 EMCCD camera (Andor Technology, Ireland) and recorded using NIS-Elements software (Nikon Instruments, Japan). For the images used in this dissertation, one pixel corresponded to a length of $8/75\ \mu m \approx 0.107\ \mu m$. Fluorophores were excited by a 200 W Hg lamp through neutral density filter(s). A Chroma 41004 filtercube (Chroma Technology Corp., VT) was used when capturing red fluorescent images. A Chroma 41001 filtercube (Chroma Technology Corp., VT) was used when capturing green fluorescent images. A motorized stage and a perfect focus system were utilized during multi-position time-lapse imaging.

2.2.2 Measuring the Point Spread Function

By imaging a point light source, the point spread function (PSF) of the imaging system in a broad or in a narrow spectrum can be measured. In particular, we imaged CdSe/ZnS quantum dots. Before aggregation, it had a emission peak at 536 nm. Unfortunately, we could not very well dissolve away the surfactant, which led to a substantial background noise and a very low signal to noise ratio. So, we were not able measure the PSF in our green band with good precision. Nevertheless, we could obtain the order of magnitude of the PSF. Meanwhile, while repeatably washing the quantum dots, a portion of them start to aggregate into bulk phase. The emission spectrum of bulk phase InP overlaps the red band of our imaging system. Since the aggregation had just occurred and we did have some knowledge about the size the PSF, we could pick out point light sources in our red band to measure PSF.

By capturing red fluorescent images at different z-positions for the objective, we could see how the captured signal of a single point light source change with respect to z (Figure 2-2 A, B). We fitted each z-slice to a Gaussian function, and plotted the fitted Gaussian width. Then, the latter plot was interpolated by the fourth degree polynomial (Figure 2-2 C). Gaussian distributions with the smallest observed PSF width (0.316 μm) was used to reconstruct simulations discussed in Section 2.7.

Table 2-1 : List of *E. coli* strains used in this dissertation

Strain	Genotype	[Selection antibiotic(s)]
AJ5	BW25113 *ΔleuB::Pj23100 tagRFP-T::aph frt*	25 $\mu g/mL$ kanamycin
BW25113+GFP	BW25113 pKenGFPmu2-amp^{R}	100 $\mu g/mL$ ampicillin
JM97	MG1655 *ΔleuB::Pj23100 tagRFP-T::aph frt* P_{lac}-*sulA cat**	25 $\mu g/mL$ chloramphenicol
JMAH9	MG1655 *ΔhupA::hupA-mCherry-frt* *ΔmatP::matP-YPet-frt-kan-frt* P_{lac}-*sulA cat**	25 $\mu g/mL$ chloramphenicol
JM57	MG1655 *ΔleuB::Pj23100 tagRFP-T::frt* *ΔhupA::hupA-mNeonGreen-frt-kan-frt*	25 $\mu g/mL$ kanamycin
DY3	MG1655 *ΔhupA::hupA-mCherry-frt* *leuB::Pj23100 mNeonGreen-frt* P_{lac}-*sulA cat**	25 $\mu g/mL$ chloramphenicol

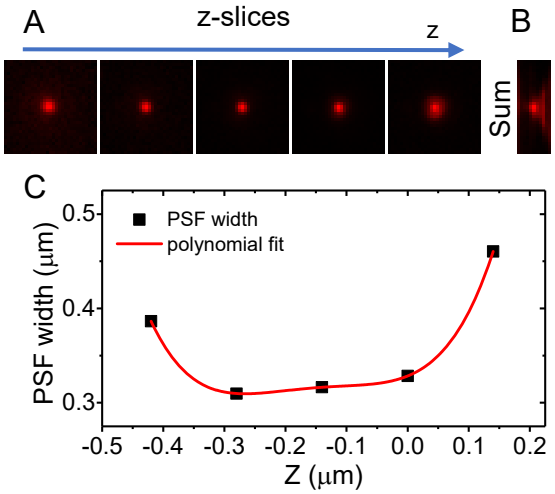


Figure 2-2 : Measuring the point spread function. (A) Images of a quantum dot at different depth relative to the focal plane (z). (B) Projection of the 3D PSF to the zy-plane, by summation each z slice in the x-direction. (C) Fitted PSF widths in the z slices and their fitting to the fourth degree polynomial.

2.2.3 Image Analysis

Image analysis was carried out using Matlab scripts based on Matlab Image Analysis Toolbox, Signal Processing Toolbox, Optimization Toolbox, and DipImage Toolbox (https://www.diplib.org/). In general, for each cell analyzed, its longitudinal axis was identified first in every frame of the time-lapse imaging. For normal cells, these axes were straight segments. Cell width, nucleoid length and width were measured based on that axis. For filamentous cells, the cell axes were polylines and individual nucleoid axes, if any, were identified independently. The corresponding widths were measured based on those axes. All those measurements of lengths were from fluorescent images. Volumes and aspect ratios, if any, were derived from length and width measurements.

2.2.3.1 Cell Axis

For the cells analyzed in Section 3.1, the cell axis was found by finding the binary mask covering the cell and the major Feret axis [FNY91] of the binary mask. To find the binary mask, the raw cytoplasmic fluorescent image was transformed to the second derivative image using the DipImage function *laplace_plus_dgg*, which computes the Laplacian and the second derivative in the gradient direction of an image [VvV94]. Thresholding of the second derivative image based on zero crossing yielded a binary image, which is then eroded and dilated (DipImage functions) to resolve individual cells and to fill them, respectively. The result was the binary mask, the major Feret axis of which was the cell axis.

For a normal cell analyzed in and Chapter 4, the cell axis was a manually identified straight segment connecting two poles of the same.

For filamentous cells analyzed in Chapters 4 and 6.2, and for the cells analyzed in Sections 3.2 and 3.3, the cell axes were polylines. A polyline was piece-wise linear and was manually drawn over each cell in every frame (of the time-lapse imaging). This polyline extended from both poles of the cell.

2.2.3.2 Length Measurements

For the cells analyzed in Section 3.1, cell lengths were measured from those binary masks covering the cells. The measurement consists of finding the greatest Feret diameter for each cell using the *measure* function from DipImage.

For all cells analyzed in Sections 3.2 and 3.3, Chapter 4, and Section 6.2, the cytoplasmic fluorescent images were interpolated parallel to the cell axes, such that the polyline or segment became straight, "orthogonal," and could be represented by a 1D array of numeric values. Subsequently, the line was broadened symmetrically for several pixels (typically four pixels on each side) and a 2D array of numeric values was extracted. The average values along the longitudinal direction were the longitudinal intensity profile of the cytoplasmic reporters of the cell. The intensity profiles of normal cells in Section 3.3 and Chapter 4 Chapter 4 were smoothed by least-square fitting them to the exponential power function, which was a generalized Gaussian function:

$$I(x) = I_0 \exp(-\frac{|x-\mu|^\kappa}{\kappa\sigma^\kappa}). \tag{2.2}$$

The skewness of this distribution was 0 and κ was given a lower bound at 2. For the filamentous cells analyzed in Chapters 4 and 6.2, and for the cells analyzed in Section 3.2, The intensity profiles of filamentous cells analyzed in Chapters 4 were smoothed by least-square fitting them to the multi-peak exponential power function. The intensity profiles of the cells analyzed in Section 3.2 and Chapter 6.2 were smoothed by moving-averaging. Finally, by finding inflection points at both ends of each smoothed longitudinal intensity profile, the end points of the polyline and the cell length were determined.

For the cells analyzed in Chapters 4 and 6.2, their nucleoid lengths were measured. For the normal cells analyzed in Chapter 4, their nucleoid lengths were measured in the way similar to how their cytoplasmic lengths were measured. Nucleoid fluorescent images were interpolated parallel to the same cell axes. Then the nucleoid intensity profiles were fitted to the exponential power function. And the nucleoid lengths were determined by finding the distance between inflection points. For the filamentous cells analyzed in Chapters 4 and 6.2, their nucleoid lengths were measured based on nucleoid axes identified manually and individually.

2.2.3.3 Width Measurements

For the cells analyzed in Section 3.1, based on the binary cell masks from the previous sub-subsection, the gray value center of mass coordinates were also determined. Next, a line perpendicular to the long axes of the cell that passes through the cell center was calculated. To improve the accuracy of the cell width measurements, an additional set of lines are calculated, where

the orientation relative to the previous lateral line was varied in small angular steps (0.01 radian). For each orientation, an intensity profile from the fluorescent image is determined, and the profile is fitted to a Gaussian function. The Gaussian with the smallest width was then found among all the fits. Due to diffraction, variance of the Gaussian is about 0.08 μm smaller than the cytoplasmic diameter of the cell in our setup [MDG+09]. An additional 0.04 μm was added to the cytoplasmic diameter to account for the width of the periplasmic space and outer membrane layer of the cell. The final calculated width thus corresponds to the outer diameter of the cell.

For the cells analyzed in Chapter 4, to determine the cytoplasmic and nucleoid widths, cell and nucleoid widths were measured at multiple points along the corresponding axes. The average values plus 0.08 μm were then reported. The final calculated widths here corresponded to the diameters of either the cytoplasm or nucleoids.

2.2.3.4 Determination of Crowder Concentration Based on the Intensity of Fluorescent Reporters

We measured nucleoids responses to changes in crowder concentration (See Chapter 4) . The relative change in concentration of any species of crowders ($\rho_c/\rho_{c,0}$) was the same during osmotic shock and squeezing measurements. Therefore, the relative change in concentration of cytoplasmic fluorescent label could be used as a proxy for ($\rho_c/\rho_{c,0}$). The concentration of the label is proportional to the fluorescent intensity of the label from unit volume. Our data showed that change in cytoplasmic width in osmotic shock measurements was less than 3% but length change was significant (as much as 40% at highest osmotic shocks). In microanvil measurements, the cell width changes were also minimal. When the cell volume decreased, the cytoplasmic fluorescent reporter became more concentrated and resulting intensity increased in proportion to concentration assuming the cell width on average remained constant. Thus,

$$\rho_c/\rho_{c,\,0} = I/I_0. \tag{2.3}$$

where I was the average pixel intensity from the cell during the shock or the squeeze and I_0 before the shock. The cell axis was shortened by five pixels (0.53 μm) from both poles as these pole regions have different a width than cell body. The cell axis was then broadened by four pixels on each side and all the covered pixels were averaged, yielding I or I_0. In the events where the longitudinal

profile were shorter than 12 values, its middle 2 or 3 values were averaged over and used. To correct for bleaching, focus shifts etc, I values were further normalized by total pixel intensity from the cell, $\sum I$. This intensity was calculated using all pixels from the cell (broadened by six pixels on each side). This rectangular region covered cell form pole to pole and was 1.4 μm wide. The final adjusted formula, which was used in calculations, was

$$\rho_c/\rho_{c,0} = \frac{\langle I \rangle / \sum I}{\langle I_0 \rangle / \sum I_0}. \tag{2.4}$$

To analyze squeezed cells, the cell center lines are again manually determined first. These resulting curves are piece-wise linear. In determining I, the polyline is broadened to cover nine pixels (about 1 μm). For a filamentous cell, the intensity profile was fitted to multi-peak exponential power functions to yield a smooth curve. Then, only values within the inflection point offset minus 5 away from corresponding centroids were taken into account for calculating mean cytoplasmic intensity I. Calculation of $\sum I$ follows the same procedure as outlined for the normal cells.

2.2.3.5 Estimations of Volume and Aspect Ratio from Lengths and Widths

Cell and nucleoid volumes were calculated assuming they were cylinders capped with half spheres on each pole. Cell and nucleoid aspect ratios were length to width ratios. For volume determination, we assume that every cell or nucleoid is a cylinder with two hemispherical caps. The volume, V, based on cell length, L, and width, W, is:

$$V = \tfrac{\pi}{6}W^3 + \tfrac{\pi}{4}W^2(L - W). \tag{2.5}$$

2.3 Statistical Analysis Methods

All descriptive statistics done in this dissertation were standard and were done with Matlab functions. Propagations of uncertainties were done in accordance with [Tay97]. For statistical significance testings, either Student's t-test or Welch's t-test was used and was done with GraphPad (`https://www.graphpad.com/`). To estimate correlations Pearson's R was used, which was done using OriginPro software (OriginLab, MA). The unconstrained averaging was done in accordance with [MBG+94].

All regression analyses were done by minimizing the sum of residuals to the second power. For the nonlinear regressions done with Matlab, the *lsqcurvefit* function was used. The unconstrained linear regressions listed in Table 4-3 were done with the considerations of the uncertainties in only the independent variables. Other linear regression analyses was done using OriginPro software.

2.4 Material and Fabrication of Microfluidic Chips

2.4.1 Material

In this dissertation, polydimethylsiloxane (PDMS) elastomer (Sylgard 184 kit, by Dow Corning, MI) was used as the material for fabricated microfluidics. Each completed device had a monolithic elastomer bonded to a microscopy use glass cover slip. PDMS was chosen due to its bio-compatibility, low shear modulus ($\sim 1\ Mpa$), and enormous allowable strain (close to 2). It mechanical properties were permissible for fabricating mechanical actuators, which could be used for mechanically perturbative experiment of microbiological samples of the micron scale. For this dissertation, mechanical actuators were fabricated to squeeze bacterial cells.

The Sylgard 184 kit comes in two separate containers. One contains "base", which was $\sim$60-mer PDMS with vinyl end-groups. The other contains "linker", which was $\sim$10-mer PDMS with at least three silicon-hydrogen (Si−H) bonds on each oligomer. The later container also contained a platinum-based catalyst. When the base and linker were mixed at the 10 : 1 weight ratio, the catalyst would open the double bond in a vinyl group of a base molecule and fuse it to the site of a Si−H bond of a linker molecule. This would result in a Si−CH_2−CH_2−Si linkage [CBC+99]. (See Figure 2-3.)

When the curing happens on a passivated substrate with topographic features (mold), the resulting elastomer would conform to the geometry of those features. Since, the PDMS pre-polymers used were $\sim$60-mer, only sub-nanometer unconformities could be expected [SSC+09]. We utilized surface micromachining technologies on Si wafers to produce molds for the soft-lithography of PDMS. The fabrication processes of the molds are discussed in Section 2.5.

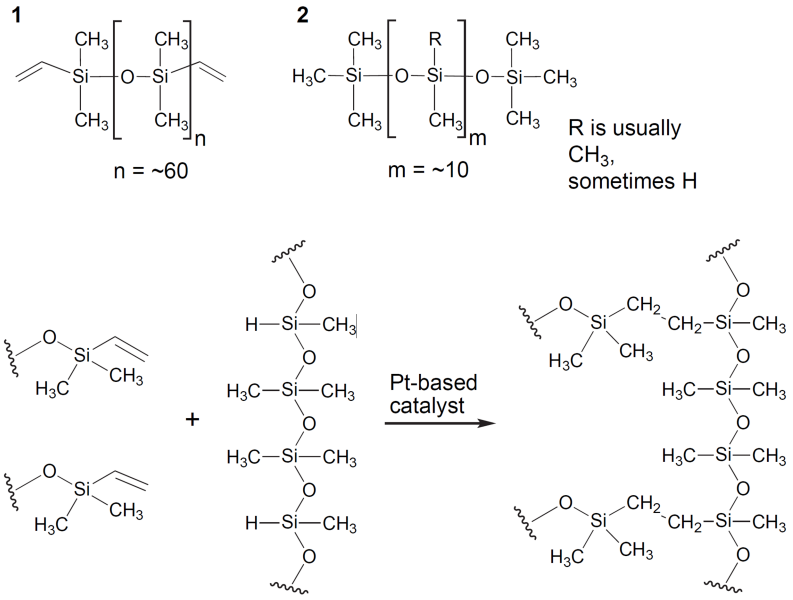


Figure 2-3 : The chemistry of oligomeric PDMS curing into elastomer. This figure is reproduced from [CBC+99]

2.4.2 Microchip Fabrication

For microfluidic chips with only one layer (i.e., mother-machine devices used in Section 3.1 and Chapter 4), the PDMS elastomer was cast on the mold in a 10 : 1 base/linker weight ratio. This layer was $\sim 3\ mm$ thick. The PDMS mixture was degassed in a desiccator at a pressure of about 0.2atm.. Then, the mixture was baked at 90°C for 20 min. in a convection oven, and was left in the oven for at least two more hours as the oven was powered off and cooled down from 90°C. This allowed the PDMS mixture to fully cure and resulted in less stressed elastomer. Individual patterns were cut out, and access holes to the main channels were punched using a biopsy needle. These pieces were subsequently bonded to coverslips.

For bonding, #1.5 coverslips were cleaned in an isopropyl alcohol bath (both from Thermo Fisher Scientific, NH) by sonication and then treated in O_2 plasma at 200 $mTorr$ for 70 s. The PDMS elastomer piece and glass coverslips are additionally treated in O_2 plasma for 7 s before bonding. After bonding, the chips were left at room temperature for at least 12 hrs. before starting live cell measurements.

The oxygen plasma treatment changes the surface chemistry of both the glass and the PDMS elastomer to $-$OH groups or $-$COOH groups. When the two surface were brought together, Si$-$O$-$Si or Si$-$CO$-$Si linkages would form. This led to covalently bonded a PDMS-glass interface.

For microfluidic chips with two layers of fluidic channels (i.e., microvalve devices used in Section 3.2 and microanvil devices used in Section 3.3 and Chapter 4), the PDMS elastomers for each layer was cast separately then the layers were bonded together (See Figure 2-4). To make the top layer, a wafer mold with the top layer pattern was placed underneath a homemade $1/4''$ ($\sim$6 mm) thick PTFE plate, which had an opening of $3.1''$ ($\sim$80 mm) in diameter in its center (Appendix A). A mixture of PDMS was poured on the wafer mold resulting in $\sim$6 mm thick layer of PDMS. The PDMS mixture in the holder was degassed in a desiccator at a pressure of about 0.2atm.. After degassing, the mixture was heated in a convection oven at 90℃ for 15 min. The assembly was then removed from the oven and allowed to cool at room temperature for $\sim$15 min. Then the Si mold was separated from the PDMS and its holder. Access holes to channels were punched without removing the partially cured elastomer from the PTFE holder. Note that the bottom of these access holes would be later sealed by the material of the bottom layer.

For the bottom layer, a degassed PDMS 10 : 1 mixture was spin-coated on its wafer mold at 5000 rpm for 2 min. The coated wafer was then heated in a convection oven at 90℃ for 12 min. Subsequently, the bonding surfaces of control and flow layers were activated using O_2 plasma treatment for 20 s. Then, the PTFE holder holding the control layer was mounted on a micromanipulator. The control and flow layers were aligned relative to each other by using the micromanipulator, while observing the layers in an optical microscope. Taking advantage of micromanipulators, the layers can be aligned within $\sim$20 μm; yet, due to the flexibility and the internal stresses of elastomers, unpredictable distortions were introduced before and during bonding. Therefore, the tolerance for design of wafer scale elastomer bonding was set at 75 μm.

After alignment, the layers were brought into contact using the vertical control of the manipulator. To strengthen the bond and to allow the PDMS to fully cure, the layers were further baked at 90℃ for 15 min. The resulting monolithic bilayer was peeled from the bottom layer mold. Then, individual chips were cut out and the access holes to bottom layer channels were punched with a biopsy needle. The last step of assembly was to bond this structure to a #1.5 glass coverslip. Prior to this bonding, glass and PDMS surfaces were activated using O_2 plasma treatment. The top

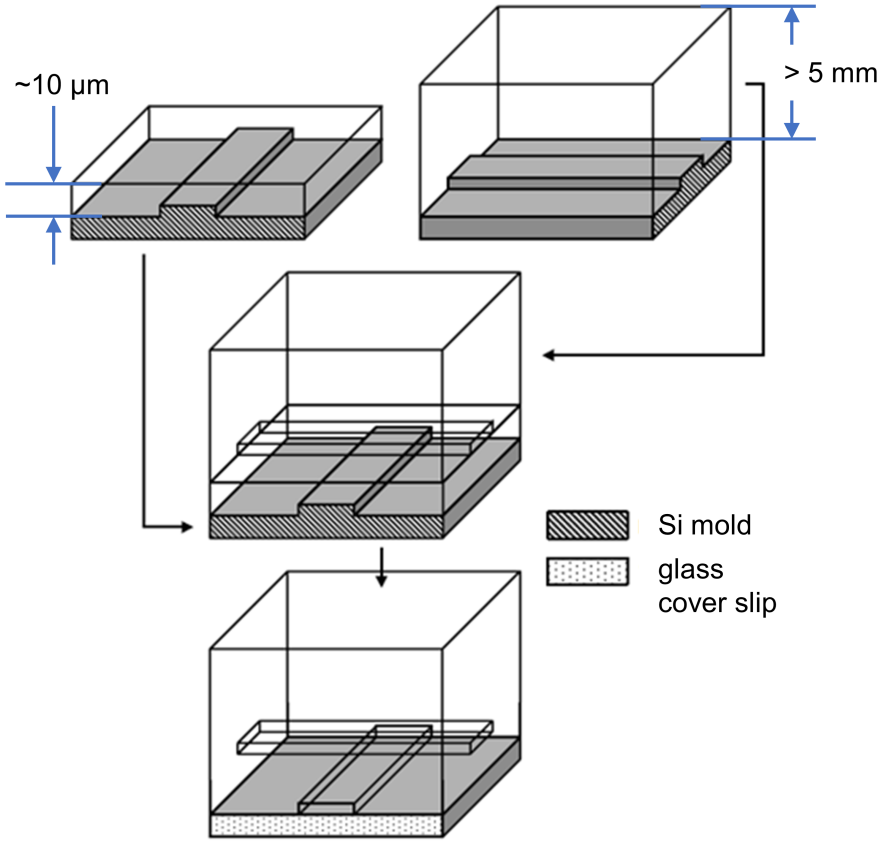


Figure 2-4 : Process flow for multilayer soft-lithography. The top layer is cast thick ($\sim 6\ mm$) for mechanical stability, whereas the other layers are cast thin ($\sim 10\ \mu m$). Each layer was separately baked at 90℃ for 15 and 12 min., respectively. The thick layer was then sealed on the thin layer, and the two were bonded at 90℃ for 15 min.. This figure is reproduced from [UCT+00] with annotations.

layer channels in the assembled chips could withstand externally applied pressures of about 6 bar. This was the highest pressure value reported for PDMS-based microfluidics at the time when we published this process [YGJ+15].

2.5 Fabrication of Silicon Wafers

As mentioned in Section 2.4, fabricated silicon (Si) wafers were used as molds for PDMS softlithography. This section outlines the fabrication processes of those molds. Si wafers are single crystal silicon slices with at lease one side polished. The dimensions of the wafers used in this dissertation were 100 mm in diameter and 500 μm in thickness. They are common substrates used in semiconductor manufacturing. Fabrication techniques of silicon can be classified as either adding or subtracting techniques. Adding techniques used in this dissertation include photolithography and physical vapor deposition. Subtracting techniques include various reactive ion etchings (RIE) and wet etching. Patterns of adding and subtracting were defined by photolithography masks or direct write electron beam lithography. In this section, we will first discuss the processes involved in fabricating the patterns defined by direct write electron beam lithography, then proceed to cover photolithography. All micromachining processes were done in the Nanofabrication Research Laboratory at the Center for Nanophase Materials Sciences at Oak Ridge National Laboratory.

2.5.1 Electron Beam Lithography Layers

Since it was possible to focus an electron beam to below 10 nm, we could use it to define smaller features and/or to define features more precisely than using ultraviolet (UV) radiation. Moreover, the electron beam lithography (EBL) system (JEOL JBX-9300FS, JEOL, Japan) provided the direct writing capability, such that we had short development cycles ($<$ 1 week). We used EBL to define micrometer-sized features.

From a blank Si wafer, we coated it with ZEP520A (ZEON Chemical, Japan), which was a positive tone e-beam resist, and wrote the desired 2D features on it. After e-beam writing, the electron beam (e-beam) resist was developed, removing the material exposed to e-beam. Then a thin ($10 \sim 20$ nm) chromium (Cr) layer was deposited and the resist layer was lifted off. Hence, the area on the wafer previously exposed to e-beam was covered by Cr. The Cr film served as a etching mask. Etching of Si was carried out using a mixture of SF_6 and O_2 gases at -110℃in an Oxford

Plasmalab 100 inductively coupled plasma reactive ion etching system (Oxford Instruments, MA). As a result of etching, rectangular cross sectioned reliefs for micron sized channels were created. The typical height of the channels ranges from 0.9 to 1.5 μm, depending on the etch rate and dwell time. The detailed protocol is given in Appendix B.

For some molds, aligned micrometer-sized features of two different heights were required. For those molds, a second layer of features was defined using EBL with a chip alignment step. That layer was written on ZEP520A. After development, the ZEP film was used as etching mask. First, the Cr mask from the previous step was etched using Argon sputtering etch in the Plasmalab RIE and the Si underneath was exposed. Second, the exposed Si was etched to specific depth using a mixture of SF_6 and C_4F_8 gases at 20℃in the Plasmalab RIE.

2.5.2 Photolithography Layers

Photolithography, typically done with near UV radiation, is one the most widely used technology in semiconductor manufacturing. Traditionally, photolithography has been used to pattern photoresist films, which in turn serve as a mask for further etching or deposition processes. Nevertheless, in this dissertation, the photoresist itself was a part of the pattern in the final wafer mold.

To connect the small channels defined by EBL to external tubing, larger flow channels were defined using photolithography of SU-8 (MicroChem, MA). SU-8 was a negative tone photoresist. In this step, SU-8 was spun, soft baked, and patterned using photomasks. After UV exposure, a post-exposure bake is carried out and then the pattern is developed in SU-8 Developer (MicroChem, MA), then rinsed with fresh SU-8 developer (over 98% 1-Methoxy-2-propyl acetate) then isopropyl alcohol (IPA), and dried with a filtered nitrogen gas stream. Finally, SU-8 on the wafer is cured at 180℃ for a few minutes.

The channel heights and widths are measured from the Si mold. For the height measurements, a KLA-Tencor P-6 Stylus (KLA-Tencor Corporation, CA) profilometer was used. All wafer molds are silanized in a desiccator using (tridecafluoro-1,1,2,2-tetrahydrooctyl)-1-trichlorosilane (UCT Specialties, CA) for at least 15 min. before using.

All photomasks used in this dissertation were written by a Heidelberg DWL66 laser lithography system (Heidelberg Instruments). A 20 mm write head was used in the writing process. The substrates of the photomasks were soda lime glass with a chrome layer covered by a photoresist.

2.6 Stress Analyses of the PDMS Pressure Actuators

Stress analyses of the microvalves and microanvils were done with the finite element method using Autodesk Inventor software (Autodesk, CA). The Young's modulus of PDMS was chosen as 1.0 MPa, and a Poisson ratio of 0.49. The adapted value for the Young's modulus falls in the range of $0.75 \sim 2.97$ MPa cited in the literature for $10:1$ base to curing agent ratio of fully cured bulk PDMS elastomer [JMTT14; ALA99; KDSB09]. Although a Poisson ratio even higher than 0.49 has been used in the literature for PDMS [YZ09], we use 0.49 because of the limits set by the Inventor software.

2.7 Langevin Dynamics Simulations

A key distinction of the Langevin dynamics (LD) simulation techniques from *ab initio* molecular dynamics simulations is that LD simulations replaces the explicit solvent molecules in the system in question with stochastic forces that act on the solute molecules. Since the time scales between the rapid motion of solvent molecules and the more sluggish motions of polymers or colloids separate far enough, the technique allows simulating much larger time scales [DU05]. Combined with coarse-graining, systems that are physically much larger than in a molecular dynamics simulation can be simulated.

As a special case of dynamics simulations, LD simulations follow the basic scheme of setting an initial configuration then—step by step—marching forward [Rea14]. Here, the initial configuration is the initial position, velocity, orientation of every partials in the system, i.e., the position in the phase space at some initial point of time. What drives the system forward in time is related to the temperature. By expressing the stochastic forces in term of time-derivative differential equations, one could integrate them forward in time and obtain trajectories of particles, $\{\boldsymbol{r}(t)\}$. In this dissertation, all simulations are performed using software package, ESPResSo [LAMH06] and run on Newton HPC or the Advanced Computing Facility cluster.

2.7.1 The Procedure

The general procedure of running a LD simulation in this dissertation is,

1. Define a list of particles and their masses and positions;

2. Define the geometry of the confinement;

3. Define how particles interact among themselves and with the confinement;

4. Warm-up by propagating the system in time (integration), while increasing the cap (upper bond) of forces experienced by particles from a suitable small value;

5. Remove the force cap;

6. Let the system propagate further in time, and modify the geometry of the confinement if desired.

Before starting the integrations, an initial system, i.e., the initial list of particles, and their positions and velocities, must be defined. In all LD simulations preformed in this dissertation, every particle had the same mass and the confinement geometries were always explicitly controlled. The list of particles were organized by types, such that some interactions could be defined between each pair of types of particles in question. The above procedure then defines the initial configuration of the system.

The defined initial configuration is often not a realistic one, due to resolutions or the lack of knowledge, such that some particles would experience unrealistically large forces from other particles in the initial configuration. Hence, it is necessary to initialize the system with warm-up steps [Smi14]. In this dissertation, initializations were not done with increasing temperatures rather than with increasing caps of the magnitudes of repulsive forces. Initial speeds of particles were set to zero. Using the term "warming-up" is thus merely for legacy reasons.

The interactions in simulations were classified in two classes, bonded interactions and non-bounded interactions. They are defined by mechanical potentials as functions of relative positions of the particles involved. The LD stochastic forces were introduced by a Langevin thermostat, which propagates the system forward in time. The geometry of confinements, the numbers of particles, and how they interact can be modified in between integration steps. A sample simulation script is given in Appendix C.

2.7.2 Velocity Verlet Algorithm

The velocity Verlet algorithm was used in all simulation integrations done in this dissertation [And83; SABW82; Des00; FS02]. For any given particle and an arbitrary discrete time step

δt, the velocity Verlet algorithm writes the kinematic equations as the following truncated Taylor expansions,

$$\boldsymbol{x}(t+\delta t) = \boldsymbol{x}(t) + \boldsymbol{v}(t+\frac{1}{2}\delta t)\cdot\delta t + \cdots, \tag{2.6}$$

$$\boldsymbol{v}(t+\delta t) = \boldsymbol{v}(t) + \boldsymbol{a}(t)\cdot\delta t + \cdots, \tag{2.7}$$

where $\boldsymbol{x}$ is the vector position of the particle; and $\boldsymbol{v}$, and $\boldsymbol{a}$ are its velocity, acceleration.

Marching, also known as time stepping, starts at simulation time 0. At time 0, the position, velocity, and acceleration of each particle are initialized. We first decide the length of time step for the simulation, Δt. Then for every time step after time 0, we use Equation 2.6 and 2.7 to propagate the system, i.e.,

$$\boldsymbol{v}(t+\frac{1}{2}\Delta t) = \boldsymbol{v}(t) + \boldsymbol{a}(t)\cdot\frac{1}{2}\Delta t, \tag{2.8}$$

$$\boldsymbol{x}(t+\Delta t) = \boldsymbol{x}(t) + \boldsymbol{v}(t+\frac{1}{2}\Delta t)\cdot\Delta t, \tag{2.9}$$

$$\boldsymbol{v}(t+\Delta t) = \boldsymbol{v}(t+\frac{1}{2}\Delta t) + \boldsymbol{a}(t+\Delta t)\cdot\frac{1}{2}\Delta t. \tag{2.10}$$

That set of equations is the velocity Verlet algorithm [All04]. This set of equations is often written in terms of momenta and forces instead of velocities and accelerations. We used the latter notions because of the uniformity of masses in our systems. Calculations of the accelerations is discussed in Sections 2.7.3 and 2.7.4.

2.7.3 Interactions

In our systems, every particle was modeled as a sphere. There were two types of interactions in our simulations, bonded and non-bonded. Both types of interactions were defined by potentials.

Non-bounded interactions were used to model volume exclusions. To model the volume exclusive interactions, the Weeks-Chandle-Anserson (WCA) potential was used. It was a purely repulsive potential. Given a pair of particles with defined sizes, the WCA potential was a function of the

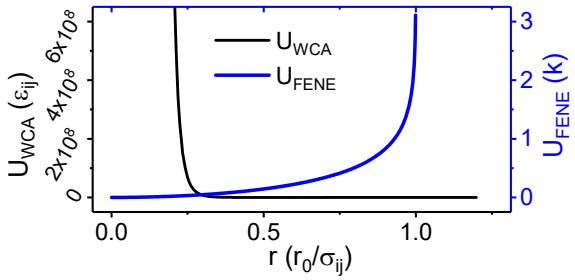


Figure 2-5 : The Weeks-Chandle-Anserson (WCA) potential and the finitely extensible nonlinear elastic (FENE) potential.

distance between the pair of particles in question:

$$U_{WCA}\left(r_{i,j}\right) = \begin{cases} 4\,\epsilon_{i,j}\left[\left(\frac{\sigma_i+\sigma_j}{2\,r_{i,j}}\right)^{12} - \left(\frac{\sigma_i+\sigma_j}{2\,r_{i,j}}\right)^{6} + \frac{1}{4}\right] & r_{i,j} < 2^{1/6}\left(\sigma_i+\sigma_j\right), \\ 0 & \text{otherwise}, \end{cases} \tag{2.11}$$

where $r_{i,j}$ was the distance between particles $(i,\, j)$, $\epsilon_{i,j}$ was a positive constant, and σ_i was the diameter of particle i. Those interactions were defined between any pair of particles in the system based on their types.

Meanwhile, a bonded interaction represented the physical bond between a pair of adjacent particles in a polymer chain. The bonds between connecting monomers were modeled as the finitely extensible nonlinear elastic (FENE) potential:

$$U_{FENE}\left(r\right) = -\frac{1}{2}kR_0^2 \ln\left(1 - \frac{r^2}{R_0^2}\right). \tag{2.12}$$

where r was the distance between a given pair of monomers, k was a positive constant, and R_0 was the maximum possible separation between that pair of monomers.

Both the WCA and the FENE potentials were only functions for distances among particles (Figure 2-5). The forces acting on a particle were the derivatives of these potentials.

2.7.4 Fluctuation-Dissipation Theorem and the Langevin Equation

During the sequential propagations of simulations, frictions and random forces were applied to every bead by a Langevin thermostat. With knowledge of potentials experienced by a particle, its

velocity, and positions of all particles, the acceleration of that particle could be calculated. Thus, the Langevin equation describing the acceleration of a monomer particle i at time t is,

$$\begin{aligned} m\boldsymbol{a}_i(t) &= -\sum \nabla U_{WCA}\left(|\boldsymbol{x}_i - \boldsymbol{x}_j|\right) - \sum \nabla U_{FENE}\left(|\boldsymbol{x}_i - \boldsymbol{x}_{i\pm1}|\right) \\ &\quad - \sum \nabla U_{WCA}\left(|\boldsymbol{x}_i - \boldsymbol{X}_{\text{constraints}}|\right) - \gamma \boldsymbol{v}_i(t) + \boldsymbol{F}(t). \end{aligned} \tag{2.13}$$

where m is the mass of the monomer, γ is the Langevin friction coefficient, $\boldsymbol{F}$ is the random force introduced by the fluctuation-dissipation theorem, $\boldsymbol{X}_{\text{constraints}}$ is the effective position of the constraints [SCM14]. Here, $\boldsymbol{F}(t)$ is also a function of the temperature specified for the system. It is defined by

$$\boldsymbol{F}(t) = \sqrt{\frac{2k_B T\gamma m}{\delta t}}\tilde{\boldsymbol{h}}_i(t), \tag{2.14}$$

where $\tilde{\boldsymbol{h}}_i$ is a vector, each component of which is a Gaussian random variable with mean 0 and variance 1.

Note, the acceleration used in Equation 2.8, $\boldsymbol{a}(t)$ is calculated based on $\boldsymbol{x}(t)$ and $\boldsymbol{v}(t)$. the the acceleration used in Equation 2.10, $\boldsymbol{a}(t+\Delta t)$ is calculated based on $\boldsymbol{x}(t+\Delta t)$ and $\boldsymbol{v}(t+\Delta t/2)$. So this value is calculated twice for every time step. Therefore, the Langevin dynamics modified velocity Verlet algorithm becomes

$$\boldsymbol{v}_i(t+\frac{1}{2}\Delta t) = \boldsymbol{v}_i(t) - \frac{1}{2}\Delta t\left(\frac{\nabla U_i(t)}{m_i} + \gamma \boldsymbol{v}_i(t)\right) + \sqrt{\frac{\Delta t k_B T\gamma}{m_i}}\tilde{\boldsymbol{h}}_i(t), \tag{2.15}$$

$$\boldsymbol{x}_i(t+\Delta t) = \boldsymbol{x}_i(t) + \boldsymbol{v}_i(t+\frac{1}{2}\Delta t)\Delta t, \tag{2.16}$$

$$\begin{aligned} \boldsymbol{v}_i(t+\Delta t) &= \boldsymbol{v}_i(t+\frac{1}{2}\Delta t) - \frac{1}{2}\Delta t\left(\frac{\nabla U_i(t+\Delta t)}{m_i} + \gamma \boldsymbol{v}_i(t+\Delta t/2)\right), \\ &\quad + \sqrt{\frac{\Delta t k_B T\gamma}{m_i}}\tilde{\boldsymbol{h}}_i(t), \end{aligned} \tag{2.17}$$

where U_i is the superposition of all potentials experienced by particle i. That set of equations was realized in the ESPResSo software package.

2.7.5 The Model

"The choice of polymer model is intrinsically a modeling decision which depends upon the real polymer one wants to model and the level of fine-scale molecular detail one needs to

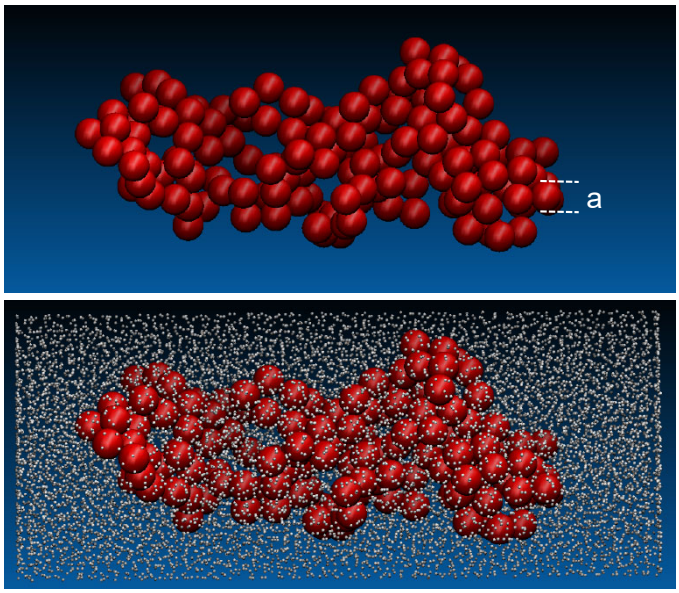


Figure 2-6 : A typical conformation of one polymer ring in a cylindrical confinement visualized by VMD [HDS96]. The two panels are from the same data shown without (top) and with (bottom) crowders.

retain or can computationally afford to simulate [DU05]." In this dissertation, we modeled the *E. coli* chromosomes as a closed string of spherical beads. Several previous works used similar approaches [KJJ+15; SBdH+15; MCY+16]. Each chromosomal bead had a diameter a. Crowders, if any, were also represented by spherical beads. Their diameter was denoted by a_c. A typical conformation of one ring polymer in a cylindrical confinement is shown in Figure 2-6. Additional parameters used in the model are:

- Langevin temperature: $T = 1.0\,\epsilon_0/k_B$;
- Langevin fraction: $\gamma = 0.1\,a^{-1}\sqrt{\epsilon_0/m}$;
- FENE potential prefactor: $k = 30\,\epsilon_0/a$;
- FENE maximum distance: $R_0 = 1.5\,a$;
- unit time: $a\sqrt{m/\epsilon_0}$.

For each simulation, the string of beads was initially placed along rectangle contour no larger than the cylindrical confinement. The crowders, if any, are randomly placed in a cylindrical region

inside that rectangle. To initialize the simulation, we set a cap to the net force experienced by each particle. Then this cap is gradually increased as the simulation progresses and eventually removed. The force cap is removed after 2.5 million simulation steps, which is the end of initialization. For all simulations in this section, δt represent $50,000$ simulation steps, where each simulation step $\tau_0 = 0.002\, a\sqrt{m/\epsilon_0}$.

2.7.6 Dynamical Properties of the Model

To validate our model and simulation platform, we ran simulations of single polymer chains of various lengths and topology, and examine their dynamical properties.

First, we put open and closed chained single polymer in a very large confinement, such that their conformation and diffusion were minimally affected by the confinement geometry. Their dynamical properties were characterized by Radii of gyration, R_g, and mean square displacements, MSD Figure 2-7. The scaling exponent of R_g^2 was 6/5 (Figure 2-7 B), which matched Equation 1.11.

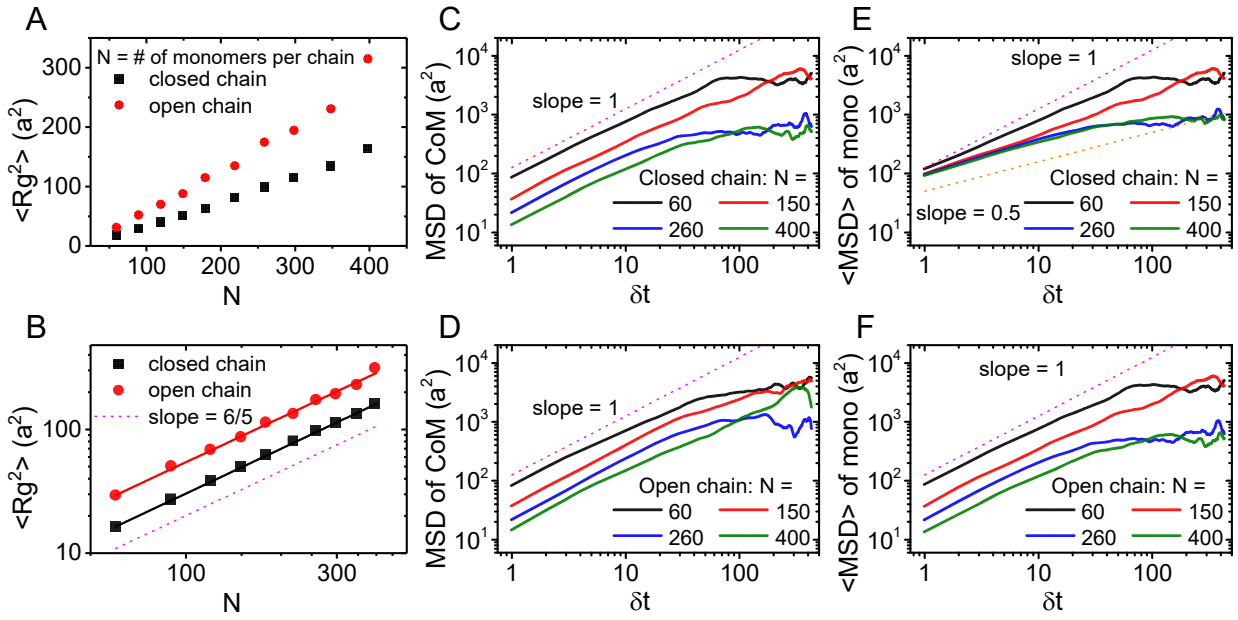


Figure 2-7 : Dynamical properties of single polymers. (A) Radii of gyration of single polymers in free space. (B) The same as (A) in log scale. (C) Centers of mass diffusion of single closed chains of various lengths. (D) The same as (C) with single open chains. (E) Average monomer diffusion of single closed chains of various lengths. (F) The same as (E) with single open chains.

Meanwhile, anomalous diffusion is a more generalized description of diffusion. It dose not require MSD to linearly depend on time.

$$MSD = D\,\delta t^{\alpha}. \tag{2.18}$$

Nevertheless, before introducing crowders, the anomalous diffusion exponent, α, should stay as 1 (Figure 2-7 C-F).

Second, we put the model in physiologically relevant length scale. In earlier works, the effective diameter of chromosome beads, a, have been estimated to range between $50 \sim 400\ nm$ [PHH+12; KJJ+15; MCY+16]. In our previous work, we have decided $a = 80\ nm$, which represents $\sim 30\ kb$ of dsDNA [MCY+16] (See Section 1.5.2). Therefore, 150 beads represent one genome equivalent of a chromosome. Here, the diameter (σ in Equation 2.11) used for the cylindrical confinements when calculating the WCA potentials was 0.

Now, we examine how the diffusion exponent change in cylindrical confinements of various sizes (Figure 2-8). We carried two series of various geometries simulations for both open and closed chained polymers of 150-bead long. In the first series of those simulations, the base diameters, $2R$, were set to be the same as the length, L, of corresponding cylinders. The chains were frozen when $L < 2\ \mu m \approx 25\,a$, i.e., anomalous diffusion exponents, α, remained at 0. As L increased, α of also increased. Until $L > 5\ \mu m \approx 60\,a$, α of the centers of mass, α_{CoM}, reached and stayed at just below 1, while the average α of the monomers, $\langle \alpha_{\mathrm{mono}} \rangle$, reached a limit at ~ 0.7 (Figure 2-8 D, E).

For the second series of simulations, only the length of cylinders was a variable, while the base diameter was fixed at $0.64 \mu m$. This diameter was close to the diameter of *E. coli* cells. While α_{CoM} was frozen at $L < 2\ \mu m$ (Figure 2-8 B, C), $\langle \alpha_{\mathrm{mono}} \rangle$ quickly reached 0.4. As L increased, α_{CoM} increased and stabilized at just below 1, and $\langle \alpha_{\mathrm{mono}} \rangle$ stabilized at ~ 0.75. For a comparison, experimental data from Wu Fabai et al. was reproduced and inserted [WSK+19]. That work presented measurements of center of mass diffusion of nucleoids in a wide range of *E. coli* cell lengths (Figure 2-8 D, E).

Finally, we introduced crowders to the system. The macro-molecular crowders were represented by beads with a diameter, $a_c = 0.4\,a = 32\ nm$, or $a_c = 0.25\,a = 20\ nm$. These were not a realistic size. However, for considerations of computational cost and of the convention that the amount of crowders in a system was measured by its volume fraction, we did not pursuit simulations with realistic crowder size.

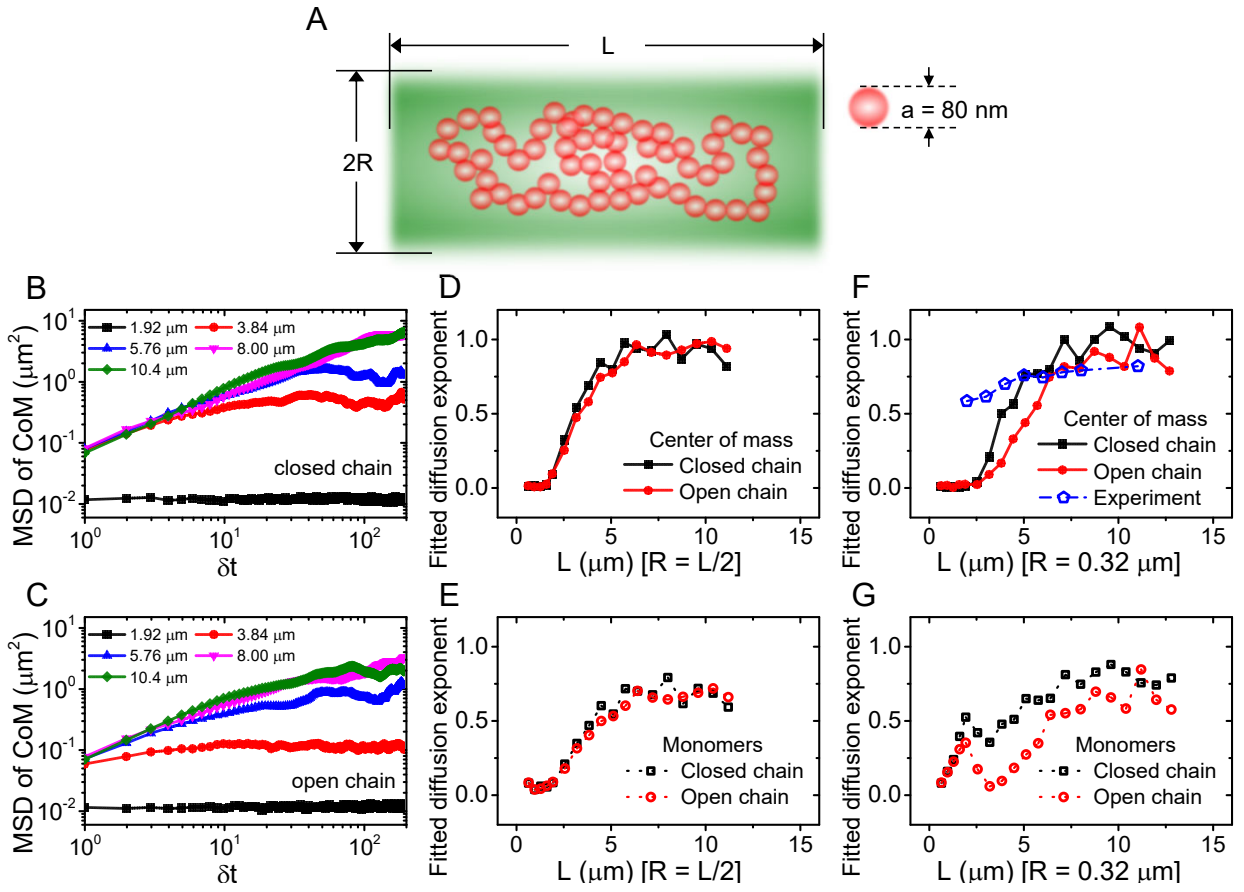


Figure 2-8 : Anomalous diffusion exponents of open and closed chains in various cylindrical confinements. (A) An illustration of a polymer chain in a cylindrical confinement. (B) Centers of mass diffusion of single 150-bead long closed chains in cylindrical confinements with $0.64\mu m$ base diameter and various lengths. (C) The same as (B) with 150 bead long closed chains. (D) Anomalous diffusion exponents of the center of mass of open and closed chains in cylindrical confinements lengths of which equal to corresponding base diameters. (E) Average anomalous diffusion exponents of monomers of open and closed chains in cylindrical confinements lengths of which equal to corresponding base diameters. (F) The same as (D) with cylinder base diameters fixed at $0.64\mu m$. Experiment refers to the result from [WSK+19]. (G) The same as (E) with cylinder base diameters fixed at $0.64\mu m$.

We carried out two series of simulations one having $a_c = 0.25\,a$ and the other $a_c = 0.4\,a$. The inner membrane of the cell was modeled as a cylinder with flat ends. The model defines two different confinements for this boundary. The chromosome experiences a confinement with a smaller radius and length than the the confinement experienced by crowders. The inner confinement has length of $20\,a = 1.6\ \mu m$ and radius of $8\,a = 0.64\ \mu m$. These values approximately match the dimensions of a cell measured in slow growth conditions. The difference in both diameters and lengths between the inner and outer cylindrical confinement are $2\,a_c$. These two confinements were needed to reduce adsorption of chromosome beads to the inner wall. Again we characterized the dynamical properties of the chromosome model Figure 2-9. The center of mass diffusion was clearly affected by the volume fraction of crowders, Φ (Figure 2-9 B). Comparing to experimental results, when $\Phi \approx 0.35$ and the crowder size was set at $a_c = 0.4\,a$, there was a good agreement (Figure 2-9 C). Here, we manually picked $12.5\,\delta t = 1\ s$ for best fit. The anomalous diffusion exponent depend positively on the crowder concentration (Figure 2-9 D, E).

To determine the nucleoid lengths and widths from simulations, we projected the coordinates of chromosomal beads to a plane parallel to long axes of the cell. On this plane we broaden the coordinate of each bead by a 2D Gaussian, the width of which corresponds to the point spread function of our microscope ($\sigma = 130\ nm$). The point spread function was measured using CdSe quantum dots (See Section 2.2.2). Here, after initialization, we recorded 600 frames of coordinates, and all results are derived from the last 500 of those frames. We add the projections of one hundred consecutive frames from the model together and measure the nucleoid length and width from the resulted image in the same way we have been measuring the nucleoids in live cells (See Sections 2.2.3.2 and 2.2.3.3). Such that the simulations were quantified comparably to the live cell images. Hence, we have five measurements for both the length and the width of the nucleoid for each simulation. The average values are plotted in Figure 2-10. Kim et al. have previously found that there is rescaling factor for the crowding effect on the chromosome string-beads. The rescaling factor apparently relates to the total cross-sectional area of the crowders [KJJ+15]. Here, we call this quantity crowding level and denote it as $\Psi = \rho_c\, a_c^2$. As discussed in Section 1.6, higher crowding levels result in more compacted nucleoids, and $\Psi = 20\ \mu m^{-1}$ was found to be close to the physiological value (See Section 4.7).

This rescaling also hold for anomalous diffusion exponents (Figure 2-11 B, C). Furthermore,

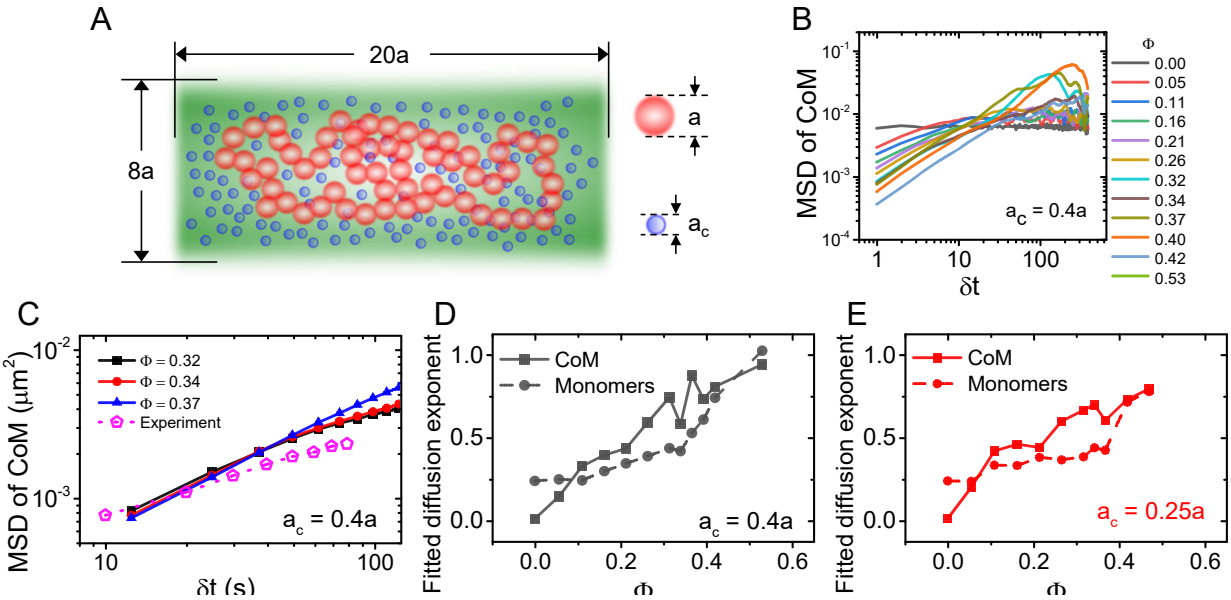


Figure 2-9 : Anomalous diffusion closed-chained polymers in various volume fractions of crowders (Part I). (A) An illustration of a polymer chain in a cylindrical confinement with crowders. The length of the cylinder is $L = 20\,a = 1.6\ \mu m$. The base diameter of the cylinder is $2R = 8\,a = 0.64\ \mu m$ (B) Center of mass diffusion of single 150 bead long closed chains at various volume fractions of crowders, Φ. (C) Comparison of center of mass diffusion between simulations and experiment. Experiment refers to the result from [WSK+19]. (D) Anomalous diffusion exponents of the centers of mass, α_{CoM}, and average anomalous diffusion exponents $\langle\alpha_{\mathrm{mono}}\rangle$ of the chains as functions of Φ, where $a_c = 0.4\,a = 32\ nm$. (E) The same as (D) bu $a_c = 0.25\,a = 20\ nm$.

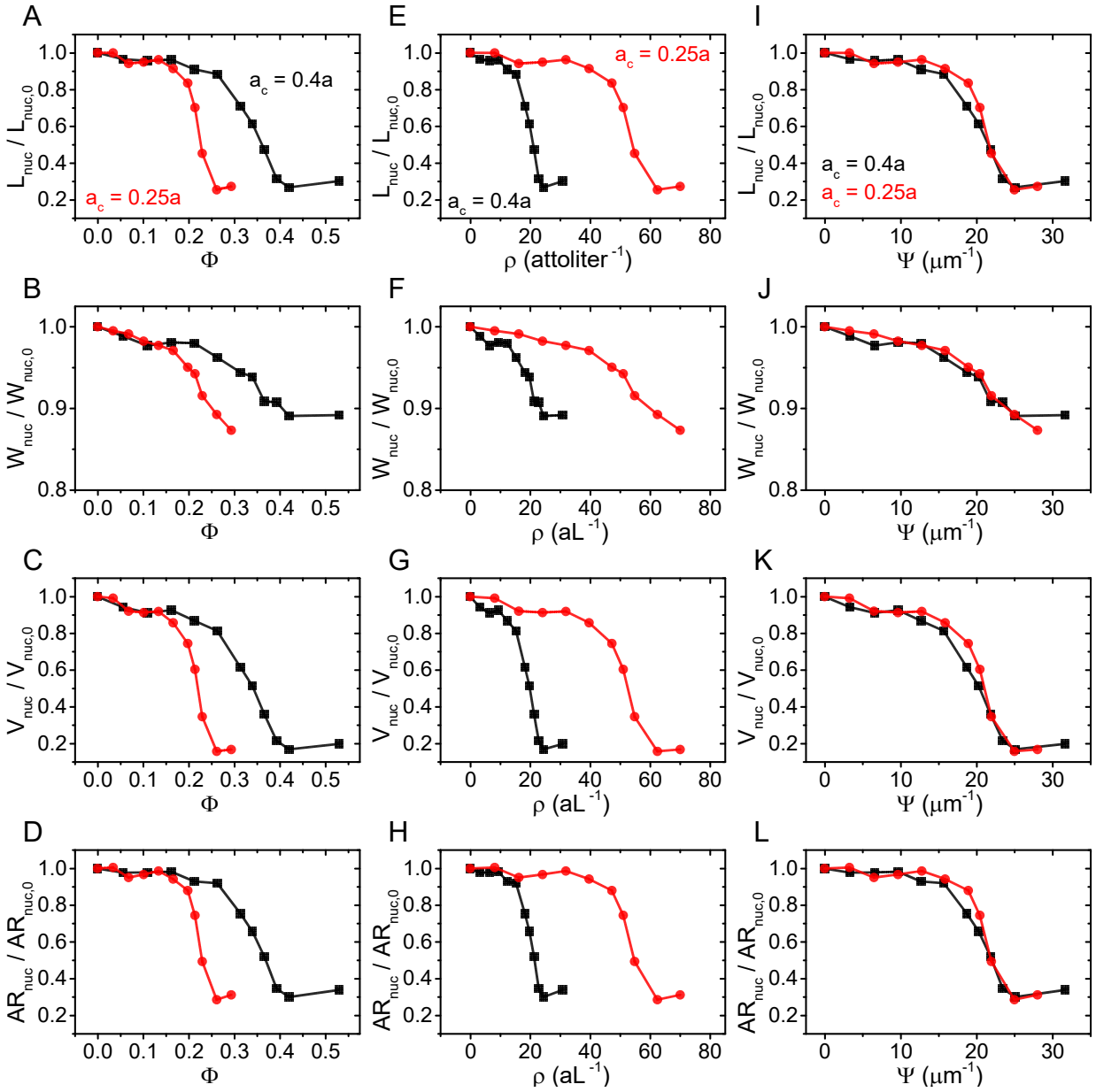


Figure 2-10 : Projected sizes of the ring model at various crowder levels. (A-D) Normalized nucleoid lengths, widths, volumes, and aspect ratios as functions of the volume fraction of crowders, Φ. (E-H) The same four quantities as functions of the numerical crowder concentration, ρ. (I-L) The same four quantities as functions of the crowding level, $\Psi = \rho_c a_c^2$. Curves related to two different crowder sizes are shown.

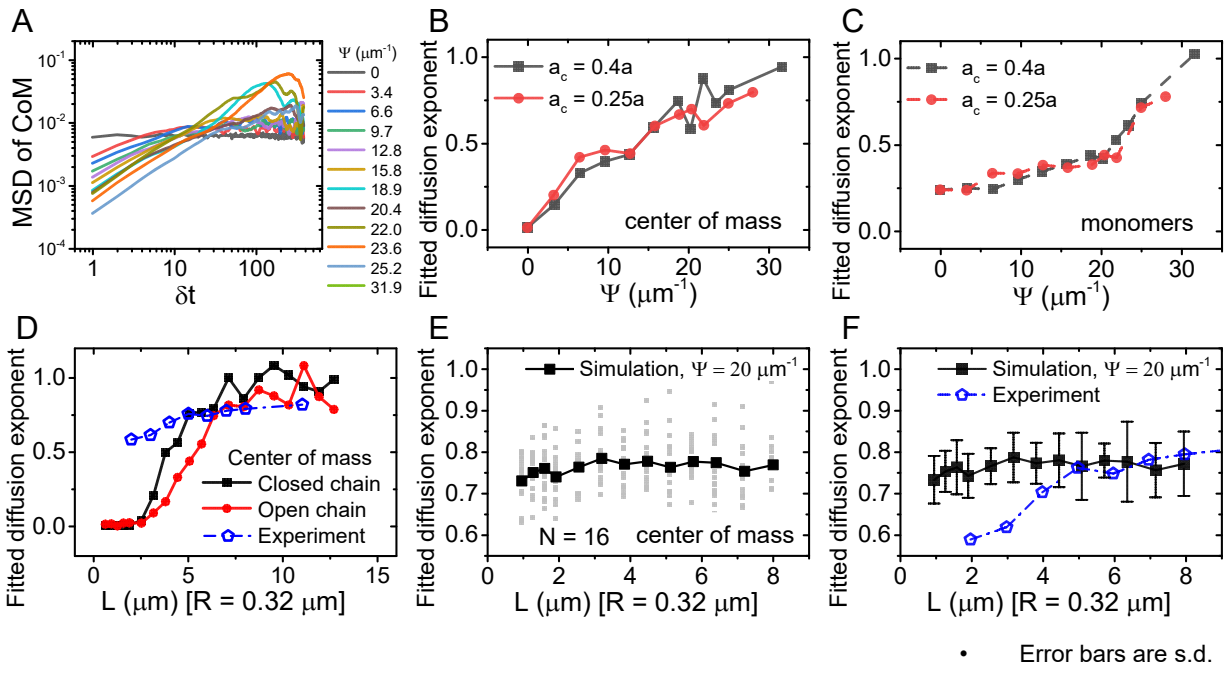


Figure 2-11 : Anomalous diffusion closed-chained polymers in various volume fractions of crowders (Part II). (A) Center of mass diffusion of single 150 bead long closed chains at various crowding levels, Ψ. The data in this panel is the same as those in Figure 2-9 B. (B) Anomalous diffusion exponents of the centers of mass of single 150 bead long closed chains, with two different sizes of crowders. (C) The same as (B) for average anomalous diffusion exponents of monomers. (D) Anomalous diffusion exponents of the centers of mass of open and closed chains in cylindrical confinements of various lengths and base diameter at $0.64\mu m$. Experiment refers to the result from [WSK+19]. No crowders present the simulations in this panel. The data in this panel is the same as those in Figure 2-8 F. (E) The same as the black curve in (D) but in presence of a crowding level, $\Psi = 20\ \mu m^{-1}$. Here, we run 16 simulations for each cell length. The solid black curve represents the averages from those simulation results. (F) Comparison between the simulations in (E) and the experiments in (D). The error bars correspond to standard deviations.

the anomalous diffusion exponents was not affected by cell length (Figure 2-11 E, F). This did not agree well with the experiment [WSK+19] when cell length was shorter than 4 μm. Note, the anomalous diffusion exponent is a dimensionless quantity. Our choice of time scaling bear no effect on the fitness to data.

Chapter 3

Development and Characterization of Microfluidic Platforms

The challenges to study bacteria stem from their rapid growth, small dimensions and often motile lifestyle which all hinder observations at a single cell level. Lab-on-a-chip (LOC) technology presents a natural choice to overcome these challenges offering new ways to grow, manipulate, and observe bacterial cells and cellular assemblies [EASJ06; HD14]. In microchips, a controlled environment for cells can be defined and maintained for extended periods of time during which high throughput measurements can be performed. Typical measurements are carried out using optical microscopy but progress has been also made in on-chip genomic studies [MOB+07; LZL+12] and electrical measurements [JHF+10; JHP+13] of bacterial cells. Unlike conventional approaches, the microchip technology enables one to perform these measurements in real time and to observe cellular responses to various physical and chemical stimuli as they unfold.

LOC technology offers a particular promise in studies of bacterial cellular organization. Although the bacterial cell was long considered to be a simple enclosure, whose only function was to carry the genome from one generation to the next, more recent research has demonstrated exquisite spatial organization within these micro-organisms [SML09]. The ordered placement of proteins and DNA within the cell arises due to many self-organizing processes. The details of these processes are still poorly understood. The most common approach to understand how cellular organization rises and is maintained is to perturb this organization and then observe a response from the cell. Essentially all approaches used by cell biologists in these studies enable the assessment

of only ensemble-averaged responses, overlooking significant cell-to-cell variations that exist in a population. The current methods are also not suitable to study processes in cells with fast response times. Here, we describe the development of two microfluidic platforms that allow mechanical and chemical perturbation of cellular organization while following the cellular response at a single cell level in real time using a high resolution fluorescence microscope.

3.1 Mother Machine Platform

3.1.1 Motivation

High resolution optical microscopy is the most widespread method to study bacterial cellular organization and physiology at the single cell level [YJB+18]. Most early studies were carried out using fixed cells that were attached to microscope slides. However, both fixation and attachment of cells to slides alter subcellular organization and can lead to artifacts. As a less invasive preparation method, thin agarose pads sandwiched between microscope cover slide and coverslip have been adopted by numerous groups (e.g., in recent reports, [BBW+14; AOM+15]). Since thin layer of agarose is prone to drying, thicker layers of agarose in Petri dishes with coverslip bottoms can be used [MBOM17]. The dishes and pads allow imaging live cells over several doublings (typically $4 \sim 5$). Longer imaging is hampered when individual cells start to overlap. Moreover, cells in the interior of the colony experience a different growth environment than the cells at the periphery and consequently grow at different rates. It is unclear for how long exactly, if at all, steady-state growth conditions can be maintained on these agarose pads.

For reproducible quantitative studies, steady-state cell growth is necessary. To be able to grow cells in steady conditions, both the physical and chemical environment of cells needs to remain the same over time. Moreover, cells should not overlap as they grow. In practical terms, this means that the colony size has to be kept fixed despite exponential growth in cell numbers over time. Different microfluidic platforms have been developed over the past decade to achieve these requirements [HD14]. Those developed devices either trap cells in narrow channels comparable to bacterial cross-sectional diameter [WRP+10; MLC12; LNJ+13] or hold them in shallow chambers where bacteria are confined to a single layer [MWH+12; UWM+13; FBW+13]. In the latter case bacteria grow packed side-by-side and quantitative analysis of individual cells

becomes more complicated after a few doublings. In addition to providing a steady growth environment, microfluidics can also be used to administer different chemical [BBT+17; KJJ+18] and mechanical stimuli [YGJ+15] to the cells *in situ* while they are imaged under the microscope.

Of these various designs, the most wide-spread one has been the so-called mother machine platform [WRP+10], where cells grow in short ($10 \sim 25\ \mu m$ long) dead-end channels (Figure 3-1 A). Mother machine platform has been used to study cell aging [WRP+10], cell cycle control [TABS+15], and effects of mechanical forces on cell wall growth [ABM+14; WA19]. The devices have been also used in studies of gene regulation [NLPL13; CRPL17; KJJ+18] and antibiotic resistance [BBT+17]. New open-source computational platforms have been specifically developed to segment and analyze cells in mother machine platforms [SGH+16; KJJ+18]. Despite such widespread interest, bacterial growth in narrow deadend channels has not been systematically compared to their growth in typical liquid media conditions. Nor has it been determined what phenotypic differences appear in cells that grow in such microfluidic devices. Here, we analyze nutritional and mechanical growth limitations to clonal *E. coli* cultures in microfluidic dead-end channels of various widths and lengths (Figure 3-1 B,C).

3.1.2 Design and Fabrication of Mother-Machine Devices

The fluidic circuitry in each chip consists of the main channel for media supply and waste product removal. There are 600 dead-end channels connected to the main channel (Figure 3-1 A) following the typical mother machine layout [WRP+10]. The designed length of the dead-end channels varies between 15 and 200 μm, and width from 0.6 to 1.0 μm. The fabrication of Mother-Machine devices was based on polydimethylsiloxane(PDMS) softlithography (See Section 2.4). The channels in PDMS elastomers are created using silicon (Si) wafer molds (See Section 2.5). The channel heights and widths were measured from the Si mold. The heights of all dead-end channels in different microfluidic chips are within $1.15 \pm 0.05\ \mu m$. The channels widths were also measured using SEM and closely followed their design widths (less than 20 nm differences) (Figure 3-1 B). The length of these channels, as measured from the optical images of completed chips (Figure 3-1 C), also closely follow their design values.

3.1.3 Dependence of Mother Cell Growth on the Channel Width

To investigate how the channel width affects the growth rate and cell dimensions we fabricated channels of 0.6, 0.7, 0.8, 0.9, 1.0, and 1.2 μm in width, 1.15 μm in height and of 15 and 20 μm in length on a single chip. The chosen channel widths were expected to be close to the cell diameter in these growth conditions. The majority of the 0.8, 0.9, and 1.0 μm wide channels had stable bacterial populations that filled the whole channel. Cells in these populations grew in single rows (Figure 3-2 A, Supplementary Movie M3-1, M3-2). In the 1.2 μm wide channels, cells grew in two parallel rows and, as such, these channels were not suitable for analysis.

On the other hand, 0.6 μm wide channels were too narrow to support stable colony growth. Although few cells loaded to these channels initially, they all moved out from the channels before imaging started. The same also occurred in the majority of the 0.7 μm wide channels (Supplementary Movie M3-3). However, in some of the 0.7 μm wide channels (8 out of 200), stable populations were present and could be imaged. In both 0.6 and 0.7 μm wide channels the bacteria appeared to be wider than the channel causing deformations to channel walls (Figure 3-3). Note that bacteria from overnight stationary cultures were loaded into channels. These cells are significantly narrower than log phase cells [MDG+09], and this made their entry to 0.6 and 0.7 μm wide channels possible. As cells started to grow in fresh medium in these channels, their diameter widened beyond the channel width. Higher deformability of open ends of channels may have provided a driving force that pushed the cells out from the channels.

Thus, of all the fabricated channels only those in the range $0.7 \sim 1.0$ μm were suitable for studying growth of stable 1D bacterial cultures. Cells in these channels were imaged in three independent measurements that each lasted at least 6 hrs. (Supplementary Movies M3-1, M3-2, Figure 3-2 B). Here, we analyze, in detail, the growth of the mother cell, which is the cell at the dead-end side of the channel. All the cells in the channel are clones of this cell. We use the mother cell for analysis because it is the only cell that strictly grows in steady state conditions. The other cells in the channel move toward the channel entrance during their growth and, because of that movement, we expect both the composition of the growth medium and the mechanical stress that the cells experience to change. Also, to guarantee that mother cells in a channel of a given size grew in comparable conditions we required the channels to be completely full of cells (< 1 μm empty space between cells) throughout the entire time-lapse imaging period.

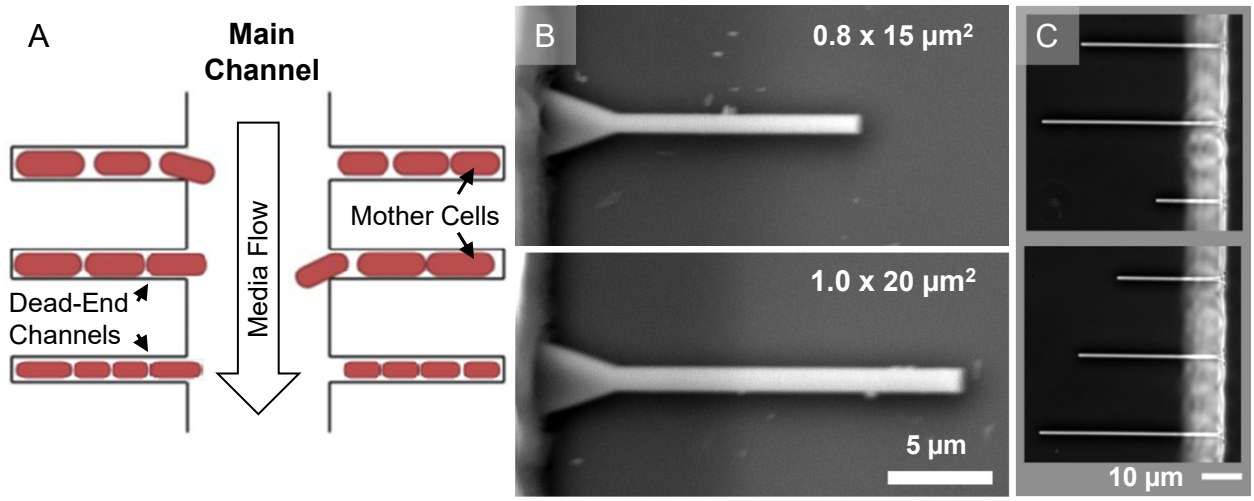


Figure 3-1 : Design of the mother machine platform. (A) Schematics showing the mother machine channel layout. Cells grow in dead-end channels. Nutrients diffuse to cells from the main channel where a constant flow is maintained. This flow also removes metabolic waste products and flushes away extra cells. Growth of the mother cell at the end of the channel is studied as a function of channel width and length. (B) SEM images of the silicon mold showing patterns of two different sized channels. (C) Channels form a completed PDMS device filled with water and imaged using phase contrast microscopy. Channel lengths in the two images vary from 20 to 50 μm. There is a total of 150 channels of each length on a single chip.

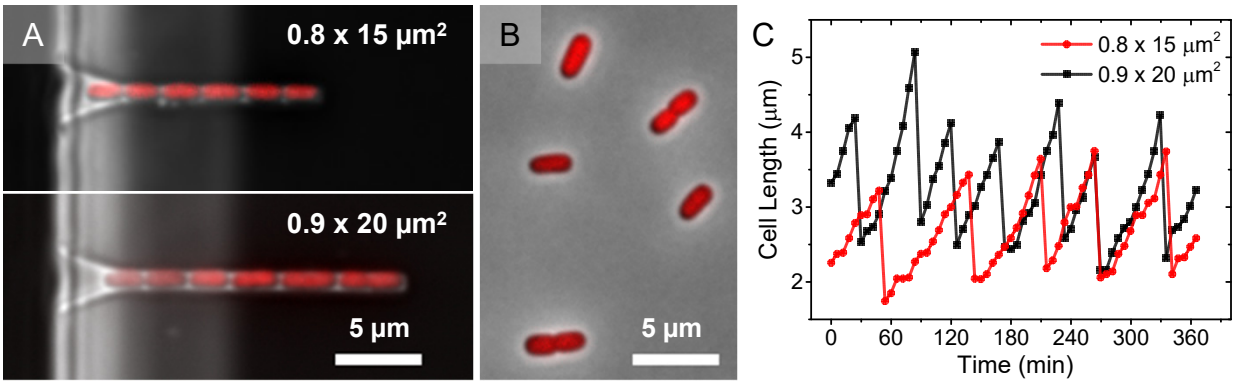


Figure 3-2 : Bacterial growth in channels. (A) Composite of phase and fluorescent images of two different size channels filled tagRFP-T labeled *E. coli* (left images). (B) For comparison, composite image of the same strain grown in liquid culture and imaged on agarose pad (right image). The difference in cell width in the two growth environments can be visualized. (C) Growth curves of mother cells from channels shown on (A).

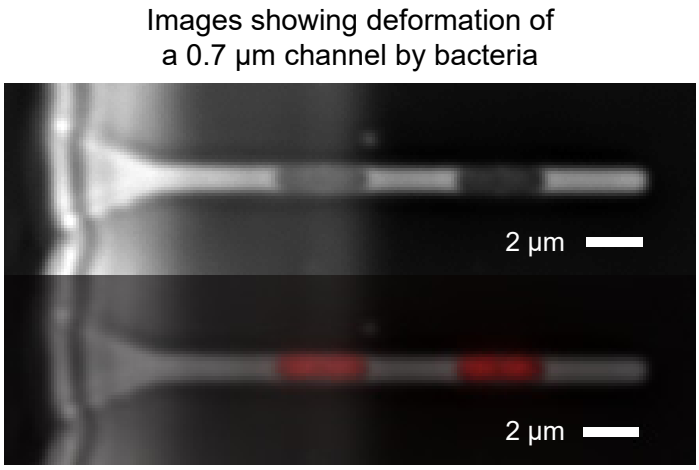


Figure 3-3 : Images of cells in a 0.7 μm wide and 15 μm long channel. Top panel is a phase contrast image and bottom overlay of phase contrast and fluorescence images. Broadening of the channel around cells is visible. The broadening is less apparent in 0.7 μm wide channels that are completely filled with cells because in this case the channels are uniformly deformed. Note that analysis for Figure 3-4 includes only data from channels that are completely filled with cells unlike what is shown in this Figure. The whole movie of growth and division of these cells are presented in Supplementary Movie M3-3. The Figure here corresponds to frame at 264 min. in Supplementary Movie M3-3.

Next, we compare birth length, width, volume and doubling time measurements of mother cells in differently sized channels to those from cells in liquid cultures. We found cell length (2.12 ± 0.05 μm) to be independent of channel width in the $0.8 \sim 1.0$ μm range (Figure 3-4 A). In 0.7 μm wide channels, where cells appeared to be in contact with channel walls, the cell lengths were significantly (9% difference, $p < 0.02$) smaller than those in other channels. Interestingly, cells were longer in all microfluidic channels than in the test-tube liquid cultures (1.84 μm; $p = 0.19$ for 0.7 μm wide channel, and $p < 10^{-16}$ for all other channels). At the same time, the coefficients of variation of the cell length at birth distributions were comparable to the values in the liquid culture (all are about 15%) (Figure 3-5 A). The coefficients of variation determined here are in agreement with previous measurements where values of $12 \sim 17\%$ have been reported from agarose pad [AOM+15] and microfluidic measurements [CSK+14; TABS+15].

While cell lengths were longer in microfluidic channels, their widths were significantly smaller (Welch's t-test $p < 10^{-8}$) (Figure 3-4 B). Also, coefficients of variation of the cell width distribution were smaller than the ones in liquid culture (by 4.5%) and decreased as the channel width decreased

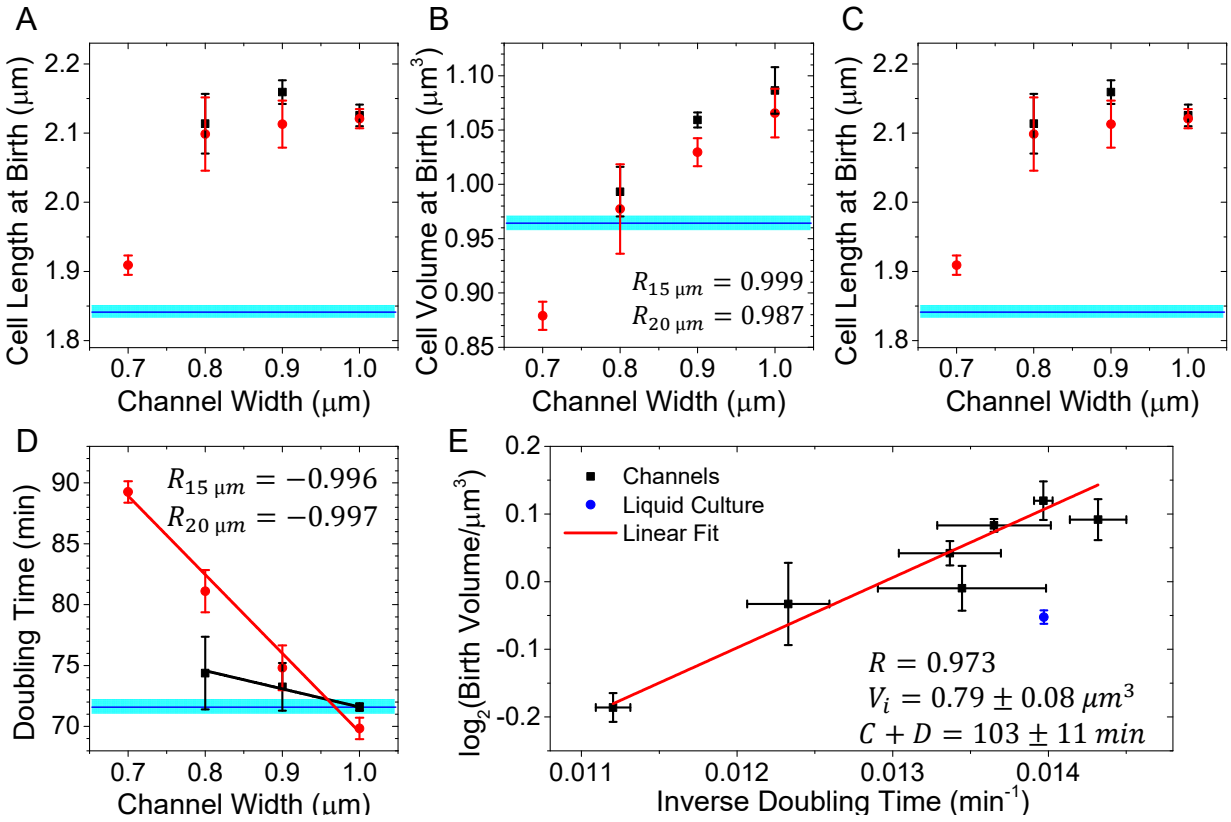


Figure 3-4 : Dimensions of the mother cell and its doubling times in dead-end channels of different widths. (A-D) Mother cell length, width, volume and doubling time as functions of channel width in channels 15 (red circles) and 20 μm (black squares) long. All measurements have been done at 28°C. Data points represent the average of three independent measurements. In each measurement, more than 300 cell births have been analyzed. Error bars are s.e.m. of the three independent measurements. Blue horizontal lines represent measurements of cells from liquid culture tubes. The width of these lines corresponds to s.e.m. All other solid lines are linear fits to the data. (E) Logarithm of birth volume, V_b, as a function of the inverse of doubling time, T_d^{-1}. Solid line shows the fit of the data to the universal growth law, $V_b = \frac{1}{2} V_i \cdot 2^{\frac{C+D}{t_d}}$. In the universal growth law, V_i is cell volume at the initiation of replication, C the time taken to replicate DNA and D the time taken from the end of replication to cell division. Here V_i and the summation, $C + D$, are treated as fitting parameters with best fit values $V_i = 0.79 \pm 0.08\ \mu m^3$ and $C + D = 103 \pm 11$ min. The errors bars are standard errors of the means.

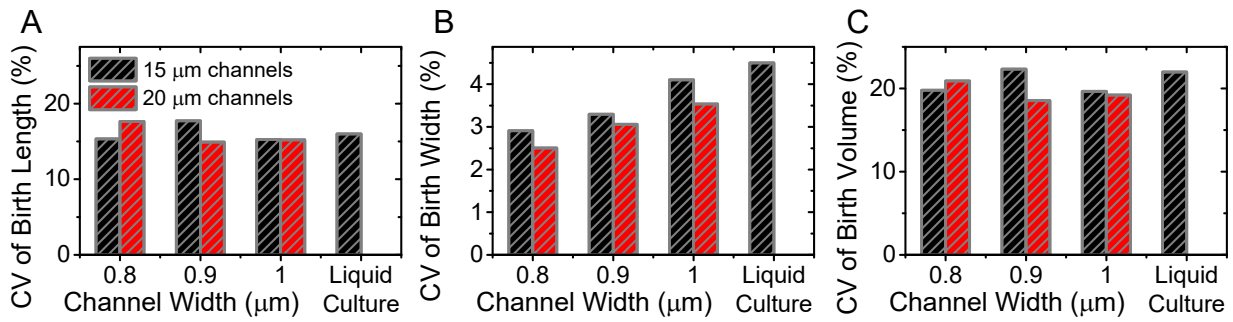


Figure 3-5 : Coefficient of variations (CV) for cell length, width and volume distributions. All the distributions have been measured at cell births. A coefficient of variation here is a pooled standard deviation from three independent measurements divided by a pooled mean.

from 4% to 3% (Figure 3-5 B). In 0.7 μm wide channels, the cell width was wider than the undeformed channel diameter indicating that channel walls prevented cells from becoming wider. In 0.8 μm wide channels, some cells could still be squeezed by channel walls. However, in 0.9 and 1.0 μm wide channels, the cells were narrower than the channels and not squeezed by the channel walls. Irrespective of squeezing or no squeezing from channel walls, the cell width at birth increased linearly with the channel width (Pearson $R = 0.999$ in 15 μm long and 0.987 in 20 μm long channels). So, in wider channels, the decrease in cell diameter was not linked to a direct mechanical force to cells but must have reflected some form of adaptation of the cells to a confined channel environment.

As expected from those two measurements above, the average mother cell volume also increased with the channel width (Figure 3-4 C). Comparison of microfluidic and the liquid culture cells showed that the differences in their lengths and widths, to some degree, compensated each other in cell volumes. In particular, for the 0.8 μm wide channels, the cell volumes matched those in liquid culture.

The doubling times also depended on channel width and increased as the channels become narrower (Figure 3-4 D). The effect was pronounced for cells in 20 μm long channels ($R = -0.997$, slope $= -65$ min./μm), but was less significant in 15 μm channels ($R = -0.996$, slope $= -15$ min./μm). In the latter case, the doubling times appeared almost indistinguishable from cells grown in liquid cultures despite changes in cell shape. The observed increase in cell doubling times with the decrease of its dimensions is expected. According to the universal growth

law, cell volumes at birth depend exponentially on growth rate, which is taken here as an inverse of doubling time [SMK58; WH17]. Such correlations are indeed evident in our data (Figure 3-4 E). The universal growth law emerged from studies where cells grew unrestricted, and the growth rate was determined by the type of carbon source rather than by its abundance [SMK58]. In later studies, growth rate was also examined in growth limiting conditions and the increase in cell size and growth rate were found to be correlated in most but not all conditions [SM71]. Accordingly, we interpreted the exponential decrease in mother cell volume as a function of doubling time to result from nutrient limiting conditions in channels ends which would arise from nutrient shielding in the channel.

3.1.4 Dependence of Mother Cell Growth on Channel Lengths

To further investigate this hypothesis, we studied how the dimensions and doubling times of mother cell depended on the channel length. We expected that doubling times should increase and cell dimensions should decrease as the length of the channel increases. For these studies, we used microfluidic chips with a fixed channel width of 0.9 μm but varied channel length from about $20 - 50$ μm (19, 29, 39, and 49 μm). We combined results from these measurements with the earlier ones in 15 and 20 μm long channels. Although the 15 and 20 μm long channels had the same designed width as the longer channels, the actual widths of longer channels appeared slightly smaller than 0.9 μm, which likely explains the differences in growth rates of the two data sets.

We found that the mother cell length, width, and volume all decreased in longer channels (Figure 3-6 A-C). The decrease was more pronounced in cell length and volume (by 17 and 33%, respectively) than that in cell width (a 7% change). This contrasts earlier measurements in Figure 3-4, where the cell width showed a larger variation while the length remained approximately constant. The decrease in cell length and volume was in good approximation proportional to channel length ($R = -0.992$ for both cases), while the decrease of cell width showed lower correlations ($R = -0.832$). The doubling time also increased linearly as a function of channel length (Figure 3-6 D). In 50 μm long channels, the doubling time was 44% longer than in 15 μm long channels. The increase in doubling time and decrease in cell volumes were, in good approximation ($R = 0.999$), related by the universal growth law (Figure 3-6 E). The fit parameters, which determine the cell volume at initiation per replication origin (V_i), and the sum of C and D periods [CH68], matched those found

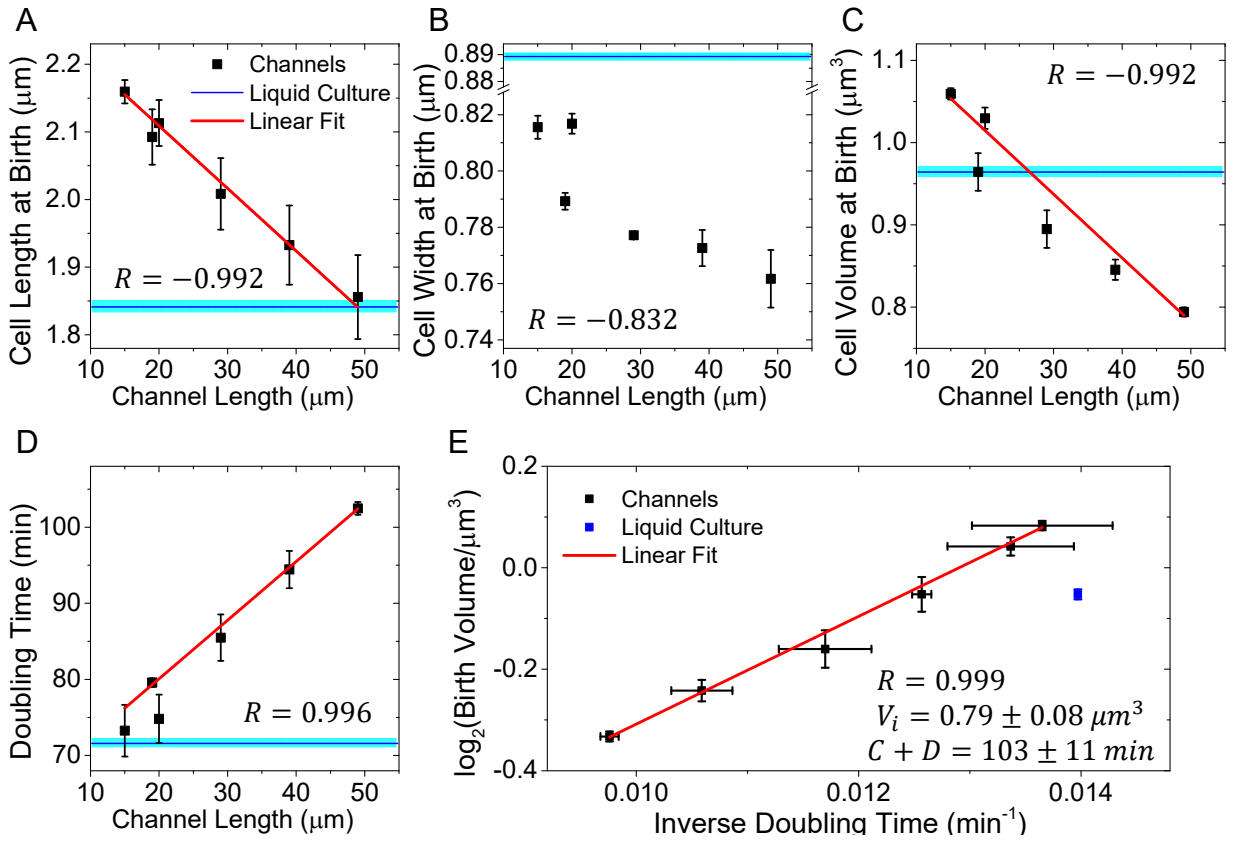


Figure 3-6 : Dimensions and doubling times of mother cells in channels of different lengths. (A–D) Mother cell length, width, and volume at birth, and doubling time as a function of channel length. All channels are 0.9 μm wide. Each data point is an average of three independent measurements. In each measurement, more than 300 cell births have been analyzed. Error bars are s.e.m. of the three independent measurements. Blue horizontal lines correspond to measurements of these quantities from liquid culture cells. Solid red lines are linear fits to data. (E) Logarithm of birth volume, V_b, as a function of inverse doubling time, T_d^{-1}, and it fits to the universal growth law, $V_b = \frac{1}{2} V_i \cdot 2^{\frac{C+D}{T_d}}$. The errors bars are standard errors of the means.

from measurements where the channel width was varied (cf. Figures 3-4 E, 3-6E). The consistency of these two datasets indicates that growth limitation likely had the same origin in the measurements where channel width and length were varied.

3.1.5 Mechanical Impediments to Cell Growth in 1D Cultures

In the above measurements, the doubling time increased linearly as the function of channel length. We hypothesized that if the channel length increased even further then the doubling time of the mother cell would show a non-linear increase and perhaps cell growth would completely stop as the nutrient levels deplete at the end of the channel. To test if doubling time of mother cells as a function of channel length would deviate from linear at longer channel lengths, we fabricated a new batch of microfluidic chips with channel lengths of 20, 50, 100, 150, and 200 μm.

Unexpectedly, during the initial passivation step of the channel walls with bovine serum albumin (BSA), which preceded cell loading, we observed an accumulation of this protein to the channel ends in 100 μm and longer channels from phase contrast images. The effect was completely missing in channels 50 μm and shorter on the same chip even for long incubation times ($>$ 12 hrs.). When the same M9 growth medium was used without BSA, no material accumulated to the ends of any channel. Aggregation of BSA was so strong that it completely excluded cells from the channel ends. Further investigation showed that the effect was not specific to BSA because if the channels were left with LB medium that did not contain any BSA, some material still accumulated to the channel ends. Similar effects have been observed before and were explained by water diffusing into the PDMS matrix [RD05]. The effect depends sensitively on channel length as will be discussed in more details later. Although BSA prevented cells from occupying the ends of 100 μm and longer channels, cells could also be cultivated without BSA. In this case, there was some aggregation of cells near the channel entrances. Thus, the omission of BSA increased sticking of cells to the channel walls, as expected. However, the growth rate of cells in $20 - 50$ μm long channels without BSA passivation were not different from these with BSA (Figure 3-7 D).

The growth of colonies in 100 μm and longer channels differed significantly from those in shorter channels ($\leq$ 50 μm). These differences were present irrespective of the presence or absence of BSA in the growth medium. Attachments of cells to channel walls combined with their continued growth

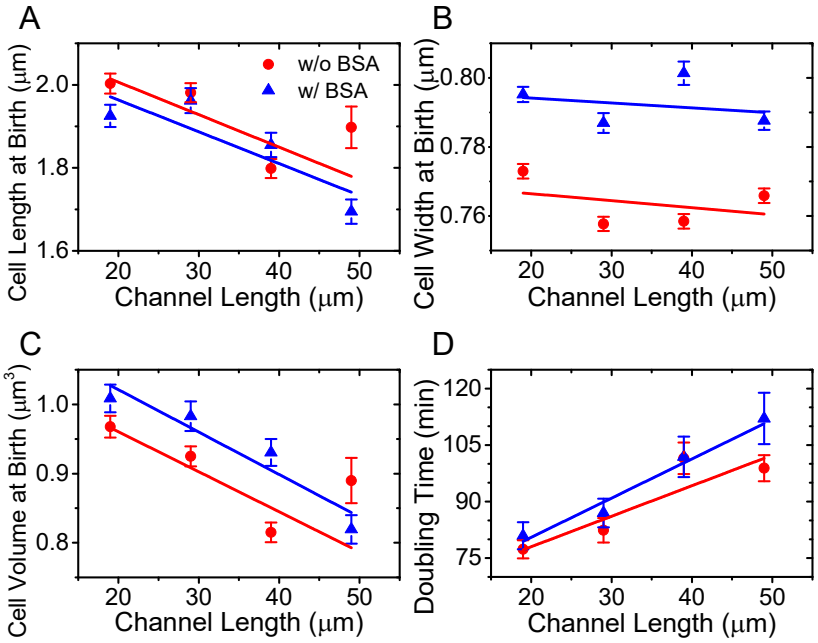


Figure 3-7 : Mother cell length, width, volume and doubling time as a function of channel length for channels with and without BSA passivation. All cell dimensions are determined at cell birth. All channels are 0.9 μm wide and 1.15 μm high. Note that the same channels and mother cells were used for the two measurements. The measurements without BSA were performed first and then the growth medium was switched to one that contains 0.1% BSA. 12 hours was waited before starting a new measurement to ensure proper BSA passivation and to allow cells to adjust to new growth conditions.

lead to considerable pressure buildup, which was evidenced by the widening of the channel in phase contrast images (Figures 3-8 A-C).

In deformed regions of the channel, the cells grow in multiple rows or were tilted relative to the direction of the channel. Based on our earlier studies [YGJ+15], stress analysis of such channels has shown that pressures in the 0.2 MPa range are needed to widen channels at their midplane by few hundred nanometers. Similar or even larger pressures must have been present in the broadened regions of the channel. From time to time, the pressure buildup resulted in a sudden release of cells from the channels as the force resulting from cell growth exceeded some critical value needed to break adhesive contacts between cells and channel walls (Figures 3-8 A). However, in some channels, these contacts were likely stronger or differently distributed, and no pressure release occurred during the 12 hrs. observation period.

The pressure buildup had pronounced effects on cell growth and morphology (Figure 3-8 C, Supplementary Movies M3-4, M3-5). As the pressure increased, cell elongation and division rates slowed down (Figure 3-8 D), and the cells started to broaden (Figure 3-8 E). For cells that grew tilted relative to the channel axes in the initial stages of pressure buildup, the broadening was not uniform along the cell length due to uneven pushing from other cells (Supplementary Movies M3-6, M3-7). The cell regions in contact with the other cells expanded less than the regions where cells were able to expand toward channel walls without these contacts. As a result, the cells acquired irregular pear-shaped morphologies that significantly differed from the regular rod shape (Figure 3-8 C). Some mass growth, albeit at a much slower rate than in liquid cultures, still occurred in these conditions (Figure 3-8 F). The mass growth in these conditions could be predominantly attributed to cell broadening rather than to elongation. Upon release of pressure, the cell shape immediately returned to the usual elongated rod-shaped morphology. This sudden change was accompanied by a decrease in cell width ($\approx 7\%$) and increase of cell length ($\approx 10\%$). Interestingly, cell elongation resumed within minutes after pressure was released (Figure 3-8 D) even though the elongation rate had been almost zero during the 9 h compression period. Along with resumption of cell elongation, the cell width, after decreasing abruptly upon release of compression, decreased further. Over the course of 1.5 h, it approached its regular value (0.78 μm). The slowdown of cell growth also appeared in measurements in 100 μm and longer channels when BSA was used (Figure 3-9, Supplementary Movie M3-8). The slowdown was followed by a period of faster growth after each pressure release.

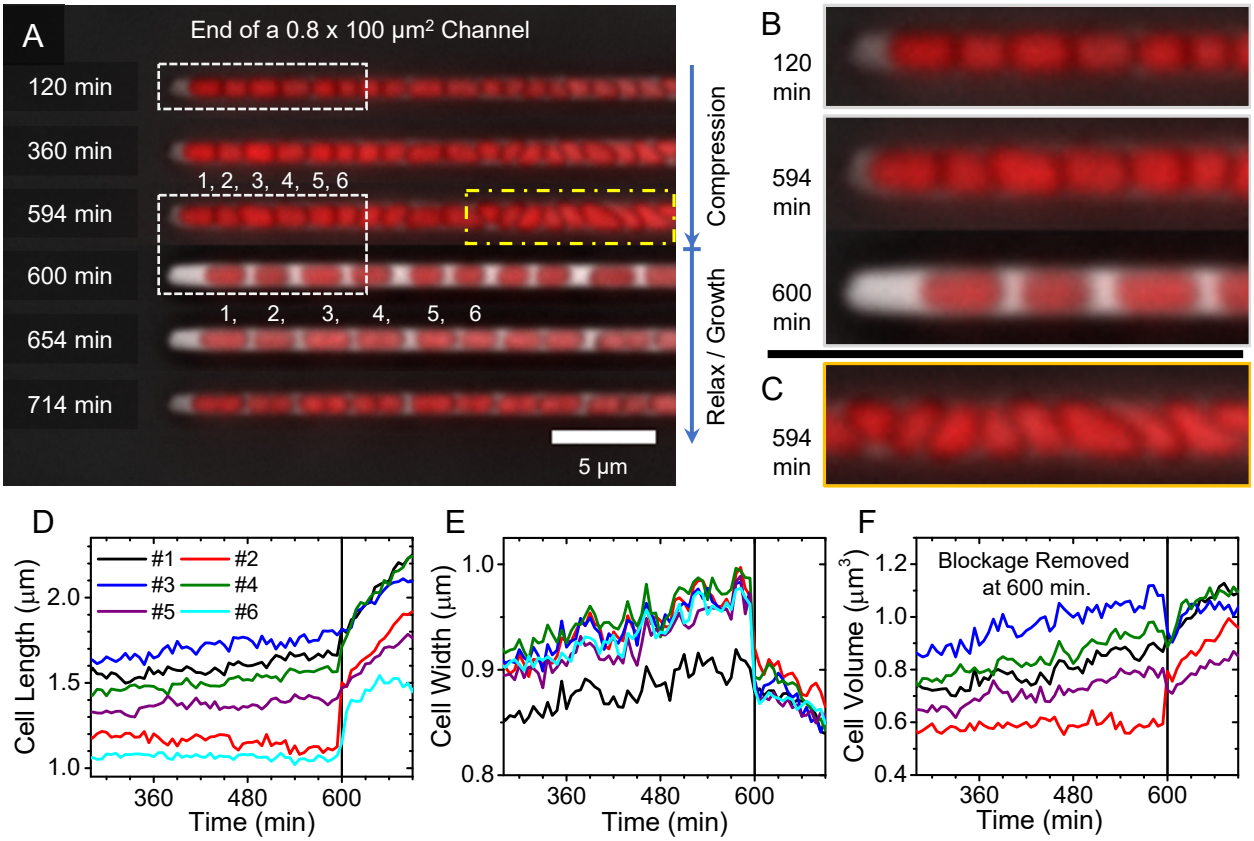


Figure 3-8 : Cell growth in 100 μm long channels. (A) Composite time-lapse images of cells growing in a 100 μm long and 0.8 μm wide channel without BSA passivation. Pressure builds up in the channel until the frame at 594 min. Pressure release occurs between 594 and 600 min. after which cell growth and division resume. Individual cells are labeled with numbers 1 to 6. (B, C) Boxed regions in (A) are magnified. (D-F) Cell lengths, widths and volumes as functions of time for the first six cells in the channel as labeled on (A). Solid vertical lines indicate the time when pressure release occurred.

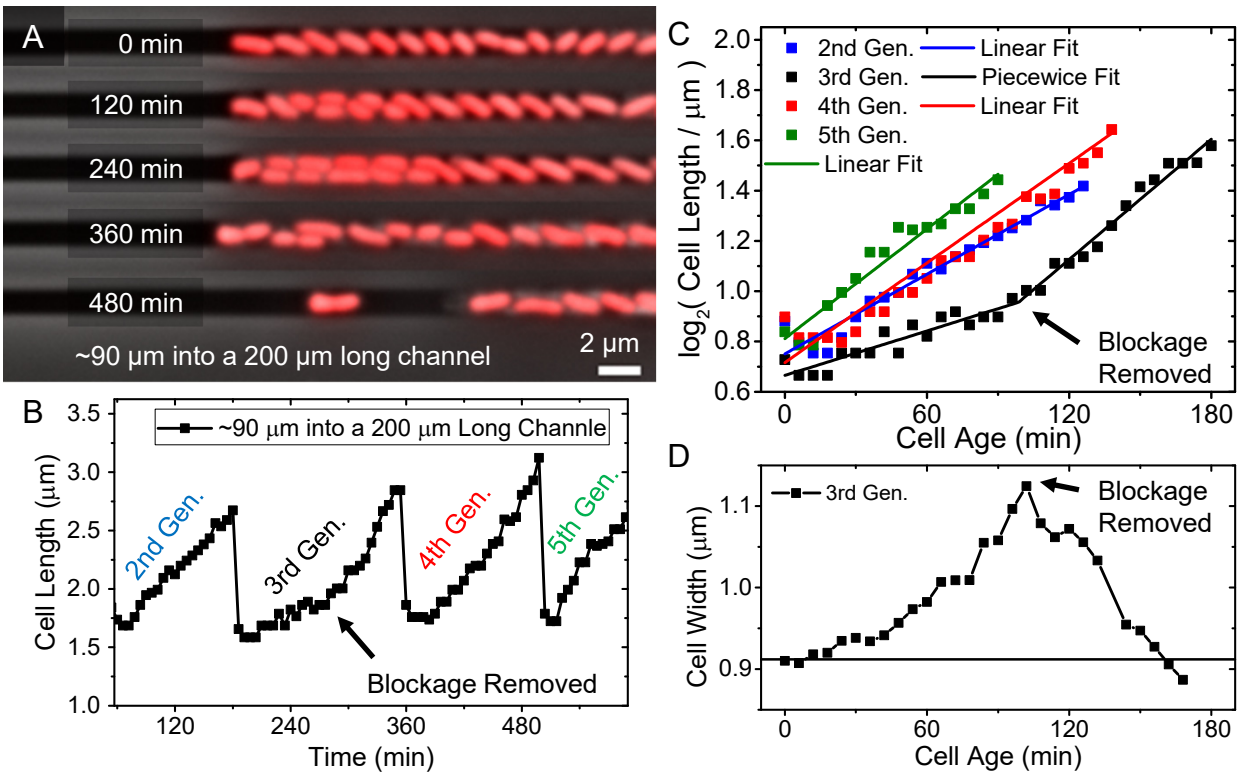


Figure 3-9 : Cell growth in 200 μm long channels with 0.1% BSA. (A) Composite time-lapse images of cells growing in a 200 μm long and 0.8 μm wide channel. The images have been captured at about 90 μm from the channel entrance. Cells do not fill the channel further than about 90 μm because of BSA accumulating to channel ends. BSA accumulation leads to darkening of channels in phase contrast images. In this measurement, pressure builds up in the channel until 300 min. (B) The elongation of the mother cell in this channel as a function of time. The elongation slows down as the pressure builds up in the channels and increases when the blockage to cell movement disappears. (C) Mother cell elongation in logarithmic scale plotted as function of cell age. (D) Width of the mother cell before and after the blockage disappears.

However, adhesion of cells to the channel wall was clearly weaker in this case; consequently, smaller pressure buildups occurred. In these conditions, cell morphology remained regular, and broadening could not be detected. Altogether, in 100 μm and longer channels, mechanical hindrances were the growth limiting factor instead of nutrient depletion.

3.1.6 Cell Shape Shows Adaptations to Channel Geometry

Here we studied how confinement changes the growth of *E. coli* cells in microfluidic channels of different widths and lengths. In 15 and 20 μm long channels with widths of 0.9 and 1.0 μm, the growth rate and cell volume were comparable and even slightly ($5 \sim 10\%$) exceeded the values from liquid cultures measurements. Although the confinement related effects to the growth rate in these conditions were negligible, cell morphology was affected. Cells were significantly longer and narrower than in liquid cultures. What factors could have led to the change of cell morphology? In the narrowest channels with widths of 0.7 μm, the cell width was physically limited by the channel walls. The same mechanical constraint could also have limited cell diameter in 0.8 μm wide channels. However, in 0.9 and 1.0 μm wide channels the cells were not squeezed by channel walls, yet they still maintained a higher length to width ratio compared to liquid culture cells (2.7 vs. 2.1, respectively). Even higher ratios (> 3.4) can be inferred from previous measurements by another group using mother machine devices at similar growth conditions [TABS+15]. We hypothesize that cell shape in these channels is narrower and longer because of contacts to channel walls. Although the cell adhesion to channel walls was weak, especially to BSA passivated channel walls, these contacts may have had an effect on peptidoglycan synthesizing machinery. Consistent with this idea, the length to diameter ratio of cells was higher when channel walls were not passivated by BSA compared to that when they were 3-7. By a common view, peptidoglycan synthesis activity is controlled via MreB and FtsZ polymer scaffolds, which reside in the cytosolic side of the inner membrane [TBGV12]. The data presented here point to the possibility that stresses in the outer envelope may also modulate peptidoglycan synthesis activities directly without being transmitted via MreB and FtsZ scaffolds.

3.1.7 Is Mass Transport Limiting Cell Growth in Channels?

Our measurements showed universal growth law-like dependence between cell volume at birth and growth rate. We interpreted this dependence as arising from nutrient limiting conditions at the channel. We hypothesized that adsorption of nutrients by cells growing between the mother cell and the channel entrance lead to depletion of nutrients at the location of the mother cell. This effect has been also referred to as nutrient shielding [LKN13]. Taking the simple geometry of channels and growth of bacteria in single rows without gaps, the nutrient shielding effects in these conditions can be quantitatively analyzed using 1D reaction-diffusion equations. Separate equations can be written for each chemical compound present in the growth medium. Here, we assume that there is just one component in the medium that is growth limiting. Denoting its concentration by c, its diffusion coefficient by D, its absorption coefficient per unit cell surface area by k_{abs}, channel width by W and height by H, and cell radius by R_c a reaction-diffusion equation as a function of distance x from the channel entrance for this component can be written as:

$$\left(W \cdot H - \pi R_c^2\right) \cdot D \frac{d^2c}{dx^2} = 2\pi R_c k_{\text{abs}} \cdot c. \tag{3.1}$$

Here we assumed that the uptake of this nutrient component is a first order process that is far from saturation. If the uptake were saturated (kinetically limited) then the corresponding compound would not be a growth limiting factor. The solution to this equation assuming non-adsorbing boundary condition at channel end is:

$$c(x) = \frac{c_0 \cosh\left(\frac{x-L}{x}\right)}{\cosh\left(\frac{L}{x}\right)} \lambda = \sqrt{\frac{(W \cdot H - \pi R_c^2) \cdot D}{2\pi R_c \cdot k_{\text{abs}}}}. \tag{3.2}$$

Here L is length of the channel and c_0 is concentration of this compound at the channel entrance. λ defines a characteristic length scale, which is referred to as the nutrient screening length [LKN13]. The screening length depends on the cross-sectional area of the channel, being longer for wider channels. We next assume that growth rate (inverse of doubling time), which is controlled by this compound, follows Michaelis-Menten type of kinetics [SM71]:

$$T_d^{-1}(x) = \frac{T_{d,\min}}{1 + \frac{K}{c(x)}}. \tag{3.3}$$

Here T_d is doubling time of cells at position x from the channel entrance, $T_{d,\,\mathrm{min}}$ is the doubling time in conditions where the compound is not growth limiting and K determines the concentration above which nutrient uptake rate starts to saturate. In dilute liquid cultures $T_{d,\,\mathrm{liquid}} = T_{d,\,\mathrm{min}}\,(1 + K/c_0)$. Using the latter expression and the solution for the reaction-diffusion equation for $c(x)$ yields:

$$T_d(x) = T_{d,\,\mathrm{min}} + (T_{d,\,\mathrm{liquid}} - T_{d,\,\mathrm{min}})\cosh\left(\frac{L}{\lambda}\right)/\cosh\left(\frac{x-L}{\lambda}\right). \tag{3.4}$$

Our data concerns mother cells. The doubling time of the mother cell T_d then becomes:

$$T_d(x) = T_{d,\,\mathrm{min}} + (T_{d,\,\mathrm{liquid}} - T_{d,\,\mathrm{min}})\cosh\left(\frac{L}{\lambda}\right). \tag{3.5}$$

Here we assumed the position of the mother cell to be $x \approx L$. The formula predicts that the doubling time in short channels $L \ll \lambda$ is independent of channel length and equals the doubling time in liquid cultures. In channels $L \approx \lambda$ it increases as $T_d \sim L^2$ and in channels $L \gg \lambda$ the increase is exponential $T_d \sim \exp(L/\lambda)$. Altogether Equation 3.4 thus predicts a distinctly non-linear relationship between doubling time and channel length. In contrast to this prediction, the data in Figure 3-6 D is in good approximation linear (Figure 3-10). The discrepancy between the model and the data also appears when one compares dependence of the doubling time on channel width. The model predicts a smaller variation of doubling time as a function of channel width, in particular for 20 μm long channel (Figure 3-10). It is possible that model treats too simplistically the relationships between concentration of growth-limiting compound and growth rate. For example, some deviations from a single Michaelis-Menten type relationship for growth rates were observed in glucose limiting conditions [SM71]. However, the underlying relationship between doubling time and channel length should still be distinctly non-linear and as such not consistent with the experimental data. Moreover, there is no obvious compound in our growth medium that can be growth limiting. Concentrations of all media components at channel opening are in the millimolar (mM) range and as such exceed several orders of magnitude the growth-limiting concentrations. For example, concentration of glucose in the channel opening is 22 mM. This is about 10^4 higher than its growth-limiting concentration of about 1 μm [SM71] (Shehata and Marr, 1971). The uptake of glucose by cells is thus completely kinetically limited in the vicinity of channel opening. One can solve the reaction-diffusion equation similar to Equation 3.1 also in a

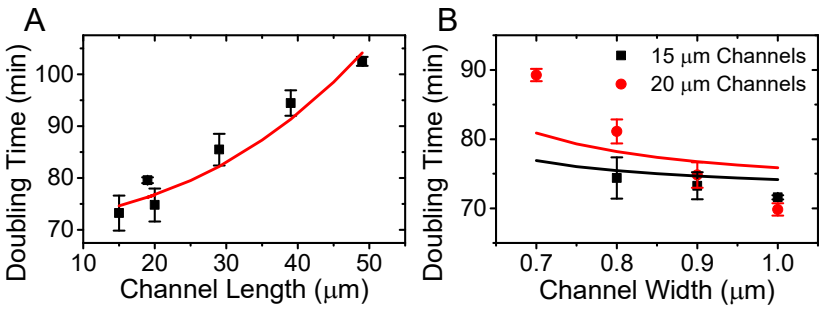


Figure 3-10 : Comparing modeling and experimental data on doubling times. (A) Doubling time as function channel length (the same data as in Figure 3-6 D). All channels are 0.9 μm wide. Solid line is fitting with the Equation 3.5 from the main text. $T_{d,\,\mathrm{liquid}}$ is taken as 72 min based on measurements of liquid cultures. The best agreement is reached as small as possible $T_{d,\,\mathrm{min}}$. However, the shortest doubling time at $T = 28°C$ of our *E. coli* strain cannot possibly be shorter than 40 min. The latter correspond to doubling time of this strain in LB medium at this temperature. Accordingly, $T_{d,\,\mathrm{min}}$ is fixed at 40 min. Curve fitting yields nutrient screening length $\lambda_{\mathrm{fit}} = 37\ \mu m$. From the screening length absorption rate $k_{\mathrm{abs}} = 0.1\ (s \cdot \mu m)^{-1}$ can be calculated using Equation 3.1 of the main text assuming diffusion constant $D = 700\ \mu m^2/s$ (pertaining to glucose). (B) Using the estimated $k_{\mathrm{abs}} = 0.1\ (s \cdot \mu m)^{-1}$ dependence of doubling time on channel width is plotted against experimental data from Figure 3-4 D in the main text.

kinetically limited regime. The solution shows that the concentration of such nutrients decreases quadratically from the channel entrance as:

$$c = c_0 - c(L) = L^2 \frac{I_{\max}}{2\,(WH - \pi R_c^2)\,L_c D}. \tag{3.6}$$

Here $I_{\max}$ is kinetically limited nutrient uptake rate per cell per second, and L_c is the average cell length. For glucose $I_{\max} = 2 \times 10^5$ molecules per cell per second [NS99] and $D = 700\ \mu m^2/s$ [Lon53] yields concentration change of 2.7 mM ($\sim$10%) at the end of a 50 μm long channel that is completely filled with bacteria. Resulting 19 mM concentration of glucose in channel end corresponds still to highly saturating level. The same arguments also apply to the casamino acids, which are present in mM concentrations too. Moreover, their depletion with exception of leucine, which is essential for the strain, would not significantly alter the doubling times. If depletion of leucine would have occurred then this would have led to increase in doubling times approximately given by Equation 3.4. Such dependence, however, would not be consistent with the experimentally observed linear dependence in Figure 3-6 D as already argued.

The previous analysis assumed mass transport of nutrients to channels is solely via diffusion. However, accumulation of BSA to the ends of 100 μm and longer channels demonstrates that there is significant influx of water into these dead-end channels because of evaporation/diffusion water into PDMS [RD05]. This influx was significant even after channels were filled with water for a 12 hrs. period. The steady uptake rate of water to PDMS has been estimated to be $J = 7 \times 10^{-6}\ kg/m^2 s$ [RD05]. This update rate explains why BSA accumulates in 100 μm long channels but not in 50 μm long channels. The steady state concentration profile for the BSA in empty channels can be found from equation that balances its diffusive and convection fluxes:

$$W \cdot H \cdot D_{\mathrm{BSA}} \frac{dc_{\mathrm{BSA}}}{dx} = \frac{J}{\rho} (2H + W) \cdot (L - x) \cdot c_{\mathrm{BSA}}(x). \tag{3.7}$$

Here ρ is the density of water. The solution to this equation is:

$$\begin{aligned} c_{\mathrm{BSA}}(x) &= c_{0,\,\mathrm{BSA}} \exp\left(\frac{L^2}{2\sigma^2}\right) \exp\left(-\frac{(L-x)^2}{2\sigma^2}\right) \sigma \\ &= \sqrt{\frac{\rho \cdot D_{\mathrm{BSA}}}{J} \frac{WH}{2H + W}}. \end{aligned} \tag{3.8}$$

Here σ is a characteristic length scale for accumulation, which depends on cross-sectional parameters of the channel but not on its length. For BSA, which diffusion coefficient is 70 $\mu m^2/s$, $\sigma = 57\ \mu m$ can be estimated for 0.9 μm wide channels. Increase in BSA concentration in channel end is 1.5 times in 50 μm, 5 times in 100 μm and 500 times in 200 μm long channels. 500 times increase corresponds to almost complete precipitation of BSA as observed in our experiments.

While water permeation to PDMS has strong effect on the BSA distribution in the channel, Equation 3.7 predicts that it does not have significant effect on distribution of nutrients, signaling molecules and metabolic waste products in the channel. The reason is that diffusion coefficients of these small molecules are about an order of magnitude larger (e.g.,, $D = 700\ \mu m^2/s$ for glucose) than for BSA. Even for 200 μm long empty channel one would expect the concentration of these molecules to be less than twice of that in the channel entrance. This increase does not likely have a significant effect on cell growth.

So far we did not consider adsorption of small molecules by channel walls. In the current treatment, the adsorption would be completely analogous to adsorption of these molecules by cells.

Consequently, adsorption by channel walls can be accounted by increasing k_{abs} in Equation 3.1, while the functional form of the equations remains the same. Accounting wall adsorption would therefore not lead to better agreement between experiment and model as inclusion of adsorption would not change functional dependence of doubling time on channel length.

Altogether our analysis shows that mass transport related limitations to cell growth in channels $\leq$ 100 μm are not significant in our experimental conditions despite our initial expectations. However, if some of the essential components in the media are present at less than saturating levels then the doubling times of the cells in the channel ends should become strongly affected. Flow of water into channels because of permeability of PDMS should not affect these conclusions because of fast diffusion of nutrients and waste molecules.

3.1.8 Mechanical Constraints to Cell Growth

Our experiments indicate that instead of nutrient limitations, the mechanical impediments set stronger constraints for bacterial growth in channels. In channels 100 μm and longer, friction forces caused cessation of cell elongation. In shorter channels friction could have also been the main growth limiting factor. In accordance with this assumption, friction leads to growth opposing force on a mother cell, F_f , which increases proportionally to channel length $F_f \sim L$. Measurements of *E. coli* growth in agarose hydrogels have shown that forces opposing cell growth decrease elongation rate approximately linearly as the magnitude of the force increases [TAR+12]. For small forces, this would mean that increase in doubling time from the bulk value is proportional to the opposing force and thus on channel length $\Delta T_d = T_d - T_{d,\,\text{liquid}} \sim F_f \sim L$ in agreement with the experimental data (Figure 3-6 D). Increased friction can also explain why in narrower channels doubling time increased (Figure 3-4 D). Although sticking of individual cells to channels walls was weak in channels longer than 50 μm, the cumulative effect of adhesion become strong enough to prevent cell elongation on the dead-end side of the channels. Interestingly, some residual mass growth still occurred in this situation that resulted in broadening of cells. Presumably due to this residual growth cells in some channels were able to overcome static friction forces and release the pressure that opposed their growth. During the release of pressure, the cells behaved similarly to a compressed elastic rod: their length increased (25%) and diameter decreased (7%). The length increase furthermore indicates that cells did synthesize new cell wall during the compression

phase. Taken the previously estimated Young modulus in the range of $50 \sim 150$ MPa for *E. coli* cell for the envelope thickness of 4 nm [TAR+12], 25% of compression corresponds to force on the 0.8 μm wide cell of $0.1 \sim 0.4$ μN. Here we assumed that turgor pressure, during and few minutes after the compression, was the same and that cell wall compression was elastic. The force of $0.1 \sim 0.4$ μN then corresponds approximately to the stall force for peptidoglycan synthesis in *E. coli*. For comparison, the stalling force has been estimated to be 11 μN in fission yeast [MBC09]. Strikingly, the cells were able to restore their growth rates very rapidly (less than 6 min.) after more than 9 hrs. of very limited growth during compression. Here the 6 min. estimate corresponds to the frame rate of measurements, but the actual lag time could have been shorter. The very short lag time, if any, is in contrast with the time needed to restore growth in stationary phase cells upon entering fresh medium. In our measurements, this time has typically been in the range of $0.5 \sim 2.0$ hrs. depending on the length of time cells spent in stationary state. A period of approximately 30 min. appears to be needed to restore transcriptional activity and assemble functional peptidoglycan synthesis complexes. Since the cell growth in channels resumed much faster, the cells must have maintained active peptidoglycan machinery throughout the compression period. The compressed cells in channels were clearly different from stationary phase cells as they had access to nutrients and were metabolically more active. Maintenance of enzymatic machinery, even when no elongation occurred, indicates that mechanical stress opposing cell growth alone is not able to suppress transcriptional peptidoglycan synthesis machinery the way the entry to stationary phase does.

3.1.9 Implications to Bacterial Growth in Microfluidic Devices and in Natural Microenvironments

Our work brings out some differences in the growth of *E. coli* in confined, relative to unconfined, conditions in mother machine platform. We find that for our mother machine platform the channels need to be in a rather narrow range of dimensions for not displaying growth-limiting effects: for *E. coli* growing in M9 medium with glucose and casamino acids only 15 and 20 μm long and 0.9 and 1.0 μm wide channels did not display these effects. However, even in these channels cell morphology differed from that in liquid cultures. The different aspect ratio that we observed is not likely significant factor for most experiments, but for those dealing with cell size control and

cell wall synthesis, these effects need to be considered. To improve the mother machine design, one can use even shorter ($< 15\ \mu m$) channels. However, this comes with the drawback of losing cells from the channel in long-term experiments. On the other hand, our data and analysis indicate that growth limitation due to nutrient and waste diffusion is minimal even in long channels ($> 100\ \mu m$). The designs that increase mass transport to channels, such as done recently by diverting some fluid flows through the channels [BBT+17; Jen17] or using shallow side channels that surround the cells [NLPL13; CRPL17], are not likely to alleviate growth limitations in these channels.

The mechanical constraints resulting from cell adhesion may be a major limiting factor for bacterial growth not only in microfluidic channels but also in natural environments such as soil where small pores and channels with dimensions comparable to bacterial size are present [RR01]. These constraints may also limit bacterial growth in unconstrained colonies such as ones on agar plates. Although nutrient limitation has been considered as the main growth limiting factor for growth of bacterial cells in the interior of the colony [JFG+15], our results point out the possibility that mechanical constraints have an equally important role in limiting growth only to the outer layers of the colony.

3.2 Development and Testing of Microvalves

3.2.1 Motivation

To carry out quantitative measurements, a platform based on pressure actuated microvalves was tested that has allowed different uniaxial stresses to be applied to *E. coli* cells. However, larger microfluidic valves used in this study encased the cells and isolated them from their growth medium. In this report, we describe the development of micron-scale valves that allow application of large forces to individual bacterial cells, while maintaining the cells in their physiological environment. Our approach enables the observation of cells in a high resolution optical microscope while being deformed. The approach is useful in understanding mechanical properties of the bacterial cell wall and to probe its internal organization by mechanically perturbing it. The micron-scale pressure actuated valves, which we characterize here in detail, may also be useful as control elements in integrated fluidic circuits [YGJ+15].

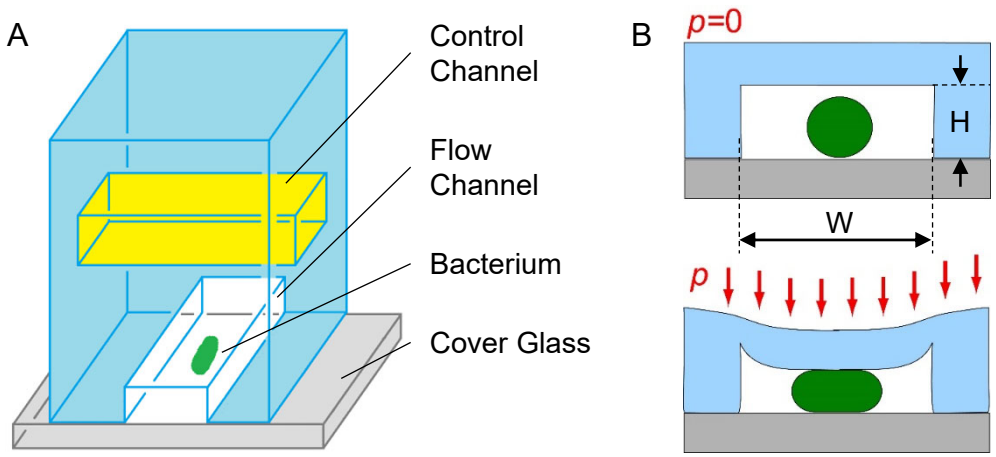


Figure 3-11 : Design of microvalve device experiment. (A) Application of uniaxial stress to bacterial cells is based on pressure actuated microvalves. The latter consists of a flow channel, where the bacteria reside, and a control channel to which a control pressure is applied externally. The two channels are separated from each other by a thin PDMS membrane. (B) Cross-section of the flow channel and the bacterium in the presence and absence of overpressure in the control channel.

3.2.2 Design of the Microvalve Devices

Our approach is to use pressure actuated microvalves to apply controlled mechanical stimuli to cells. The cells reside in flow channels, the ceiling of which deforms when external pressure is applied to the control channels (Figure 3-11 A). The ceiling, in turn, deforms the bacterium (Figure 3-11 B). To position the bacteria under the valves, we flow a highly diluted cell culture through partially closed valves. If the flow channel height under the control line is lower than the diameter of the bacterium, then that valve traps the bacterial cell flowing in the channel. Frequently more than one bacterium can be trapped under the valve. If multiple cells end up grouped together under the valve, then image analysis becomes more complicated. However, the number of trapped cells can be controlled by changing concentration of cells, flow rate, and duration of flow pulses. Moreover, taking that about 20 valves are present in one microfluidic chip, it is usually not concern if some valves do not produce usable data. The pressure actuated microvalves have been ubiquitously used to control fluid flows in LOC devices [UCT+00]. In latter applications, it is important that valves close leak tight and, for that purpose, the flow channels have semicircular crosssections. In contrary, to apply controlled forces to the cell it is not desirable that the valve closes fully because in this case

the cell would become enclosed in a PDMS membrane and it will have no access to growth medium. To avoid this unwanted outcome, we use much smaller valves and flow channels with a rectangular crosssection, with width W and height H, instead of a semicircular cross-section (Figure 3-11 B).

3.2.3 Modeling

While the closing of large ($W = 50 \sim 100\ \mu m$) round fluidic lines have been extensively characterized and modeled [SHP+04; KSQ+07], the behavior of small valves ($W = 1 \sim 10\ \mu m$) with rectangular flow line cross-sections have not yet been well studied. Here, we use finite element modeling to investigate the closure of these valves in a parameter space pertinent to our experimental conditions. The valves are modeled in 3D using AUTODESK INVENTOR software. The Young's modulus of PDMS is chosen as 1.0 MPa, and a Poisson ratio of 0.49. The adapted value for the Young's modulus falls in the range of $0.75 \sim 2.97\ MPa$ cited in the literature for 1:10 curing agent to base ratio of fully cured bulk PDMS elastomer [JMTT14; ALA99; KDSB09]. Although a Poisson ratio even higher than 0.49 has been used in the literature for PDMS [YZ09], we use 0.49 because of the limits set by the INVENTOR software. Note that these material parameters give a good fit to our experimental data as will be described below.

In all simulations, we use fixed heights for the flow channel (1.45 μm) and the control channel (50 μm), which correspond to measured values of our devices. The typical channel profiles for 5 and 3 μm wide flow channels at various control line pressures are shown in Figure 3-12 A, B. The deflection of the flow channel center is linear in applied pressure for all studied channels (Figure 3-12 C). The deflection also scales approximately linearly as a function of flow channel width (Figure 3-12 D). The narrower channels are more difficult to close, but even as the channel width approaches to zero, the deflection of flow channel ceiling remains finite.

The deflection of the valves depends also on the thickness of the flow layer and on the control channel width. Wider control channels facilitate closure as does a thinner membrane layer (Figure 3-12 E). However, we find the deflection of valves per unit pressure decreases approximately only as the logarithm of flow layer thickness. Accordingly, it is more advantageous to work with thicker membranes ($> 15\ \mu m$), which are less challenging to fabricate than thinner ones. A good strategy to compensate for the somewhat higher stiffness of thicker valves is to increase the width of the control channel.

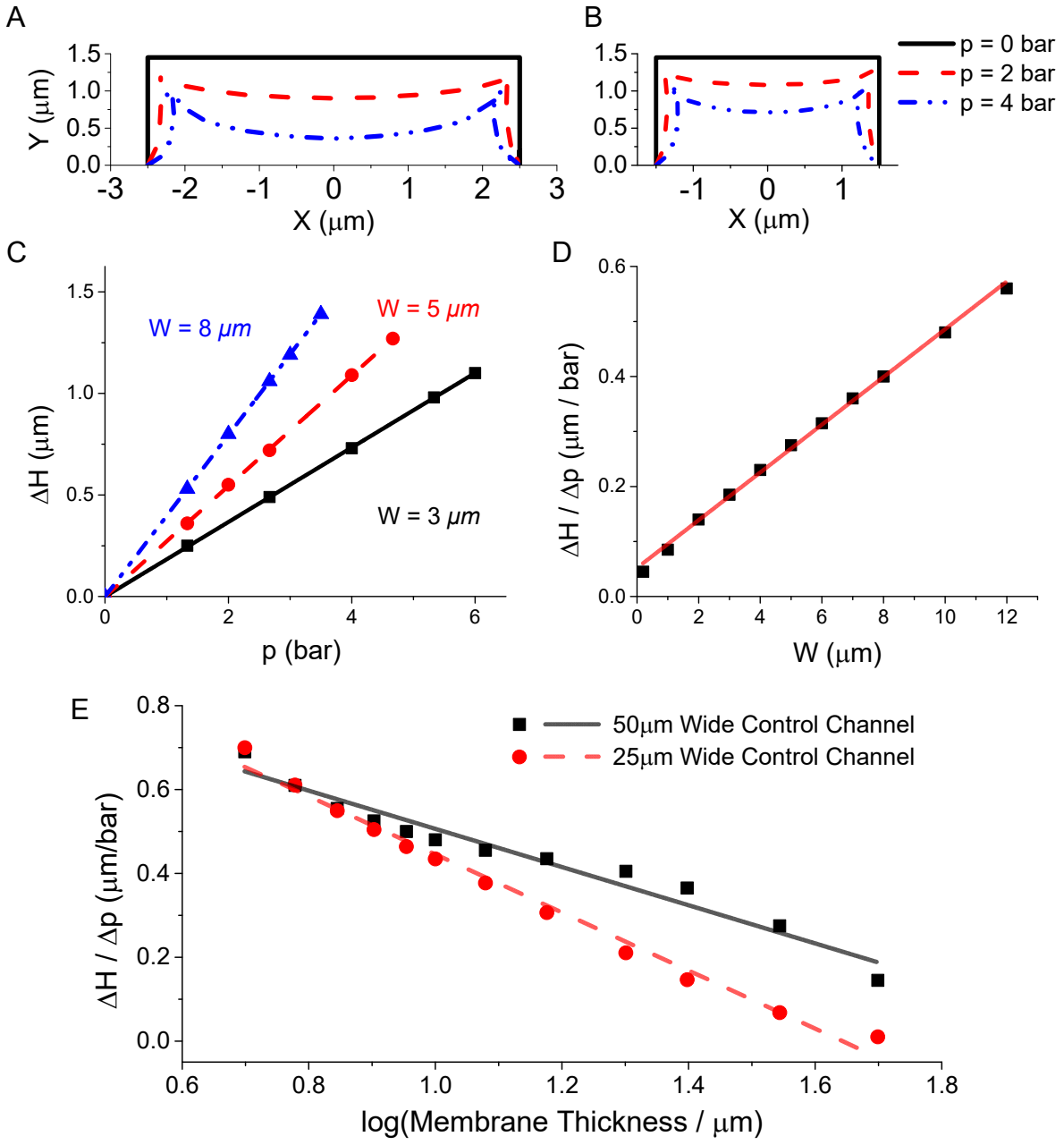


Figure 3-12 : Modeling the closure of small pressure actuated valves. (A) Cross-sectional profiles of a 5 μm wide flow channel at control line pressures 0, 2, and 4 bar (from top to bottom). The height of the flow channel is 1.45 μm and the thickness of the flow layer is 35 μm. The control line is 50 μm wide and 25 μm high. (B) The same for a 3 μm wide flow channel. (C) The deflection of the channel ceiling at the center of the valve as a function of control line pressure. The lines are linear fits to the data. (D) The slopes of the linear fits from the previous panel, $\Delta H/\Delta p$, plotted as a function of flow channel width. Solid line is linear fit to the data. (E) $\Delta H/\Delta p$ as a function of flow layer thickness. Note logarithmic scale of the horizontal axes. The straight lines are fittings to the data.

3.2.4 Comparison of modeling with experimentally measured flow channel profiles

To compare the modeling results to the deflections in actual pressure activated valves, we use absorption measurements in an optical microscope to determine the flow channel profiles at various control channel pressures. This method has been used before to characterize profiles of large channels, which depth and width are in 100 μm range but, as demonstrated here, the approach is suitable also for much smaller and shallower channels. In these measurements, we fill the flow channel with a 1:1 volume ratio of brilliant blue dye (Walmart) to glycerol (Fischer Scientific) and image the channels in the microscope using brightfield diascopic imaging (Figure 3-13 A). Glycerol is added because otherwise the diffraction patterns due to the channel sidewalls will appear on the images. We convert the resulting absorption images to thickness images using the Beer-Lambert's law,

$$H(x) = (1/a) \cdot \log(I_0/I(x)). \tag{3.9}$$

Here, $H(x)$ is the height of the channel across its cross-section, a is the (decadic) attenuation coefficient of dye and glycerol mixture, I_0 is the intensity of light far away from the channel, and $I(x)$ is the intensity of light within the channel. Using a spectrophotometer, we measure the attenuation coefficient at peak absorption of the dye at 628 nm to be $a_{\max} = 1800\ cm^{-1}$. To find the attenuation coefficient in the bandwidth of the red bandpass filter used in the lightpath of the microscope (Chroma 41004), spanning from $605 \sim 685$ nm, we approximate the average absorption of the measured spectrum over the band window of our filter and find this average to be $a_{av} = 1226\ cm^{-1}$. This approximation is justified because spectrum of the illumination source, which is a tungsten halogen lamp, does not vary significantly as a function of wavelength, absorption within channels is weak ($< 20\%$), and dark current of camera is negligible compared to signal. Further discussion of these approximations can be found in Refs. [BFH+01; WRTP+12, Refs.]. In these conditions, applying Beer-Lambert's formula (Equation 3.2.4) to the whole image results in a height image (Figure 3-13 A, right column).

From these images, we determine the contour heights of the flow channels directly at the center of the valve (Figure 3-13 B). Qualitatively, the experimentally measured profiles are similar to the modeling results (dashed lines), although the profiles appear more rounded. It is expected that part of this rounding comes from the point spread function of the microscope. In accordance

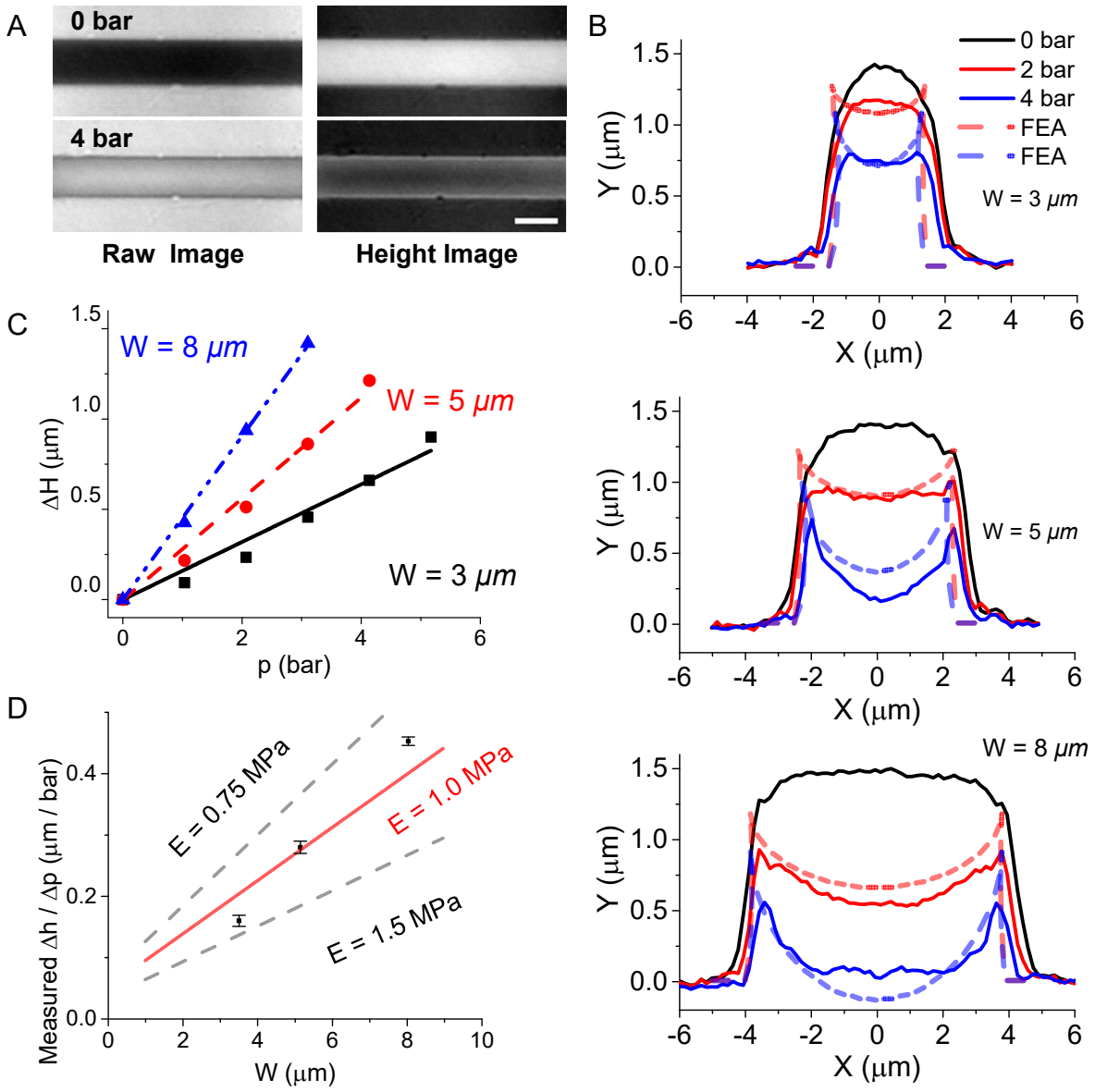


Figure 3-13 : Comparison of modeling and actual valve closure. (A) Left column: Brightfield diascopic images of a dye filled microvalve at pressures 0 bar and 4 bar. The microvalve consists of a 5 μm wide flow channel and 50 μm wide control channel. The flow layer has a thickness of 35 μm. Right column: The height image of the same valve. The brighter and darker colors correspond to the higher and lower regions, respectively. Scale bar is 5 μm. (B) The height profiles of 3, 5, and 8 μm wide flow lines at different applied pressures. The height profiles are determined from optical transmission measurements (see text). The dashed lines correspond to a model with Young modulus set to 1.0 MPa and a Poisson ratio of 0.49. (C) The displacement of flow channel ceiling at the center of the valves at different control channel pressures. The lines are linear fits to the experimental data. (D) The slopes of the linear fits from panel (C) vs the width of the flow channel. The solid line is from modeling using above mentioned parameters.

with modeling results, it is also noticeable that the width of the channels becomes smaller as the pressure in control channels increases. Although we did not model situations where the PDMS channel ceiling touches the glass bottom of the channel, this process can also studied in detail based on the measurements.

The optically measured flow channel heights of unpressurized valves ($1.40 \sim 1.49\ \mu m$) agree reasonably with the channel heights measured from the Si mold using a profilometer ($1.45\ \mu m$). The method thus allows quantitative measurements of channel profiles even without any height calibration needed. Further analysis of channel profiles show that the displacement of channel height at the center of the valve is approximately a linear function of the control channel pressure for all tested flow channel widths ($W = 3, 5, and 8\ \mu m$). This finding is in qualitative agreement with the modeling results [cf. Figure 3-12 C]. However, quantitative comparison of the slopes of these lines with values from the model show differences, which cannot be accounted for by possible variations in the elastic modulus of PDMS (Figure 3-13 D). We found the best agreement between the data and the calculations for a Young's modulus of 1 MPa. Understanding the discrepancy between the experiment and model will require further studies. Our current model treats PDMS as a simple elastic medium while in reality strain depends in a nonlinear way on the applied stress. Nonlinear stress–strain relation is particularly important in the center region of the flow channel ceiling where the strain is very large. More advanced software needs to be used to incorporate nonlinear effects in the calculation. To conclude, at the current stage our model provides good guidance in understanding the behavior of the valves. However, experimental verifications are still needed at a quantitative level. The absorbance based method that we have described in this section offers simple and convenient approach to improve the predictive power of modeling in the future.

3.2.5 Cell deformations using pressure actuated valves

In this section, we will first demonstrate a proof-of-principle operation of small pressure actuated valves in applying uniaxial stress to *E. coli* cells and then discuss optimal dimensions of the flow channel that can be used in future experiments. As an example, we will first follow a GFP-labeled *E. coli* cell in a 5 μm wide channel at different control channel pressures (Figure 3-14 A). Very large deformations to a bacterial cell can be applied in this channel. We find that the cell width, as determined from the fluorescent image, can broaden as much as 1.6 times (Figure 3-14 B) while

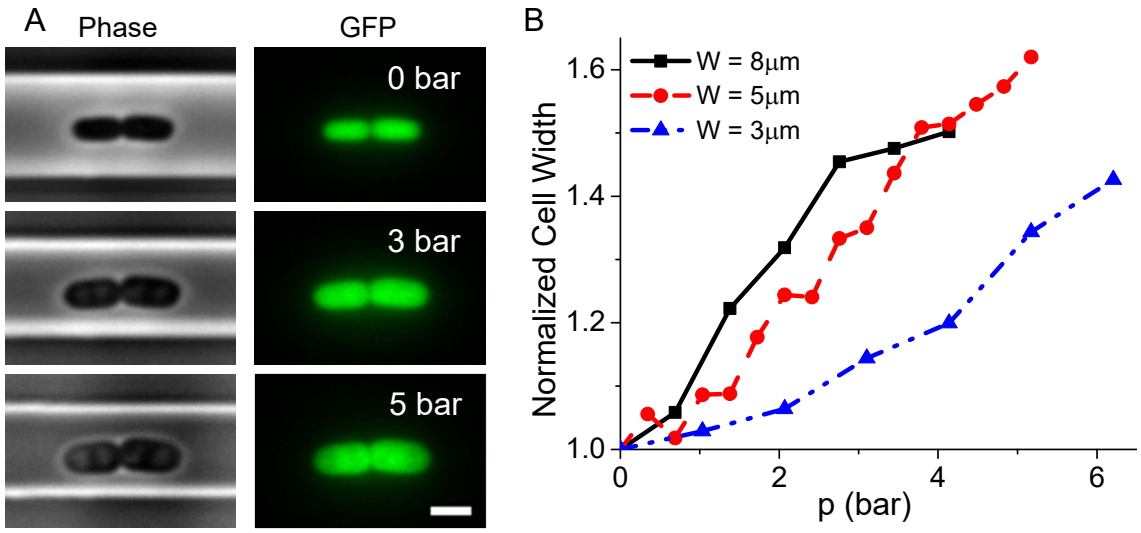


Figure 3-14 : Application of pressure actuated valves to study effects of uniaxial compression to *E. coli* cells. (A) An *E. coli* cell in a $W = 5\ \mu m$ channel at different control line pressures (values indicated on the left). The left column shows the phase image of the cell and the flow channel, and the right column the fluorescent image of a GFP-labeled cell. Note distinctly visible chromosomes in the phase image at pressures 3 and 5 bar. The scale bar is 2 μm. (B) The cell width as a function of control line pressure. The cell widths are normalized by the cell width at $p = 0$. Data for representative cells in three differently sized channels are shown.

the cell length increases by factor of about 1.25 at control line pressure of 5 bars. The larger increase in cell width compared to its length is expected because increase in length results only from cell wall stretching. At the same time, the width increase results both from stretching and bending of cylindrical cell wall. Furthermore, we expect that bending deformation accounts for a larger portion of the overall width increase than cell wall stretching because it is energetically less costly to bend a thin shell, such as is peptidoglycan cell wall, than to stretch it. It will require further studies that combine experiment and modeling to separate contributions from bending and stretching deformations to cell broadening. These studies can shed more light on the stress anisotropy and on the organization of the peptidoglycan strands in the *E. coli* cell wall.

For efficient use of pressure actuated valves in squeezing cells, it is important to establish optimal dimensions of the flow channel that allow to achieve maximum range of cell deformations. For that purpose we compare cell squeezing in $3 and 8\ \mu m$ wide flow channels to that of $5\ \mu m$ wide channels. As can be seen from Figure 3-14 B, broadening of cell contours in $3\ \mu m$ wide flow channels is significantly smaller than in $5\ \mu m$ channel. Very high pressures (> 6 bar) need to be applied to significantly deform a bacterial cell. In practice, our measurement setup starts to leak at pressures higher than 6 bar. We therefore consider $3\ \mu m$ channels too small for further studies. Closing $8\ \mu m$ wide channels, as expected, requires lower control line pressures than needed for $5\ \mu m$ wide channels yet the maximum broadening of the cell is smaller in this channel when compared to the $5\ \mu m$ one (Figure 3-14 B). The reason for smaller broadening is that for pressures exceeding about 2.5 bars the ceiling of the flow channel makes contact with the glass bottom of the channel. In this situation, the bacterium underneath the valve becomes encased in PDMS. The $8\ \mu m$ channels allow thus to explore smaller range of cell deformations than do the $5\ \mu m$ channels. Therefore, flow channel widths of about $5\ \mu m$ appear to be optimal for studies of bacterial deformations.

3.2.6 Remarks

Mechanical properties of bacterial cells are a poorly understood area of microbiology even though these properties play a key role in bacterial survival in many environmental conditions. Moreover, many known antibiotics (beta-lactams) affect mechanical integrity of bacterial cells. Small pressure actuated microvalves enable to study the effects of uniaxial stress on bacterial cells over a wide range of stress values. The mechanical properties that can be studied by this approach include

stress anisotropy in the cell wall, maximum breaking strain, and localization of weak spots in the cell wall. The devices we have developed are able to deform bacterial cells while maintaining physiological conditions for cell growth and to allow imaging of cells at subcellular resolution. However, some issues remain to be solved to use these devices in a high throughput manner. These issues stem from the ability to position and retain bacterial cells under the center of the valve. Instead of being trapped under the center of the valve, the bacteria frequently load adjacent to the lateral sidewalls of the flow channel. In this case, the deformation of the cell is not uniaxial and the range of deformations that can be achieved is much lower. The rectangular flow channel profiles are also problematic because the channel ceiling acquires a convex shape upon closure and this shape forces the cells toward the channel edges. The force is zero when the cell is at the center of the flow channel but increases with the distance from the center. At some distance from the center, the force overcomes the friction between the cell and channel and causes movement of the cell to the edges of the flow channel. This problem is alleviated in wider flow channels, but then, the encasement of cells becomes an issue. Alternatively, one can build shallow pockets or recessions in the center of the valve, which would prevent cells from shifting in lateral directions. Further improvements in the valve design that increase measurement throughput are thus clearly feasible.

Overall, we have characterized a microfluidic platform based on miniature pressure actuated valves that enables to study uniaxial compression of bacterial cells in a high resolution optical microscope. We used an absorption based method to determine channel height profiles during closure of the valve and showed that this simple quantitative technique is applicable to channels down to 1 μm height and of 3 μm width. The comparison of channel height measurements with finite element modeling showed qualitative agreement. To achieve full quantitative agreement, more sophisticated models are needed that possibly account for stress dependent strain at higher stress values.

We showed at a proof-of-principle level that very large deformations of bacterial cells can be achieved using these pressure actuated valves. We found that the largest deformations can be achieved in 5 μm wide flow channels where we observed increase in bacterial widths more than 1.6 times. Narrower flow channels, in agreement with modeling results, required too high closing pressures to be practically usable while in wider channels the PDMS ceiling encased the cells. The encasement prevented further deformations and cut off cells from their growth medium. The

platform presents a very promising approach to study the mechanical properties of bacterial cells and their subcellular organization. Further work remains to be done to improve the loading of bacterial cells under the valve and to prevent them from shifting during pressure application.

3.3 Development and Testing of Microanvils

To combat the draw backs of our device described in Section 3.2, we further extended the microvalve platform by redesigning valve shape. We have achieved artificial cell division with this device and quantitatively studied *E. coli* nucleoid compaction with this platform.

3.3.1 Design of the Microanvil Devices

The new type of valve, which we referred to as the microanvil, has a small anvil-like protrusion on the ceiling of the valve (Figure 3-15). Externally applied pressure deflects the anvil downward and squeezes about a 2 μm long portion of the underlying cell. We aimed to use this device to apply uniaxial stress along the cell axis and measure the cytoplasmic and nucleoid responses.

3.3.2 Stress Analyses of the Microanvils

The si wafer mold of the flow layer of the microanvil platform had the tallest features shorter than 6 μm, such that we could fabricate thinner flow layer PDMS elastomer ($\sim$11 μm) In this device, we broadened parts of the flow channels (forming pockets), such that less pressure was needed to deform the elastomer. The narrower portion of the flow channel could hold the cell close to the mid portion of the anvil. Moreover, by adding an anvil, which was not connected to the side walls in the pocket, the bottom tip of the anvil would be under tension just before coming into contact with the underlying cell. This was verified with finite element modeling Figure 3-16 A. The modeling also showed that the cell would tend to bend away from the glass slit at lower control pressures, but at higher pressures the ceiling of the flow channel would come into contact with the cell and hug it back to the glass Figure 3-16 B. This modification overcomes some of the drawbacks we had before, e.g., the ceiling of the flow channel tended to enclose the bacterium when undergoing mechanical deformations.

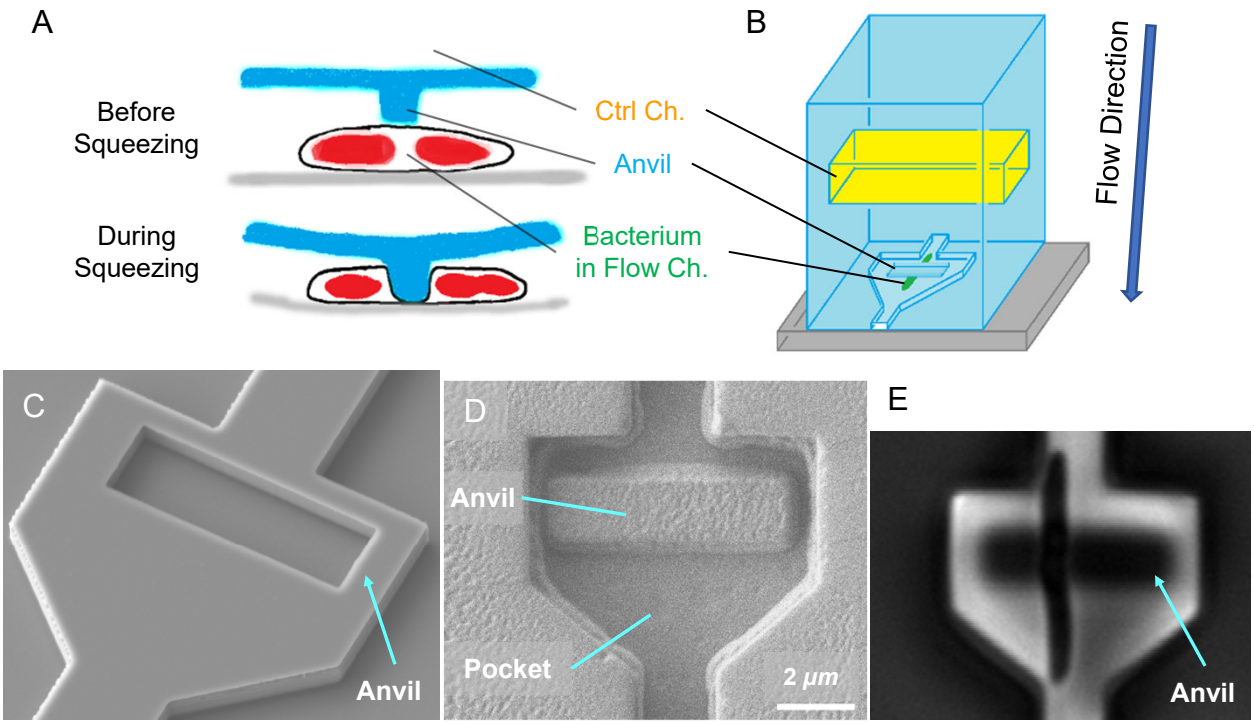


Figure 3-15 : Design of the microanvil device. (A) The scheme of an experiment using a microanvil device. The cell envelopes are shown as black lines. The nucleoids are shown in red. The glass slides are shown in gray, and the PDMS flow channel ceilings are shown in cyan. The top half of this panel illustrates the flow channel ceiling almost in contact with the cell envelope, and the bottom half of this panel illustrates when the pressure in the control channel is high enough, such that the cell envelope forms two compartments. (B) An illustration of a bacterium in a flow channel. The bacterium is placed under the microanvil. The gray part represents a microscope cover slip, blue PDMS, green a bacterium, and yellow the control channel filled with liquid. (C) A scanning electron microscope (SEM) image of the flow channel wafer mold of the microanvil. For this particular wafer, the anvil was misaligned relative to the pocket, due to the lacking of the chip alignment step and there was a stage drift in the EBL system (See Section 2.5). (D) A SEM image of a pocket in the PDMS flow channel. The surface of PDMS elastomer is coated with 30 nm thick Chromium. (E) A phase contrast optical image of an assembled microanvil that trapped an filamentous cell. Panel A and B are not to scale. The widths of the anvil is 2 μm in Panel C-E.

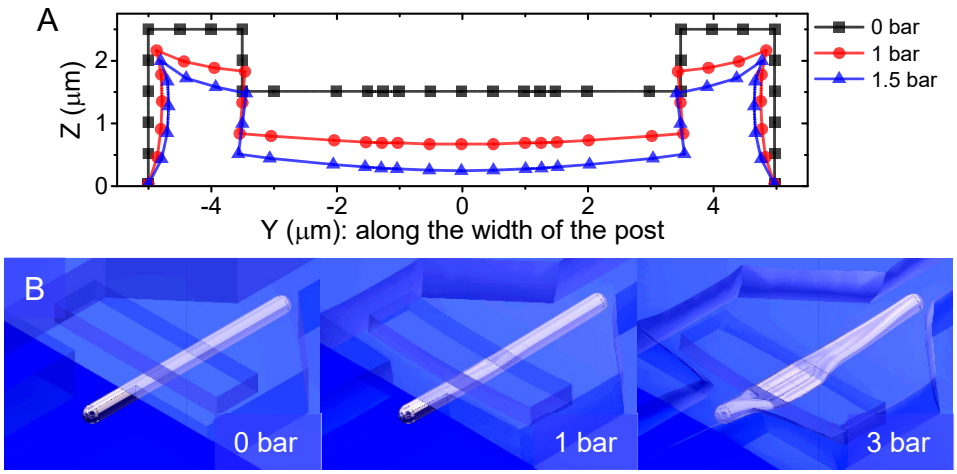


Figure 3-16 : Stress analyses of the microanvils. (A) Cross-sectional profiles of a microanvil. The cross section was picked along the lateral center line of the anvil. The width of the bottom tip of the anvil increases with the control pressure. (B) Isometric view of modeling the closure of microanvil in presence of an underlying cell.

3.3.3 Cellular Response to the Microanvils

We have characterized the cellular response to squeezing by the anvil. By applying pressure to the control channel, cellular water was pushed out from bacterial cells, while ions and small metabolite molecules could leave the cell. To demonstrate this, we studied the response to squeezing by cells with a cytoplasmic protein reporter (tagRFP-T, $\sim 4\ nm$ in diameter) and supply a florescent glucose (2-NBDG, subnanometer in diameter) in its growth media. We observed that the total cytoplasmic protein reporter intensity was not disturbed, while the signal from the small molecules was dissipated (Figure 3-17 A, B). Meanwhile, by gradually increasing then decreasing the control pressure, we characterized the cellular response to the anvil at various control pressure (Figure 3-17 C). As the control pressure increased and decreased, we noticed that the end to end cell lengths followed the rise-and-fall of the control pressure but this change was only a small fraction of cell length. At the same time, cytoplasmic cell width change was minimal and the cytoplasmic volume of the cell decreased in the squeezed region. These results indicate that pressure in the cell is maintained essentially constant while water is pressed out from the cell. Moreover, we quantified the normalized crowder concentration indicated by cytoplasmic protein reporter intensity and the normalized cell height at anvil (Figure 3-17 E). These quantities followed nearly linearly to the

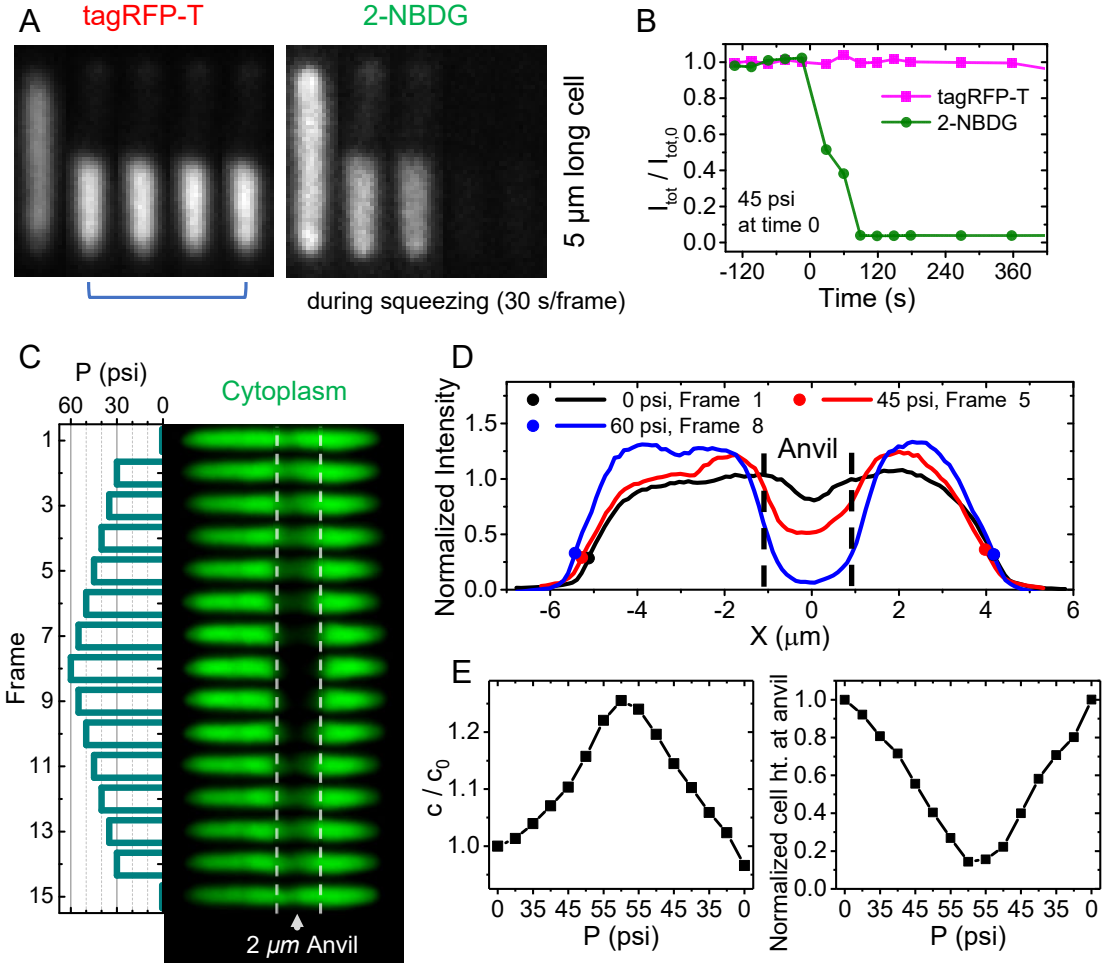


Figure 3-17 : Cellular response to the microanvil. (A) Florescent images of a squeezed cell in two cytoplasmic reporters. (B) Total intensities of from the same reporters shown in (A) as functions of time. (C) Response of an filamentous *E. coli* cell to a pressure cycle. Left panel: Change of externally applied pressure during the measurements. In the first and the last frame, the cell is not squeezed. Right panel: images of cytoplasmic reporter during this pressure cycle. The region between dashed lines correspond to the portion of the cell where the anvil touches it. (D) Intensity traces of cytosolic mNeonGreen label along the cell axis at three different control pressure in a squeezing measurement. Traces correspond to the cell shown in Panel (C). (E) Normalized minimal intensity at the cell center at different pressures applied to the valve. All intensities are normalized by the intensity at the beginning of the measurements. Strain shown in (A) is JM97. Strain shown in (C) is DY3 (See Table 2-1).

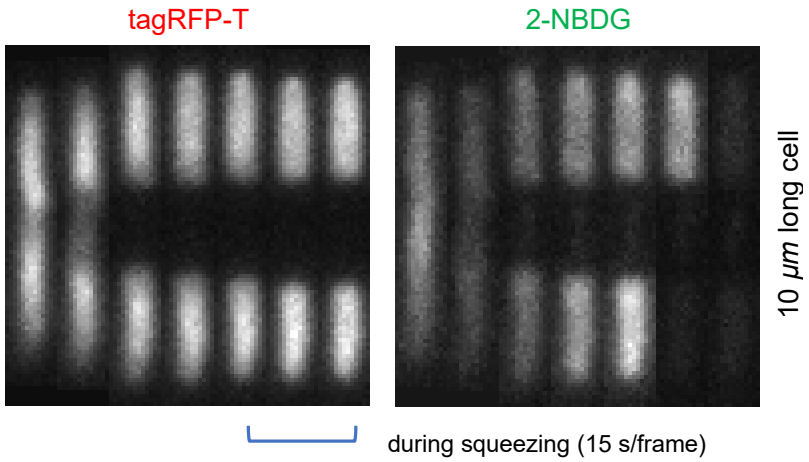


Figure 3-18 : Artificial cell division. Florescent images of a squeezed cell in two cytoplasmic reporters. Strain shown is JM97 (See Table 2-1).

applied control pressure; nevertheless, the correlations varied from valve to valve. There for we use the normalized crowder concentration as the metric for the measurements discussed in Chapter 4.

Furthermore, the anvil allowed us to artificially divide the cytoplasm of filamentous *E. coli* cells into two chambers. In the squeezing experiment shown in Figure 3-18, we observed the signal of the subnanometer cytoplasmic reporter on one side of the anvil dissipated first, while the signal on the other side of the anvil was persistent. Diffusion would have allowed some reporter to move to the side without signal, if those to compartment was not segregated. To the best of our knowledge, this was the first time any cell has been artificially divided into two compartments.

3.3.4 Compression of Nucleoids by Microvalves

We studied the nucleoids responding to squeezing. The an *E. coli* strain had an mCherry labeled *hupA* gene, and YPet labeled *matP* gene, which and is transformed with a plasmid containing an IPTG inducible *sulA* gene, JMAH9 (See Table 2-1). With this strain we could observe the responses to squeezing by a nucleoid with an idea of its stage in replication (Figure 3-19).

The lengths of nucleoids were reduced while the cell was being squeezed. This reduction did not depend strongly on the distance of nucleoid from the post. The lengths of the gaps, despite the variations of modulation, are distributed within a small range. Moreover, the nucleoid gaps persist while the cell is being squeezed. We noticed separated nucleoids would not mix or even

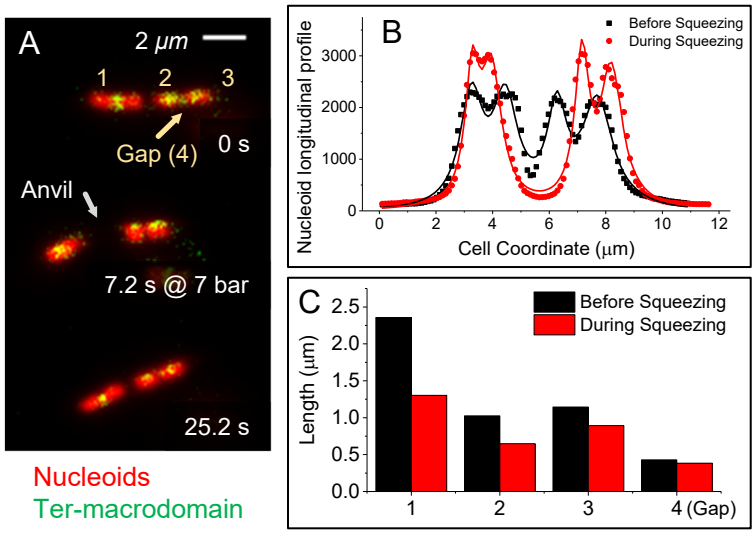


Figure 3-19 : Nucleoids response to the microanvil. (A) The fluorescent images of a filamentous cell, with a nucleoid label and Ter-macrodomain label. From top to bottom are images before, during, and after squeezing. (B) The longitudinal profile of the nucleoid signal. (C) The lengths of nucleoids and a inter-nucleoid gap before and during squeezing.

come into contact with each other when pushed toward each other. This observation has led us to start fully appreciating the role of macromolecular crowding in compacting the *E. coli* nucleoid. We carried on this study with *E. coli* strains with both a cytoplasmic reporter and a nucleoid reporter (See Chapter 4).

Note, in Figure 3-19 A, the gap in the left half of the cell has not matured, since the Ter-region has not separated. The lengths of chromosomes are reduced while the cell is being squeezed.

Chapter 4

Macromolecular Crowding Compacts *Escherichia coli* Chromosomes into Nucleoids

4.1 Motivations

To date, quantitative experimental studies to understand DNA compaction by macromolecular crowding have been carried out *in vitro*, using purified DNA [ZSvKvdM09; JvdMD11] or DNA liberated from cells [CWO01; PHH+12]. In these studies, charge-neutral polymers, dextran or polyethylene glycol (PEG), have been used as crowding agents to mimic the cytoplasmic environment even though most cytoplasmic crowders do not have a neutral charge. All these experiments agree that crowding can lead to significant compaction of the DNA. However, those experiment results were in disagreement on whether the compaction occurs gradually via a second order transition as the concentration of crowding agents increases [CWO01] or it is an abrupt first order transition involving a metastable state [PHH+12].

Thus far, there are no quantitative experimental studies on how osmolality and associated changes in macromolecular crowding affect nucleoid size in living bacteria. At a qualitative level, it is known that hyperosmotic shock leads to the compaction of nucleoids [WSK+19; CGJ+13]. Here we carry out microfluidic experiments to quantitatively study the role of molecular crowders in the compaction of the *E. coli* nucleoid i) by rapidly changing the osmolality of the growth media for

steady-state growing bacteria in the mother machine device, and ii) by squeezing individual cells in a device specially designed for such measurements. We show that *in vivo E. coli* nucleoids respond to the osmolality continuously. Close to physiological crowder concentrations, the nucleoid length and width change linearly. As the crowder concentration exceeds the physiological level by 30% the compressibility significantly decreases. Also, our data show that the compressibility is strongly anisotropic being higher along the long axes of the cell and it is independent of growth conditions (slow and moderately fast growth). The latter finding indicates that the overall crowding level rather than the exact composition of crowders controls the compaction in these growth conditions. Furthermore, our results indicate that poly-ribosomes are the dominant crowder species in fast growth conditions while the soluble cytosolic proteins are dominant in slow growth conditions.

4.2 Compaction of the Nucleoid under Osmotic Shock Is Anisotropic and Larger than Compaction of the Cytoplasm

Our first goal is to find a quantitative relationship between crowder concentrations/volume fractions and sizes of the nucleoids. Since altering the amount of crowders in a cell is not practically possible because all macromolecules are potential crowders, one has to rely on changing the volume of a cell instead. One possibility to vary the cytoplasmic volume, and thereby alter the crowder concentration, is to change the osmolality of the growth media. By increasing the external osmolality, cytoplasmic water leaves the cell and intracellular crowder concentration increases, while the decrease in osmolality leads to the opposite result. To vary the external osmolality and observe cellular changes in real time, we image bacteria in microfluidic mother-machine devices [WRP+10; YJB+18], which allowed us to quickly change media without c cell imaging (Figure 4-1, Supplementary Movies M4-1, M4-2). To induce osmotic shock, we changed the concentration of NaCl in a chemically defined growth medium. To quantify the changes in both cytoplasmic and nucleoid sizes, the cells carried the tagRFP-T and HupA-mNeonGreen labels (Table 2-1). The former label diffusively fills the cytoplasm while the latter binds non-specifically to DNA [WWRY01]. To understand how different macromolecular crowders affect DNA compaction, we studied cells in slow and moderately fast growth conditions. The doubling times in these two conditions at 28℃are $Td = 226 \pm 103$ min. and $Td = 95 \pm 24$ min., respectively (Table 4-1).

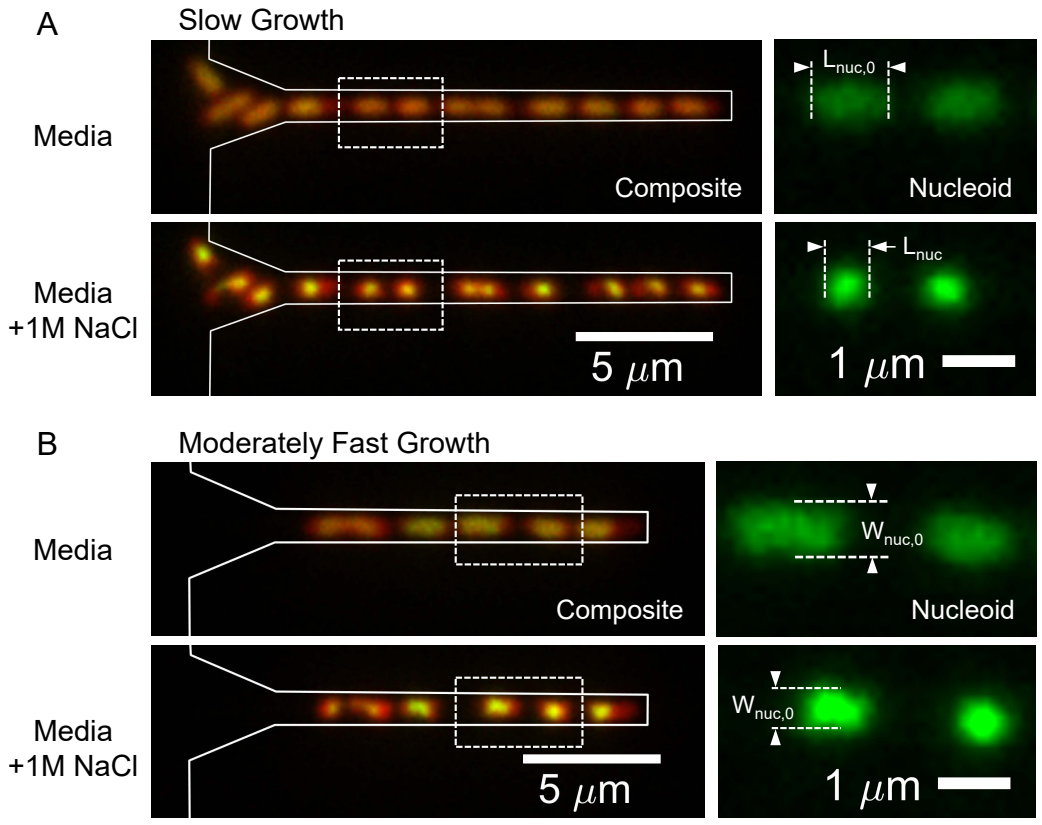


Figure 4-1 : Compaction of the cytoplasm and nucleoid by hyperosmotic shocks. (A) Left: Images of *E. coli* cells growing in mother machine channels before (top) and 1 min. after osmotic shock (bottom). The images are composites of fluorescence images of nucleoid (green) and cytoplasm (red). Channel contours, which are determined from phase images, are indicated by solid white lines. Right: Nucleoid images for the two cells indicated by a dashed box in the left image. The cells were grown in slow growth conditions in M9 glycerol medium. (B) The same strain in moderately fast growth conditions (in M9 glucose + CAS medium).

Table 4-1 : The average cytoplasm and nucleoid dimensions during unperturbed growth, and doubling times in mother machine channels ($T_{d,\,\mathrm{MM}}$) and in liquid culture tubes ($T_{d,\,\mathrm{liquid}}$). $T_{d,\,\mathrm{liquid}}$ was determined based on OD_{600} measurements from four replicas. The values correspond to the averages over the analyzed cells. These cells are all at the early stages of cell cycle ($0 \sim 0.25\, T_d$). Numbers in parenthesis indicate standard deviations.

Cytoplasm	$L_{\mathrm{cyto},\,0}$ (μm)	$W_{\mathrm{cyto},\,0}$ (μm)	$V_{\mathrm{cyto},\,0}$ (μm^3)	Aspect Ratio$_0$	$T_{d,\,\mathrm{MM}}$ (min.)	$T_{d,\,\mathrm{liquid}}$ (min)
M9 + Gly	1.97(35)	0.589(27)	0.482(100)	3.35(64)	226(103)	223(5)
M9 + Glu + CAS	2.12(29)	0.680(21)	0.688(121)	3.12(43)	95(24)	85.7(9)
Nucleoids	$L_{\mathrm{nuc},\,0}$ (μm)	$W_{\mathrm{nuc},\,0}$ (μm)	$V_{\mathrm{nuc},\,0}$ (μm^3)	Aspect Ratio$_0$	$V_{\mathrm{nuc},\,0}/V_{\mathrm{cyto},\,0}$	
M9 + Gly	1.24(35)	0.528(22)	0.233(84)	2.35(66)	0.48(12)	
M9 + Glu + CAS	1.27(28)	0.615(23)	0.317(90)	2.06(46)	0.46(8)	

We excluded fast growth because a much more complicated DNA topology and nucleoid shape in these conditions would have made the interpretation of the results ambiguous. From slow to moderately fast growth, one would expect the ribosome protein ratio in the cells to increase by $1.5 \sim 2.0$ times [BD08; EBD13; DZW$^+$17] allowing differentiation of the effects arising from stable RNA and protein based crowders on the compaction of the nucleoid.

To quantify changes in nucleoid and cell sizes at different crowding levels, we analyzed cells in the early stages of the cell cycle when their nucleoid has an ellipsoidal shape. In the studied growth conditions, such morphology appears in nucleoids that are less than half replicated while in later stages of replication, the nucleoids obtain a characteristic bilobed shape [BK05; MCY$^+$16]. We limit our study to single-lobed nucleoids because these can be easily characterized by their length and width measured along the long and short axes of the cell, respectively. We followed changes in these two parameters along with changes in cytoplasmic sizes in both hypo- and hyper-osmotic conditions. However, changes in cytoplasmic volume were essentially negligible even for the most hypoosmotic shock possible when the regular growth medium was replaced by deionized water ($0\ Osm$). Thus, almost all of our studies cover hyperosmotic conditions.

As expected, the change in external osmolality by NaCl leads to rapid changes in cell volume and nucleoid size for both growth conditions (Figure 4-2). These changes occurred during a one-minute period. The rapid changes in cell shape observed here are consistent with earlier

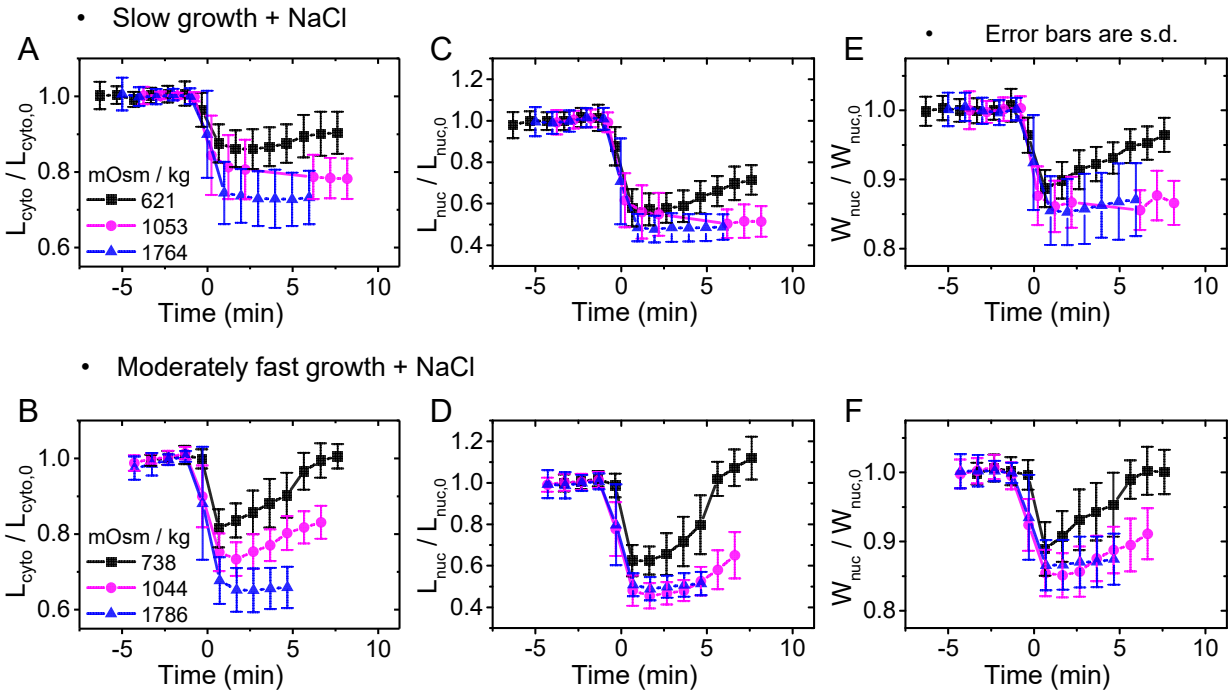


Figure 4-2 : Kinetics of the cytoplasm and nucleoid compaction during hyperosmotic shocks. (A, B) Relative changes of lengths of the cytoplasm for three hyperosmotic shocks in slow and moderately fast growth conditions, respectively. The shock magnitudes are indicated in the lower left. $L_{\mathrm{cyto},0}$ is the cytoplasmic length right before the shock. The same for nucleoid length (C, D) and width (E, F). Error bars correspond to standard deviations. The number of cells analyzed in each measurement is reported in Table 4-2.

Table 4-2 : List of mother-machine measurements. Columns from left to right: growth conditions, agent and concentration for osmotic and antibiotic treatment, osmolality prior the measurement, osmolality during the measurement, and number of cells analyzed in each measurement (N).

Regular Media	Treatment	Regular Media Osmolality ($mOsm/kg$)	Treatment Media Osmolality ($mOsm/kg$)	N
M9 + Gly	Water	244	3	46
M9 + Gly	0.1 M NaCl	239	397	45
M9 + Gly	0.3 M NaCl	239	737	42
M9 + Gly	0.4 M NaCl	239	860	46
M9 + Gly	0.5 M NaCl	239	1137	47
M9 + Gly	0.55 M NaCl	239	1185	16
M9 + Gly	0.6 M NaCl	241	1294	47
M9 + Gly	0.8 M NaCl	252	1633	44
M9 + Gly	1.0 M NaCl	252	2016	46
M9 + Gly	Rifampicin	–	–	20
M9 + Gly	Rif. + 0.1 M NaCl	244	411	19
M9 + Gly	Rif. + 0.2 M NaCl	251	601	21
M9 + Gly	Rif. + 0.4 M NaCl	251	930	25
M9 + Gly	Rif. + 0.6 M NaCl	251	1290	20
M9 + Glu + CAS	Water	238	3	22
M9 + Glu + CAS	0.1 M NaCl	240	423	23
M9 + Glu + CAS	0.2 M NaCl	231	628	43
M9 + Glu + CAS	0.4 M NaCl	242	981	43
M9 + Glu + CAS	0.5 M NaCl	228	1142	36
M9 + Glu + CAS	0.6 M NaCl	242	1286	42
M9 + Glu + CAS	0.8 M NaCl	235	1657	44
M9 + Glu + CAS	1.0 M NaCl	233	2019	48
M9 + Glu + CAS	Rifampicin	244	–	11
M9 + Glu + CAS	Rif. + 0.2 M NaCl	239	609	21
M9 + Glu + CAS	Rif. + 0.4 M NaCl	245	964	22
M9 + Glu + CAS	Rif. + 0.6 M NaCl	245	1285	19
M9 + Glu + CAS	Rif. + 1.0 M NaCl	224	2009	22

Table 4-3 : Slopes of linear fittings shown in Figure 4-3 and 4-5 in kg/Osm.

Series of experiments	Measurement	Fitted slopes		Ratio of slopes
		Cytoplasm	Nucleoids	
M9 + Gly + NaCl	Length	-0.20(6)	-0.53(8)	2.7(9)
	Width	-0.01(2)	-0.14(3)	9.9(139)
	Volume	-0.24(7)	-0.72(7)	3.0(9)
	Aspect Ratio	-0.19(7)	-0.44(9)	2.3(10)
M9 + Glu + CAS + NaCl	Length	-0.27(6)	-0.52(8)	1.9(5)
	Width	-0.02(2)	-0.13(4)	6.1(71)
	Volume	-0.35(8)	-0.71(7)	2.0(5)
	Aspect Ratio	-0.26(7)	-0.44(9)	1.7(6)

reports [PS13; RTH14]. Interestingly, the changes in nucleoid dimensions followed the same time-dependence as changes in cell dimensions. However, dimensions of the nucleoid changed to a larger extent than the overall dimensions of the cell, as will be detailed later. Although the focus of this study is not on recovery processes, in milder osmotic shocks (less than about 0.7 Osm/kg), the recovery of the cells is visible within 5 minutes after the shock. In these mild shocks, recovery of cell shape and nucleoid shape followed the same time-dependence, which is consistent with the idea that crowding is responsible for the nucleoid compaction.

In some cells, the hyperosmotic treatment resulted in plasmolysis. The majority of these cases showed detachment of the plasma membrane from the cell wall at the cell poles; detachments from the cylindrical parts of the cell body were less frequent, which has also been reported by others [PS13]. In cells that plasmolyzed from their sidewalls, the cell width is poorly defined. Moreover, in such cells, nucleoids become irregularly shaped. For these reasons, we excluded side-wall-plasmolyzed cells from further analyses. We found that in both moderately fast and slow growth conditions, the increase in external osmolality leads to an approximately linear decrease in cell length for osmotic shocks although above 1.2 Osm/kg the decrease slowed (Figure 4-3 A, B).

Similar to cell length, the nucleoid length also decreased linearly with the osmolality change for smaller osmotic shocks ($< 0.9\ Osm/kg$). At the same time, the relative changes in nucleoid length were about 2.5 times as large as the relative changes in cell length (Table 4-3). At above about 0.9 Osm/kg the change of nucleoid length ceased. Nucleoid width behaved qualitatively similar to nucleoid length while the cytoplasmic width did not show significant changes throughout the range of osmolalities studied (Figure 4-3 C, D). To rule out that the plateauing of nucleoid dimensions

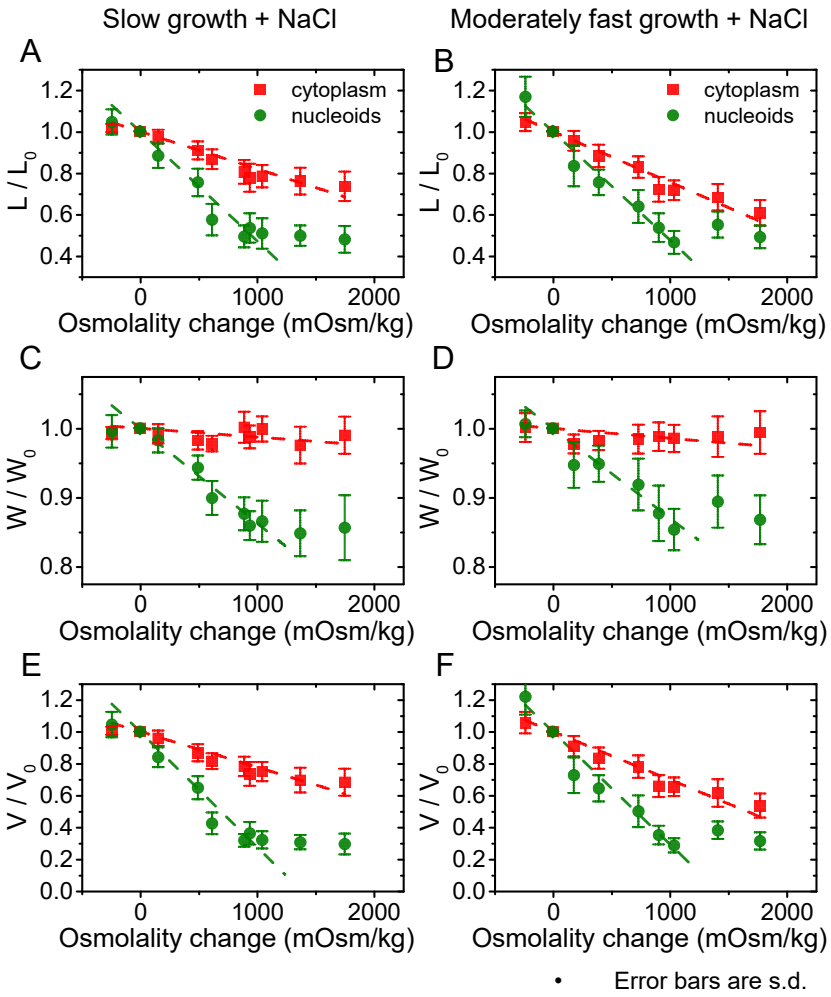


Figure 4-3 : Change in nucleoid dimensions as a function of the change in external osmolality. (A, B) Relative change of nucleoid (green circles) and cytoplasmic (red squares) lengths at different osmotic shock in slow and moderately fast growth conditions, respectively. Each osmolality value corresponds to a separate measurement. Error bars correspond to standard deviations. Dashed lines are linear fits to the experimental data in the range $-0.25 \sim 1.25\ Osm/kg$. The best fit parameters are listed in Table 4-3. The same for nucleoid and cell widths (C, D) and calculated volumes (E, F) in these two growth conditions.

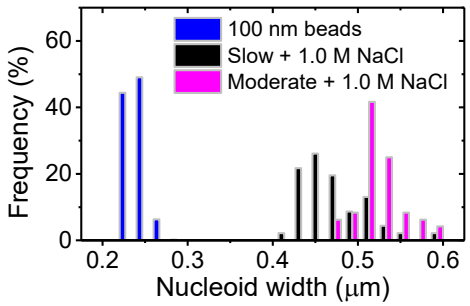


Figure 4-4 : Comparison of nucleoid widths in slow (black bar, $N = 46$) and moderately fast (magenta bar, $N = 43$) growth conditions during 1 M NaCl shock to the widths of 100 nm fluorescent beads (blue bar, $N = 491$). 1 M NaCl corresponds to an osmolality of about 2 Osm/kg (the highest concentration used in the measurements). The beads were from Life Technologies TetraSpeck Fluorescent Microspheres Sampler Kit. These beads were imaged with the same filter set and analyzed using the same analysis program as the nucleoids. The measured widths of beads correspond approximately to the width of the point spread function of the microscope. The latter width is about two times smaller than the width of the nucleoid in the most compressed conditions for the nucleoid.

at higher osmolalities is caused by the point-spread- function of the microscope, we measured the diameters of 100 nm fluorescent beads for comparison. The measured diameters of the beads were, by more than a factor of two, smaller than the smallest measured nucleoid dimension at the highest osmotic shock (Figure 4-4). Thus, these measurements confirmed that the measured dimensions reflect the intrinsic size of the nucleoid in the plateau region. The presence of a plateau region shows that, *in vivo*, the nucleoid undergoes a transition from a linear high compressibility regime to a non-linear low compressibility regime upon compaction.

A comparison of nucleoid width and length curves showed strongly anisotropic compaction. The changes in nucleoid width at smaller osmolality changes (< 0.9 Osm/kg) was by a factor of 3.7 smaller than the corresponding change in the nucleoid length. The anisotropy was also present in the plateau region where the nucleoid length was compressed to 50%, while its width only compressed to 70% of its original size. The nucleoid volume calculated based on these values decreased to 30% of its original size (Figure 4-3 E, F). The anisotropic compaction leads to a spherical nucleoid having an aspect ratio of one at osmolalities of about 0.9 Osm/kg and above (Figure 4-5). The spherical shape indicates the underlying isotropic organization of the nucleoid in the compacted state. Since our measurement time-scale is 1 minute, this conclusion furthermore implies that

the native uncompressed nucleoid should also have globally isotropic organization because global rearrangement from anisotropic to isotropic is unlikely to occur during this timescale.

4.3 Nucleoid Compaction Is a Second Order Phase Transition and Independent of Growth Conditions

To relate changes in osmolality to the changes in crowding of the cytoplasmic environment, we calculated the ratio of crowder concentration immediately after the osmotic shock, c, relative to that during regular growth conditions, c_0. This concentration ratio, c/c_0, applies to any cytoplasmic molecular species whose diffusion across the plasma membrane during osmotic shock can be neglected. It includes not only macromolecular crowders but also all small molecules and ions. For all these molecules the relative concentration change, c/c_0, equals the inverse of their relative cytoplasmic volume change, $V_{\mathrm{cyto},\,0}/V_{\mathrm{cyto}}$. However, instead of using cytoplasmic volumes to calculate the latter, we determined the relative concentration of cytoplasmic tagRFP-T proteins before and after the salt treatment (for details see Section 2.2.3.4), and used this value for c/c_0. We chose this approach because even though we only analyzed cells that did not show apparent plasmolysis from their lateral cell walls, we could have overlooked some plasmolyzed regions during a visual inspection of the images. Overall, the two methods yielded comparable results at smaller osmotic shocks but deviated marginally from each other at larger ones (Figure 4-6).

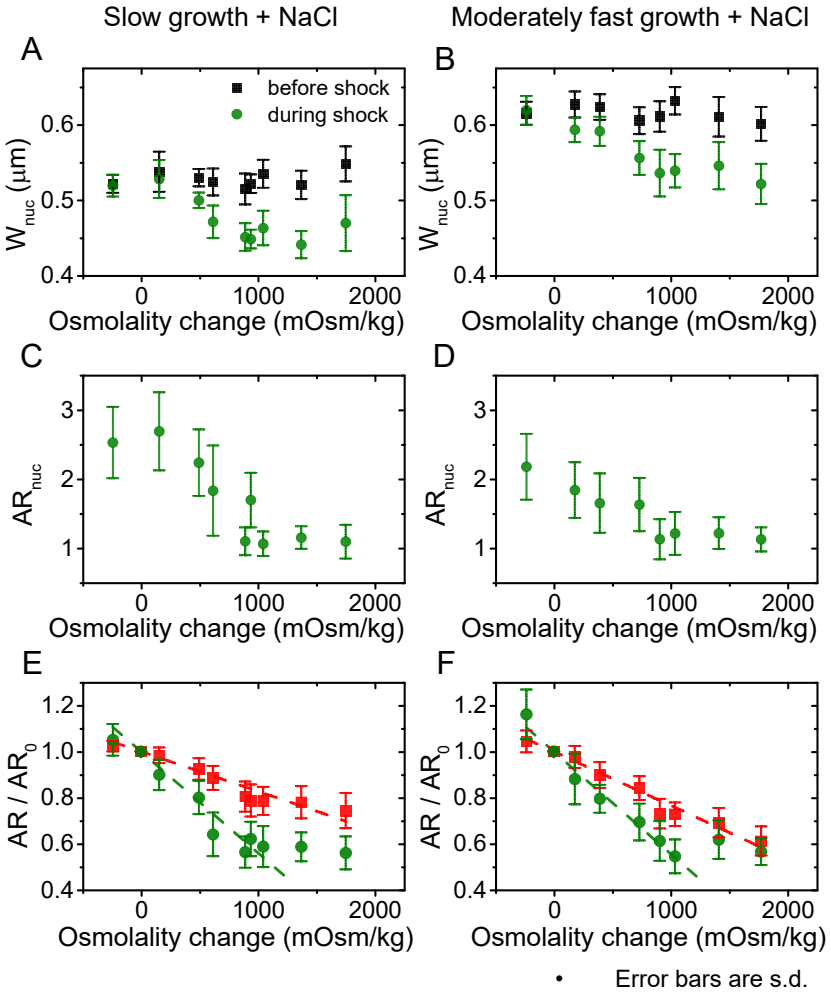


Figure 4-5 : Measured widths and aspect ratios of nucleoids. (A) Nucleoid widths before (black) and about 1 min. after an osmotic shock (red) in slow growth conditions. Shown are unscaled widths in μm. In Figure 4-3, nucleoid widths are scaled by nucleoid widths before the shock. (B) The same in moderately fast growth conditions. (C) The aspect ratio of nucleoids during different osmotic shocks. The aspect ratio is defined as $L_{\mathrm{nuc}}/W_{\mathrm{nuc}}$. (D) The same in moderately fast growth conditions. (E) Aspect ratios of nucleoids (green circles) and cytoplasm (red squares) right after osmotic shock relative to that prior the shock as a function of osmolality during the shock in slow growth conditions. (F) The same in moderately fast growth conditions. All error bars correspond to standard divisions.

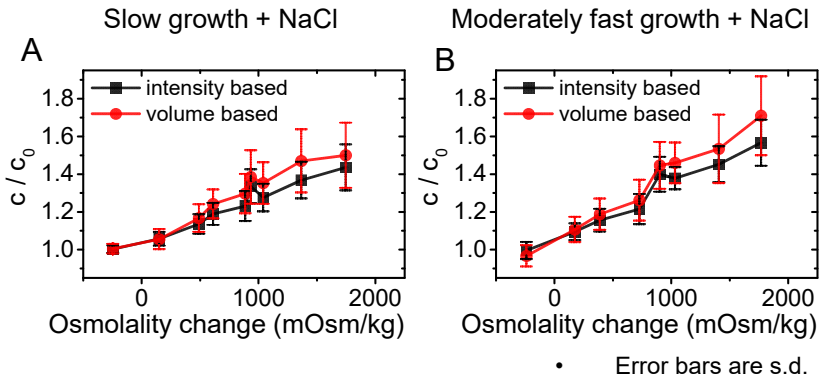


Figure 4-6 : Comparison of cellular crowder concentrations determined using two different methods (Part I). The crowder concentration during osmotic shock, c, is determined relative to the concentration that cell maintains at regular growth medium, c_0. In intensity based method cytoplasmic tagRFP-T intensity is used as a proxy for the relative change of crowder concentration. The method is in further details described in Section 2.2: Determination of crowder concentration based on intensity of fluorescent reporter. In volume based method, the ratio c/c_0 is taken equal to $V_{\mathrm{cyto},0}/V_{\mathrm{cyto}}$. The cytoplasmic volume, V_{cyto}, is calculated based on the measured length and width of the cytoplasmic region assuming that this volume is a spherocylinder. (A, B) Relative crowder concentrations as a function of external osmolality change. Black curves correspond to data reported in previous figures in this chapter. Error bars correspond to standard divisions.

Hence, we pool all our data gathered from the same growth condition and make scatter plots of the relative changes of nucleoid dimensions against the relative changes of crowder concentration (Figure 4-7 left column). To extract of the principle curve, we average the raw data binned along the x-axis (Figure 4-7 right column). Our data show that the length, width, and volume of the nucleoid decreased, initially, linearly as the crowder concentrations increased (Figure 4-8). Again, we compare the results from determining c/c_0 using those two aforementioned methods (Figure 4-9). The linear relationship corresponds to a constant compressibility of the nucleoid by the crowders. Here the compressibility, κ, is defined as the relative change in volume upon the change in osmotic pressure, ΔP, by $\kappa = -\left(\Delta V_{nuc}/V_{nuc}\right)/\Delta P$. In the lowest order approximation $P \sim c$, and in this case, κ is proportional to $-\Delta V_{\mathrm{nuc}}/\Delta\left(c/c_0\right)$. The latter corresponds to the slope of the curves in Figure 2I. Once the crowding level exceeded about 30% of the level in normal growth conditions, the compressibility decreased sharply. The transition to the low compressibility regime was smooth unlike in several previous *in vitro* studies [PHH+12; KVM+10; YHMY10]. There was no sign of co-existence of collapsed and extended DNA conformations during a visual inspection of the nucleoid

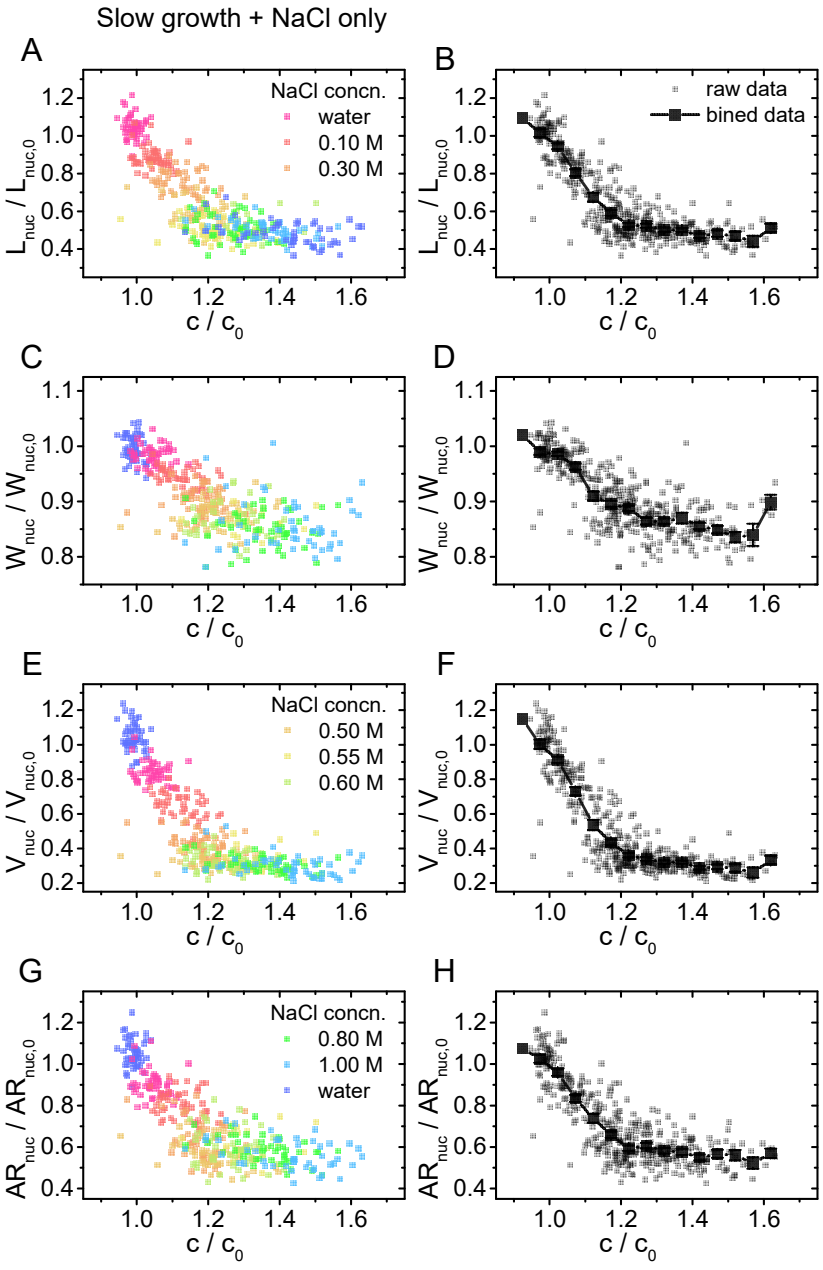


Figure 4-7 : Extracting principle curves of the change in nucleoid dimensions as a function of the change in crowder concentrations. (A) Relative changes of the nucleoid length, $L_{\mathrm{nuc}}/L_{\mathrm{nuc},0}$, as a function of crowder concentration, c/c_0. The crowder concentrations, c, are relative to those in normal growth medium without excess NaCl, c_0. The data from different measurements are plotted in different color. (B) The raw data (small gray square) are binned along the x-axis and the mean values in each bin are plotted in larger black square. The center of each bin is used as the x-values of corresponding larger black square. (C-H) The same for nucleoid width (C, D), volume (E, F), and aspect ratio (G, H).

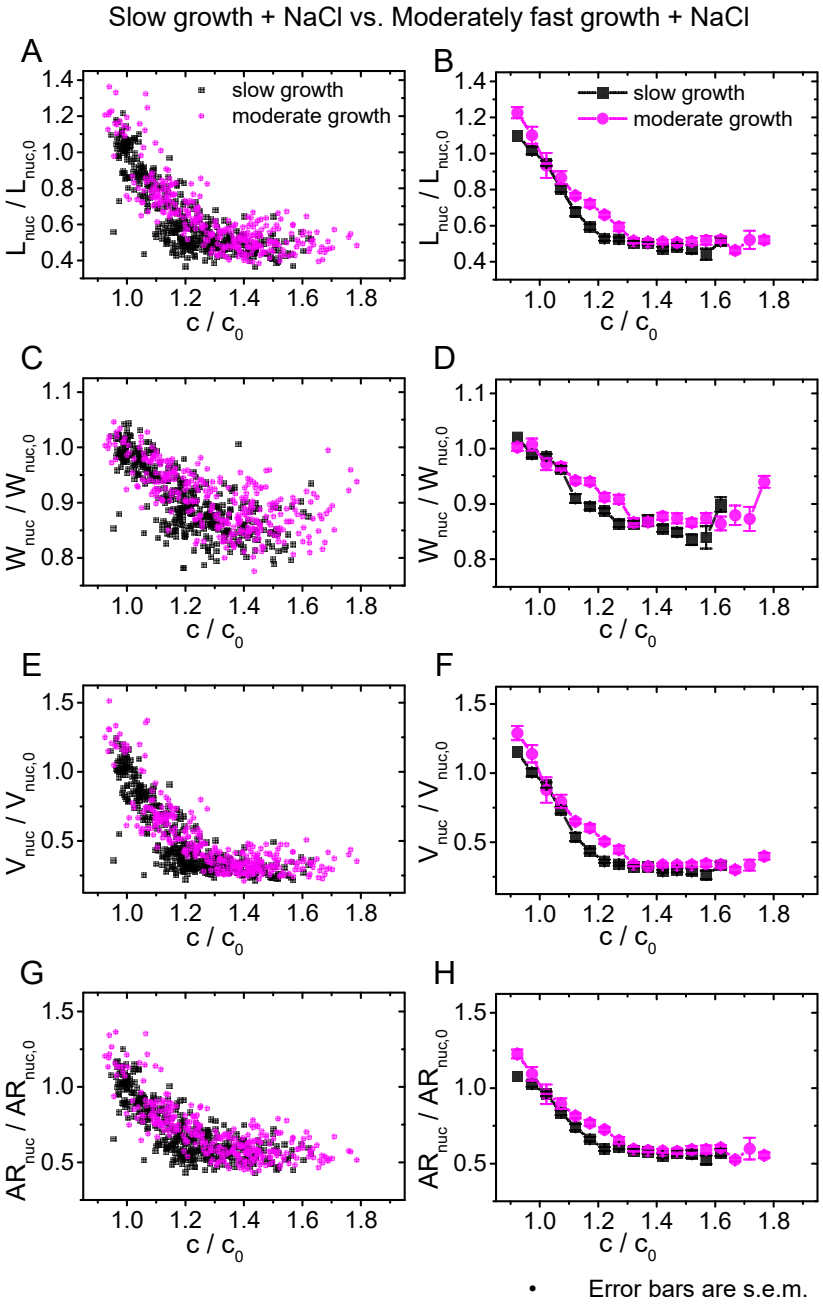


Figure 4-8 : Change in nucleoid dimensions as a function of the change in crowder concentration. (A) Relative changes of the nucleoid length in slow (black squares) and moderately fast (magenta circles) growth conditions as a function crowder concentration. (B) The principle curves extracted from data plotted in (A). (C-H) The same for nucleoid width (C, D), volume (E, F), and aspect ratio (G, H). Error bars shown correspond to standard errors of the means.

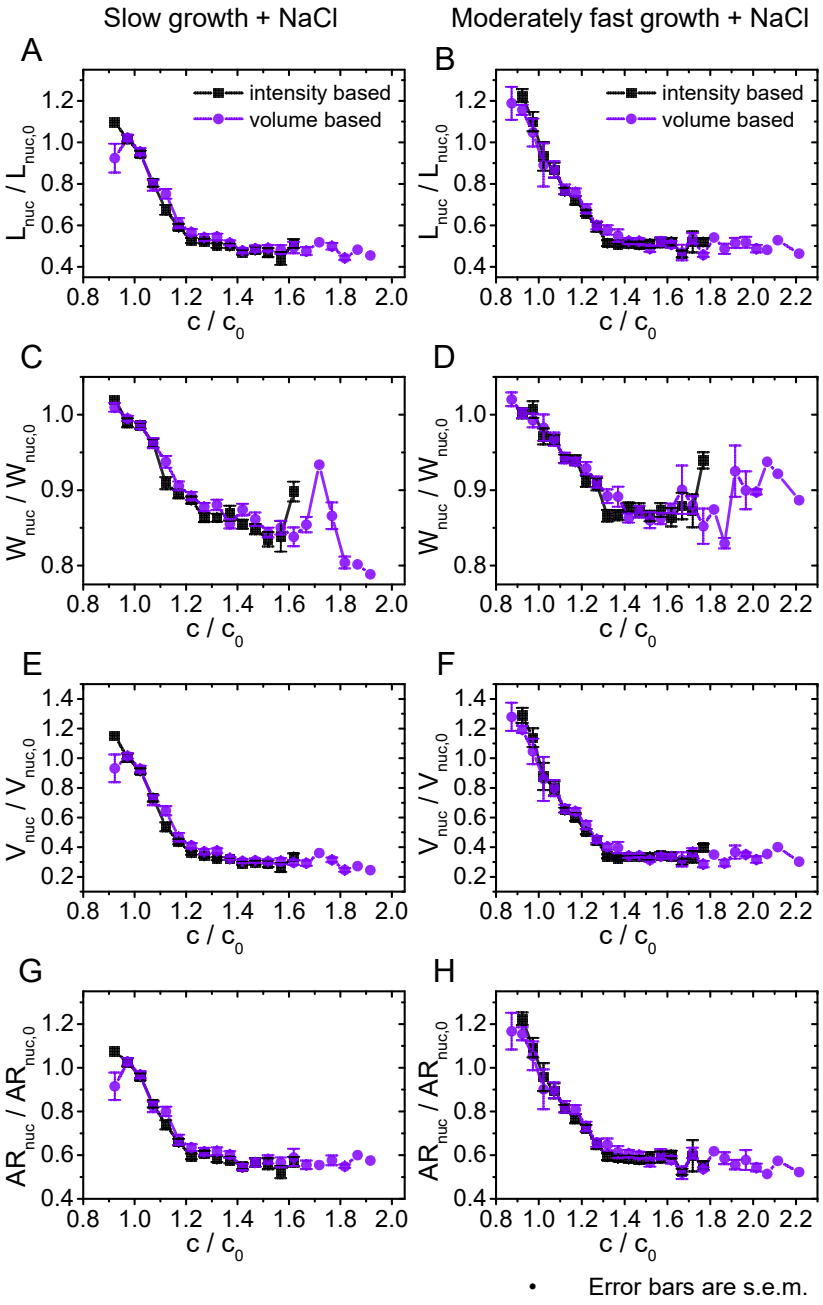


Figure 4-9 : Comparison of cellular crowder concentrations determined using two different methods (Part II). (A, B) Relative changes of the nucleoid length as a function of crowder concentration. (C, D) Relative changes of the nucleoid width as a function of crowder concentration. (E, F) Relative changes of the calculated nucleoid volume as a function of crowder concentration. (G, H) Relative changes of the calculated nucleoid aspect ratio as a function of crowder concentration. All error bars correspond to standard errors of the means.

images nor in the raw data of nucleoid lengths and widths (Figure 4-8 left column). Both findings together indicate that the coil-globule transition of the nucleoid is a second rather than first order phase transition *in vivo* conditions.

Interestingly, we found that the dependence of the nucleoid size on the crowder concentration is almost the same in both studied growth conditions (Figure 4-8). This outcome is surprising because concentrations of the main macromolecular crowders, the ribosomes, and the proteins, are expected to be significantly different in these two growth conditions [EBD13; DZW+17]. Based on available published data, we estimate the concentration of soluble cytoplasmic proteins to be about two-fold higher and ribosomes about two-fold lower in slow compared to moderately fast growth conditions (Table 4-4 and appendix D).

We hypothesized that the insensitivity of nucleoid compaction to the crowder composition could indicate the importance of some other factor than the macromolecular crowders to the compaction process. It is known that *E. coli* responds to osmotic shock by pumping K^+ ions from its surrounding environment [ES65; RCM+87]. Furthermore, it was reported that an *E. coli* nucleoid did not compact under osmotic shock in a medium depleted of K^+, albeit the presented evidence relied on an image of a single cell [CGJ+13]. To further understand the effect of influx on nucleoid compaction, we substituted in the moderately fast growth medium with Na^+ 20 min. prior to osmotic shock. Osmotic shock with 0.75 Osm/kg NaCl in K^+ depleted medium yielded the same result as the osmotic shock where K^+ was present at the regular 24 mM concentrations, although nucleoid recovery was altered for times longer than 5 min. (Figure 4-10).

While this finding contradicts the earlier report [CGJ+13], it is consistent with *in vitro* findings that monovalent ions such as K^+ only modestly influence DNA condensation; unlike tri and higher valent cations [Joy16]. Also, previous *in vivo* measurements support the idea that the influx of is relatively minor during shorter time scales of about 5 min. to significantly alter ($< 10\%$) the intracellular K^+ concentration [ES65]. Several past works thus support our findings show that at short time scales (< 5 min.) following hyperosmotic shock, the influx into the cytoplasm does not affect nucleoid dimensions.

Table 4-4 : Estimation of ribosome and protein numbers is slow and moderately fast growth conditions.

	Slow growth	Moderately fast growth	Explanation/Reference
Total number of ribosomes	15000	44000	Ehrenberg et al. (2013) [EBD13]
Polysome fraction	0.65	0.85	Mohapatra and Weisshaar (2018) [MW18] Dai et al. (2017) [DZW+17]
Free 70S fraction	0	0	Mohapatra and Weisshaar (2018) [MW18] Dai et al. (2017) [DZW+17]
Subunit fraction	0.34	0.15	1-(Polysome fraction)
Ribosomes per polysome	10	13	Mondal et al. (2011) [MBL+11]
Total proteins	2.10E+06	3.00E+06	Assuming the same concentration as in moderate growth Milo (2013) [Mil13]
Cytoplasmic crowder fraction for proteins	0.4	0.2	Li et al. (2014) [LBGW14]
Average Cell Volume (μm^3)	0.63	0.89	Based on this work
Volume at Birth (μm^3)	0.43	0.61	Based on this work

Cytoplasmic crowder fraction for proteins is based on [Figure 5A in LBGW14]. Protein crowders belong to three sectors in this chart and include proteins involved in carbohydrate metabolism, nucleotide and amino acid metabolism, and in protein folding and decay. In fast growth conditions, these sectors account for 20% of all proteins. According to the text accompanying [Figure 5A in LBGW14], the contribution of these proteins can be expected to rise to 40% at the expense of decrease proteins involved in translation-related processes. Note, that we do not count sectors labeled unknown and other proteins although some of the proteins in these sectors qualify as cytosolic crowders. The rationale for leaving these sectors out is that we are seeking a conservative estimate (lower limit) for the crowder fraction. The lower limit is relevant for the question if proteins can be large enough source of crowding to have significant effect on compaction of the nucleoid.

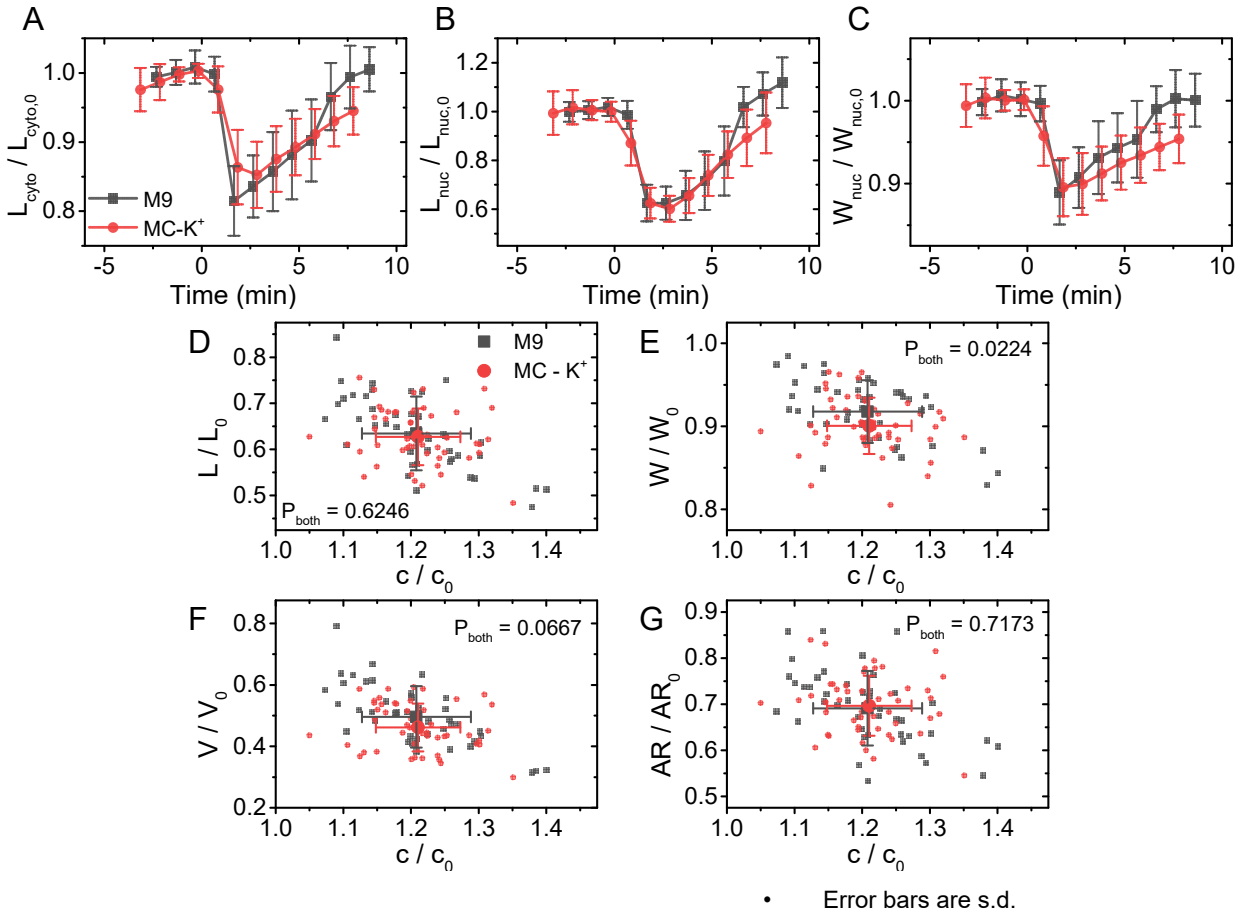


Figure 4-10 : Changes of cell and nucleoid dimensions under osmotic shock in medium where Potassium ions are substituted by an equal amount of Sodium ions. (A-C) Red points correspond to medium that where K^+ has been replaced by Na^+ and black to medium where K^+ is present (24 mM). Cells were first grown in regular M9 medium in mother machine channels overnight. 20 min. prior to osmotic shocks, the medium was replaced by the one where K^+ were replaced by Na^+. Osmotic shock was induced by adding 0.4 M NaCl to the the growth medium shifting osmolality from about 250 $mOsm/kg$ to about 1000 Osm/kg. (A) Time dependent change of cytoplasmic length of the cell. The length is normalized by the length just prior to osmotic shock. (B,C) The same for nucleoid length and width, respectively. (D-G) Relative changes of nucleoid length, widths, volumes, and aspect ratios as a function of relative change of crowder concentration. Error bars correspond to standard deviations.

4.4 Mechanical Squeezing Measurements Confirm Osmotic Shock Data

In addition to removing cellular water content via osmosis, we also carried out measurements where we removed water by the mechanical squeezing of the cells. For that purpose, we used a microfluidic device, which we refer to as the microanvil. This device allowed us to mechanically press out part of the cytoplasmic content while imaging the cells (See Section 3.3). Since the applied pressure to the cells can be expected to activate mechanosensitive channels [KMS10], one could expect in addition to water molecules also ions and small metabolite molecules could leave the cell. Our first proof-of-principle devices had the smallest anvil dimension of about 2 μm. In future designs, this dimension can be reduced (Section 6.1). Since 2 μm constitutes a sizeable portion of the cell length ($2 \sim 4$ μm), we studied longer than normal cells. The cells were elongated by inducing SulA expression from an extra plasmid copy, thereby inhibiting cell division [DML08]. The elongated cells had lengths in the range of $7 \sim 15$ μm and had multiple nucleoids. The amount of cytoplasmic content that can be removed from the cells can be controlled by an external pressure applied by the anvil. However, at higher pressures, the anvil divides the cell into two distinct compartments (Figure 4-11 A, Supplementary Movie M4-3). In the region between the two compartments, the cytoplasmic content of the cell is almost completely removed (See Section 3.3). Further increases to the externally applied pressure by the anvil do not appreciably change the cytoplasmic volume of the cell. For this reason, the maximum volume that was removed was limited to about 25% of the initial cytoplasmic volume in these experiments.

The compaction of the nucleoid increased during stepwise pressure ramps and recovered when the pressure was lowered (Figure 4-11 B). As with measurements with osmolality variation, efflux and influx of water and other cytoplasmic components were taking place at a faster time scale than the measurement rate (2 frames/min.). After one pressure cycle, the majority of cells were capable of resuming growth.

We determined nucleoid dimensions and volumes from these measurements as a function of the changes in crowder concentrations and compared these results with the findings from the osmotic shock measurements (Figure 4-12). Within uncertainties of the measurement, the two approaches yielded indistinguishable results, thus further confirming the osmotic shock measurements. The data also implies that increased ion concentration during osmotic shock measurements does not

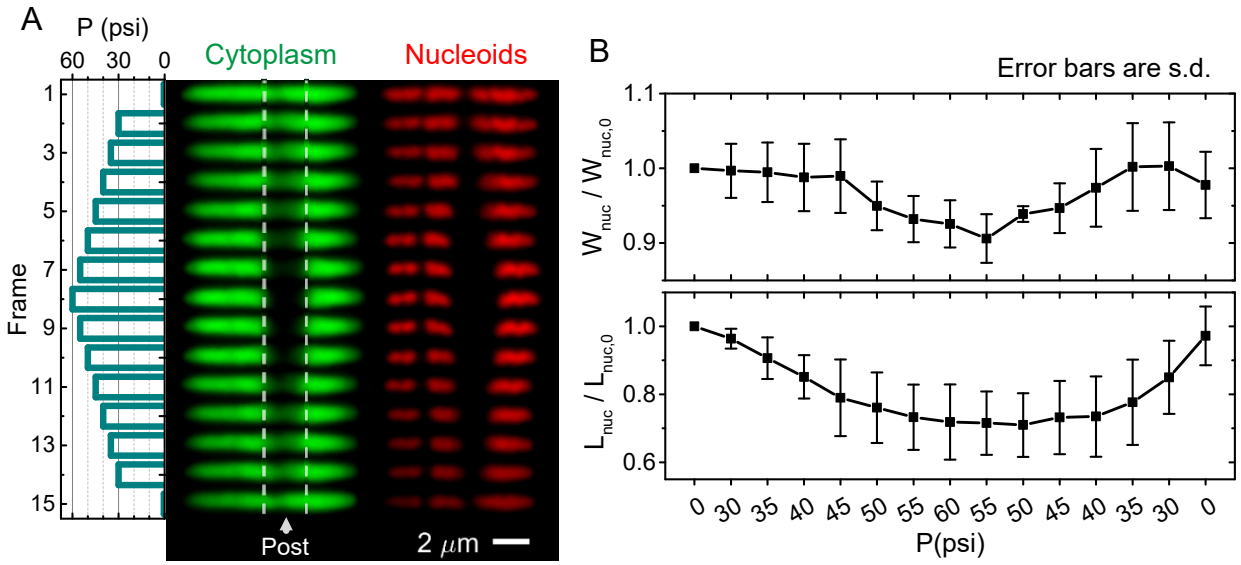


Figure 4-11 : Measurements of nucleoid compaction during cell squeezing. (A) Response of an elongated *E. coli* cell to a pressure cycle. Left panel: Change of externally applied pressure during the measurements. In the 1st (top) and the last (bottom) frame the cell is not squeezed. Middle panel: images of cytoplasmic mNG label during this pressure cycle. The region between dashed lines correspond to the portion of the cell where the anvil touches it. Right panel: Nucleoid images for this cell. (B) The average normalized nucleoid widths (top) and length (bottom) for this cell. The average is calculated over three nucleoids in this cell and error bars reflect standard divisions. Both the width and length of the nucleoids are normalized to those at the beginning of the squeezing cycle.

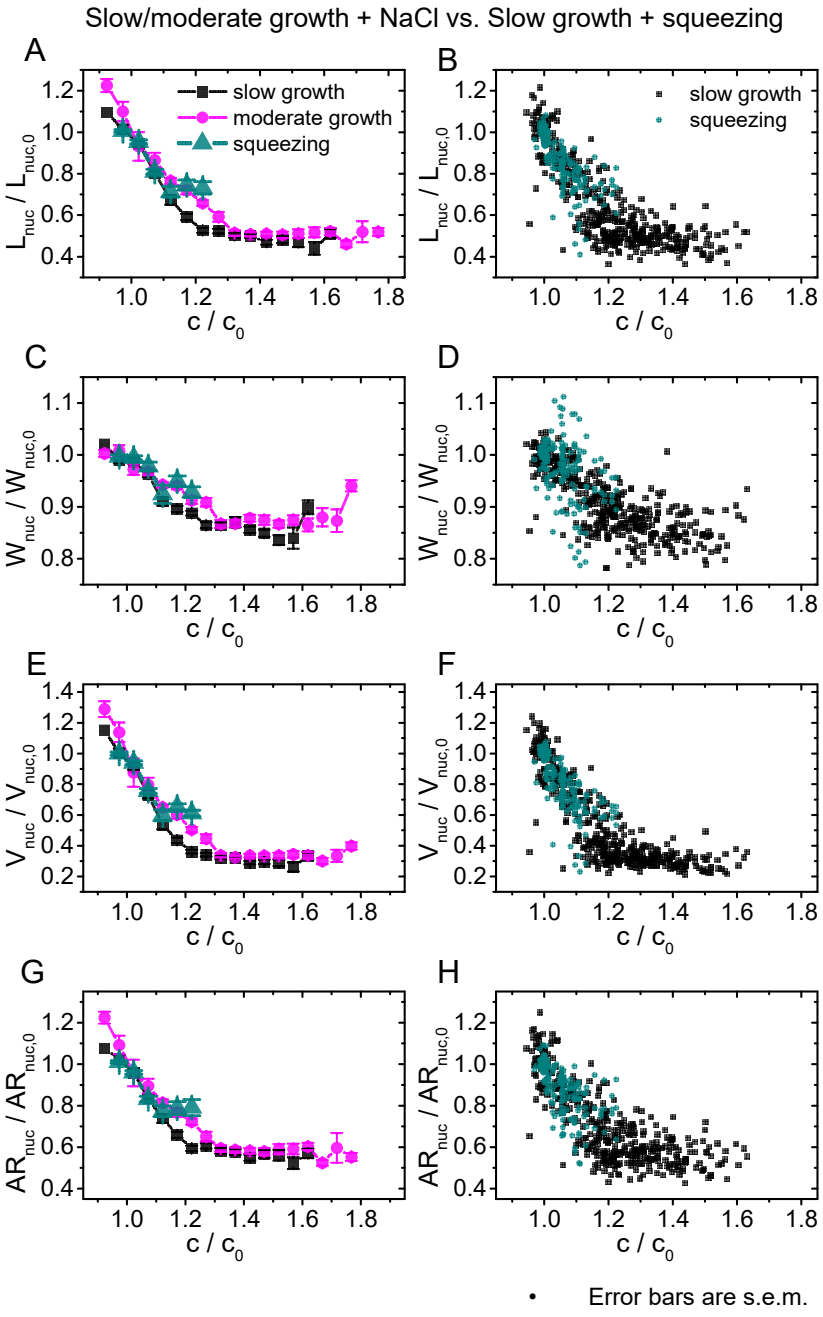


Figure 4-12 : Comparison of data from squeezing measurements (dark cyan) to osmotic shock measurements (black/magenta). (A, B) Comparison of relative nucleoid length as a function of crowder concentration from squeezing measurements to that from osmotic shock measurements. The same for nucleoid width (C, D) and calculated volume (E, F) and calculated aspect ratio (G, H). Both squeezing and osmotic shock measurements have been performed in slow growth conditions. Error bars shown correspond to standard errors of the means.

significantly affect nucleoid compaction, because in squeezing measurements, one could expect the ionic strength of the cytoplasmic to not significantly change if the assumption of the opening of mechanosensitive channels is correct.

4.5 Transertion Linkages and Crowding by Polysomes Have a Limited Effect on Nucleoid Size in Slow Growth Conditions

Next, we aim to understand which of the macromolecular crowders in the bacterial cytoplasm play the dominant role in compaction of the nucleoid. Several lines of research point out that the main compacting agents among different macromolecular crowders species are poly-ribosomes (polysomes) [Joy16; MBL+11; BCMW14; BCW15]. This conclusion has been partially drawn from studies of cells treated with rifampicin, a transcription halting drug. The drug appears to affect the nucleoid size via two different mechanisms in fast growth conditions [BCMW14]. The measurements by Bakshi et al., which were carried out in EZ Rich Defined Medium at 30℃ where the cell doubling times were 48 min., have shown that the nucleoids compact at shorter time scales ($0 \sim 5$ min.). The compaction has been explained to be the result of severing transertional linkages between DNA and the inner cell membrane. These linkages are expected to keep the nucleoid in an expanded state and to resist the compaction effects from the crowders. In longer timescales (> 10 min.), rifampicin leads to the expansion of chromosomal DNA so that it appears to fill the whole cytosolic volume [BCW15]. The expansion has been interpreted as the result of polysomes dissociating into 30S and 50S ribosomal subunits and by the lower ability of these subunits to compact the nucleoid [MBL+11; BCMW14; BCW15]. Since the dissociation of the polysomes during rifampicin treatment has such drastic effects on the nucleoid size, one can expect them to be the dominant species in compacting the nucleoid. We were interested in understanding if the above described nucleoid behaviors during rifampicin treatment also hold in moderately fast and slow growth conditions where ribosome and polysome concentrations are expected to be lower [EBD13; DZW+17]. Treating moderately fast growing cells with rifampicin, we observed an initial compaction of the nucleoid at about the 5 min. timescale (Figure 4-13 E-H), which is consistent with the earlier reports [BCMW14; SGG+18]. Although the effect of compaction in our experiments was smaller ($3 \sim 5\%$) (Figure 4-13 E-H) than in the previous reports (about 8%),

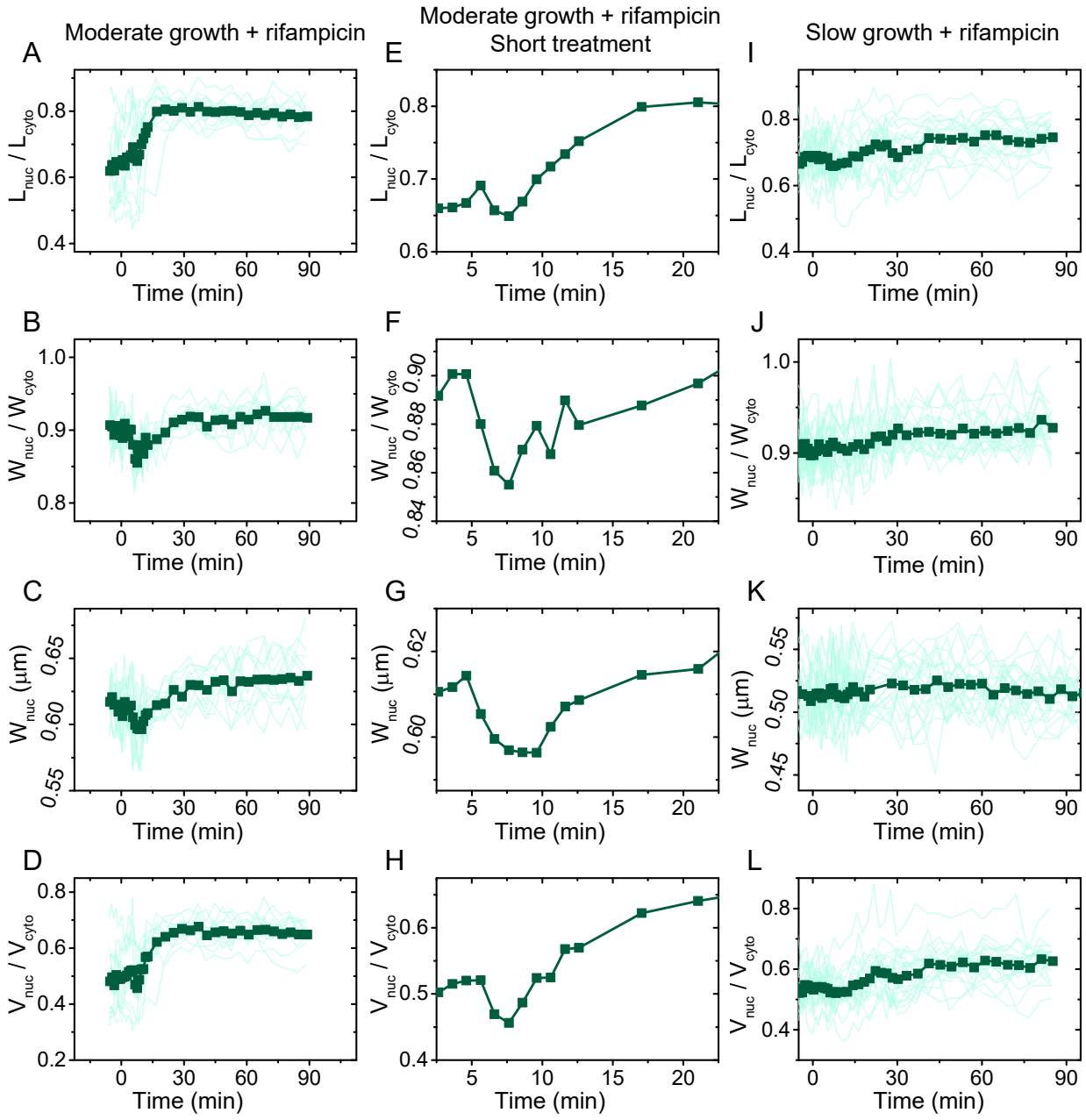


Figure 4-13 : Change in nucleoid dimensions under rifampicin treatment in moderately fast (left) and slow (right) growth conditions. 300 $\mu g/ml$ rifampicin is administered to cells at 0 min.. There is $2\sim3$ min. delay in fluidic lines before the drug reaches the cells. (A, E, I) Ratio of nucleoid to cell length as a function of time. In (A, I), traces from individual cells are shown by thin lines, and the population average trace by a thick line with squares. $N = 20$ for slow and $N = 11$ for moderately fast growth conditions. (E) Zoomed in from the beginning of the trace from (A). (B, F, J) The same for nucleoid width. (C, G, K) The same for measured nucleoid width. (D, H, L) The same for the calculated nucleoid volume.

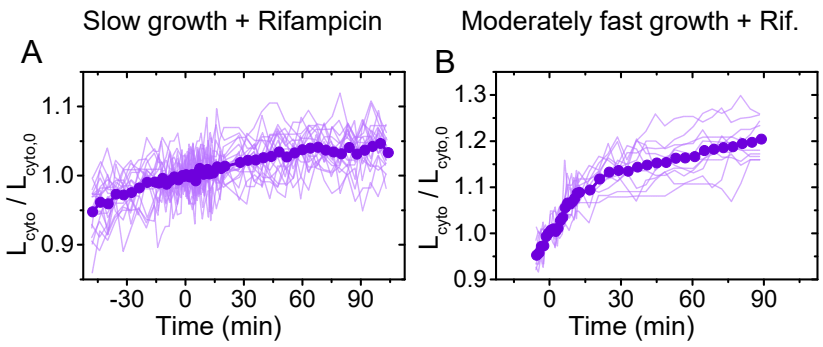


Figure 4-14 : Growth curves prior to and during 300 $\mu g/ml$ rifampicin treatment. Traces from individual cells are shown by thin light lines and population average curve by thick line with markers. Rifampicin circulation in microfluidic lines was started at 0 min.. The drug is expected to reach cells within $1 \sim 3$ min. after the start of circulation. (A) Data for slow growth ($N = 20$), and (B) for moderately fast growth conditions ($N = 11$).

which were carried out in fast growth conditions, the presence of nucleoid contraction supports the idea of the existence of transertional linkages. However, their effect in determining the size of the nucleoid appears rather modest in this growth condition. At timescales longer than 5 minutes, we observed the expansion of the nucleoid (Figure 4-13 A-D). Note that in these data, nucleoid dimensions have been normalized by cell dimensions instead of nucleoid dimensions at the beginning of the drug treatment. We used this scaling because of nucleoid length and its volume increase approximately proportionally to the corresponding cell dimensions. Since the cell growth does not stop immediately after the drug is introduced to the growth medium (Figure 4-14), normalization using the cell dimensions compensates for the growth related expansion of the nucleoid. Our data show that the expansion of the nucleoid dimensions unaccounted by the cell growth stops about 20 minutes after introduction of the drug (Figure 4-13 A-D). The observed expansion is qualitatively consistent with the earlier reports [BCMW14; CCQ+09]. At a quantitative level, we find that the expansion leads to a 27% increase in nucleoid length and a 2% increase in nucleoid width in moderately fast growth conditions.

All of the above changes in nucleoid dimensions were significantly diminished in slow growth conditions (Figure 4-13 I-L), although rifampicin manifested itself in stopping cell growth (Figure 4-14). There was no distinctly detectable decrease in nucleoid dimensions at short time scales (< 5

min), indicating that the effect of transertion in determining nucleoid size is negligible in slow growth conditions. This can be expected. Lower growth rate means a proportionally lower total protein synthesis rate in cells while the number of transertion linkages at any given time should scale with this rate. In longer time periods of about 30 minutes, the nucleoid length and width increased by 7% and 2%, respectively. While the change in width was comparable to that found in moderately fast growth conditions, the change in length was four times smaller. The significantly smaller nucleoid expansion could result from about a twice smaller concentration of polysomes in this growth condition (Appendix D). Their dissociation to the 30S and 50S subunits would, therefore, lead to the smaller expansion of the nucleoid as observed in the experiments. The latter conclusion leads then to a further inference that polysomes have a minor contribution to the compaction of the nucleoid in slow growth conditions.

4.6 Effect of Osmotic Shock on Nucleoids after Rifampicin Treatment

To further understand the role of polysomes in the compaction of the nucleoid, we applied osmotic shocks to cells that had been treated for 25 ∼ 30 min. with rifampicin (Figures 4-15 and 4-16). The latter period corresponds approximately to the time of nucleoid expansion (cf. Figure 4-13 A-D). In Figures 4-15 and 4-16, rifampicin treatment data shown in the left columns are nucleoid dimension right after osmotic shock divided by the same dimension right before the shock. Rifampicin treatment data shown in the middle columns are calculated using extrapolated untreated nucleoid lengths, i.e., $L_{\mathrm{nuc},0}$ were linearly extrapolated from the beginning of the rifampicin treatment to the point just before the osmotic shock was administered (25 ∼ 30 min. later). The linear extrapolation is based on Figure 4-17. Nucleoid widths $W_{\mathrm{nuc},0}$ are considered being the same as prior to rifampicin treatment. The compaction curves based on extrapolated nucleoid dimensions are shown in red. Rifampicin treatment data shown in the right columns uses nucleoid dimensions just before rifampicin treatment started for calculations.

During this treatment period, the majority of the polysomes should dissociate into 30S and 50S subunits based on single molecule tracking results [BSGW12; SPL+14] and on estimated the mRNA lifetime in *E. coli* of about 5 min. [BKL+02]. Note that the chosen 25 ∼ 30 min. period is

- Slow growth

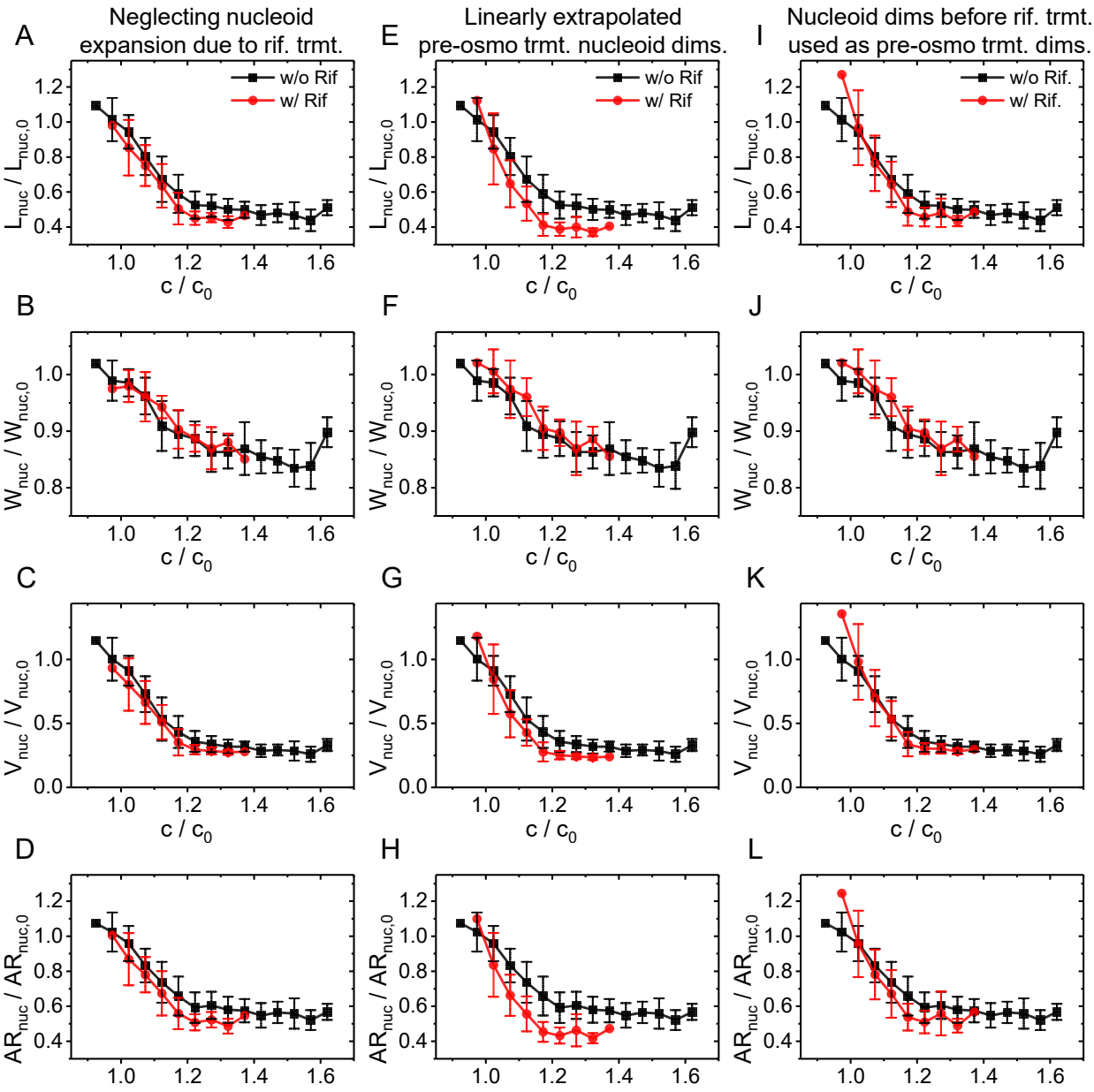


Figure 4-15 : Effect of osmotic shock after rifampicin treatment in slow growth. Cells were first treated for about 30 min. with 300 $\mu g/ml$ rifampicin and then the concentration of NaCl in the medium was changed. Rifampicin was also present in the medium during osmotic shock. Nucleoid dimension right after osmotic shock divided by the same dimension right before the shock are plot in red. Those dimensions are nucleoid length (A, E, I), width (B, F, J), volume (C, G, K), and aspect ratio (D, H, L). For comparison the same ratio without rifampicin treatment is also shown (in black for all three columns; from Figure 4-8 right column). Only principle curves are shown in this figure. Error bars correspond to standard divisions.

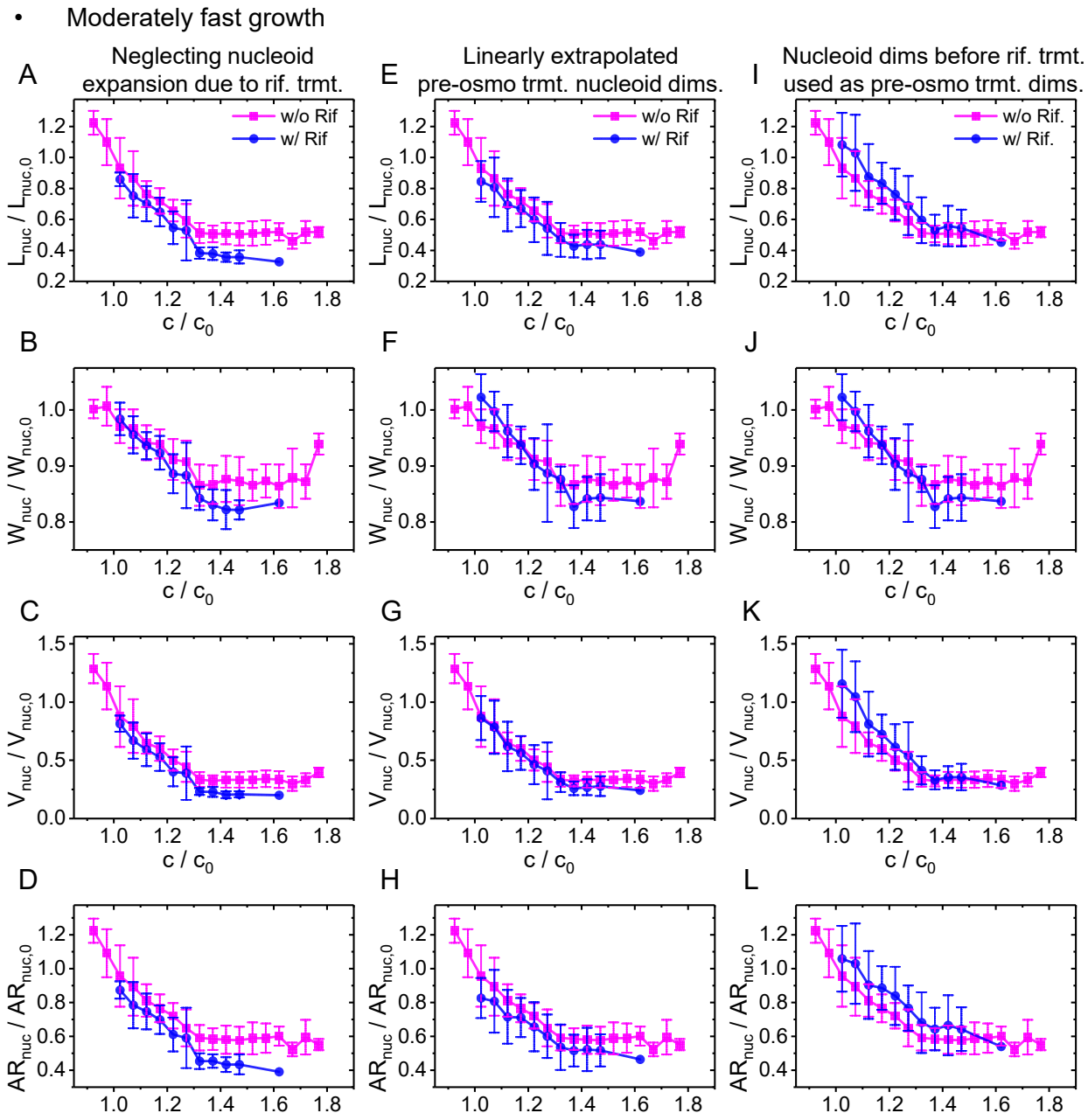


Figure 4-16 : Effect of osmotic shock after rifampicin treatment in moderately fast growth. Cells were first treated for about 25 min. with 300 $\mu g/ml$ rifampicin and then the concentration of NaCl in the medium was changed. Rifampicin was also present in the medium during osmotic shock. Nucleoid dimension right after osmotic shock divided by the same dimension right before the shock are plot in blue. Those dimensions are nucleoid length (A, E, I), width (B, F, J), volume (C, G, K), and aspect ratio (D, H, L). For comparison the same ratio without rifampicin treatment is also shown (in magenta for all three columns; from Figure 4-8 right column). Only principle curves are shown in this figure. Error bars correspond to standard divisions.

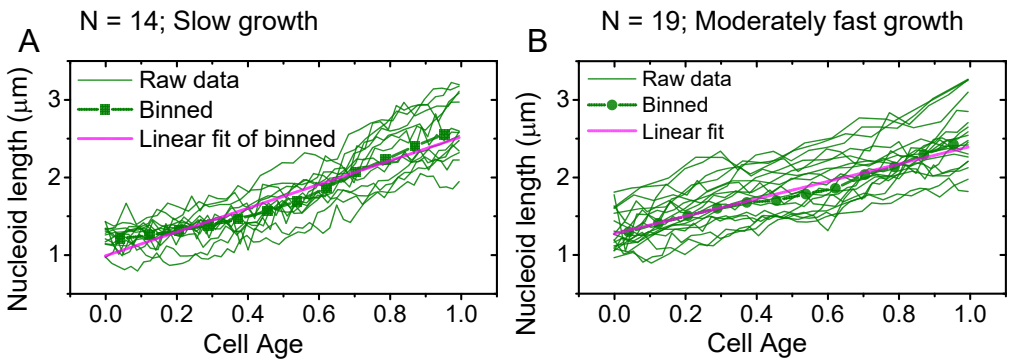


Figure 4-17 : Nucleoid length as a function of normalized cell cycle time in slow (A) and in moderately fast (B) growth conditions. Thin curves are from individual cells. A thick solid line with filled circles is the population-averaged curve. A linear fit to the population is shown by the magenta line. In slow growth conditions, nucleoids elongate at the average rate of 6.8 nm/min. and in moderately fast growth conditions at the rate of 12 nm/min.. These values were used in extrapolating nucleoid lengths in osmotic shock measurements that followed rifampicin treatment. (A) Data for slow growth ($N = 14$), and (B) for moderately fast growth conditions ($N = 19$).

short enough for the concentration of the proteins and stable RNA species in the cytoplasm to not alter significantly. We estimate their change to be less than 10% due to their dilution by residual cell growth while their decrease due to degradation can be expected to be minimal during this period. If ribosomal subunits are less effective in compacting the chromosomes [BCMW14; BCW15] then we would expect weaker compaction of nucleoids in rifampicin treated cells during osmotic shock measurements. Contrary to this expectation, the nucleoid compaction was somewhat larger in rifampicin treated cells in both growth conditions (Figures 4-15 and 4-16, left columns). In moderately fast growth conditions, a slight increase in compaction could be assigned to the fact that prior to the osmotic shock, the nucleoid was significantly larger in rifampicin-treated cells than in untreated ones. To compensate for this effect, we extrapolated nucleoid lengths from the beginning of the treatment to the point where salt shock occurred, assuming an increase in nucleoid length would have followed the same increase as during normal growth (Figure 4-17). The resulting data still showed negligible effects from rifampicin treatment on the nucleoid compaction curves (Figures 4-15, 4-16, central and right columns). Furthermore, we found the distribution of the absolute, as opposed to normalized, nucleoid widths to be indistinguishable between rifampicin treated and untreated cells after the osmotic shock (Figure 4-18). Thus, the nucleoid is compacted into the same final width (in μm) as a result of hyperosmotic shock irrespective of a prior rifampicin

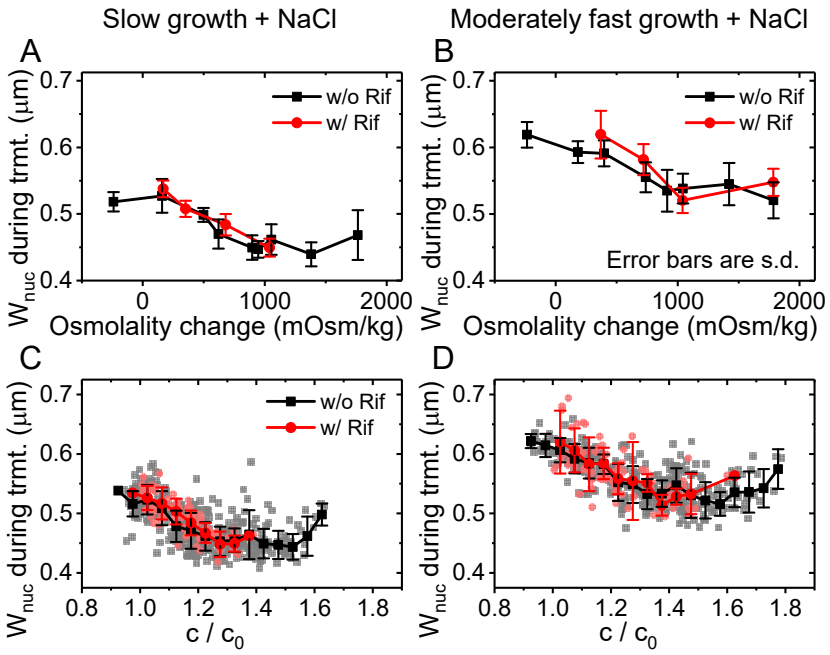


Figure 4-18 : Nucleoid widths in μm before and during different treatments. (A, B) The average nucleoid width as a function of external osmolality in slow and in moderately fast growth conditions, respectively. Red circles correspond to $25 \sim 30$ min. 300 $\mu g/ml$ rifampicin treatment of cells prior to osmotic shock and black squares to the same shock without rifampicin treatment. (C, D) The nucleoid widths as a function relative crowder concentration in slow and in moderately fast growth conditions, respectively. Overlaid to raw data are binned data points. Error bars shown are standard divisions. In both slow and moderately fast growth conditions, the widths during osmotic shock are independent on whether a prior rifampicin treatment was carried out or not.

treatment or not. This result is consistent with our earlier inference that polysomes play a minor role in compaction of the nucleoid in slow growth conditions. However, at moderately fast growth, the same explanation would be an apparent contradiction with our prior reasoning for nucleoid expansion upon polysome dissociation. A possible way to reconcile these conflicting explanations is that only part of the nucleoid expansion under rifampicin treatment can be explained by polysome dissociation in moderately fast growth conditions, while the rest may be the result of some other effect rifampicin has on the nucleoid. This idea is also supported by examining the structure of the nucleoids before and after rifampicin treatment. In fast growth conditions (in defined EZ-Rich medium) and to some extent in moderately fast growth conditions, nucleoids display a distinct structure in our images (Figure 4-19). This structure was completely lost following the $25 \sim 30$ min. treatment by the drug, indicating that beyond affecting crowding and transertion, rifampicin has some further effects on nucleoid size and structure.

4.7 Crowding Model Qualitatively Agrees with Experimental Findings

We sought to explain the measured data by using Langevin dynamics simulations of chromosomes in crowded and confined environments. Our computational approach is similar to the one reported by Kim et al. [KJJ+15] (for more details, see Section 2.7). Extending that previous report, we also calculate the nucleoid width and volume in addition to the nucleoid length to compare these quantities to experimental values. The model represents the chromosome as a chain of linked beads and crowders as smaller-sized unlinked beads. Both species interact via repulsive excluded volume interactions and are confined to a cylindrical volume (Figure 2-9 A). The model chromosome corresponds to a single fully replicated circular *E. coli* chromosome.

According to model calculations, the length, width, and volume show approximately sigmoidal dependence on the volume fraction of crowders, Φ, or the concentration of crowders, ρ_c (Figure 2-10). The former is defined as the total volume of crowders divided by the volume of the cytoplasm and it is proportional to the concentration of crowders [RC03]. Similar dependence for nucleoid length on the volume fraction was also observed in earlier models [SBdH+15; KJJ+15]. The model predicts that in both low and high crowder volume fractions, nucleoid dimensions are insensitive

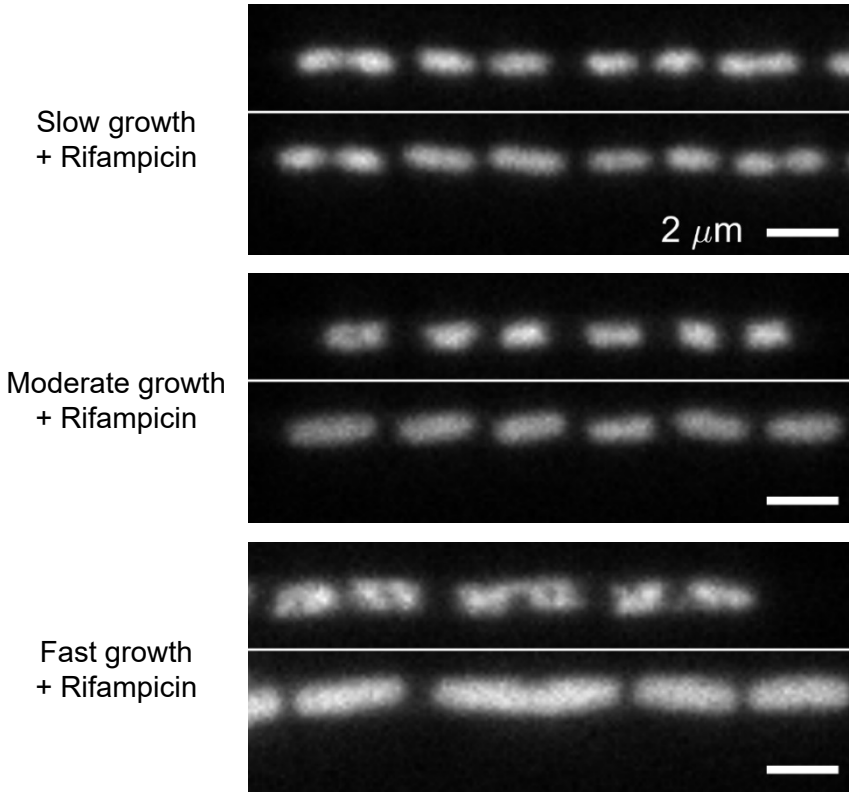


Figure 4-19 : Nucleoid images before and after rifampicin treatment. In each panel, the top row corresponds to cells prior to the treatment and bottom row to the same cells during the treatment with 300 $\mu g/ml$ rifampicin. Images of rifampicin treated cells were taken once cell and nucleoid dimensions stopped to change. In fast growth conditions the cells were grown in EZ Rich Defined Medium (Teknova, Inc., CA), which was supplemented with 0.2% glucose (Millipore Sigma, MO).

to the number of crowders in the cellular volume. The transition between the two regimes occurs continuously, i.e., the coil-globule transition in this model is second order. All these predictions are consistent with our experimental data on a qualitative level.

We calculate the aforementioned dependencies for two different crowder sizes. The model predicts that the mid-point of nucleoid compaction occurs at larger volume fractions for larger crowders. However, a smaller concentration of larger crowders is needed to compact the nucleoid to the same level (Figure 2-10 central column). Kim et al. have previously found that multiplying crowder concentration by the square of the crowder diameter, i.e., by a_c^2, collapses L_{nuc} for different size crowders to a single curve [KJJ+15]. Our model indicated that this scaling applied in addition to the nucleoid length also to its width and volume (Figure 2-10 right column). Furthermore, results by Kim et al. showed that for a polydisperse ensemble of crowders L_{nuc} vs $\sum_i \rho_{c,\,i}\, a_{c,\,i}^2$ curves collapsed for different crowder mixtures into a single curve [KJJ+15]. The above sum is taken over all crowder species. Thus, the level of crowding in polydisperse samples is, according to the model, characterized by a single parameter $(\rho_c\, a_c^2)$ which one could calculate knowing the concentrations and diameters of all crowders. Note that even though the $\rho_c\, a_c^2$ scaling was found semi-empirically for the above described course grained model, it has a clearer meaning at the microscopic level. The quantity, where L_{DNA} is the contour length and d the effective diameter of chromosomal DNA ($> 2.2\ nm$) [Odi98], is approximately the excluded volume fraction associated with DNA and crowder interactions [Odi98]. So, in leading order $\rho_c\, a_c^2$ is proportional to the relevant volume fraction. This argument applies to small crowders such as proteins. Large crowders, such as polysomes, can be expected to interact predominantly with DNA supercoils. In this case the above quantity is not relevant but the coarse-grained model can be expected to capture the interaction well. Furthermore, the sum rule ($\Psi_{\mathrm{tot}} \equiv \left(\rho_c\, a_c^2\right)_{\mathrm{tot}} = \sum_i \rho_{c,\,i}\, a_{c,\,i}^2$) found by Kim et al. [KJJ+15] indicates that crowder-crowder interactions (crowding between crowders) can be effectively neglected and each crowder species acts independently of each other on DNA via their partial osmotic pressures.

We used the scaling behavior of model curves to compare them to our experimental data. By adjusting the crowding parameter, Ψ, which corresponds to the crowding level in the regular medium, we found the best match between experiment and model for, Ψ, which corresponds to the crowding level in the regular medium, we found the best match between experiment and model

for ($\Psi \approx 20\ \mu m^{-1}$ (Figure 4-20) In this comparison, we also accounted that at zero crowder concentration, the nucleoid must fill the whole cell volume. This extra constraint was determined as the ratio of the measured cytoplasmic size to nucleoid size in regular growth medium (violet triangles in Figure 4-20). As can be seen from Figure 4-20 A-C, the model predicts the experimentally observed length dependence on the crowding level reasonably well. The agreement is poorer for the nucleoid width, where the experiment shows much larger variations and thus smaller anisotropy in the compressibility (Figure 4-20 D-F). Taking the coarse-grained nature of the model, some quantitative discrepancies can be expected; yet the main experimental characteristics are clearly represented in the model.

4.8 Smooth Coil-Globule Transition of Nucleoids in the Cellular Environment

Our measurements show that under hyperosmotic treatment and during mechanical squeezing, *E. coli* nucleoids undergo rapid compaction on a timescale of about one minute. The compaction occurs concurrent with the changes in the cytoplasmic volume, but during mild shocks, the nucleoid volume decreases by a factor of about 2.5 times more than the cytoplasm. The shrinkage of the nucleoid can be explained by an increased osmotic pressure from cytosolic macromolecular crowders, macromolecular crowders, concentration of which arises when the cytosolic volume of the cell decreases. Our *in vivo* findings are in overall agreement with previous *in vitro* studies where artificial crowding agents or ions have been used. However, several *in vitro* studies have reported an abrupt transition from an extended state of the liberated nucleoid (coil) to a highly compacted state (globule) [KVM$^+$10; PHH$^+$12; YHMY10]. Here, we find that *in vivo*, the compaction of the nucleoid is a continuous function of cytoplasmic crowder concentration. Therefore, the associated coil-globule transition of the chromosome is the second rather than the first order phase transition in the cellular environment. The difference between *in vivo* and *in vitro* experiments can be related to the different nature of crowders, the different organization of DNA, or the differences in ionic composition of the environment. The *in vitro* measurements used relatively small crowders (PEG and BSA) compared for example, to polysome particles. Also, there was a reduced level [PHH$^+$12] or no [KVM$^+$10; YHMY10] supercoiling and DNA cross-linking via DNA binding proteins present in measurements

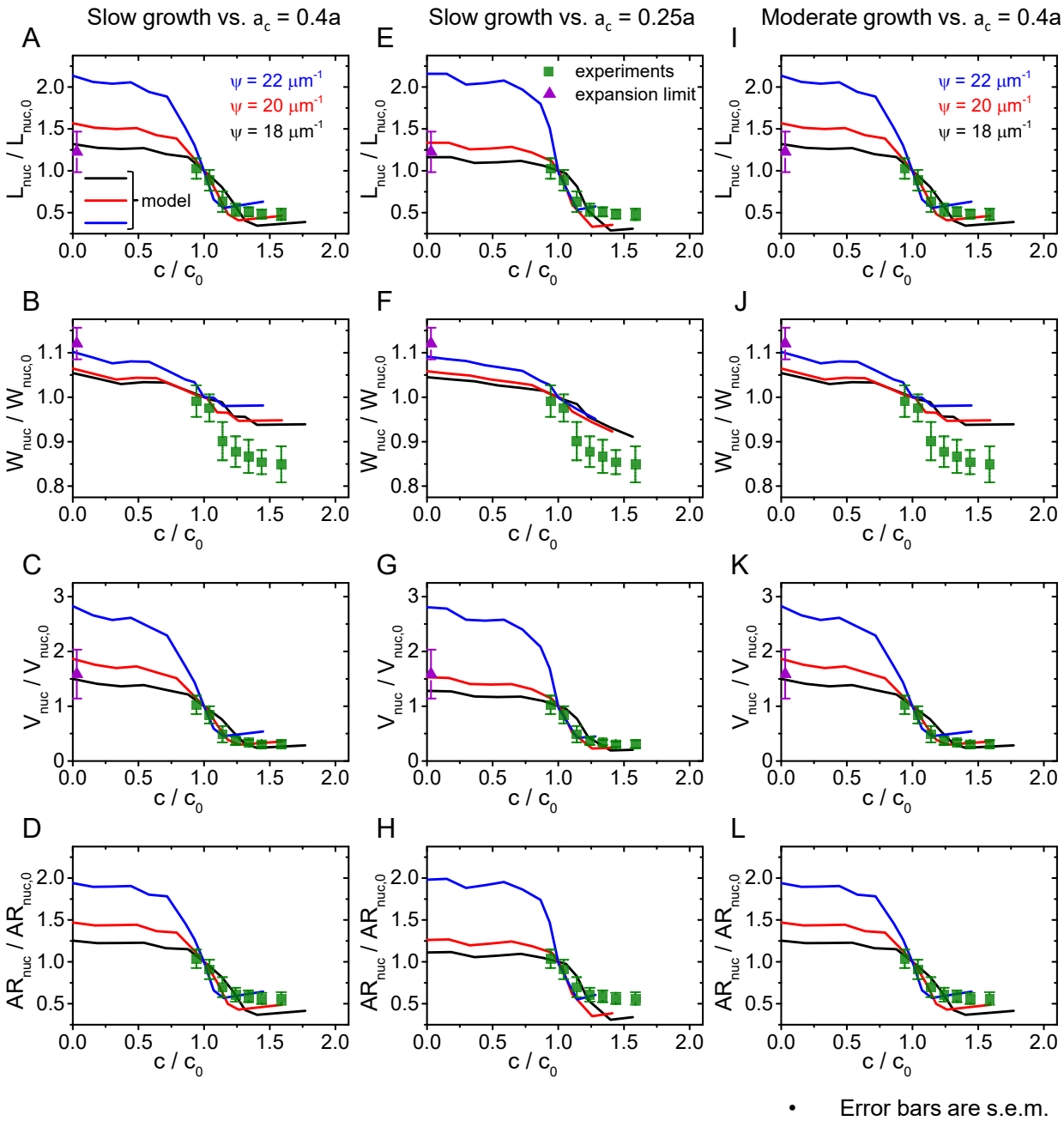


Figure 4-20 : Comparing modeled and observed nucleoids. Experimental data (green squares) are from Figure 4-8). The experimental data is augmented by a data point at the zero crowder concentration limit where the nucleoid is expected to extend over the whole cytosolic volume (violet triangle). A set of curves from the model with "crowding level" 18, 20, 22 μm^{-1} are plotted. Of those the best agreement between the experiment and the model is at 20 μm^{-1}. The error bars for the data are standard deviations.

in vitro. Moreover, in measurements by Krotova et al. [KVM+10] and Yoshikawa et al. [YHMY10], changes in the salt concentration in the medium played an important role in the abrupt change from the coil to the globular configuration of DNA.

The physiological implication of the second order transition is that the nucleoid and cellular processes related to the nucleoid respond to osmolality changes continuously, instead of maintaining a steady nucleoid homeostasis up to a certain shock magnitude and then completely losing this homeostasis in the fashion of an on-off switch.

4.9 Anisotropic Compressibility of the Nucleoid and Bottlebrush-Like Organization of the Chromosome

Our data show that the nucleoid compresses anisotropically at lower crowder concentrations. Its longitudinal compressibility (or in term of Young's modulus) is about four times as high as its radial one. At osmotic shocks of about 1 Osm/kg, nucleoids become spherical and remain spherical at higher shocks (Figure 4-5 C, D). Based on EM images of lysed cells [KB76], it has been proposed that *E. coli* nucleoids have a bottlebrush-like organization with supercoiled segments or just DNA loops stretching out radially from a backbone, which is aligned with the long axes of the cell [WMLR13]. This view also has some support from 3C/Hi-C studies of *Caulobacter crescentus* [LIML13], *Bacillus subtilis* [MLGC+15], and *E. coli* [LCM+18] chromosomes. These studies all show well-defined chromosomal interaction domains, which could correspond to supercoiled segments that stretch radially out from a common backbone.

It can be expected that bottlebrush-like organization leads to anisotropic compressibility. It should be harder to compact plectonemic supercoils along their length, which according to this model, are oriented radially relative to the long axes of the cell. At the same time spacing between supercoils allows them to be easily compacted along the cell length. Although our data appears consistent with the above explanation, the modeling results show that anisotropic compaction can be expected even for the chromosome that lacks supercoiling and is a consequence of cylindrical confinement of the chromosome by the inner membrane. Moreover, it would be unlikely that the anisotropic bottlebrush-like chromosome would be compacted to a spherical entity. The bottlebrush-like structure should retain its anisotropy, and as a result, its aspect ratio should

differ from one, which is contrary to what is found in our experiments (Figure 4-5 C, D). One could argue that a bottlebrush-like organization, which is present in the native state of the nucleoid, could be significantly perturbed by osmotic compaction. This seems to be an unlikely scenario for us because plectonemic interactions should increase rather than decrease as the nucleoid becomes more compacted. Therefore one would expect higher rather than lower anisotropy at higher compression levels, i.e., the stiffness along the backbone should be higher. Altogether, our data favor a more disordered organization of plectonemic supercoils than envisioned by the bottlebrush model where supercoils emanate from a single linear backbone.

4.10 Interplay of Different Crowders in Compacting the Nucleoid

Our data provide new information on how different cytoplasmic macromolecular crowders affect nucleoid compaction. In particular, we find that polysomes cannot be the sole dominant crowder species that leads to nucleoid compaction despite their large volume fraction, high charge state, and prominent exclusion from the nucleoid. These conclusions are based on essentially identical nucleoid compaction curves in two different growth rates, and the insensitivity of these curves to rifampicin treatment. In the following discussions, in order to further rationalize these findings, we estimate the contribution of different macromolecular crowders in compacting the nucleoid based on their literature reported abundances and sizes (Table 4-4). The crowder groups that we consider are cytoplasmic proteins, 30S and 50S ribosomal subunits, tRNA, and poly-ribosomes (polysomes). Not all cytoplasmic proteins qualify as crowders. We exclude DNA binding proteins from this group. Also, we group proteins that are involved in translation together with their rRNA and tRNA counterparts. There are an estimated 3 million proteins in *E. coli* in fast growth conditions [Mil13]. Of those, $20\sim25\%$ qualify as cytoplasmic crowders that are not part of ribosomes, chromosomes, and envelope layers. In slow growth, where the cell needs to synthesize metabolic components from simpler molecules, the fraction of cytosolic crowders can increase to 40% of the total proteome [LBGW14]. $80\sim85\%$ of the cellular RNA content should be a part of the actively translating ribosomes. These ribosomes form polysomes. The remaining 15% of the RNA mass should be in the form of 30S and 50S subunits in moderately fast growth conditions [DZW+17]. In slow growth conditions, the corresponding numbers are 65% for polysomes and 35% for subunits. tRNA abundance is about nine molecules per one ribosome [BD08]. In slow growth conditions,

ribosome to protein mass ratio is estimated to be $1.5 \sim 2.0$ times smaller than that in moderately fast growth conditions [EBD13]. This appears to be the result of a decrease in ribosome concentration in slow growth while its protein concentration remains approximately unchanged.

The results from Kim et al. [KJJ+15] and from our modeling predict that different crowders (indexed by i) contribute to the nucleoid compaction not by their volume fraction but via their crowding level given by Ψ_i. Contributions of different crowder species to the total crowding level $\Psi_{\rm tot} = \sum_i \Psi_i$ can then be characterized by ratio $\Psi_i/\Psi_{\rm tot}$. Using the crowder sizes and abundancies from Appendix D, we estimate that in moderately fast growth conditions polysome and protein based crowders are the main contributors (54%, and 29%, respectively) while the contributions from rRNA subunits and tRNA are smaller (5% and 12%, respectively) (Appendix D). In slow growth conditions, we find the roles of cytosolic proteins and ribosomes reversed. We estimate that proteins contribute 65% and polysomes 22% to the total crowding level (Appendix D). The overall crowding levels, $\Psi_{\rm tot}$, in these two growth conditions are comparable (10% lower in slow growth).

The large contribution of polysomes in the above estimates stems from their large (excluded) volume, which also leads them to be spatially separated from the nucleoid; even at small concentrations. Large contributions of proteins arise from their much larger numbers. Unlike ribosomes, the fraction of proteins that are excluded from the nucleoid needs not to be very large. Even a small fractional difference ($1 \sim 5\%$) in protein concentration between the nucleoid and cytosolic phase is sufficient to cause a similar effect on nucleoid compaction than the ribosomes because of their much larger numbers and translational entropy. Altogether, polysomes and protein crowders are distributed very differently between cytosolic and nucleoid phases but they both have significant contributions to nucleoid compaction. Clearly, the above estimates contain significant uncertainties, as they are based on limited and scattered quantitative data from the concentrations of cellular crowders and their dimensions. Despite these uncertainties, the above analysis points out that cytosolic proteins, beyond polysomes, can be expected to have a significant contribution to nucleoid compaction. Furthermore, the analysis also indicates that the contribution of protein crowders to nucleoid compaction increases as the growth rate slows down. These two broader predictions are consistent with our experimental data.

4.11 Role of Transcription in Determining the Global Size of the Nucleoid

Our experiments indicate that the transcription halting drug, rifampicin, causes a significant increase in nucleoid dimensions in moderately fast growth, but much more limited ones in slow growth conditions longer time scales (> 5 min.). Increased nucleoid expansion at a higher growth rate is consistent with the estimates provided by the crowding level, Ψ_{tot}. Upon dissociation of polysomes in the slow growth condition, we estimate the crowding level to decrease by 9% while in moderately fast conditions, the decrease is 25% (Appendix D). While associated with significant uncertainties, these estimates are consistent with the overall trend in the data. We also found that prior treatment of cells with rifampicin did not significantly alter the size of the nucleoid upon osmotic shock in both growth conditions. While this explanation is consistent with the idea that polysomes have a relatively minor contribution to the nucleoid compaction in slow growth conditions, the same appears not to apply to moderately fast growth conditions where the nucleoid expanded significantly under rifampicin treatment. This finding implies that inhibition of transcription likely has some additional effect on nucleoid compaction beyond the one leading to the dissociation of polysomes. It is likely that transcription could increase supercoiling levels, which in turn could result in more compacted nucleoids. However, the link between increased supercoiling levels and nucleoid compaction has so far not found experimental support *in vivo* [SWvdW+02; CGJ+13]. It has been also reported that at faster growth rates, ribosomal operons (rrnA-G) cluster into a nucleolus-like particle and this clustering might to lead to compaction of the nucleoid [JCM+15]. Nevertheless, the underlying mechanism is not known. Irrespective of the exact mechanism, some transcription related process that is not associated with polysome dissociation appears to play a role in determining the nucleoid size at faster growth rates and alters the nucleoid organization. This effect diminishes at lower growth rates where the total transcription rate (per genome) is also lower.

4.12 Physiological Consequences of Nucleoid Size

Our measurements bring out the importance of macromolecular crowders in determining the size of the nucleoid. It appears to be the leading factor in determining the nucleoid size at slower

growth rates. Furthermore, we find that in slow growth, the contribution from cytosolic proteins dominates over the contribution from polysomes for nucleoid compaction. As the growth rate increases, and with it, the number of polysomes. The latter becomes the dominant crowder species. In all growth conditions, polysomes are essentially excluded from the nucleoid [BCMW14; BSGW12; MW18] while the exclusion of proteins is minor (cf. Figure 4-1). Nevertheless, proteins are capable of contributing to the nucleoid compaction because of their much larger number compared to polysomes. Our data also indicates that at higher growth rates, transertion and likely some other processes influenced by transcription also contribute to the size of the nucleoid and to its distinct folding. The latter mechanism remains to be elucidated.

Finally, our data lend strong support to theoretical ideas and prior *in vitro* measurements that macromolecular crowders confine the nucleoid into a distinct state/phase in *E. coli*. Our data also show that this phase is limited to a relatively narrow level of crowding (Figure 4-21). As predicted by our modeling, a 25% decrease in the crowding level can lead to a completely diffuse chromosome, which fills the whole cytoplasmic volume. This scenario appears in some bacteria. It has been reported, that in *C. crescentus* the chromosomal DNA extends throughout the cytosolic volume [MLJS+10], although it may be excluded from the immediate vicinity of the inner membrane [Wol10]. At the same time, a 30% increase in crowding levels leads to a highly compressed nucleoid according to both experimental and modeling results. Such a nucleoid state would possibly hinder some DNA transactions, such as replication and transcription, as the unwinding of DNA strands requires more energy in a compacted nucleoid. It remains an intriguing question for further research to understand if it is a coincidence that crowding levels are just right to maintain the nucleoid in a sensitive part of the compaction curve or is there some dedicated regulatory mechanisms involved. These mechanisms could possibly control either the cell volume or the number of crowding molecules, although the former seems more plausible.

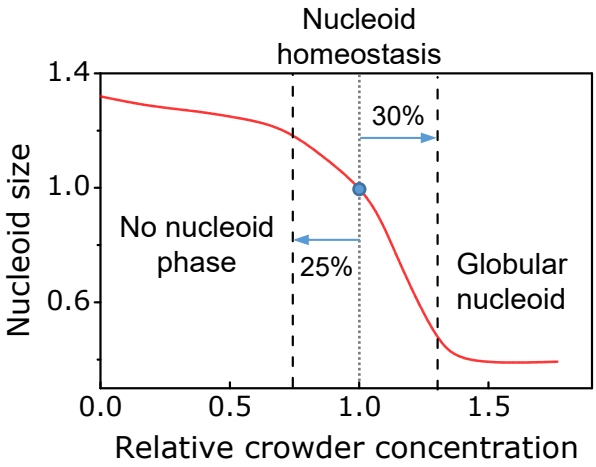


Figure 4-21 : Nucleoid homeostasis in the presence of crowders. A distinct nucleoid where DNA is moderately compacted exists in a limited range of the crowding level. A 25% reduction in crowding levels leads to the abolishment of distinct nucleoid phase from which crowders to some degree are excluded. At the same time, a 35% increase in crowder concentration leads to the formation of globular nucleoid with high compressibility and likely of limited functionality. Red curve is model data at $\Psi = 20\ \mu m^{-1}$ matched approximately to experimentally measured nucleoid length. The blue circle corresponds to a nucleoid size in physiological conditions.

Chapter 5

Concluding Remarks

This dissertation has provided new insights into how the crowded cellular environment compacts the *E. coli* chromosomal DNA using novel microfluidic devices, live-cell microscopy, image analysis, and Langevin dynamics simulations.

Chapter 3 has summarized the development and characterization of three PDMS based microfluidic lab-on-a-chip platforms, which were used to perturb cellular organizations of *E. coli* cells and simultaneously perform high-resolution optical microscopy. Our studies of the dead-end mother-machine platform showed that *E. coli* cells adapted to the confined channel environment by becoming narrower and longer compared to cells growing in liquid culture. Importantly, we found that the primary limiting factor to cell growth (characterized by growth rates and newborn cell dimensions) was the friction between cells and channel walls. In channels, 100 μm and longer, cell doublings could completely stop as a result of friction forces. At the same time, we found the effect of nutrient shielding of the mother cell by the other cells in the channel to be negligible.

In parallel, we improved the performance of the monolithic bilayer microvalves by sealing the bottom of the control channel access hole with the flow layer material and utilizing a soft (FEP) tubing. Pressure in excess of 6 bar could be applied to these devices. At the time of publishing, this was the record pressure under which microfluidic valves had been reported to operate. Using this platform, we were the first to publicly demonstrate that the bilayer monolithic microvalve could be used to deform a bacterial cell at a considerable magnitude (up to 60% cell width increase). We further extended the microvalve platform by redesigning the shape of the valve. The new type of microvalve, which we referred to as the microanvil, has a protrusion on the ceiling of the flow

channel. These protrusions allowed us to divide the cytoplasm of filamentous *E. coli* cells into two chambers. To the best of our knowledge, this was the first time any cell had been artificially divided into two compartments. Moreover, using this device, we noticed separated nucleoids would not mix or even come into contact with each other when pushed toward each other. This observation showed that nucleoids strongly repulse each other, presumably entropically, as had been suggested earlier [JM06]. It invited us to begin the investigation of the role of macromolecular crowding in compacting the *E. coli* nucleoid.

Chapter 4 has described the first quantitative investigation of the effects of macromolecular crowders on the compaction of the *E. coli* nucleoid. In this work, we combined experimental measurements with modeling. In the experimental studies, we used mechanical squeezing and osmotic shocks to vary water content of the bacteria, which led to changes in the volume fraction of crowders. The measurements showed that the nucleoid size decreased linearly as the volume fraction of crowders until the volume fraction exceeded the physiological value by about 30%. Beyond this value, the compressibility diminished to almost zero. In the linear regime, the compressibility of nucleoids was anisotropic. The compressibility ratio along the long and the short axes was about four. Altogether, our data showed that the compression of nucleoids in living cells underwent a smooth coil-globule transition rather than an abrupt transition, which was observed in some *in vitro* experiments [PHH$^+$12; JvdMD11]. Our coarse-grained Langevin dynamics simulations supported these conclusions and were in semiquantitative agreement with the experimental results. Altogether, these data brought out the importance of macromolecular crowders in determining the size of the nucleoid. Also, the data combined with modeling predicted that a physiologically feasible nucleoid phase in limited to a relatively narrow level of crowding. About a 25% decrease in the cellular crowding level would abolish the nucleoid phase, and approximately 30% increase would lead to highly compressed nucleoid where DNA transactions would be likely hindered.

Surprisingly, all the findings mentioned above were independent of the growth conditions of bacteria. Moreover, we have found that the compressibility of the nucleoid is not significantly affected by the halting of transcription. Our interpretation of these data was that in addition to poly-ribosomes, which had been considered as the dominant crowder species, the cytoplasmic proteins have a significant contribution in determining the size of the nucleoid. The contribution of poly-ribosomes dominates at faster and soluble proteins at slower growth rates.

The work presented in this dissertation has provided new insights into the physical organization of the *E. coli* chromosome at the global (whole cell) level. Nevertheless, a complete picture of nucleoid size regulation is yet to emerge. In turn, how the nucleoid size modulates the accessibility of genetic loci to the central dogma machines is another interesting question. Further studies on the intermediate scales ($\sim 100\ nm$) are needed to address these questions.

Chapter 6

Outlook on Future Work

This work has inspired some interesting questions. Compaction of the nucleoid can be expected to affect the accessibility of genetic loci to the RNA polymerases (RNAPs). At which crowding level would the RNAP diffusion or transcription activities be shut down? To answer that question, one could use single-molecule tracking of RNAP or fluorescent recovery after photobleaching (FRAP) of some transcription activity indicator.

Meanwhile, when the crowding level mildly increases, the accessibility of genetic loci to RNAPs should decrease, and the RNAP search speed should be reduced. In turn, transcription activities should be hindered. This will lead to a reduction of polysome concentration, and the crowding level will go down. Overall, there should be an oscillation in the crowding level at some time scale. On the other hand, it has been observed that the nucleoid size oscillates throughout the cell cycle [FBW+13]. The frequency of the oscillation was thought to be independent of growth conditions.

Therefore, we could try and find out whether the crowding level oscillates. If the answer is positive, how it depends on the growth condition is the next question. To study that, one could utilize cytoplasmic Förster resonance energy transfer (FRET) sensors [BZP15] as a reporter for the crowding levels. Finally, those two frequencies can be compared. One could even create an *E. coli* strain that has both a FRET reporter and a nucleoid reporter if the other results were promising.

I also summarize some preliminary results on other fronts in Sections 6.1 and 6.2.

6.1 Design of Valve Chips with Tapered Anvils

Our current device for mechanical perturbations have performed as expected. Though with a low throughput, we were able to obtain interesting data (Section 3.3). The idea for improvement was making the anvils tapered. A tapered anvil would provide narrower contact area between post and cell, and also prevents itself from crumpling when squeezing. Further, it would ensure mold releasing. The PDMS pre-polymers used are $\sim$60 mer, which results in a sub-nanometer surface roughness [SSC+09]. We have identified the desisted dimensions of the taper and we searched for the corresponding reactive ion etching parameters. We also wish to design and fabricate devices that allow us to work with rich medium, which does not work well with our current devices (microanvil). Here, the search for design and etching parameters has been summarized.

6.1.1 Design of Valve Post Chips with Tapered Posts

We decided the tip of the tapered post to be 0.5 μm; then considering the Young's modulus of PDMS being lower than that of the cells, we decided the height of the tapered post to be 1.5 μm–to work with cells with typical diameter of 0.6 μm.

The dimension of the flow channel is set at 2.5 μm wide by 2.5 μm high, and the length of post is set at 11 μm. Then we adjust sizes of the pocket opening, O, and the width of the base of tapered anvils, B (Figure 6-3 A).

When the pocket opening is fixed at 2 μm, we modeled chips with different widths of the tapered posts. Post profiles at various pressures are plotted separately in Figure 6-3 B-D and comparatively in Figure 6-1 A. We compared the post center displacements and post center tensile stresses of these designs and find that it is optimal when the base width of the post is 1.2 μm (Figure 6-1 B, C) Therefore, we fix the base width at 1.2 μm, and modeled chips with different pocket openings. And, we find that it is optimal when the pocket opening is at 4.0 μm (Figure 6-1 D, E). Thus, we are looking to fabricate tapered post with tip width, 0.5 μm, base width, 1.2 μm, and long 11 μm.

We also compared these results to our original design, VPC8; and our original design with tapered posts. Though the center displacements do not differ much, the post center tensile stresses is increased with this new design (Figure 6-2 A, C).

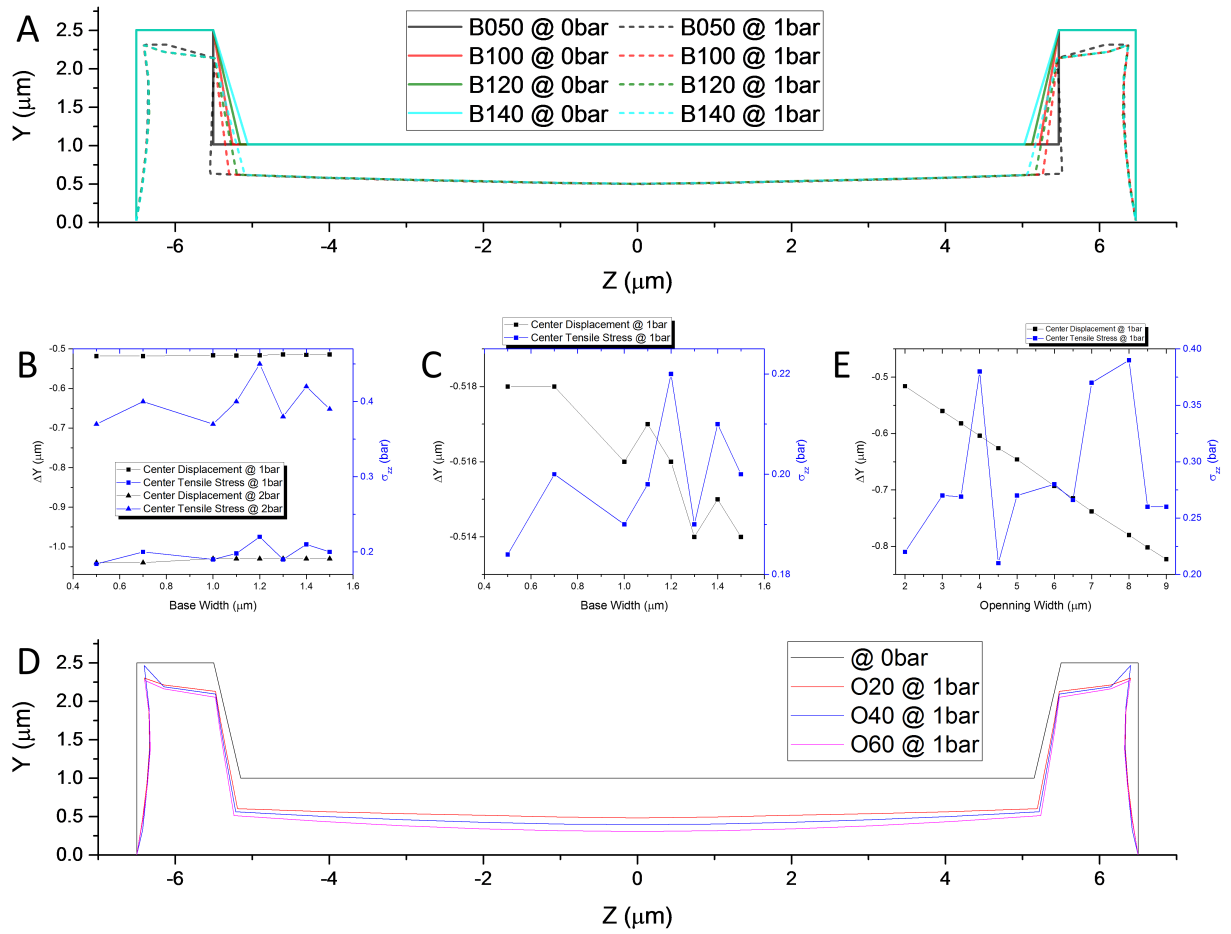


Figure 6-1 : Finite element analysis (Part II). (A) Profiles of tapered posts with pocket opening fixed at 2 μm and various post base width, and under various applied pressure, plotted collectively; (B, C) Comparison of the post center displacements and post center tensile stresses with pocket opening fixed at 2 μm and various post base width; (D) Profiles of tapered posts with post base width fixed at 1.2 μm and various pocket opening; (E) Comparison of the post center displacements and post center tensile stresses with post base width fixed at 1.2 μm and various pocket opening.

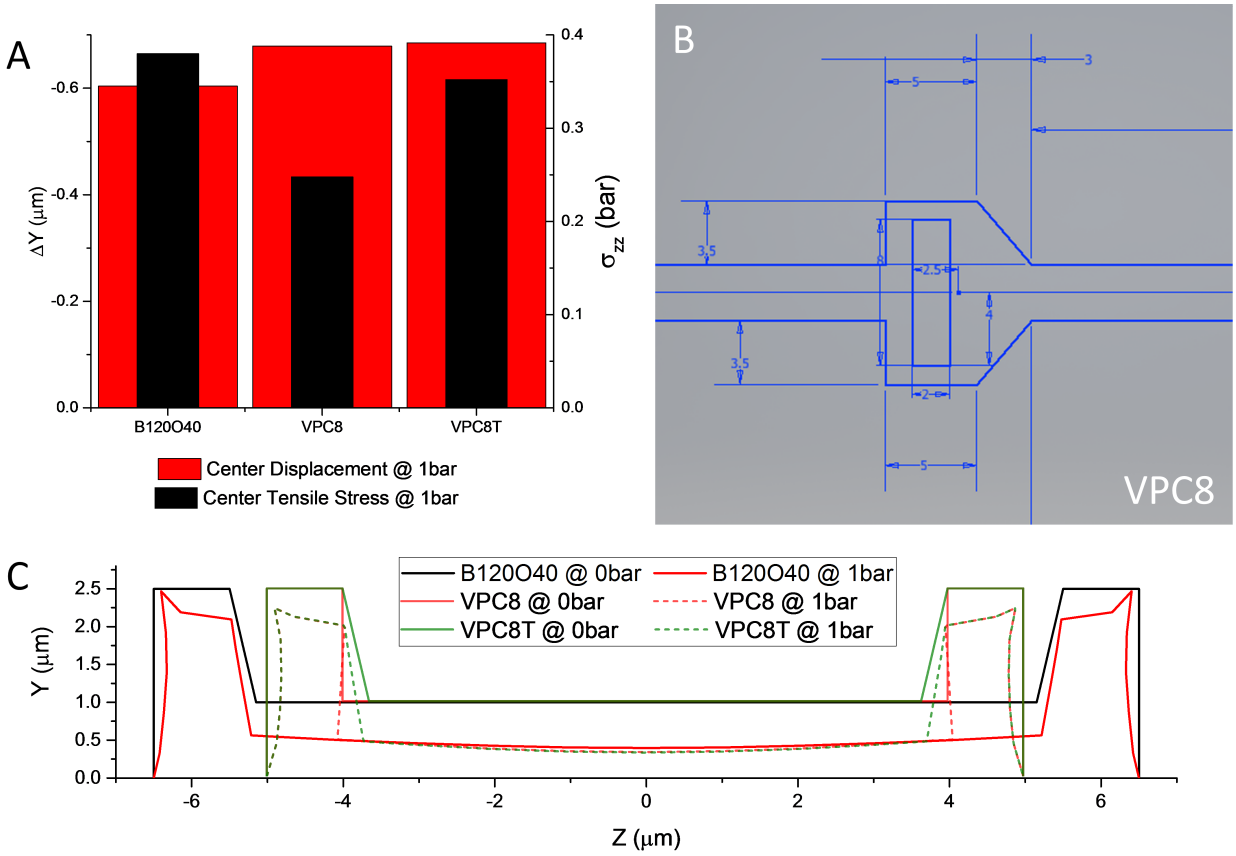


Figure 6-2 : Finite element analysis (Part III). (A) Comparison of the post center displacements and post center tensile stresses among different designs; (B) Design of the original valve post chip; (C) Profiles of posts in various designs.

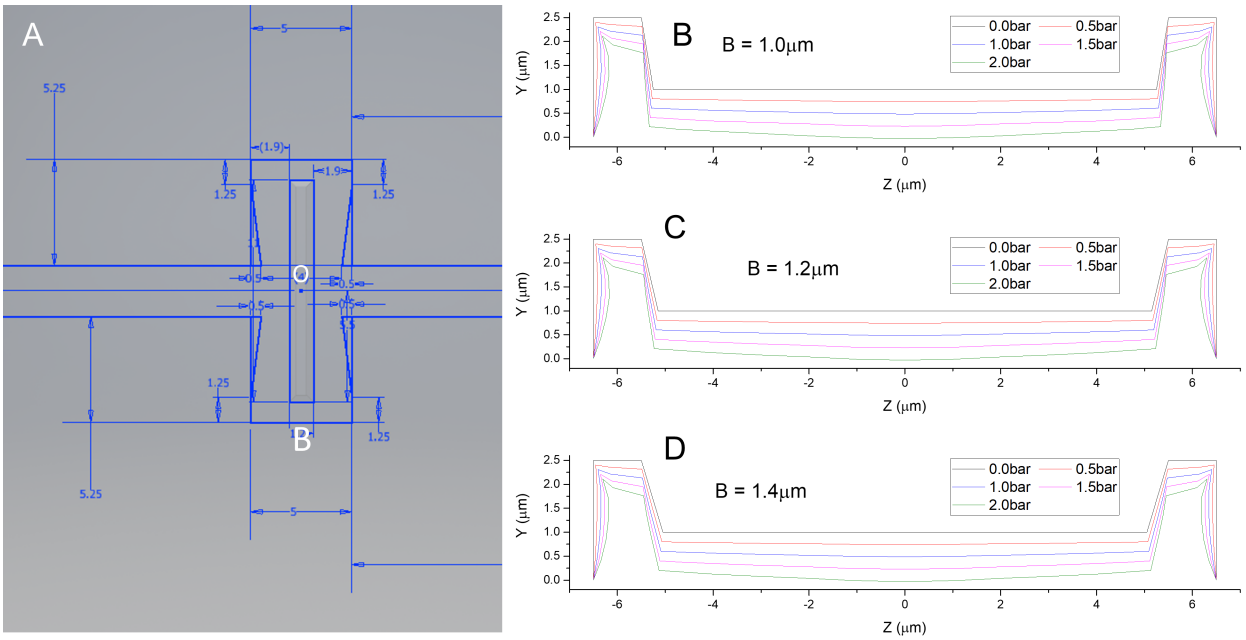


Figure 6-3 : Finite element analysis (Part I). (A) Design of the new valve vhip with tapered posts; (B-D) Profiles of tapered posts with pocket opening fixed at $2\mu m$ and various post base width, and under various applied pressure.

6.1.2 Searching for Corresponding Reactive Ion Etching Parameters

We first obtained the e-beam pattern to PDMS transfer function (Figure 6-4). Then we try to find the etching parameters that correspond to our design (Figure 6-5). The etching process was not particularly clean, i.e., leaving a lot of polymer residuals, which hindered the etch rate. It might be necessary to increase the proportion of Ar in the processing chamber or run a O_2 cleaning between two etching cycles.

6.2 Septum Constriction Induces Partitioning of Nucleoids During Cell Division

6.2.1 Motivation

In wild-type *E. coli* cells, the division plane is accurately placed relative to chromosomes [BBW+14; MB15], and there is minimal need for chromosomes to move during cell division. However, when the placement of cell division plane is perturbed, chromosomes move during cell division. The majority of chromosomal movement during cell division appears to be the result of DNA pumping by FtsK protein [MBOM17]. Nevertheless, the data show that in cells with inactive FtsK, some movement of chromosomes still occurs during cell division. This movement appears to help in partitioning chromosomes to daughter cells. We have hypothesized that this movement can be explained by equilibrium thermodynamics. Here, we summarized the preliminary experimental and modeling results that showed support of this hypothesis.

6.2.2 Mechanical Squeezing Induces Movement of Nucleoids During Cell Division

By applying a steady pressure to the control line, we have observed a large-scale movement of nucleoids out from constricted regions (Figure 6-6 A, B). When pressure is released these nucleoids move back to the previously constricted region (6-6 B, to the right of the dashed rectangle). The extent and speed of the movement depend on how much cell has been constricted (squeezed) by the post. We have scored the nucleoid movements caused by different levels of squeezing: 0 for no visible movements, 0.5 for movement when nucleoid partially moves away from the constricted region (such as shown in Figure 6-6 A, B), and 1 for a total displacement of chromosomal mass

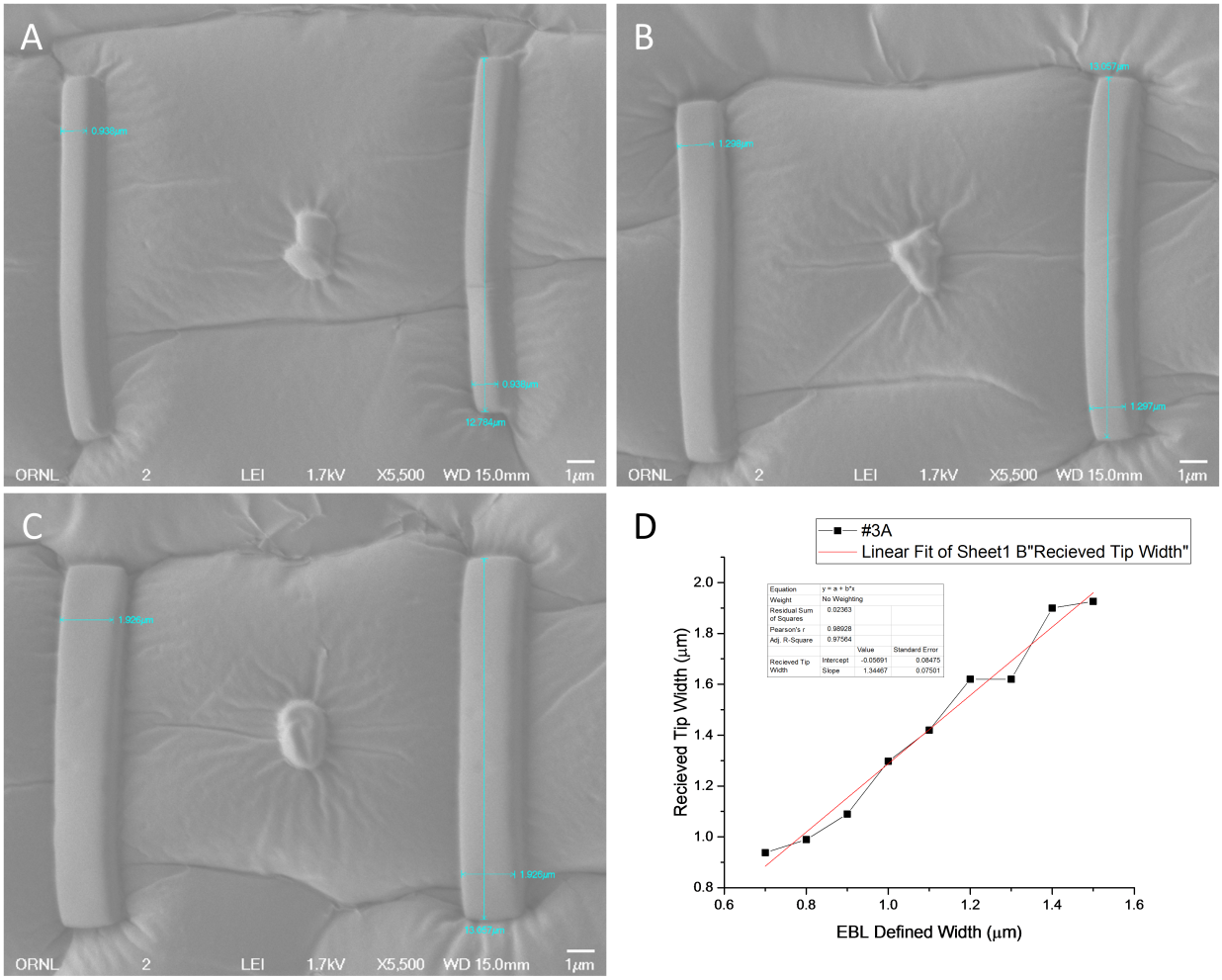


Figure 6-4 : RIE for tapered anvils (Part II). (A-C) SEM images of PDMS replica of silicon wafer etched with original waveguide etch recipe for different e-beam patterns; A: 0.7; μm, B: 1.0 μm, C: 1.5; μm; (D) Plot and fitting for the e-beam pattern to PDMS transfer function.

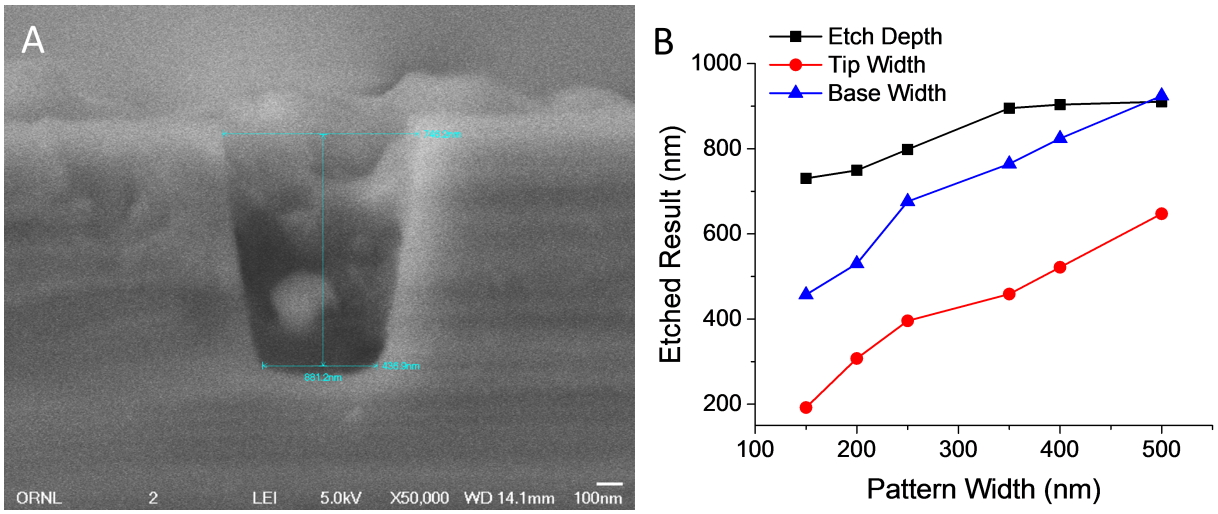


Figure 6-5 : RIE for tapered anvils (Part II). (A) SEM image of etched silicon with ZEP520A mask patterned 250 *nm* wide line. (B) Plot of length measurements of etching results with various ZEP520A mask width. The machine parameter used here are: C_4F_8 flowing at 50.0 ± 0.3 *sccm*, SF_6 at 25.0 ± 0.2 *sccm*, and Ar at 5.0 *sccm*, the ICP forward power at 1200 ± 30 W, RF Forward Power at 40 ± 1 W, processing pressure 12.0 ± 0.1 $mTorr$, processing temperature, 20℃.

from the region under the post. We find the nucleoid movement scores strongly correlated with the level of squeezing (6-6 C). Here, the degree of squeezing is quantitatively given by the normalized height of the cell at the center of the post (Figure 3-17 E).

We have also studied the kinetics of the nucleoid movement. To characterize the time it takes for the nucleoid to move from the constricted region, we follow the position of nucleoid edge as a function of time. We fit the gap length under post versus time curve to an exponential function (Figure 6-6 D). The characteristic times from the fitted exponents are plotted in Figure 6-6 E for both the chromosomal responses to applying pressure and releasing pressure.

6.2.3 Equilibrium Thermodynamics Allows Triple Deletion Cells to Survive

We have hypothesized that this movement can be explained by equilibrium thermodynamics. DNA trapping by the closing septum can lead to a significant reduction of local DNA phase-space volume. This decrease produces an entropic force that pushes DNA from the septum to one or another daughter cell. This very primitive partitioning mechanism could have been present in early cells,

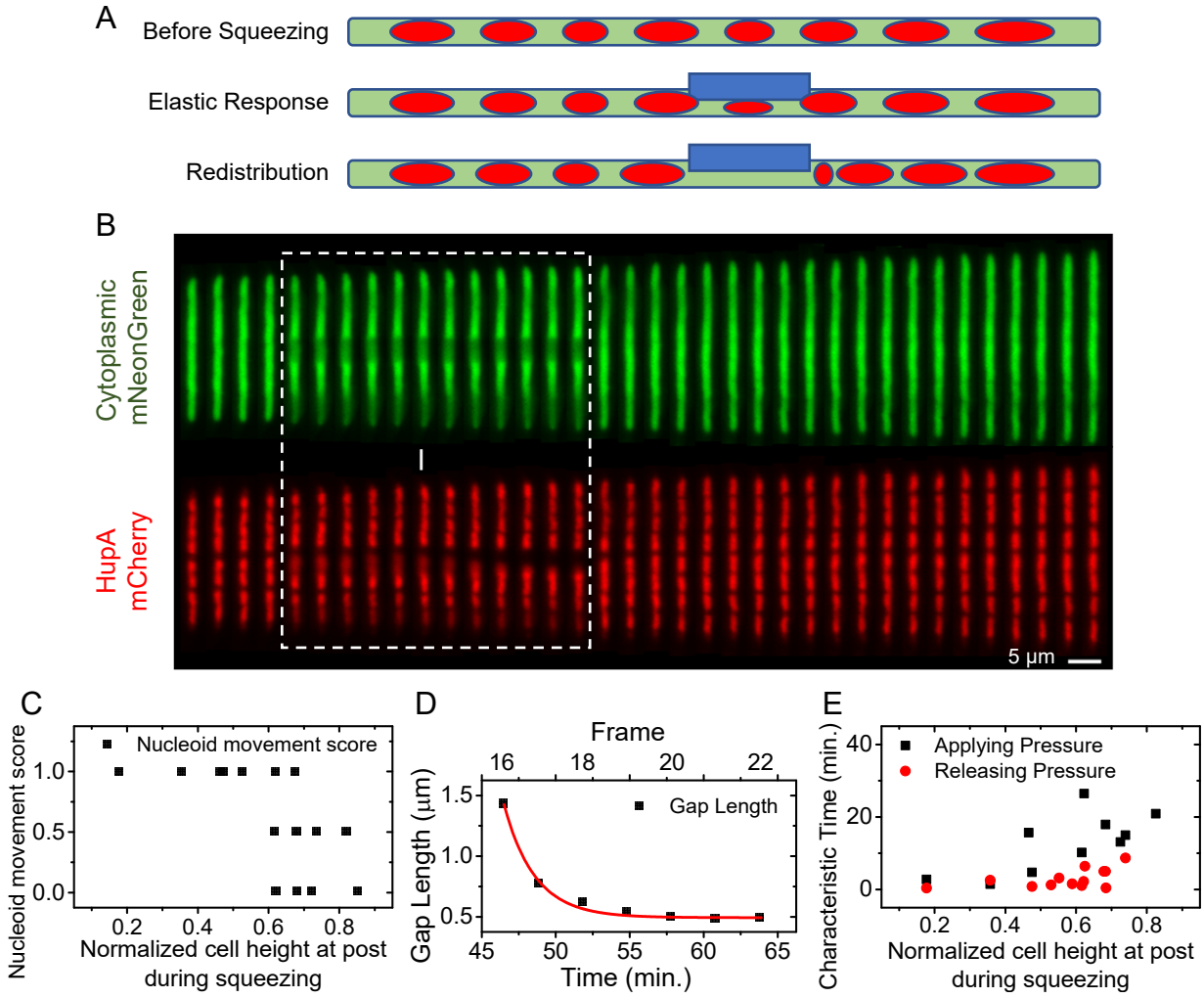


Figure 6-6 : Nucleoid deformation and displacement Due to squeezing. (A) An abstraction of our observations. The nucleoid under the post before squeezing is first compressed then contracts, and later completely moves our of under the post. (B) Fluorescent montages of cytoplasm (green) and nucleoids (red) of an experiment showing chromosome reorganization during and after squeezing. The modulated signals near cell middle in the green montage are at the location of the post. A control pressure of 45 psi is applied for frames inside the dashed rectangle. The white mark labels the first frame for nucleoid edge movement. (C) Nucleoid movement scores as a function of normalized cell height at post. (D) The recover of gap length under the post after squeezing in the experiment shown in (B). The data is fitted to an exponential decay function. (E) Characteristic time of nucleoid movement as a function of the normalized cell height at post. The values of characteristic times are from fittings similar to what is shown in (D).

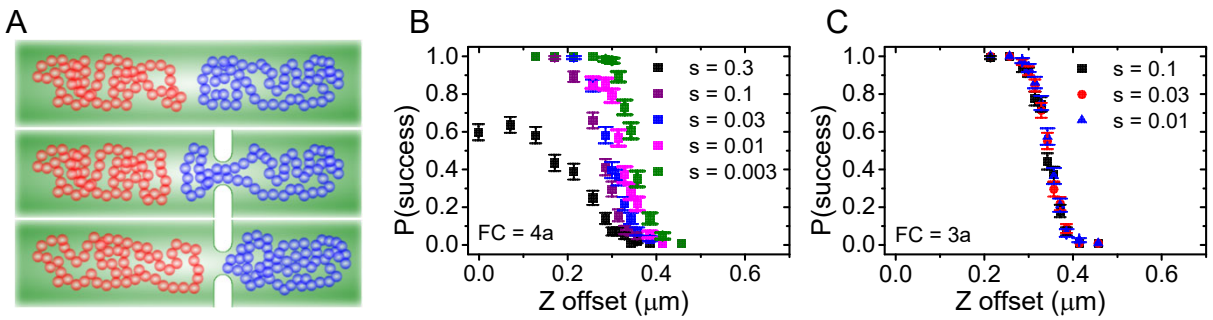


Figure 6-7 : Effect of septum closing with various speed. (A) The evolution of geometry of the simulations. Top panel: two ring polymers were placed in opposite halves of a cylindrical constraint. Each polymer has one monomer subunit fixed at the cell middle. Middle panel: After the system was equilibrated, an off-middle constriction was slowly tightened until it reached a preset final constriction diameter ($FC = 3a$ or $4a$). Bottom panel: Previously fixed monomers are unfixed, and the system is allowed to equilibrate. (B) Success rate of septum closing at $FC - 3a$. (C) The same as (B) at $FC - 4a$.

which lacked sophisticated positioning systems for the Z-ring and were absent of DNA translocase FtsK.

First, two ring polymers were placed in opposite halves of a cylindrical constraint (Figure 6-7 A). In the beginning, each polymer had one monomer subunit fixed at the cell middle. After the system was equilibrated, an off-middle constriction was slowly tightened until it reached a preset final constriction diameter ($FC = 3a$ or $4a$). Then, those two previously fixed monomers are unfixed, and the system was allowed to equilibrate for $50,000$ simulation time (sampled in 100 simulation time/frame). Often, misaligned constrictions would induce movement of polymer chains, such that an entire chain would be on the same side of the constriction Finally, we attempted to close the pore constriction fully.

If one or more FENE bonds were broken by the action of septum closing, we counted the simulation as a failed trial. We run 128 simulations for each offset of division plane placement and each septum closing speed, s. Here, septum closing speed is in the unit of $a/100$ simulation time. We found that at $FC - 3a$, septum closing speed does not affect the success rate of cell division. Cell divisions are more likely to succeed if the offset of division plane placement is less than 12% of cell length (Figure 6-7 B). While at $FC = 4a$, at the lowest septum closing speed we have simulated, the critical offset is also at 12% of cell length. Nevertheless, as the septum closing speed increase,

the critical offset decreases (Figure 6-7 C). At the septum closing speed of $s = 0.3$, the cell division success rate does not reach 1, even when the division plane is placed at cell middle (Z offset = 0).

We fitted the success rates shown in Figure 6-7 C to the Boltzmann sigmoid function and plotted the fitted parameters (Figure 6-8). The data shown in Figure 6-7 C was fitted in two ways. First, we did not set any constraints on the fitting to the sigmoidal function (Figure 6-8 A). Second, the limits of the sigmoidal functions were fixed at 0 and 1 (Figure 6-8 B). The parameter fixing did not effect the characteristics in which we were interested (Figure 6-8 C, D). The fitted critical offset, z_0, decreases with the septum closing speed, while the fitted slope increases with the septum closing speed. Within the range of our simulations, the critical offset is no less than 0.2 μm, which would allow the majority of triple deletion cells to survive.

6.2.4 Mode of Septum Constriction Has No Effect on Cell Division Success Rate

Similar to Section 6.2.3, we placed two ring polymers in opposite halves of a cylindrical constraint. But, we did not fix any monomers throughout simulations. After the system is equilibrated, we directly attempted to close an off-center constriction. If one or more FENE bond was broken by the action of septum closing, we count the simulation as a failed trial. We run 64 simulations for each offset of division plane placement and each septum closing setting. The septum closing was described by the pore radius as a function of simulation time.

$$R(j) = R_0 \left(1 - (j \cdot \tau)^{\alpha}\right)^{1/\alpha} . \tag{6.1}$$

We found that with all three different mode of septum constriction, α, simulated, faster septum closing led to smaller critical division plane offset (Figure 6-9 A, B, C). However, with the same septum closing speed, i.e., the time required for septum closing, the critical division plane offset did not significantly change with α (Figure 6-9 D).

6.2.5 Longer Cells Are More Likely to Survive Division Plane Offset

Furthermore, we explored the effect of cell lengths on critical division plane offset (fitted z_0). Similar to our simulations in the previous section ($\alpha = 2$ and $\tau = 0.01$).

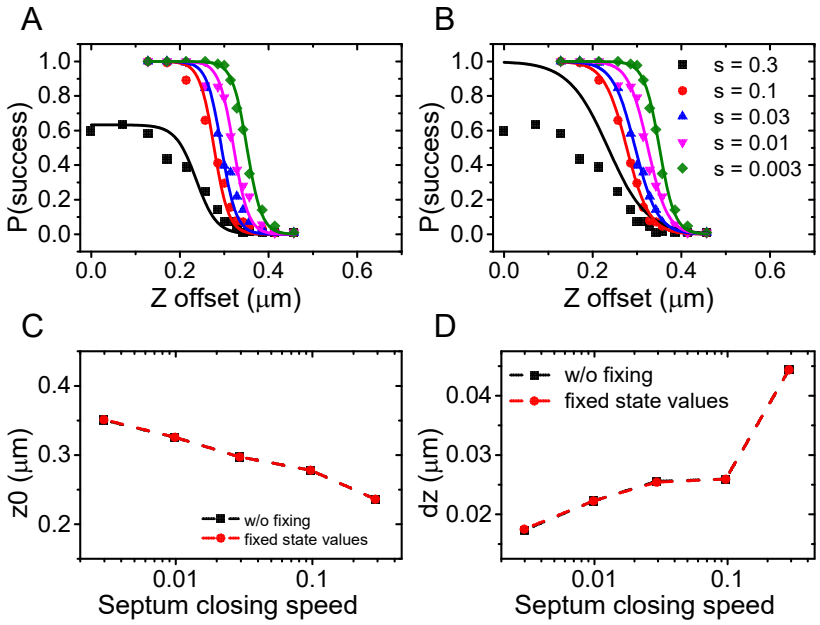


Figure 6-8 : Parameters describing the dependencies of cell division success rate on the offset of division plane placement. (A) Curve fitting to sigmoidal functions. The data if from Figure 6-7 C. (B) The same as (A) but the limits of the sigmoidal functions are fixed at 0 and 1. (C) The fitted critical offset as a function of the septum closing speed. (D) The fitted slope as a function of the septum closing speed.

In cells longer than 6 μm, cell division can successfully close with dependence probability regardless of division plane offset (Figure 6-10 A, B). We fitted data from cells shorter than 6 μm to sigmoid functions (Figure 6-10 C). In cells shorter than 6 μm, critical division plane offset increases with cell length (Figure 6-10 D, E).

6.2.6 Further Experiments

So far, we do not have any experimental results with spontaneously dividing cells to compare to these modeling results. A good *E. coli* strain for this could be a $\Delta slmA$ $\Delta zapB$ double deletion strain (cf. Chapter 1).

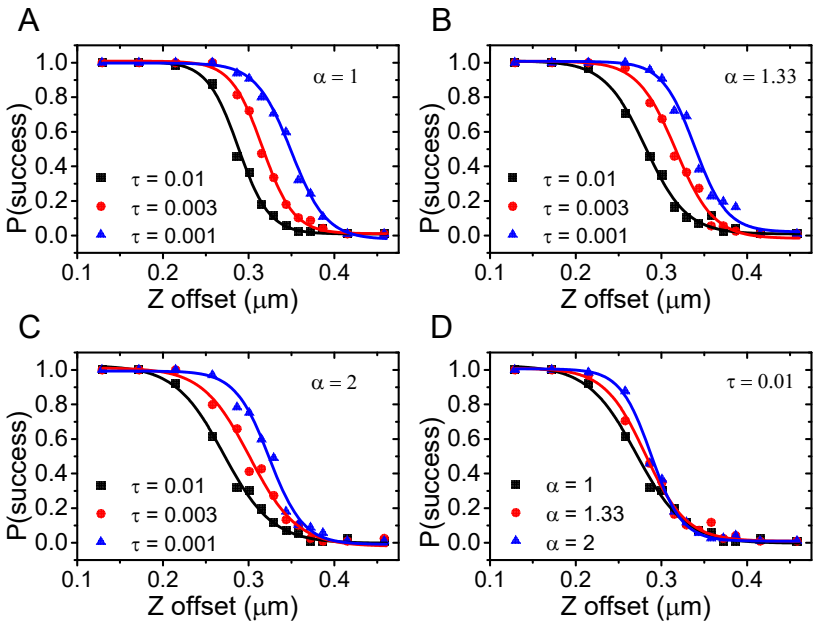


Figure 6-9 : Success rate for asymmetric cell divisions of different mode of septum closing. (A-C) Success rate of septum closing at various plane off-set for three different mode of septum constriction, α at three different septum closing speed. (D) Success rate of septum closing at various plane off-set for three different α at $\tau = 0.01$.

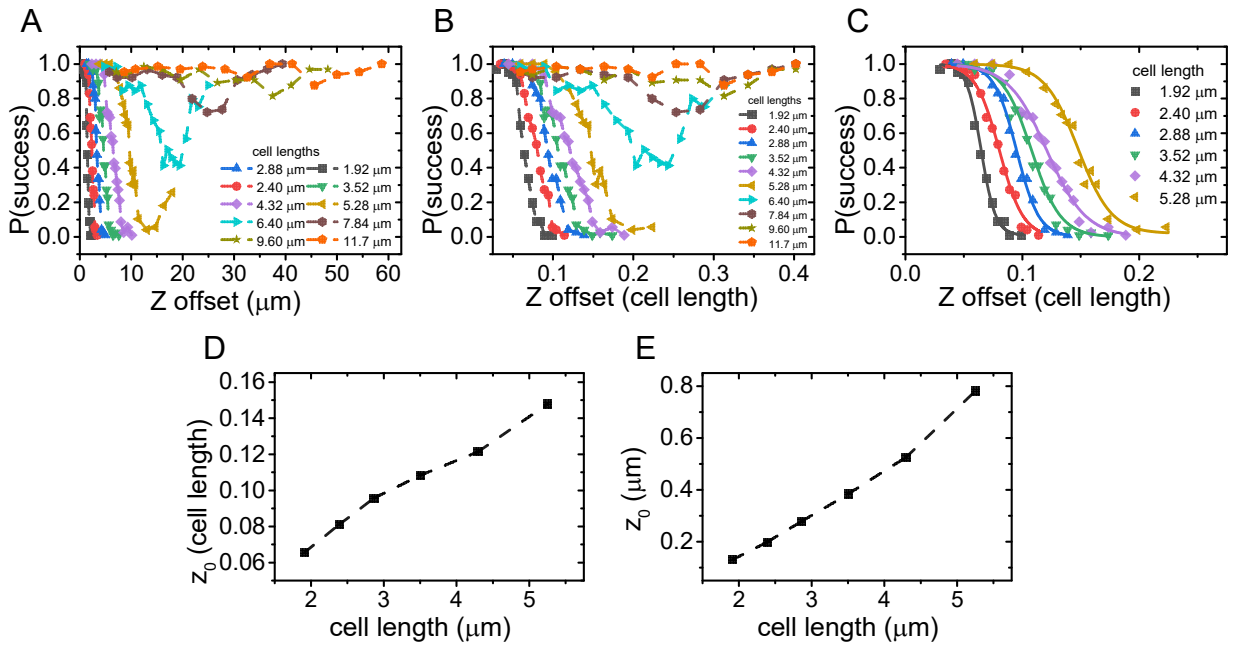


Figure 6-10 : Success rate for asymmetric cell divisions of various cell lengths. (A) Success rate for asymmetric cell divisions of various cell lengths using um as unit of division plane offset. (B) The same as (A) using cell length as unit of division plane offset. (C) Fitting a portion of the results to sigmoidal functions. (D, E) Parameters describing the dependencies of cell division success rate on the offset of division plane placement using the same two different units of division plane offset.

Bibliography

[ABM+14] Ariel Amir, Farinaz Babaeipour, Dustin B. McIntosh, David R. Nelson, and Suckjoon Jun. Bending forces plastically deform growing bacterial cell walls. *Proceedings of the National Academy of Sciences of the United States of America*, 111(16):5778, 2014. 67

[AJL+14] B. Alberts, A. Johnson, J. Lewis, D. Morgan, M. Raff, K. Roberts, and P. Walter. *Molecular Biology of the Cell*. Garland Science, sixth edition, 2014. 5

[ALA99] D. Armani, C. Liu, and N. Aluru. Re-configurable fluid circuits by pdms elastomer micromachining. In *MEMS '99: Twelfth IEEE International Conference on Micro Electro Mechanical Systems, Technical Digest*, Proceedings: Ieee Micro Electro Mechanical Systems Workshop, pages 222–227, 1999. 51, 89

[All04] Michael P Allen. Introduction to molecular dynamics simulation. In Norbert Attig, Kurt Binder, Helmut Grubmüller, and Kurt Kremer, editors, *Computational soft matter: from synthetic polymers to proteins - Lecture Notes*, volume 23 of *NIC Series*, pages 1–28, Jülich, Germany, 2004. John von Neumann Institute for Computing, NIC-Directors. 53

[And83] Hans C. Andersen. Rattle: A "velocity" version of the shake algorithm for molecular dynamics calculations. *J. Comput. Phys.*, 52(1):24, 1983. 52

[ANH+06] S. Araki, T. Nakai, K. Hizume, K. Takeyasu, and K. Yoshikawa. Hydrodynamic radius of circular dna is larger than that of linear dna. *Chem Phys Lett*, 418(1-3):255, 2006. 14

[AOM+15] Aileen Adiciptaningrum, Matteo Osella, M. Charl Moolman, Marco Cosentino Lagomarsino, and Sander J. Tans. Stochasticity and homeostasis in the e. coli replication and division cycle. *Scientific reports*, 5, 2015. 66, 70

[Bai16] Matthew Wayne Bailey. *Biophysical Studies of Cell Division Protein Localization Mechanisms in Escherichia coli*. Thesis, University of Tennessee, 2016. 38

[BBS+14] N. A. Baeshen, M. N. Baeshen, A. Sheikh, R. S. Bora, M. M. M. Ahmed, H. A. I. Ramadan, K. S. Saini, and E. M. Redwan. Cell factories for insulin production. *Microb. Cell. Fact.*, 13:9, 2014. 3

[BBT+17] Ozden Baltekin, Alexis Boucharin, Eva Tano, Dan I. Andersson, and Johan Elf. Antibiotic susceptibility testing in less than 30 min using direct single-cell imaging. *Proceedings of the National Academy of Sciences of the United States of America*, 114(34):9170, 2017. 67, 87

[BBW+14] Matthew W. Bailey, Paola Bisicchia, Boyd T. Warren, David J. Sherratt, and Jaan Maennik. Evidence for divisome localization mechanisms independent of the min system and slma in escherichia coli. *PLoS genetics*, 10(8), 2014. 9, 66, 151

[BC87] James B. Bliska and Nicholas R. Cozzarelli. Use of site-specific recombination as a probe of dna structure and metabolism in vivo. *Journal of molecular biology*, 194(2):205, 1987. 19

[BCMW14] S. Bakshi, H. Choi, J. Mondal, and J. C. Weisshaar. Time-dependent effects of transcription- and translation-halting drugs on the spatial distributions of the escherichia coli chromosome and ribosomes. *Molecular microbiology*, 94(4):871, 2014. 20, 23, 124, 126, 130, 141

[BCW15] S. Bakshi, H. Choi, and J. C. Weisshaar. The spatial biology of transcription and translation in rapidly growing escherichia coli. *Front Microbiol*, 6:636, 2015. 23, 124, 130

[BD08] H Bremer and P Dennis. Modulation of chemical composition and other parameters of the cell at different exponential growth rates. *EcoSal Plus*, 2008. 8, 24, 106, 138, 205

[BdG77] F. Brochard and P. G. de Gennes. Dynamics of confined polymer chains. *The Journal of chemical physics*, 67(1):52, 1977. 14

[BFH+01] I. Broadwell, P. D. Fletcher, S. J. Haswell, T. McCreedy, and X. Zhang. Quantitative 3-dimensional profiling of channel networks within transparent lab-on-a-chip microreactors using a digital imaging method. *Lab on a chip*, 1(1):66, 2001. 91

[BK05] D. Bates and N. Kleckner. Chromosome and replisome dynamics in e. coli: Loss of sister cohesion triggers global chromosome movement and mediates chromosome segregation. *Cell*, 121(6):899, 2005. 106

[BKC+99] M. J. Borgnia, D. Kozono, G. Calamita, P. C. Maloney, and P. Agre. Functional reconstitution and characterization of aqpz, the e-coli water channel protein. *Journal of molecular biology*, 291(5):1169, 1999. 8

[BKL+02] J. A. Bernstein, A. B. Khodursky, P. H. Lin, S. Lin-Chao, and S. N. Cohen. Global analysis of mrna decay and abundance in escherichia coli at single-gene resolution using two-color fluorescent dna microarrays. *Proceedings of the National Academy of Sciences of the United States of America*, 99(15):9697, 2002. 127

[BLY+16] R. Buda, Y. X. Liu, J. Yang, S. Hegde, K. Stevenson, F. Bai, and T. Pilizota. Dynamics of escherichia coli's passive response to a sudden decrease in external osmolarity. *Proceedings of the National Academy of Sciences of the United States of America*, 113(40):E5838, 2016. 8

[BM05] C. J. Benham and S. P. Mielke. Dna mechanics. *Annu Rev Biomed Eng*, 7:21, 2005. 17

[BOPM18] Y. M. Bar-On, R. Phillips, and R. Milo. The biomass distribution on earth. *Proceedings of the National Academy of Sciences of the United States of America*, 115(25):6506, 2018. 2

[Bot15] D. Botstein. *Decoding the Language of Genetics*. Cold Spring Harbor Laboratory Press, 2015. 4

[BSGW12] S. Bakshi, A. Siryaporn, M. Goulian, and J. C. Weisshaar. Superresolution imaging of ribosomes and rna polymerase in live escherichia coli cells. *Molecular microbiology*, 85(1):21, 2012. 23, 127, 141

[BZP15] A. J. Boersma, I. S. Zuhorn, and B. Poolman. A sensor for quantification of macromolecular crowding in living cells. *Nature methods*, 12(3):227, 2015. 146

[CBC+99] D. J. Campbell, K. J. Beckman, C. E. Calderon, P. W. Doolan, R. M. Ottosen, A. B. Ellis, and G. C. Lisensky. Replication and compression of bulk and surface structures with polydimethylsiloxane elastomer. *J. Chem. Educ.*, 76(4):537, 1999. 45, 46

[CCQ+09] J. E. Cabrera, C. Cagliero, S. Quan, C. L. Squires, and D. J. Jin. Active transcription of rrna operons condenses the nucleoid in escherichia coli: Examining the effect of transcription on nucleoid structure in the absence of transertion. *Journal of bacteriology*, 191(13):4180, 2009. 20, 126

[CGJ+13] C. Cagliero, R. S. Grand, M. B. Jones, D. J. Jin, and J. M. O'Sullivan. Genome conformation capture reveals that the escherichia coli chromosome is organized by replication and transcription. *Nucleic acids research*, 41(12):6058, 2013. 19, 103, 118, 140

[CH68] S. Cooper and C. E. Helmstetter. Chromosome replication and division cycle of escherichia coli b/r. *Journal of molecular biology*, 31(3):519, 1968. 73

[Cha01] J. J. Champoux. Dna topoisomerases: structure, function, and mechanism. *Annual review of biochemistry*, 70:369, 2001. 17, 18

[CRPL17] Matthew T. Cabeen, Jonathan R. Russell, Johan Paulsson, and Richard Losick. Use of a microfluidic platform to uncover basic features of energy and environmental stress responses in individual cells of bacillus subtilis. *PLoS genetics*, 13(7), 2017. 67, 87

[CSK+14] Manuel Campos, Ivan V. Surovtsev, Setsu Kato, Ahmad Paintdakhi, Bruno Beltran, Sarah E. Ebmeier, and Christine Jacobs-Wagner. A constant size extension drives bacterial cell size homeostasis. *Cell*, 159(6):1433, 2014. 70

[Cĕ61] G. Călugăreanu. Sur les classes d'isotopie des noeuds tridimensionnels et leurs invariants. *Czechoslovak Mathematical Journal*, 11(4):588, 1961. 15

[CVF96] B. P. Cormack, R. H. Valdivia, and S. Falkow. Facs-optimized mutants of the green fluorescent protein (gfp). *Gene*, 173(1 Spec No):33, 1996. 33

[CWO01] S. Cunha, C. L. Woldringh, and T. Odijk. Polymer-mediated compaction and internal dynamics of isolated escherichia coli nucleoids. *Journal of structural biology*, 136(1):53, 2001. 19, 30, 103

[CYWL15] Y. Chen, W. Yu, J. Wang, and K. Luo. Polymer segregation under confinement: Influences of macromolecular crowding and the interaction between the polymer and crowders. *The Journal of chemical physics*, 143(13):134904, 2015. 26

[Dam05] R. T. Dame. The role of nucleoid-associated proteins in the organization and compaction of bacterial chromatin. *Molecular microbiology*, 56(4):858, 2005. 19

[DD10] S. C. Dillon and C. J. Dorman. Bacterial nucleoid-associated proteins, nucleoid structure and gene expression. *Nature reviews. Microbiology*, 8(3):185, 2010. 19, 22

[Des00] Markus Deserno. *Counterion condensation for rigid linear polyelectrolytes*. Thesis, Johannes Gutenberg-Universität in Mainz, 2000. 52

[DKG11] R. T. Dame, O. J. Kalmykowa, and D. C. Grainger. Chromosomal macrodomains and associated proteins: implications for dna organization and replication in gram negative bacteria. *PLoS genetics*, 7(6):e1002123, 2011. 9, 22

[DML08] A. Dajkovic, A. Mukherjee, and J. Lutkenhaus. Investigation of regulation of ftsz assembly by sula and development of a model for ftsz polymerization. *Journal of bacteriology*, 190(7):2513, 2008. 34, 121

[DRLP+07] O. Danilova, R. Reyes-Lamothe, M. Pinskaya, D. Sherratt, and C. Possoz. Mukb colocalizes with the oric region and is required for organization of the two escherichia coli chromosome arms into separate cell halves. *Molecular microbiology*, 65(6):1485, 2007. 30

[DSS11] Y. Deng, M. Z. Sun, and J. W. Shaevitz. Direct measurement of cell wall stress stiffening and turgor pressure in live bacterial cells. *Physical Review Letters*, 107(15):4, 2011. 8

[DU05] Patrick S. Doyle and Patrick T. Underhill. Brownian dynamics simulations of polymers and soft matter. In Sidney Yip, editor, *Handbook of Materials Modeling: Methods*, pages 2619–2630, Dordrecht, 2005. Springer Netherlands. 51, 56

[dV10] R. de Vries. Dna condensation in bacteria: Interplay between macromolecular crowding and nucleoid proteins. *Biochimie*, 92(12):1715, 2010. 20

[DW00] K. A. Datsenko and B. L. Wanner. One-step inactivation of chromosomal genes in escherichia coli k-12 using pcr products. *Proceedings of the National Academy of Sciences of the United States of America*, 97(12):6640, 2000. 33

[DZW+17] X. F. Dai, M. L. Zhu, M. Warren, R. Balakrishnan, V. Patsalo, H. Okano, J. R. Williamson, K. Fredrick, Y. P. Wang, and T. Hwa. Reduction of translating ribosomes enables escherichia coli to maintain elongation rates during slow growth. *Nat. Microbiol*, 2(2):9, 2017. 9, 106, 118, 119, 124, 138

[EAO10] H. P. Erickson, D. E. Anderson, and M. Osawa. Ftsz in bacterial cytokinesis: cytoskeleton and force generator all in one. *Microbiology and molecular biology reviews : MMBR*, 74(4):504, 2010. 9

[EASJ06] J. El-Ali, P. K. Sorger, and K. F. Jensen. Cells on chips. *Nature*, 442(7101):403, 2006. 65

[EBD+12] O. Espeli, R. Borne, P. Dupaigne, A. Thiel, E. Gigant, R. Mercier, and F. Boccard. A matp-divisome interaction coordinates chromosome segregation with cell division in e. coli. *The EMBO journal*, 31(14):3198, 2012. 9, 22

[EBD13] M. Ehrenberg, H. Bremer, and P. P. Dennis. Medium-dependent control of the bacterial growth rate. *Biochimie*, 95(4):643, 2013. 106, 118, 119, 124, 139

[EM06] R. J. Ellis and A. P. Minton. Protein aggregation in crowded environments. *Biol. Chem.*, 387(5):485, 2006. 26

[ES65] W. Epstein and S. G. Schultz. Cation transport in escherichia coli: V. regulation of cation content. *J Gen Physiol*, 49(2):221, 1965. 118

[FBW+13] J. K. Fisher, A. Bourniquel, G. Witz, B. Weiner, M. Prentiss, and N. Kleckner. Four-dimensional imaging of e. coli nucleoid organization and dynamics in living cells. *Cell*, 153(4):882, 2013. 66, 146

[FCR+09] J. M. Fogg, D. J. Catanese, G. L. Randall, M. C. Swick, and L. Zechiedrich. Differences between positively and negatively supercoiled dna that topoisomerases may distinguish. *Mathematics of DNA Structure, Function and Interactions*, 150:73, 2009. 15

[FCS+13] D. Fowler, M. Coyle, U. Skiba, M. A. Sutton, J. N. Cape, S. Reis, L. J. Sheppard, A. Jenkins, B. Grizzetti, J. N. Galloway, P. Vitousek, A. Leach, A. F. Bouwman, K. Butterbach-Bahl, F. Dentener, D. Stevenson, M. Amann, and M. Voss. The global nitrogen cycle in the twenty-first century. *Philosophical Transactions of the Royal Society B-Biological Sciences*, 368(1621):13, 2013. 2, 3

[FKZ17] H. Fang, J. Kang, and D. W. Zhang. Microbial production of vitamin b-12: a review and future perspectives. *Microb. Cell. Fact.*, 16:14, 2017. 3

[FNY91] L. T. Fan, D. Neogi, and M. Yashima. *Elementary Introduction to Spatial and Temporal Fractals*. Lecture Notes in Chemistry. Springer Berlin Heidelberg, Berlin, Heidelberg, 1991. 41

[FS02] Daan Frenkel and Berend Smit. *Understanding Molecular Simulation*. Academic Press, San Diego, second edition edition, 2002. 52

[Ful71] F. B. Fuller. The writhing number of a space curve. *Proceedings of the National Academy of Sciences of the United States of America*, 68(4):815, 1971. 15

[Ful78] F. B. Fuller. Decomposition of the linking number of a closed ribbon: A problem from molecular biology. *Proceedings of the National Academy of Sciences of the United States of America*, 75(8):3557, 1978. 15

[GRSL81] M. S. Guyer, R. R. Reed, J. A. Steitz, and K. B. Low. Identification of a sex-factor-affinity site in e. coli as gamma delta. *Cold Spring Harb Symp Quant Biol*, 45 Pt 1:135, 1981. 33

[HBD07] C. C. Hsieh, A. Balducci, and P. S. Doyle. An experimental study of dna rotational relaxation time in nanoslits. *Macromolecules*, 40(14):5196, 2007. 24, 30

[HD14] Felix J. H. Hol and Cees Dekker. Zooming in to see the bigger picture: Microfluidic and nanofabrication tools to study bacteria. *Science*, 346(6208):438, 2014. 65, 66

[HDS96] W. Humphrey, A. Dalke, and K. Schulten. Vmd: Visual molecular dynamics. *Journal of Molecular Graphics & Modelling*, 14(1):33, 1996. 56

[Hig07] N. P. Higgins. Under dna stress, gyrase makes the sign of the cross. *Nat. Struct. Mol. Biol.*, 14(4):256, 2007. 17, 18

[HMW+08] K. C. Huang, R. Mukhopadhyay, B. Wen, Z. Gitai, and N. S. Wingreen. Cell shape and cell-wall organization in gram-negative bacteria. *Proceedings of the National Academy of Sciences of the United States of America*, 105(49):19282, 2008. 8

[HYGJM12] N. Hadizadeh Yazdi, C. C. Guet, R. C. Johnson, and J. F. Marko. Variation of the folding and dynamics of the escherichia coli chromosome with growth conditions. *Molecular microbiology*, 86(6):1318, 2012. 20, 25

[JCM+15] D. J. Jin, C. Cagliero, C. M. Martin, J. Izard, and Y. N. Zhou. The dynamic nature and territory of transcriptional machinery in the bacterial chromosome. *Front. Microbiol.*, 6:14, 2015. 140

[JCZ13] D. J. Jin, C. Cagliero, and Y. N. Zhou. Role of rna polymerase and transcription in the organization of the bacterial nucleoid. *Chem. Rev.*, 113(11):8662, 2013. 3

[Jen17] Anna D. Jennings. *Development of Microfluidic Platforms for Studies of Cellular Organization in Escherichia coli.* Master's thesis, University of Tennessee, 2017. 87

[JFG+15] Sophie Jeanson, Juliane Floury, Valerie Gagnaire, Sylvie Lortal, and Anne Thierry. Bacterial colonies in solid media and foods: A review on their growth and interactions with the micro-environment. *Front. Microbiol.*, 6, 2015. 87

[JHF+10] Xiaocheng Jiang, Jinsong Hu, Lisa A. Fitzgerald, Justin C. Biffinger, Ping Xie, Bradley R. Ringeisen, and Charles M. Lieber. Probing electron transfer mechanisms

in shewanella oneidensis mr-1 using a nanoelectrode platform and single-cell imaging. *Proceedings of the National Academy of Sciences of the United States of America*, 107(39):16806, 2010. 65

[JHP+13] X. Jiang, J. Hu, E. R. Petersen, L. A. Fitzgerald, C. S. Jackan, A. M. Lieber, B. R. Ringeisen, C. M. Lieber, and J. C. Biffinger. Probing single- to multi-cell level charge transport in geobacter sulfurreducens dl-1. *Nat Commun*, 4:2751, 2013. 65

[JKJ+15] C. Jeon, J. Kim, H. Jeong, Y. Jung, and B. Y. Ha. Chromosome-like organization of an asymmetrical ring polymer confined in a cylindrical space. *Soft Matter*, 11(41):8179, 2015. 26

[JM06] Suckjoon Jun and Bela Mulder. Entropy-driven spatial organization of highly confined polymers: Lessons for the bacterial chromosome. *Proceedings of the National Academy of Sciences of the United States of America*, 103(33):12388, 2006. 144

[JMTT14] I. D. Johnston, D. K. McCluskey, C. K. L. Tan, and M. C. Tracey. Mechanical characterization of bulk sylgard 184 for microfluidics and microengineering. *Journal of Micromechanics and Microengineering*, 24(3):035017, 2014. 51, 89

[Joy16] M. Joyeux. In vivo compaction dynamics of bacterial dna: A fingerprint of dna/rna demixing? *Curr. Opin. Colloid Interface Sci.*, 26:17, 2016. 118, 124

[Joy18] M. Joyeux. A segregative phase separation scenario of the formation of the bacterial nucleoid. *Soft Matter*, 14(36):7368, 2018. 24

[JvdMD11] J. J. Jones, J. R. van der Maarel, and P. S. Doyle. Effect of nanochannel geometry on dna structure in the presence of macromolecular crowding agent. *Nano Lett*, 11(11):5047, 2011. 30, 31, 103, 144

[JW10] Suckjoon Jun and Andrew Wright. Entropy as the driver of chromosome segregation. *Nature Reviews Microbiology*, 8(8):600, 2010. 22

[Kam93] R. D. Kamien. Flory exponents from a self-consistent renormalization-group. *J Phys I*, 3(8):1663, 1993. 30

[KB76] R. Kavenoff and B. C. Bowen. Electron microscopy of membrane-free folded chromosomes from escherichia coli. *Chromosoma*, 59(2):89, 1976. 16, 137

[KDSB09] K. Khanafer, A. Duprey, M. Schlicht, and R. Berguer. Effects of strain rate, mixing ratio, and stress-strain definition on the mechanical behavior of the polydimethylsiloxane (pdms) material as related to its biological applications. *Biomedical microdevices*, 11(2):503, 2009. 51, 89

[KJJ+15] J. Kim, C. Jeon, H. Jeong, Y. Jung, and B. Y. Ha. A polymer in a crowded and confined space: effects of crowder size and poly-dispersity. *Soft Matter*, 11(10):1877, 2015. 24, 26, 27, 56, 58, 60, 132, 134, 139

[KJJ+18] Matthias Kaiser, Florian Jug, Thomas Julou, Siddharth Deshpande, Thomas Pfohl, Olin K. Silander, Gene Myers, and Erik van Nimwegen. Monitoring single-cell gene regulation under dynamically controllable conditions with integrated microfluidics and software. *Nat. Commun.*, 9(1):212, 2018. 67

[KMJK18] T. J. Krogh, J. Moller-Jensen, and C. Kaleta. Impact of chromosomal architecture on the function and evolution of bacterial genomes. *Front. Microbiol.*, 9:15, 2018. 20, 22

[KMS10] C. Kung, B. Martinac, and S. Sukharev. Mechanosensitive channels in microbes. In S. Gottesman and C. S. Harwood, editors, *Annual Review of Microbiology*, volume 64 of *Annual Review of Microbiology*, pages 313–29, Palo Alto, 2010. Annual Reviews. 121

[KP49] O. Kratky and G. Porod. Rontgenuntersuchung geloster fadenmolekule. *Recl. Trav. Chim. Pays-Bas-J. Roy. Neth. Chem. Soc.*, 68(12):1106, 1949. 11

[KSQ+07] E. P. Kartalov, A. Scherer, S. R. Quake, C. R. Taylor, and W. F. Anderson. Experimentally validated quantitative linear model for the device physics of elastomeric microfluidic valves. *J Appl Phys*, 101(6):64505, 2007. 89

[KVM+10] M. K. Krotova, V. V. Vasilevskaya, N. Makita, K. Yoshikawa, and A. R. Khokhlov. Dna compaction in a crowded environment with negatively charged proteins. *Phys Rev Lett*, 105(12):128302, 2010. 114, 135, 137

[KYH+04] J. Kim, S. H. Yoshimura, K. Hizume, R. L. Ohniwa, A. Ishihama, and K. Takeyasu. Fundamental structural units of the escherichia coli nucleoid revealed by atomic force microscopy. *Nucleic acids research*, 32(6):1982, 2004. 23

[LAMH06] H. J. Limbach, A. Arnold, B. A. Mann, and C. Holm. Espresso—an extensible simulation package for research on soft matter systems. *Computer Physics Communications*, 174(9):704, 2006. 51

[LBGW14] G. W. Li, D. Burkhardt, C. Gross, and J. S. Weissman. Quantifying absolute protein synthesis rates reveals principles underlying allocation of cellular resources. *Cell*, 157(3):624, 2014. 119, 138

[LCM+18] V. S. Lioy, A. Cournac, M. Marbouty, S. Duigou, J. Mozziconacci, O. Espeli, F. Boccard, and R. Koszul. Multiscale structuring of the e. coli chromosome by nucleoid-associated and condensin proteins. *Cell*, 172(4):771, 2018. 22, 137

[LIML13] T. B. Le, M. V. Imakaev, L. A. Mirny, and M. T. Laub. High-resolution mapping of the spatial organization of a bacterial chromosome. *Science*, 342(6159):731, 2013. 137

[LKN13] Maxim O. Lavrentovich, John H. Koschwanez, and David R. Nelson. Nutrient shielding in clusters of cells. *Phys. Rev. E*, 87(6):17, 2013. 81

[LNJ+13] Zhicheng Long, Eileen Nugent, Avelino Javer, Pietro Cicuta, Bianca Sclavi, Marco Cosentino Lagomarsino, and Kevin D. Dorfman. Microfluidic chemostat for measuring single cell dynamics in bacteria. *Lab on a chip*, 13(5):947, 2013. 66

[Lon53] L. G. Longsworth. Diffusion measurements, at 25°, of aqueous solutions of amino acids, peptides and sugars. *Journal of the American Chemical Society*, 75(22):5705, 1953. 83

[LRG12] E. A. Libby, M. Roggiani, and M. Goulian. Membrane protein expression triggers chromosomal locus repositioning in bacteria. *Proceedings of the National Academy of Sciences of the United States of America*, 109(19):7445, 2012. 23

[Lut07] J. Lutkenhaus. Assembly dynamics of the bacterial mincde system and spatial regulation of the z ring. *Annual review of biochemistry*, 76:539, 2007. 9

[LZL+12] Kaston Leung, Hans Zahn, Timothy Leaver, Kishori M. Konwar, Niels W. Hanson, Antoine P. Page, Chien-Chi Lo, Patrick S. Chain, Steven J. Hallam, and Carl L. Hansen. A programmable droplet-based microfluidic device applied to multiparameter analysis of single microbes and microbial communities. *Proceedings of the National Academy of Sciences of the United States of America*, 109(20):7665, 2012. 65

[MB15] J. Mannik and M. W. Bailey. Spatial coordination between chromosomes and cell division proteins in escherichia coli. *Front Microbiol*, 6:306, 2015. 9, 10, 151

[MBC09] Nicolas Minc, Arezki Boudaoud, and Fred Chang. Mechanical forces of fission yeast growth. *Curr. Biol.*, 19(13):1096, 2009. 86

[MBG+94] L. Montanet, R. M. Barnett, D. E. Groom, T. G. Trippe, C. G. Wohl, B. Armstrong, G. S. Wagman, H. Murayama, J. Stone, J. J. Hernandez, F. C. Porter, R. J. Morrison, A. Manohar, M. Aguilarbenitez, C. Caso, P. Lantero, R. L. Crawford, M. Roos, N. A. Tornqvist, K. G. Hayes, G. Hohler, S. Kawabata, D. M. Manley, K. Olive, R. E. Shrock, S. Eidelman, R. H. Schindler, A. Gurtu, K. Hikasa, G. Conforto, R. L. Workman, and C. Grab. Review of particle properties. *Phys. Rev. D*, 50(3):1173, 1994. 44

[MBL+11] J. Mondal, B. P. Bratton, Y. Li, A. Yethiraj, and J. C. Weisshaar. Entropy-based mechanism of ribosome-nucleoid segregation in e. coli cells. *Biophysical journal*, 100(11):2605, 2011. 9, 24, 119, 124

[MBOM17] Jaana Mannik, Matthew W. Bailey, Jordan C. O'Neill, and Jaan Mannik. Kinetics of large-scale chromosomal movement during asymmetric cell division in escherichia coli. *PLoS genetics*, 13(2):22, 2017. 11, 66, 151

[MBvdHvN14] H. Meng, J. Bosman, T. van der Heijden, and J. van Noort. Coexistence of twisted, plectonemic, and melted dna in small topological domains. *Biophysical journal*, 106(5):1174, 2014. 17

[MBW13] J. Ma, L. Bai, and M. D. Wang. Transcription under torsion. *Science*, 340(6140):1580, 2013. 17

[MCY+16] J. Mannik, D. E. Castillo, D. Yang, G. Siopsis, and J. Mannik. The role of matp, zapa and zapb in chromosomal organization and dynamics in escherichia coli. *Nucleic acids research*, 44(3):1216, 2016. 22, 24, 25, 26, 56, 58, 106

[MDG+09] Jaan Mannik, Rosalie Driessen, Peter Galajda, Juan E. Keymer, and Cees Dekker. Bacterial growth and motility in sub-micron constrictions. *Proceedings of the National Academy of Sciences of the United States of America*, 106(35):14861, 2009. 43, 68

[MFC06] D. Marenduzzo, K. Finan, and P. R. Cook. The depletion attraction: an underappreciated force driving cellular organization. *J. Cell Biol.*, 175(5):681, 2006. 20

[Mil13] R. Milo. What is the total number of protein molecules per cell volume? a call to rethink some published values. *Bioessays*, 35(12):1050, 2013. 119, 138

[Mir05] Sergei M. Mirkin. Dna topology: Fundamentals. In *Encyclopedia of Life Sciences*, volume 5, pages 621–31, Chichester, UK, 2005. John Wiley & Sons. 15

[MLC10] J. A. Mosberg, M. J. Lajoie, and G. M. Church. Lambda red recombineering in escherichia coli occurs through a fully single-stranded intermediate. *Genetics*, 186(3):791, 2010. 33

[MLC12] Jeffrey R. Moffitt, Jeffrey B. Lee, and Philippe Cluzel. The single-cell chemostat: an agarose-based, microfluidic device for high-throughput, single-cell studies of bacteria and bacterial communities. *Lab on a chip*, 12(8):1487, 2012. 66

[MLGC+15] M. Marbouty, A. Le Gall, D. I. Cattoni, A. Cournac, A. Koh, J. B. Fiche, J. Mozziconacci, H. Murray, R. Koszul, and M. Nollmann. Condensin- and replication-mediated bacterial chromosome folding and origin condensation revealed by hi-c and super-resolution imaging. *Molecular Cell*, 59(4):588, 2015. 137

[MLJS+10] P. Montero Llopis, A. F. Jackson, O. Sliusarenko, I. Surovtsev, J. Heinritz, T. Emonet, and C. Jacobs-Wagner. Spatial organization of the flow of genetic information in bacteria. *Nature*, 466(7302):77, 2010. 141

[MOB+07] Y. Marcy, C. Ouverney, E. M. Bik, T. Losekann, N. Ivanova, H. G. Martin, E. Szeto, D. Platt, P. Hugenholtz, D. A. Relman, and S. R. Quake. Dissecting biological "dark matter" with single-cell genetic analysis of rare and uncultivated tm7 microbes from the human mouth. *Proceedings of the National Academy of Sciences of the United States of America*, 104(29):11889, 2007. 65

[MPS+08] R. Mercier, M. A. Petit, S. Schbath, S. Robin, M. El Karoui, F. Boccard, and O. Espeli. The matp/mats site-specific system organizes the terminus region of the e. coli chromosome into a macrodomain. *Cell*, 135(3):475, 2008. 22

[MW18] S. Mohapatra and J. C. Weisshaar. Functional mapping of the e-coli translational machinery using single-molecule tracking. *Molecular microbiology*, 110(2):262, 2018. 119, 141

[MWH+12] Jaan Mannik, Fabai Wu, Felix J. H. Hol, Paola Bisicchia, David J. Sherratt, Juan E. Keymer, and Cees Dekker. Robustness and accuracy of cell division in escherichia coli in diverse cell shapes. *Proceedings of the National Academy of Sciences of the United States of America*, 109(18):6957, 2012. 66

[NLPL13] Thomas M. Norman, Nathan D. Lord, Johan Paulsson, and Richard Losick. Memory and modularity in cell-fate decision making. *Nature*, 503(7477):481, 2013. 67, 87

[NS99] Arvind Natarajan and Friedrich Srienc. Dynamics of glucose uptake by single escherichia coli cells. *Metabolic Engineering*, 1(4):320, 1999. 83

[NS14] S. Nolivos and D. Sherratt. The bacterial chromosome: architecture and action of bacterial smc and smc-like complexes. *Fems Microbiol. Rev.*, 38(3):380, 2014. 22

[Odi98] T. Odijk. Osmotic compaction of supercoiled dna into a bacterial nucleoid. *Biophys Chem*, 73(1-2):23, 1998. 19, 20, 24, 27, 134, 206

[oEB01] The Editors of Encyclopaedia Britannica. Encyclopædia britannica online, 2001. 1

[PHAC04] L. Postow, C. D. Hardy, J. Arsuaga, and N. R. Cozzarelli. Topological domain structure of the escherichia coli chromosome. *Genes & development*, 18(14):1766, 2004. 19

[PHH+12] J. Pelletier, K. Halvorsen, B. Y. Ha, R. Paparcone, S. J. Sandler, C. L. Woldringh, W. P. Wong, and S. Jun. Physical manipulation of the escherichia coli chromosome reveals its soft nature. *Proceedings of the National Academy of Sciences of the United States of America*, 109(40):E2649, 2012. 26, 30, 58, 103, 114, 135, 144

[PKT+12] Rob Phillips, Jane Kondev, Julie Theriot, Hernan G. Garcia, and Nigel Orme. *Physical biology of the cell*. Garland Science, New York, NY, 2nd edition, 2012. 6, 8

[Por76] J. R. Porter. Antony van leeuwenhoek: Tercentenary of his discovery of bacteria. *Bacteriological Reviews*, 40(2):260, 1976. 1, 2

[PR03] Eduardo Perozo and Douglas C. Rees. Structure and mechanism in prokaryotic mechanosensitive channels. *Current Opinion in Structural Biology*, 13(4):432, 2003. 8

[PS13] T. Pilizota and J. W. Shaevitz. Plasmolysis and cell shape depend on solute outer-membrane permeability during hyperosmotic shock in e. coli. *Biophysical journal*, 104(12):2733, 2013. 109

[PSC+14] B. R. Parry, I. V. Surovtsev, M. T. Cabeen, C. S. O'Hem, E. R. Dufresne, and C. Jacobs-Wagner. The bacterial cytoplasm has glass-like properties and is fluidized by metabolic activity. *Cell*, 156(1-2):183, 2014. 8

[PW10] U. Pul and R. Wagner. Nucleoid-associated proteins: Structural properties. In R. T. Dame and C. J. Dorman, editors, *Bacterial Chromatin*, pages 149–173, Berlin, 2010. Springer-Verlag Berlin. 20, 21

[RC03] M. Rubinstein and R.H. Colby. *Polymer Physics*. OUP Oxford, 2003. 11, 12, 13, 132

[RCM+87] B. Richey, D. S. Cayley, M. C. Mossing, C. Kolka, C. F. Anderson, T. C. Farrar, and M. T. Record. Variability of the intracellular ionic environment of escherichia-coli - differences between invitro and invivo effects of ion concentrations on protein-dna interactions and gene-expression. *J. Biol. Chem.*, 262(15):7157, 1987. 118

[RD05] G. C. Randall and P. S. Doyle. Permeation-driven flow in poly(dimethylsiloxane) microfluidic devices. *Proceedings of the National Academy of Sciences of the United States of America*, 102(31):10813, 2005. 75, 84

[Rea14] Kenneth F. Read. Lecture notes on computational physics, 2014. 51

[RFK07] T. Romantsov, I. Fishov, and O. Krichevsky. Internal structure and dynamics of isolated escherichia coli nucleoids assessed by fluorescence correlation spectroscopy. *Biophysical journal*, 92(8):2875, 2007. 19, 23

[RKV13] A. I. Rico, M. Krupka, and M. Vicente. In the beginning, escherichia coli assembled the proto-ring: an initial phase of division. *The Journal of biological chemistry*, 288(29):20830, 2013. 9

[RR01] L. Ranjard and A. S. Richaume. Quantitative and qualitative microscale distribution of bacteria in soil. *Res. Microbiol.*, 152(8):707, 2001. 87

[RTH14] E. Rojas, J. A. Theriot, and K. C. Huang. Response of escherichia coli growth rate to osmotic shock. *Proceedings of the National Academy of Sciences of the United States of America*, 111(21):7807, 2014. 109

[SABW82] William C. Swope, Hans C. Andersen, Peter H. Berens, and Kent R. Wilson. A computer simulation method for the calculation of equilibrium constants for the formation of physical clusters of molecules: Application to small water clusters. *The Journal of chemical physics*, 76(1):637, 1982. 52

[SBdH+15] T. N. Shendruk, M. Bertrand, H. W. de Haan, J. L. Harden, and G. W. Slater. Simulating the entropic collapse of coarse-grained chromosomes. *Biophysical journal*, 108(4):810, 2015. 22, 24, 56, 132

[SBH+05] B. S. Schuwirth, M. A. Borovinskaya, C. W. Hau, W. Zhang, A. Vila-Sanjurjo, J. M. Holton, and J. H. D. Cate. Structures of the bacterial ribosome at 3.5 angstrom resolution. *Science*, 310(5749):827, 2005. 9

[SCM14] J. Shin, A. G. Cherstvy, and R. Metzler. Mixing and segregation of ring polymers: spatial confinement and molecular crowding effects. *New J. Phys.*, 16:19, 2014. 24, 26, 55

[SG01] M. Schaechter and The View From Here Group. Escherichia coli and salmonella 2000: the view from here. *Microbiol. Mol. Biol. Rev.*, 65(1):119, 2001. 3

[SGG+18] C. K. Spahn, M. Glaesmann, J. B. Grimm, A. X. Ayala, L. D. Lavis, and M. Heilemann. A toolbox for multiplexed super-resolution imaging of the e. coli nucleoid and membrane using novel paint labels. *Scientific reports*, 8:12, 2018. 124

[SGH+16] Christian Carsten Sachs, Alexander Gruenberger, Stefan Helfrich, Christopher Probst, Wolfgang Wiechert, Dietrich Kohlheyer, and Katharina Noeh. Image-based single cell profiling: High-throughput processing of mother machine experiments. *PloS one*, 11(9), 2016. 67

[She03] D. J. Sherratt. Bacterial chromosome dynamics. *Science*, 301(5634):780, 2003. 19

[SHP+04] V. Studer, G. Hang, A. Pandolfi, M. Ortiz, W. F. Anderson, and S. R. Quake. Scaling properties of a low-actuation pressure microfluidic valve. *Journal of Applied Physics*, 95(1):393, 2004. 89

[SKW10] T. J. Silhavy, D. Kahne, and S. Walker. The bacterial cell envelope. *Cold Spring Harbor perspectives in biology*, 2(5):a000414, 2010. 8

[SM71] T. Shehata and A. G. Marr. Effect of nutrient concentration on growth of escherichia coli. *Journal of bacteriology*, 107(1):210, 1971. 73, 81, 82

[Smi14] Jeremy C. Smith. Lecture notes on introduction to molecular biophysics, 2014. 52

[SMK58] M. Schaechter, O. Maaloe, and N. O. Kjeldgaard. Dependency on medium and temperature of cell size and chemical composition during balanced growth of

salmonella-typhimurium. *Journal of General Microbiology*, 19(3):592, 1958. 24, 73

[SML09] L. Shapiro, H. H. McAdams, and R. Losick. Why and how bacteria localize proteins. *Science*, 326(5957):1225, 2009. 65

[SPL+14] A. Sanamrad, F. Persson, E. G. Lundius, D. Fange, A. H. Gynna, and J. Elf. Single-particle tracking reveals that free ribosomal subunits are not excluded from the escherichia coli nucleoid. *Proceedings of the National Academy of Sciences of the United States of America*, 111(31):11413, 2014. 127

[SS16] R. Saxena and V. K. Sharma. A metagenomic insight into the human microbiome. *Medical and health genomics*, page 107, 2016. 2

[SSC+09] W. Schrott, Z. Slouka, P. Cervenka, J. Ston, M. Nebyla, M. Pribyl, and D. Snita. Study on surface properties of pdms microfluidic chips treated with albumin. *Biomicrofluidics*, 3(4):44101, 2009. 45, 147

[SWvdW+02] R. Stuger, C. L. Woldringh, C. C. van der Weijden, N. O. E. Vischer, B. M. Bakker, R. J. M. van Spanning, J. L. Snoep, and H. V. Westerhoff. Dna supercoiling by gyrase is linked to nucleoid compaction. *Mol. Biol. Rep.*, 29(1-2):79, 2002. 19, 140

[TABS+15] Sattar Taheri-Araghi, Serena Bradde, John T. Sauls, Norbert S. Hill, Petra Anne Levin, Johan Paulsson, Massimo Vergassola, and Suckjoon Jun. Cell-size control and homeostasis in bacteria. *Curr. Biol.*, 25(3):385, 2015. 67, 70, 80

[TAR+12] Hannah H. Tuson, George K. Auer, Lars D. Renner, Mariko Hasebe, Carolina Tropini, Max Salick, Wendy C. Crone, Ajay Gopinathan, Kerwyn Casey Huang, and Douglas B. Weibel. Measuring the stiffness of bacterial cells from growth rates in hydrogels of tunable elasticity. *Molecular microbiology*, 84(5):874, 2012. 85, 86

[Tay97] John R. Taylor. *An introduction to error analysis : the study of uncertainties in physical measurements*. University Science Books, Sausalito, CA, 2nd ed. edition, 1997. 44

[TBE+17] T. Terakawa, S. Bisht, J. M. Eeftens, C. Dekker, C. H. Haering, and E. C. Greene. The condensin complex is a mechanochemical motor that translocates along dna. *Science*, 358(6363):672, 2017. 22

[TBGV12] Athanasios Typas, Manuel Banzhaf, Carol A. Gross, and Waldemar Vollmer. From the regulation of peptidoglycan synthesis to bacterial growth and morphology. *Nature Reviews Microbiology*, 10(2):123, 2012. 80

[TCC07] L. C. Thomason, N. Costantino, and D. L. Court. E. coli genome manipulation by p1 transduction. *Current protocols in molecular biology / edited by Frederick M. Ausubel ... [et al.]*, Chapter 1:Unit 1 17, 2007. 33

[TH90] W. H. Taylor and P. J. Hagerman. Application of the method of phage-t4 dna ligase-catalyzed ring-closure to the study of dna-structure .2. nacl-dependence of dna flexibility and helical repeat. *Journal of molecular biology*, 212(2):363, 1990. 12

[UCT+00] M. A. Unger, H. P. Chou, T. Thorsen, A. Scherer, and S. R. Quake. Monolithic microfabricated valves and pumps by multilayer soft lithography. *Science*, 288(5463):113, 2000. 48, 88

[UWM+13] G. Ullman, M. Wallden, E. G. Marklund, A. Mahmutovic, Ivan Razinkov, and J. Elf. High-throughput gene expression analysis at the level of single proteins using a microfluidic turbidostat and automated cell tracking. *Philosophical Transactions of the Royal Society B-Biological Sciences*, 368(1611):20120025, 2013. 66

[VLF11] A. Vendeville, D. Lariviere, and E. Fourmentin. An inventory of the bacterial macromolecular components and their spatial organization. *Fems Microbiol. Rev.*, 35(2):395, 2011. 206

[VvV94] P. W. Verbeek and L. J. van Vliet. On the location error of curved edges in low-pass filtered 2-d and 3-d images. *IEEE Trans. Pattern Anal. Mach. Intell.*, 16(7):726, 1994. 41

[WA19] F. Wong and A. Amir. Mechanics and dynamics of bacterial cell lysis. *Biophysical journal*, 116(12):2378, 2019. 67

[WAOW12] A. S. Wegner, S. Alexeeva, T. Odijk, and C. L. Woldringh. Characterization of escherichia coli nucleoids released by osmotic shock. *Journal of structural biology*, 178(3):260, 2012. 19, 20

[WB18] F. Watanabe and T. Bito. Vitamin b-12 sources and microbial interaction. *Exp. Biol. Med.*, 243(2):148, 2018. 2, 3

[WH17] Lisa Willis and Kerwyn Casey Huang. Sizing up the bacterial cell cycle. *Nature Reviews Microbiology*, 15(10):606, 2017. 73

[Whi69] James H. White. Self-linking and the gauss integral in higher dimensions. *Am. J. Math.*, 91(3):693, 1969. 15

[WJW95] C. L. Woldringh, P. R. Jensen, and H. V. Westerhoff. Structure and partitioning of bacterial-dna - determined by a balance of compaction and expansion forces. *Fems Microbiology Letters*, 131(3):235, 1995. 19

[WLC+11] W. Wang, G. W. Li, C. Chen, X. S. Xie, and X. Zhuang. Chromosome organization by a nucleoid-associated protein in live bacteria. *Science*, 333(6048):1445, 2011. 19

[WMLR13] X. Wang, P. Montero Llopis, and D. Z. Rudner. Organization and segregation of bacterial chromosomes. *Nat Rev Genet*, 14(3):191, 2013. 17, 22, 23, 137

[WO99] Conrad L. Woldringh and Theo Odijk. Structure of dna within the bacterial cell: Physics and physiology. In Robert L. Charlebois, editor, *Organization of the Prokaryotic Genome*, pages 171–87, Washington, DC, 1999. ASM Press. 27

[Wol02] C. L. Woldringh. The role of co-transcriptional translation and protein translocation (transertion) in bacterial chromosome segregation. *Molecular microbiology*, 45(1):17, 2002. 20, 23

[Wol10] C. L. Woldringh. Nucleoid structure and segregation. In R. T. Dame and C. J. Dorman, editors, *Bacterial Chromatin*, pages 71–96, Berlin, 2010. Springer-Verlag Berlin. 141

[Wor05] Michael Worboys. *History of Bacteriology*, volume 9, pages 8–13. Wiley, Chichester, UK, 2005. 1

[WRP+10] Ping Wang, Lydia Robert, James Pelletier, Wei Lien Dang, Francois Taddei, Andrew Wright, and Suckjoon Jun. Robust growth of escherichia coli. *Curr. Biol.*, 20(12):1099, 2010. 66, 67, 104

[WRTP+12] M. H. Werts, V. Raimbault, R. Texier-Picard, R. Poizat, O. Francais, L. Griscom, and J. R. Navarro. Quantitative full-colour transmitted light microscopy and dyes for concentration mapping and measurement of diffusion coefficients in microfluidic architectures. *Lab on a chip*, 12(4):808, 2012. 91

[WSK+19] Fabai Wu, Pinaki Swain, Louis Kuijpers, Xuan Zheng, Kevin Felter, Margot Guurink, Jacopo Solari, Suckjoon Jun, Thomas S. Shimizu, Debasish Chaudhuri, Bela Mulder, and Cees Dekker. Cell boundary confinement sets the size and position of the e. coli chromosome. *Curr. Biol.*, 29(13):2131, 2019. 22, 58, 59, 61, 63, 64, 103

[WWRY01] M. Wery, C. L. Woldringh, and J. Rouviere-Yaniv. Hu-gfp and dapi co-localize on the escherichia coli nucleoid. *Biochimie*, 83(2):193, 2001. 104

[YGJ+15] Da Yang, Clayton M. Greer, Branndon P. Jones, Anna D. Jennings, Scott T. Retterer, and Jaan Männik. Characterization of small microfluidic valves for studies of mechanical properties of bacteria. *Journal of Vacuum Science & Technology B, Nanotechnology and Microelectronics: Materials, Processing, Measurement, and Phenomena*, 33(6):06F202, 2015. 49, 67, 77, 87

[YHMY10] K. Yoshikawa, S. Hirota, N. Makita, and Y. Yoshikawa. Compaction of dna induced by like-charge protein: Opposite salt-effect against the polymer-salt-induced condensation with neutral polymer. *J. Phys. Chem. Lett.*, 1(12):1763, 2010. 114, 135, 137

[YJB+18] D. Yang, A. D. Jennings, E. Borrego, S. T. Retterer, and J. Mannik. Analysis of factors limiting bacterial growth in pdms mother machine devices. *Front Microbiol*, 9:871, 2018. 66, 104

[YJPB99] X. Yao, M. Jericho, D. Pink, and T. Beveridge. Thickness and elasticity of gram-negative murein sacculi measured by atomic force microscopy. *Journal of bacteriology*, 181(22):6865, 1999. 8

[YMRM20] Da Yang, Jaana Mannik, Scott T. Retterer, and Jaan Mannik. The effects of polydisperse crowders on the compaction of the escherichia coli nucleoid. *Molecular microbiology*, 2020. 27

[YZ09] Y. S. Yu and Y. P. Zhao. Deformation of pdms membrane and microcantilever by a water droplet: comparison between mooney-rivlin and linear elastic constitutive models. *Journal of colloid and interface science*, 332(2):467, 2009. 51, 89

[ZSvKvdM09] C. Zhang, P. G. Shao, J. A. van Kan, and J. R. van der Maarel. Macromolecular crowding induced elongation and compaction of single dna molecules confined in a nanochannel. *Proceedings of the National Academy of Sciences of the United States of America*, 106(39):16651, 2009. 30, 31, 103

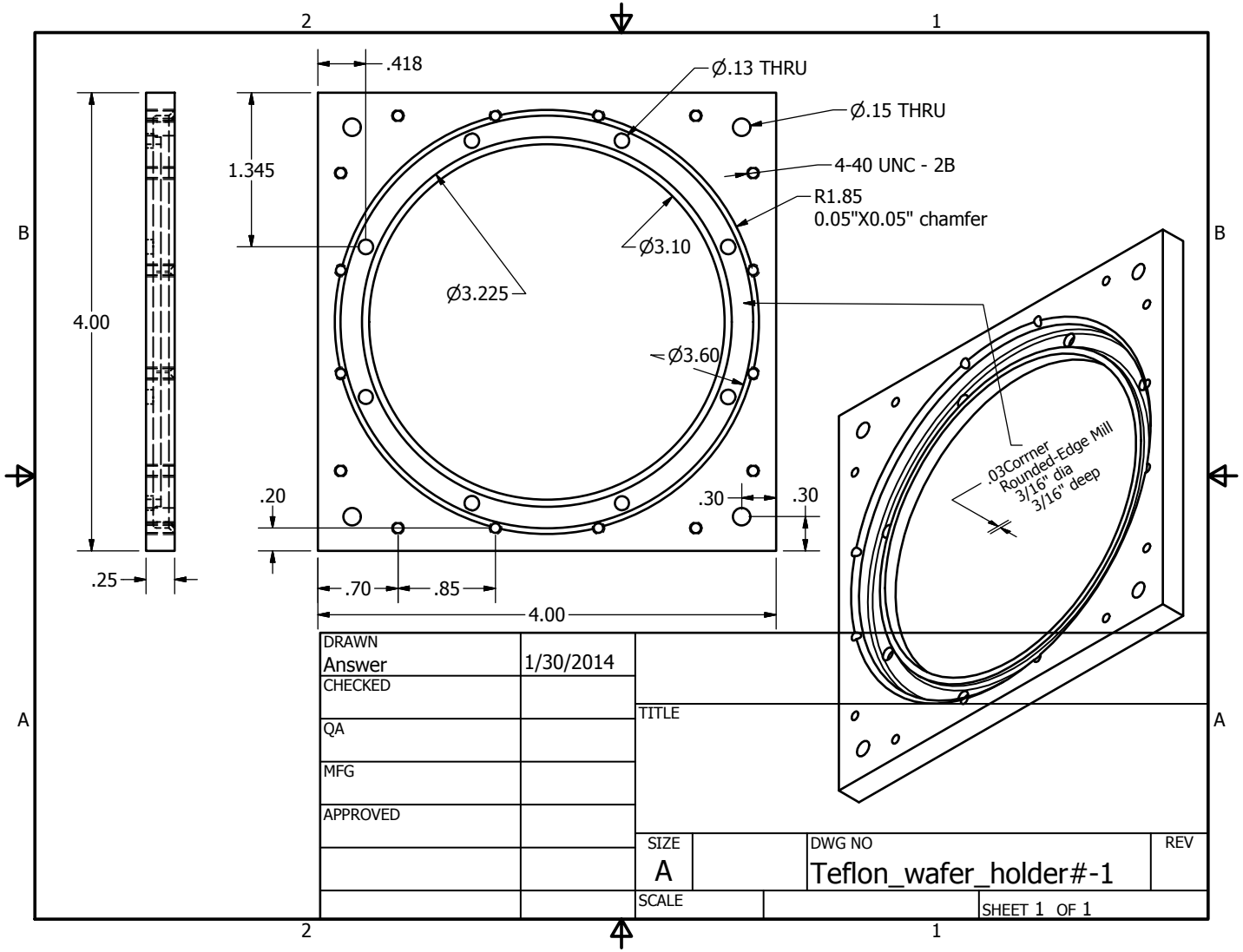
[ZT91] S. B. Zimmerman and S. O. Trach. Estimation of macromolecule concentrations and excluded volume effects for the cytoplasm of escherichia coli. *Journal of molecular biology*, 222(3):599, 1991. 8

[ZVL+13] Y. Zhao, A. Vararattanavech, X. Li, C. Helixnielsen, T. Vissing, J. Torres, R. Wang, A. G. Fane, and C. Y. Tang. Effects of proteoliposome composition and draw solution types on separation performance of aquaporin-based proteoliposomes: implications for seawater desalination using aquaporin-based biomimetic membranes. *Environ Sci Technol*, 47(3):1496, 2013. 8

[ZWF+12] X. Zhang, J. Wang, Y. Feng, J. Ge, W. Li, W. Sun, I. Iscla, J. Yu, P. Blount, Y. Li, and M. Yang. Structure and molecular mechanism of an anion-selective mechanosensitive channel of small conductance. *Proceedings of the National Academy of Sciences of the United States of America*, 109(44):18180, 2012. 8

Appendices

A Control-Layer PDMS Holder



B Protocol of Fabricating the First Electron Beam Lithography Layer on a Silicon Wafer

This appendix describes the silicon wafer fabrication processes defined by a electron beam lithography (EBL) layer exposed onto a blank wafer. This protocol applies to wafer molds fabricated for Mother Machine devices and the first flow layer of pressure actuated devices. In the Mother Machine devices and the flow layer of the Microvalves devices, there is only one EBL layer fabricated. In the Microanvils devices, a second EBL layer is defined for its flow layer. But the protocol for the second EBL layer is not given in this appendix.

B.1 Exposing a Wafer Spin Coated With ZEP520A to Electron Beam

1. Clean a $4''$ wafer by spinning, and alternatively spraying Acetone and IPA.
2. Spin coat ZEP520A at 2000 rpm for 60 s on the wafer.
3. Bake the wafer at $180°C$ for 3 min. to let the solvent in ZEP520A (anisol, a monomethoxybenzene) evaporate.
4. Expose the wafer to direct writing electron beam using JEOL JBX-9300fx electron beam lithography system at 2 nA, 100 kV, 6 nm, and 400 $\mu C/cm^2$. The area exposed will have e-beam resist with a drastically smaller molecular weight (or drastically shorter chain length).

B.2 Developing ZEP520A at Room Temperature ($\sim$20℃)

1. Soak a wafer exposed to EBL in about $1/2''$ deep of xylenes for 35 s. Gently agitate the container. This step allows the e-beam resist with small molecular weight to be dissolved and to diffuse away.
2. Move the wafer to another container containing IPA and soak for 35 s. Gently agitate the container. This step stops the development process.
3. Rinse the wafer with IPA from a squeeze bottle.
4. Dry the wafer with a filtered stream of nitrogen gas.
5. Bake the wafer at 110℃. for 1 min. to let the IPA evaporate.

B.3 Chromium (Cr) Physical Vapor Deposition

1. Hold a wafer with e-beam resist in a vacuum of less than $5 \times 10^{-6}\ Torr$.

2. Create a Cr vapor in the same vacuum by shooting an electron beam on pellets of Cr at 10 kV and $\sim 0.1\ A$. The resulted deposition rate should be less than 10 Å/s.

3. The final film thickness is set to 150 Å.

B.4 Lift-Off *e*-Beam Resist at Room Temperature

1. Soak a wafer with the deposited metal film in Acetone for 5 min..

2. Sonicate for 5 min. Be careful not to let any spot on the wafer dry after it is wetted by Acetone until the end of this lift-off process.

3. Move the wafer to another container containing Microposit Remover 1165 (mostly NMP) and soak for more than 36 hrs. This step can be done in 2 hrs. at 70℃.

4. Sonicate for 5 min.

5. Move the wafer to another container containing Acetone and ardently scratch the surface of the wafer with clean-room swabs. This step aims to remove loosely connected materiel from the Cr film mask. Spend 5 min. on this step.

6. Rinse the wafer with Acetone then with IPA from squeeze bottles.

7. Harshly blast the wafer with water from spray gun. Use a PE container as a backing for the wafer, instead holding the wafer with a pair of tweezers. The wafer might be cracked during this step but live dangerously.

B.5 Reactive Ion Etching (recipe: Cryo-Si Etch + O2 Clean)

In this recipe, the wafer is first cleaned by oxygen plasma, then etched by a mixture of SF_6 and O_2, and finally cleaned by O_2 plasma again.

1. Pre-clean with O_2 plasma for 10 min. at -110℃.

2. Etch silicon for $\sim$30 s at -110℃. The etch rate is about 35 nm/s in the range of time relevant to this dissertation. The etch rate varies from day to day within 10%.

3. Post-clean with O_2 plasma for 10 min. at -110℃. Without this step, the surface of a etched wafer will likely be hydrophobic with a H_2S-like smell.

C A Sample ESPResSo Script in the Scripting Language Tcl

OneRingDoubleShell08.tcl

```
1  ############################################################
2  #   Geometric Parameters                                   #
3  ############################################################
4  # Start of all files written by this script
5  set name "OneRingDoubleShell08"
6  ### The following are in unit of monomer diameter
7  # Half cylinder length
8  set L 10
9  # Cylinder Radius
10 set R 4
11 # Number of DNA chains
12 set N 1
13 # Number of monomers per chain
14 set Nm 150
15 # Crowder diameter
16 set ac1 0.4
17 set ac2 0.2
18 # Number of crowders
19 set Nc1 100
20 set Nc2 200
21 # Cylinder Length Compaction
22 set Lr 0.4
23 set Cr 0.1
24 # Compaction # about 300 steps
25 set CompactionStep  0.025  ;# 0.025
26 set CompactionRatio 0.999  ;# 0.999
27 set Rr 1.5
28 # Ourter shell parameters
29 set Ro 1.0
30 set Outer [expr $ac1*$Ro]
31
32 ############################################################
33 #   Integration Settings                                   #
34 ############################################################
```

```
35 # General
36 set MDtime_step 0.002
37 set MDskin       0.4
38 set FrameTime    100
39 set bl 60.0 ;#box length in z-direction
40 set bw 24.0 ;#box width in xy-direction
41 set cl 30   ;#center coord in z-direction
42 set cw 12   ;#center coord in xy-direction
43 # Langevin thermostat
44 set LangTemp 1.0
45 set LangFrac 0.1
46 # Warm Up
47 set warm_cap_init 1.0
48 set warm_incr      1.003;#1.003
49 set min_dist  0.95
50 set warm_step 1
51 set warm_time 5000 ;#5000
52 # Lag (with full LJ potential)
53 set lag_time 20000
54 # Compaction
55 set comp_step 100
56 set comp_time 0;#10000
57
58 ##################################################################
59 #   Papare Master Report                                         #
60 ##################################################################
61 set MRpt [open "$name.txt" w]
62 puts $MRpt " "
63 puts $MRpt "================================================="
64 puts $MRpt "= One ring polymers in cylindircal confinement ="
65 puts $MRpt "================================================="
66 puts $MRpt " "
67 puts $MRpt "Half Cylinder Length   = $L"
68 puts $MRpt "Cylinder Radius        = $R"
69 puts $MRpt "No. of DNA chains      = $N"
70 puts $MRpt "No. of Beads per Chain = $Nm"
71 puts $MRpt "DNA Beads diameter     = unit"
```

```
72  puts $MRpt "Type 1 Crowder Diameter        = $ac1"
73  puts $MRpt "No. of type 1 crowders         = $Nc1"
74  puts $MRpt "Type 2 Crowder Diameter        = $ac2"
75  puts $MRpt "No. of type 2 crowders         = $Nc2"
76  puts $MRpt "Cyl Length Compaction  = $Lr"
77  puts $MRpt "=          END Simulation Discription           ="
78  puts $MRpt "================================================="
79  puts $MRpt " "
80  puts $MRpt " "
81  puts $MRpt "================================================="
82  puts $MRpt "=              Program Information              ="
83  puts $MRpt "================================================="
84  puts $MRpt "[code_info]"
85  puts $MRpt "=            END Program Information            ="
86  puts $MRpt "================================================="
87  puts $MRpt " "
88
89  ###############################################################
90  # Random Number Generator Related                             #
91  ###############################################################
92  # Random Number Generator Seed shift
93  set rngoffset 63498
94  puts $MRpt " "
95  puts $MRpt "================================================="
96  puts $MRpt "=       Random Number Generator Related         ="
97  puts $MRpt "================================================="
98  puts $MRpt "Defult Seeds: [t_random seed]"
99  puts $MRpt "Defult Status:"
100 puts $MRpt "[t_random stat]"
101
102 set cmd "t_random seed"
103 for {set i 0} {$i < [setmd n_nodes]} { incr i } {
104   lappend cmd [expr [pid] + $i + $rngoffset]
105 }
106 eval $cmd
107 puts "n_nodes = [setmd n_nodes];\n"
108 puts $MRpt "n_nodes = [setmd n_nodes];"
```

```
109 puts $MRpt "Returned Seeds: [t_random seed]"
110 puts $MRpt "Returned Status:"
111 puts $MRpt "[t_random stat]"
112 puts $MRpt "=     END Random Number Generator Related      ="
113 puts $MRpt "================================================="
114 puts $MRpt " "
115
116 ###################################################################
117 #  Interaction Parameters                                         #
118 ###################################################################
119 # 6th root of 2
120 set SixthRoot2  1.12246204830937
121 # Define particle sizes
122 set r_mono 0.5
123 set r_crow1 [expr 0.5 * $ac1]
124 set r_crow2 [expr 0.5 * $ac2]
125 set r_wall 0
126
127 # repulsive Lennard Jones (WCA)
128 set lj_eps_mm     1.0
129 set lj_sig_mm     [expr 2*$r_mono]
130 set lj_cut_mm     [expr $lj_sig_mm * $SixthRoot2]
131 set lj_shift_mm   [calc_lj_shift $lj_sig_mm $lj_cut_mm]
132 set lj_off_mm     0.0
133
134 set lj_eps_c1c1     1.0
135 set lj_sig_c1c1     [expr 2*$r_crow1]
136 set lj_cut_c1c1     [expr $lj_sig_c1c1 * $SixthRoot2]
137 set lj_shift_c1c1   [calc_lj_shift $lj_sig_c1c1 $lj_cut_c1c1]
138 set lj_off_c1c1     0.0
139
140 set lj_eps_c1c2     1.0
141 set lj_sig_c1c2     [expr $r_crow1 + $r_crow2]
142 set lj_cut_c1c2     [expr $lj_sig_c1c2 * $SixthRoot2]
143 set lj_shift_c1c2   [calc_lj_shift $lj_sig_c1c2 $lj_cut_c1c2]
144 set lj_off_c1c2     0.0
145
```

```
146 set lj_eps_c2c2     1.0
147 set lj_sig_c2c2     [expr 2*$r_crow2]
148 set lj_cut_c2c2     [expr $lj_sig_c2c2 * $SixthRoot2]
149 set lj_shift_c2c2   [calc_lj_shift $lj_sig_c2c2 $lj_cut_c2c2]
150 set lj_off_c2c2     0.0
151
152 set lj_eps_mc1     1.0
153 set lj_sig_mc1     [expr $r_mono + $r_crow1]
154 set lj_cut_mc1     [expr $lj_sig_mc1 * $SixthRoot2]
155 set lj_shift_mc1   [calc_lj_shift $lj_sig_mc1 $lj_cut_mc1]
156 set lj_off_mc1     0.0
157
158 set lj_eps_mc2     1.0
159 set lj_sig_mc2     [expr $r_mono + $r_crow2]
160 set lj_cut_mc2     [expr $lj_sig_mc2 * $SixthRoot2]
161 set lj_shift_mc2   [calc_lj_shift $lj_sig_mc2 $lj_cut_mc2]
162 set lj_off_mc2     0.0
163
164 set lj_eps_mw     1.0
165 set lj_sig_mw     [expr $r_mono + $r_wall]
166 set lj_cut_mw     [expr $lj_sig_mw * $SixthRoot2]
167 set lj_shift_mw   [calc_lj_shift $lj_sig_mw $lj_cut_mw]
168 set lj_off_mw     0.0
169
170 set lj_eps_c1w     1.0
171 set lj_sig_c1w     [expr $r_crow1 + $r_wall]
172 set lj_cut_c1w     [expr $lj_sig_c1w * $SixthRoot2]
173 set lj_shift_c1w   [calc_lj_shift $lj_sig_c1w $lj_cut_c1w]
174 set lj_off_c1w     0.0
175
176 set lj_eps_c2w     1.0
177 set lj_sig_c2w     [expr $r_crow2 + $r_wall]
178 set lj_cut_c2w     [expr $lj_sig_c2w * $SixthRoot2]
179 set lj_shift_c2w   [calc_lj_shift $lj_sig_c2w $lj_cut_c2w]
180 set lj_off_c2w     0.0
181
182 puts $MRpt " "
```

```
183 puts $MRpt "=============================================================="
184 puts $MRpt "=        Interaction Parameters Check                        ="
185 puts $MRpt "=============================================================="
186
187 puts $MRpt "lj_shift_mm   = $lj_shift_mm"
188 puts $MRpt "lj_shift_c1c1 = $lj_shift_c1c1"
189 puts $MRpt "lj_shift_c1c2 = $lj_shift_c1c2"
190 puts $MRpt "lj_shift_c2c2 = $lj_shift_c2c2"
191 puts $MRpt "lj_shift_mc1  = $lj_shift_mc1"
192 puts $MRpt "lj_shift_mc2  = $lj_shift_mc2"
193 puts $MRpt "lj_shift_mw   = $lj_shift_mw"
194 puts $MRpt "lj_shift_c1w  = $lj_shift_c1w"
195 puts $MRpt "lj_shift_c2w  = $lj_shift_c2w"
196
197 # attractive FENE bond
198 set fene_k       30.0
199 set fene_r        1.5
200
201 puts $MRpt "=      End Interaction parameters Check                      ="
202 puts $MRpt "=============================================================="
203 puts $MRpt " "
204
205 ###################################################################
206 #   MD Parameters                                                 #
207 ###################################################################
208 setmd time_step $MDtime_step
209 setmd skin      $MDskin
210 thermostat langevin $LangTemp $LangFrac
211 setmd box_l $bw $bw $bl
212
213 ###################################################################
214 #   Setup Particles                                               #
215 ###################################################################
216 # cylindrical boundary
217 constraint cylinder center $cw $cw $cl axis 0 0 1 radius $R length $L
    direction -1 type 5 penetrable 0 reflecting 1
```

```
218 constraint cylinder center $cw $cw $cl axis 0 0 1 radius [expr $R + $Outer]
    length [expr $L + $Outer] direction -1 type 6 penetrable 0 reflecting 1
219 puts $MRpt " "
220 puts $MRpt "=========================================================="
221 puts $MRpt "=          Particle Parameters Check                     ="
222 puts $MRpt "=========================================================="
223 puts $MRpt "constraint(s):"
224 puts $MRpt "[constraint]"
225
226 # Particle setup
227 set DistL_mono  [expr $L - 1.5 * $r_mono]
228 set DistR_mono  [expr $R - $Rr * $r_mono]
229 set n_long_top  [expr {floor(0.5 * $Nm * $DistL_mono / ($DistL_mono +
    $DistR_mono))}]
230 set n_lat_right [expr {floor(0.5 * $Nm - $n_long_top)}]
231 set n_long_bot $n_long_top
232 set n_lat_left [expr $Nm - $n_long_top - $n_lat_right - $n_long_bot]
233
234 set top_step   [expr 2*$DistL_mono/$n_long_top]
235 set right_step [expr 2*$DistR_mono/$n_lat_right]
236 set bot_step   [expr 2*$DistL_mono/$n_long_bot]
237 set left_step  [expr 2*$DistR_mono/$n_lat_left]
238
239 for {set p 0} {$p < $N} {incr p} {
240   set i_t 0
241   set i_r 0
242   set i_b 0
243   set i_l 0
244   for {set i 0} {$i < $Nm} {incr i} {
245     set part_i [expr $p*$Nm + $i]
246     set pos_y  [expr $cw + $p - 0.5 * $N + 0.5]
247     if {[expr ($i < $n_long_top)]} {
248       set pos_x  [expr $cw + $DistR_mono]
249       set pos_z  [expr $cl - $DistL_mono + $i_t * $top_step]
250       set i_t [expr $i_t + 1]
251     } elseif {[expr ($i < ($n_long_top + $n_lat_right))]} {
252       set pos_x  [expr $cw + $DistR_mono - $i_r * $right_step]
```

```
253       set pos_z  [expr $cl + $DistL_mono]
254       set i_r [expr $i_r + 1]
255     } elseif {[expr ($i < ($n_long_top + $n_lat_right + $n_long_bot))]} {
256       set pos_x  [expr $cw - $DistR_mono]
257       set pos_z  [expr $cl + $DistL_mono - $i_b * $bot_step]
258       set i_b [expr $i_b + 1]
259     } else {
260       set pos_x  [expr $cw - $DistR_mono + $i_l * $left_step]
261       set pos_z  [expr $cl - $DistL_mono]
262       set i_l [expr $i_l + 1]
263     }
264     part $part_i pos $pos_x $pos_y $pos_z type 0
265   }
266 }
267 set n_mono [expr $part_i + 1]
268 puts $MRpt "$n_mono DNA beads are placed"
269
270 #Set up crowders1
271 set DistL_crow [expr $DistL_mono - 1.1 * $r_mono - 1.1 * $r_crow1]
272 set DistR_crow [expr $DistR_mono - 1.1 * $r_mono - 1.1 * $r_crow1]
273 for {set i 0} {$i < $Nc1} {incr i} {
274   set part_i [expr $n_mono + $i]
275   set pos_r  [expr $DistR_crow*[t_random]]
276   set pos_t  [expr 6.28318530718*[t_random]]
277   set pos_x  [expr $cw + $pos_r*cos($pos_t)]
278   set pos_y  [expr $cw + $pos_r*sin($pos_t)]
279   set pos_z  [expr $cl + 2.0*$DistL_crow*([t_random]-0.5)]
280   part $part_i pos $pos_x $pos_y $pos_z type 1
281 }
282 set n_crow1 [expr $part_i - $n_mono + 1]
283 puts $MRpt "$n_crow1 type 1 crowders are placed"
284
285 #Set up crowders2
286 set DistL_crow [expr $DistL_mono - 1.1 * $r_mono - 1.1 * $r_crow2]
287 set DistR_crow [expr $DistR_mono - 1.1 * $r_mono - 1.1 * $r_crow2]
288 for {set i 0} {$i < $Nc2} {incr i} {
289   set part_i [expr $n_mono + $n_crow1 + $i]
```

```
290   set pos_r  [expr $DistR_crow*[t_random]]
291   set pos_t  [expr 6.28318530718*[t_random]]
292   set pos_x  [expr $cw + $pos_r*cos($pos_t)]
293   set pos_y  [expr $cw + $pos_r*sin($pos_t)]
294   set pos_z  [expr $cl + 2.0*$DistL_crow*([t_random]-0.5)]
295   part $part_i pos $pos_x $pos_y $pos_z type 2
296 }
297 set n_crow2 [expr $part_i - $n_mono - $n_crow1 + 1]
298 puts $MRpt "$n_crow2 type 2 crowders are placed"
299
300 set n_part [setmd n_part]
301 puts $MRpt "Totally, $n_part particles are placed"
302 puts $MRpt "=        End Particle Parameters Check         ="
303 puts $MRpt "==============================================="
304 puts $MRpt " "
305
306 ############################################################
307 #   Setup Interactions                                     #
308 ############################################################
309 # Interactions for monomers
310 inter 0 0 lennard-jones $lj_eps_mm $lj_sig_mm $lj_cut_mm $lj_shift_mm
      $lj_off_mm
311 # Interactions for crowders
312 inter 1 0 lennard-jones $lj_eps_mc1 $lj_sig_mc1 $lj_cut_mc1 $lj_shift_mc1
      $lj_off_mc1
313 inter 2 0 lennard-jones $lj_eps_mc2 $lj_sig_mc2 $lj_cut_mc2 $lj_shift_mc2
      $lj_off_mc2
314
315 inter 1 1 lennard-jones $lj_eps_c1c1 $lj_sig_c1c1 $lj_cut_c1c1 $lj_shift_c1c1
       $lj_off_c1c1
316 inter 1 2 lennard-jones $lj_eps_c1c2 $lj_sig_c1c2 $lj_cut_c1c2 $lj_shift_c1c2
       $lj_off_c1c2
317 inter 2 2 lennard-jones $lj_eps_c2c2 $lj_sig_c2c2 $lj_cut_c2c2 $lj_shift_c2c2
       $lj_off_c2c2
318 # Interactions between constraints
319 inter 5 0 lennard-jones $lj_eps_mw $lj_sig_mw $lj_cut_mw $lj_shift_mw
      $lj_off_mw
```

```
320 inter 6 1 lennard-jones $lj_eps_c1w $lj_sig_c1w $lj_cut_c1w $lj_shift_c1w
    $lj_off_c1w
321 inter 6 2 lennard-jones $lj_eps_c2w $lj_sig_c2w $lj_cut_c2w $lj_shift_c2w
    $lj_off_c2w
322 # FENE bond between adjecent monomers
323 inter 0   FENE          $fene_k   $fene_r
324
325 #  Connect the last and the first monomer to form circular polymers
326 #  Connect particles together to ring polymers
327 for {set p 0} {$p < $N} {incr p} {
328   for {set i 1} {$i < $Nm} {incr i} {
329     set part_i0 [expr $p*$Nm + $i]
330     set part_i1 [expr $part_i0 - 1]
331     part $part_i0 bond 0 $part_i1
332   }
333   set part_i0 [expr $p*$Nm]
334   set part_i1 [expr $part_i0 + $Nm - 1]
335   part $part_i0 bond 0 $part_i1
336 }
337
338 puts $MRpt " "
339 puts $MRpt "=============================================================="
340 puts $MRpt "=            Interaction Settings                            ="
341 puts $MRpt "=============================================================="
342 puts $MRpt "Simulating a closed ring polymer chains with $n_mono beads,"
343 puts $MRpt "$n_crow1 type 1 crowders, and $n_crow2 type 2 crowders,"
344 puts $MRpt "in a simulation volume of length [setmd box_l] at temp [setmd
    temp] with gamma [setmd gamma]."
345 puts $MRpt "Interactions:"
346 puts $MRpt "[inter]"
347 puts $MRpt "=          End Interaction Settings                          ="
348 puts $MRpt "=============================================================="
349 puts $MRpt " "
350 puts "Simulating a closed ring polymer chains with $n_mono beads, $n_crow1
    type 1 crowders, and $n_crow2 type 2 crowders,"
351 puts "in a simulation volume of length [setmd box_l] at temp [setmd temp]
    with gamma [setmd gamma]."
```

```
352
353 ##################################################################
354 #   Prepare output of VTF file (for VMD)                         #
355 ##################################################################
356 set vtf_file [open "$name.vtf" w]
357 writevsf $vtf_file
358 writevcf $vtf_file
359
360 ##################################################################
361 #   Warm-up Integration (with capped LJ-potential)               #
362 ##################################################################
363 puts $MRpt " "
364 puts $MRpt "================================================="
365 puts $MRpt "=                Integration Log                ="
366 puts $MRpt "================================================="
367 puts $MRpt "Particle coordinats are recorded in $name.vtf."
368 puts $MRpt "Frame to frame time is $FrameTime."
369 setmd time 0
370 set cap $warm_cap_init
371 set n_step_warm [expr {int($warm_step/$MDtime_step)}]
372 set n_loop_warm [expr $warm_time/$warm_step]
373 set f_loop_warm [expr $FrameTime/$warm_step]
374 set n_fram_warm [expr $warm_time/$FrameTime]
375 puts "Warm up has $n_loop_warm loops, which are sampled in $n_fram_warm
      frames."
376 puts $MRpt " "
377 puts $MRpt "Warm up has $n_loop_warm loops, which are sampled in $n_fram_warm
       frames."
378
379 set Fm 0
380 set StartTime [clock seconds]
381 set MDtime [setmd time]
382 if {[expr ($CompactionRatio < 1)]} {
383   set Lc [expr $L * pow($CompactionRatio,-$n_loop_warm*0.1)]
384   set Rc [expr $R * pow($CompactionRatio,-$n_loop_warm*0.1)]
385   constraint delete
```

```
386   constraint cylinder center $cw $cw $cl axis 0 0 1 radius $Rc length $Lc
        direction -1 type 5 penetrable 0 reflecting 1
387   constraint cylinder center $cw $cw $cl axis 0 0 1 radius [expr $Rc + $Outer
        ] length [expr $Lc + $Outer] direction -1 type 6 penetrable 0 reflecting 1
388 } else {
389   set Lc $L
390   set Rc $R
391 }
392 puts $MRpt "Frame MDTime    LJ's cap    Temperature CylL"
393 puts $MRpt "$Fm, $MDtime, $warm_cap_init, 0, $Lc, $Rc;"
394 for { set j 0 } { $j < $n_fram_warm } { incr j } {
395   for { set f 0 } { $f < $f_loop_warm } { incr f } {
396     inter forcecap $cap
397     integrate $n_step_warm
398     set MDtime [setmd time]
399     set temp [expr [analyze energy kin]/$n_part/([degrees_of_freedom]/2.0)]
400     set cap [expr $cap * $warm_incr]
401     if {[expr ($CompactionRatio < 1)]} {
402       set wstep [expr $j*$f_loop_warm + $f]
403       if {[expr ($wstep % 10) == 0]} {
404         set Lc [expr $Lc * $CompactionRatio]
405         set Rc [expr $Rc * $CompactionRatio]
406         constraint delete
407         constraint cylinder center $cw $cw $cl axis 0 0 1 radius $Rc length
      $Lc direction -1 type 5 penetrable 0 reflecting 1
408         constraint cylinder center $cw $cw $cl axis 0 0 1 radius [expr $Rc +
      $Outer] length [expr $Lc + $Outer] direction -1 type 6 penetrable 0
      reflecting 1
409       }
410     }
411   }
412 writevcf $vtf_file
413 set Fm [expr $Fm + 1]
414
415 puts "t = $MDtime, LJ's cap = $cap, Temp = $temp, Lc = $Lc, Rc = $Rc."
416 flush stdout
417
```

```
418 puts $MRpt "$Fm, $MDtime, $cap, $temp, $Lc;"
419 }
420
421 ###############################################################
422 #    Lag Integration (with full LJ-potential)                 #
423 ###############################################################
424 # lag portion, allowing chain to stablize
425 puts "\nRemove capping of LJ-interactions."
426 inter forcecap 0
427
428 constraint delete
429 constraint cylinder center $cw $cw $cl axis 0 0 1 radius $R length $L
        direction -1 type 5 penetrable 0 reflecting 1
430 constraint cylinder center $cw $cw $cl axis 0 0 1 radius [expr $R + $Outer]
        length [expr $L + $Outer] direction -1 type 6 penetrable 0 reflecting 1
431
432 set n_step_lag [expr {int($FrameTime/$MDtime_step)}]
433 set n_fram_lag [expr $lag_time/$FrameTime]
434
435 puts $MRpt " "
436 puts $MRpt "Lagging has $n_fram_lag frames, with capping of LJ-interactions
        removed."
437 puts "Lag Integration has $n_fram_lag frames."
438 puts $MRpt "Frame MDTime    Temperature"
439 for { set j 0 } { $j < $n_fram_lag } { incr j } {
440   integrate $n_step_lag
441   puts " Lagging step [expr $j+1]/$n_fram_lag (t=[setmd time]): "
442   flush stdout
443   writevcf $vtf_file
444   set Fm [expr $Fm + 1]
445   set MDtime [setmd time]
446   set temp [expr [analyze energy kin]/$n_part/([degrees_of_freedom]/2.0)]
447   puts $MRpt "$Fm, $MDtime, $temp;"
448 }
449
450 ###############################################################
451 #   Compaction Integration (with full LJ-potential)           #
```

```
452 ##################################################################
453 if {[expr ($comp_time > 0)]} {
454 set n_step_comp [expr {int($FrameTime/$MDtime_step)}];#100/0.002
455 set n_loop_comp [expr $comp_time/$comp_step];#10000/100
456 set f_loop_comp [expr $comp_step/$FrameTime];#100/100
457 set n_fram_comp [expr $comp_time/$FrameTime];#10000/100
458 set CompLoops [expr round((1-$Lr)/$Cr)];#(1-0.4)/0.1
459 puts $MRpt " "
460 puts $MRpt "Compaction has $n_fram_comp frames."
461 puts "Compaction Integration has $n_fram_comp frames."
462 puts $MRpt "Frame MDTime    CylL    Temperature"
463 set Lc $L
464
465 for {set c 0} {$c < $CompLoops} {incr c} {
466   set Lt [expr $L*(1 - ($c+1)*$Cr)]
467   for { set j 0 } { $j < $n_loop_comp } { incr j } {
468     if {[expr $Lc > $Lt]} {
469       set Lc [expr $Lc - $CompactionStep]
470       constraint delete
471       constraint cylinder center $cw $cw $cl axis 0 0 1 radius $R length $Lc
    direction -1 type 5 penetrable 0 reflecting 1
472       constraint cylinder center $cw $cw $cl axis 0 0 1 radius [expr $R +
    $Outer] length [expr $Lc + $Outer] direction -1 type 6 penetrable 0
    reflecting 1
473       puts "constraint(s): [constraint]"
474     }
475     for { set f 0 } { $f < $f_loop_comp } { incr f } {
476       integrate $n_step_comp
477       writevcf $vtf_file
478       set Fm [expr $Fm + 1]
479       set MDtime [setmd time]
480       set temp [expr [analyze energy kin]/$n_part/([degrees_of_freedom]/2.0)]
481       puts $MRpt "$Fm, $MDtime, $Lc, $temp;"
482     }
483     puts "Compaction step [expr $c + 1]/[expr round($CompLoops)]: [expr $j
    +1]/$n_loop_comp (t=[setmd time]): "
484   }
```

```
485 }
486
487 set Lc [expr $L * $Lr]
488 constraint delete
489 constraint cylinder center $cw $cw $cl axis 0 0 1 radius $R length $Lc
        direction -1 type 5 penetrable 0 reflecting 1
490 constraint cylinder center $cw $cw $cl axis 0 0 1 radius [expr $R + $Outer]
        length [expr $Lc + $Outer] direction -1 type 6 penetrable 0 reflecting 1
491 puts "constraint(s): [constraint]"
492 for { set j 0 } { $j < $n_fram_lag } { incr j } {
493   integrate $n_step_lag
494   puts " Extra Lagging step [expr $j+1]/$n_fram_lag (t=[setmd time]): "
495   flush stdout
496   writevcf $vtf_file
497   set Fm [expr $Fm + 1]
498   set MDtime [setmd time]
499   set temp [expr [analyze energy kin]/$n_part/([degrees_of_freedom]/2.0)]
500   puts $MRpt "$Fm, $MDtime, $temp;"
501 }
502 }
503
504 close $vtf_file
505 set EndTime [clock seconds]
506 set TimeTaken [expr $EndTime - $StartTime]
507 puts "\nFinished with simulation: $TimeTaken s"
508 puts "\nDone."
509 puts $MRpt "=              End Interaction Log              ="
510 puts $MRpt "================================================="
511 puts $MRpt "Finished with simulation."
512 puts $MRpt "Wallclock timetaken is $TimeTaken s."
513 close $MRpt
514 exit
```

D Estimation of Crowder Dimensions

Estimated of crowder diameters (a_c), numbers (N), volume fractions (Φ_0), concentrations (c_0) and crowding levels ($\rho_0\, a_c^2$) during normal growth conditions. % in the last columns shows crowding level for a given species relative to the total crowing level.

Slow growth

	a_c $[nm]$	N	Φ_0	c_0 [molecules/μm^3]	$\rho_0\, a_c^2$ $[\mu m^{-1}]$	%
Polysomes	84	975	0.43	1.41E+03	9.88	0.22
Subunits	14	1.02E+04	0.02	1.52E+04	2.98	0.06
70S	21	0	0.00	0	0.00	0.00
tRNA	4	1.35E+05	0.01	1.96E+05	3.13	0.07
Proteins	5	8.12E+05	0.08	1.18E+06	29.41	0.65
Total					45.4	

Moderately fast growth

	a_c $[nm]$	N	Φ_0	c_0 [molecules/μm^3]	$\rho_0\, a_c^2$ $[\mu m^{-1}]$	%
Polysomes	98	2942	1.00	2.88E+03	27.62	0.54
Subunits	14	1.35E+04	0.019	1.32E+04	2.59	0.05
70S	21	0	0	0	0.00	0.00
tRNA	4	4.05E+05	0.013	3.97E+05	6.35	0.12
Proteins	5	6.00E+05	0.038	5.88E+06	14.71	0.29
Total					51.3	

Slow growth + Rifampicin

	a_c $[nm]$	N	Φ_0	c_0 [molecules/μm^3]	$\rho_0\, a_c^2$ $[\mu m^{-1}]$	%
Polysomes	84	0	0.000	0	0.00	0.00
Subunits	14	3.00E+04	0.062	4.35E+04	8.52	0.21
70S	21	0	0.000	0	0.00	0.00
tRNA	4	1.35E+05	0.007	1.96E+05	3.13	0.08
Proteins	5	8.12E+05	0.077	1.18E+06	29.41	0.72
Total					41.1	

Moderately fast growth + Rifampicin

	a_c $[nm]$	N	Φ_0	c_0 [molecules/μm^3]	$\rho_0\, a_c^2$ $[\mu m^{-1}]$	%
Polysomes	98	0	0.000	0	0.00	0.00
Subunits	14	9.00E+04	0.127	8.82E+04	17.29	0.45
70S	21	0	0.000	0	0.00	0.00
tRNA	4	4.05E+05	0.013	3.97E+05	6.35	0.17
Proteins	5	6.00E+05	0.038	5.88E+06	14.71	0.38
Total					38.4	

Estimation of crowder numbers

Following calculations are based on entries on Table 4-3. Number of Polysomes = (Total Ribosomes)x(Polysome Fraction)/(Ribosomes per Polysome) Number of Subunits = 2x(Total Ribosomes)x(Subunit Fraction) Number of tRNA = 9x(Total Ribosomes) According to ([BD08]) Number of proteins based on Table 4-3.

Estimation of polysome size

Polysome size is estimated from the diameter of 70S ribosome subunit (21 nm) and from the number ribosomes per polysome using Flory formula

$$a_{c,\,\text{polysome}} = a_{c,\,\text{ribosome}}\, N_{\text{ribo/poly}}^{3/5}.$$

Number ribosomes per polysome, $N_{\text{ribo/poly}}$, values are listed in Table 4-3. This size reflects the effective excluded volume size of polysome in polysome-polysome interaction and exceeds significantly (60 times) the excluded molecular volume of the polysome components. It can be expected that this size is an overestimation. Clearly, Flory formula is solely an estimation rather than a numerically accurate value, especially in the limit of a small number of monomers. Moreover, crowding from proteins can be expected to compact polysomes. We choose here to overestimate the size of polysomes to be confident in our claim that polysomes do not have the predominant contribution to the compaction.

Estimation of subunit sizes

30S and 50S shell volumes have been estimated to be $1.3\times10^3\ nm^3$ and $2.3\times10^3\ nm^3$ (Bionumbers, N. R. Voss 'Geometric Studies of RNA and Ribosomes, and Ribosome Crystallization' 2006 p. 97). Although both complexes are oblate shape treating them as spheres yields effective radii 6.8 nm and 8.2 nm, respectively. Furthermore, we consider both subunits to be of the same size with an average diameter, 15 nm.

Estimation of tRNA sizes

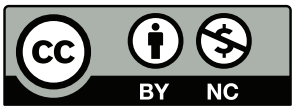
The estimate is based on yeast Phe tRNA volume of 36 nm^3 (Bionumbers, N. R. Voss 'Geometric Studies of RNA and Ribosomes, and Ribosome Crystallization' 2006 p. 97). This yields an average diameter of 4 nm. The effective volume fraction is likely an underestimation taken the boomerang-like shape of the molecule.

Estimation of protein sizes

Clearly, proteins and protein complexes have a broad range of sizes–from the small ones, the diameters of ~2 nm, to GroEL chaperone complex, which has a molecular volume comparable to a 70S ribosome. The latter is estimated to be about 10 times less abundant than ribosomes though [VLF11]. The available information remains too limited to calculate $\rho_i\, a_{c,\,i}^2$ for every protein. Therefore, we use 5 nm diameter as an average number as has been used in some estimations before [Odi98].

E License

This work is licensed under a Creative Commons "Attribution-NonCommercial 4.0 International" license.



Da Yang (杨答). 2020.

Vita

Da Yang (杨答) was born and raised by intellectual parents in Heilongjiang, China. Before attending the University of Tennessee, he attended Stony Brook University, where he earned a Bachelor of Science with majors in Physics and Mathematics, and a minor in Mechanical Engineering in 2011. He served as the treasurer and ME team leader of the Stony Brook Robot Design Team.

While at UT, Da passed the Physics Departmental Ph.D. qualifying exam with the high score. He studied and worked in the Männik Laboratory for seven years. He received a chancellor's citation for extraordinary professional promise. He published four peer-reviewed original research articles, three of which were first-authored by him. Additionally, he made eight poster presentations at various scientific conferences.

Outside classrooms and research labs, Da was a volunteer firefighter. He plays basketball and soccer. He has also served as a panelist for events organized by UT chapter of the Society of Physics Students and as a judge of UT-Exhibitions of Undergraduate Research and Creative Achievement.